New Applications of Atmospheric Noble Gases in Hydrogeology, Atmospheric Sciences, Paleoclimate and Tectonics

by

Rohit Balakrishna Warrier

A dissertation submitted in partial fulfillment
of the requirements for the degree of
Doctor of Philosophy
(Earth and Environmental Sciences)
in the University of Michigan
2013

Doctoral Committee:

Associate Professor Maria Clara Cruz Da Silva Castro, Chair
Associate Professor Avery H. Demond
Associate Research Scientist Chris Michael Hall
Professor Kyger C. Lohmann
Professor Daniele L. Pinti, Université du Québec à Montréal

To my family

ACKNOWLEDGEMENTS

I am deeply indebted to my advisor, Clara Castro for being a wonderful mentor and providing invaluable guidance throughout my Ph.D. Clara constantly encouraged me to address challenging research questions and has always pushed me to think critically about my research. I have learned a great deal under Clara's guidance and I am thankful for her patience and trust in my scientific ability through all these years. I look forward to her continued mentorship in the future. I also owe a great deal of thanks to Chris Hall for patiently answering my numerous queries and for our discussions that have helped me think more critically. I also extend my thanks to my committee members Kacey Lohmann, Avery Demond and Daniele Pinti for their thoughtful discussions and valuable feedback on my work presented in this dissertation. I am also thankful to past and present members of this research group especially Lin Ma, Jess Malone and Tao Wen, for helping me in this endeavor. My four years at Michigan have certainly been easier with all the help from the departmental staff especially Anne, Julie, Nancy, Dale, Jaimie, Janine and Bill. I am also thankful to many other faculty members for lending career advice and sharing their experiences.

My deepest gratitude goes to my family for their support and encouragement throughout graduate school. I also owe a great deal of thanks to some amazing friends and colleagues for showing me an especially good time in Michigan. Special thanks go to the various sports teams I was part of for keeping me active and focused. Finally, I would

like to thank Rackham and all other funding agencies for their financial assistance.

Thank you all!

TABLE OF CONTENTS

LIST OF TABLES

CHAPTER 2

CHAPTER 5

APPENDIX A

APPENDIX B

APPENDIX C

LIST OF FIGURES

CHAPTER 2

CHAPTER 3

CHAPTER 4

CHAPTER 5

LIST OF APPENDICES

.

ABSTRACT

Atmospheric noble gases are routinely used as a paleoclimate proxy in sedimentary systems. In contrast, noble gas studies in fractured media are rare. The work here presented pioneers the use of atmospheric noble gases as natural tracers of groundwater flow in fractured systems, and expands their use as a paleoclimate indicator in sedimentary systems. Pioneer noble gas work carried out in rainwater is also presented, and the connection between noble gas composition in precipitation and weather patterns investigated. Finally, atmospheric noble gases are also used to provide insights into the thermal history of a stable tectonic region.

The noble gas study in fractured media was carried out in the Galapagos Islands. The noble gas study in rainwater, the paleoclimate reconstruction, and the use of atmospheric noble gases to derive thermal and tectonic information were all carried out in southeast Michigan. Below, the main results of each one of these studies are presented.

Dissolved atmospheric noble gases from basal and perched aquifers in the Galapagos Islands of Santa Cruz and San Cristobal are used to identify location and timing of recharge of these fractured, basaltic hydrologic systems. Atmospheric noble gases from the basal aquifer and low-altitude springs record seasonality rather than the common mean annual air temperature (MAAT) typically recorded in sedimentary systems. However, samples from high-altitude springs point to recharge altitudes and temperatures inconsistent with conditions on the ground. These high-altitude springs display a unique, previously unknown noble gas pattern of Ne, Kr and Xe depletion together with relative Ar enrichment. It was hypothesized that this previously unknown noble gas pattern might be the result of mixing of low altitude (≤400m) fog droplets

with high-altitude (≥1.5 km) rainwater. The discovery of this unknown noble gas pattern in the Galapagos Islands lead to the first comprehensive study of noble gases carried out in rainwater, of which the first results are reported here. In addition to the presence of atmospheric He excesses, these results show that rainwater is in disequilibrium with surface conditions. Two noble gas patterns in rainwater emerge. The first one, associated with low pressure systems, presence of fog and light rainfall, displays a relative Ar enrichment together with Ne, Kr, and Xe depletion, similar to the pattern first identified in high-altitude springs in the Galapagos Islands. The second one, associated with the passage of frontal systems, displays a mass-dependent depletion pattern for Ne, Ar, Kr and Xe with respect to surface conditions. Precipitation associated with this pattern is characterized by thunderstorms, heavy rainfall, and high cloud ceiling heights. Noble gas patterns are shown to originate from ice and complete re-equilibration of noble gases in rainwater with surface conditions should occur within hours. These findings validate the use of noble gases as paleoclimate indicators in sedimentary systems where infiltration is slower that in fractured systems, and where NGTs are expected to represent the MAAT.

The noble gas temperature (NGT) study, carried out in the shallow Saginaw aquifer in southeast Michigan, extends over a ~13.1 kyr period and reveals an overall warming trend since the last glacial maximum (LGM). Here, the onset and termination of the Younger Dryas and Mid-Holocene climatic oscillations are identified for the first time based on NGTs. This record also suggests a change in air mass distribution over the Great lakes region during the late Mid-Holocene, and places new constraints on timing and sources of subglacial meltwater contributions from the Laurentide Ice Sheet, both prior and following the LGM. However, Saginaw aquifer samples located in the main discharge area of the Michigan Basin display

unusually large atmospheric noble gas excesses (~80%-120%) with respect to modern conditions and thus, cannot be used to derive paleoclimate information. Mechanisms leading to unusually large atmospheric noble gas excesses for these samples are examined. It is shown that these unusually large atmospheric excesses do not result from increased hydrostatic pressure but instead, are the result of sources external to the aquifer. Large excesses of atmospheric noble gases found in the discharge area are subsequently shown to be the remnants of a previously identified past thermal event in the Michigan Basin.

The work presented in this dissertation is of relevance to the fields of hydrogeology, hydrology, environment, meteorology, atmospheric and climate sciences, paleoclimatology, and tectonics.

CHAPTER 1

INTRODUCTION

Stable noble gases (He, Ne, Ar, Kr and Xe) are elements located in the rightmost column of the periodic table. Because of their orbital configurations and electron-filled outer shells, noble gases are chemically inert and stable and thus, are mostly sensitive to physical processes making them excellent geochemical tracers [e.g., *Ozima and Podosek*, 2002]. Consequently, the study of noble gases dissolved in groundwater systems has gained increasing importance in the last four decades. In addition to a brief overview of dissolved noble gases in groundwater systems, this introductory chapter provides a discussion on: (i) current issues and new research areas of the noble gas tracer; (ii) the goals of this dissertation in the context of the problems identified, and; (iii) how these goals are investigated in this dissertation.

Among the numerous applications of noble gas geochemistry, the study of noble gases dissolved in groundwater can enhance our understanding of surface and groundwater dynamics [e.g., *Andrews and Lee*, 1979; *Andrews et al.*, 1982; *Castro et al.*, 1998a; *Castro et al.*, 1998b], reconstruct past climatic records archived in groundwater [e.g., *Aeschbach-Hertig et al.,* 2002; *Kipfer et al.*, 2002; *Ma et al.*, 2004; *Castro et al.*, 2007a] as well as provide insights into the tectonic and thermal history of continental regions [e.g., *Castro et al.*, 2005; *Castro et al.*, 2007b; *Castro et al.*, 2009; *Ma et al.*, 2009a, b]. Dissolved noble gases in groundwater systems are derived from the atmosphere, crust and mantle, all of

which show distinct isotopic and elemental signatures [*Ozima and Podosek*, 2002; *Porcelli et al.*, 2002]. While crustal noble gases are produced by the radioactive decay of parent materials in rocks such as U/Th and ^{40}K for ^{4}He and ^{40}Ar, respectively, the mantle presents an important reservoir of primordial noble gases, which were trapped during the early accretion of the Earth [e.g., *Ozima and Podesek*, 2002]. This dissertation, on the other hand, is entirely focused on the atmospheric component of noble gases dissolved in groundwater systems.

The atmospheric component of noble gases is introduced into aquifer systems through dissolution in rainwater and subsequent infiltration of rainwater through the unsaturated zone of the recharge area to the water table. Infiltrated rainwater (or recharge water) at the water table, commonly referred to as air saturated water (ASW), is systematically assumed to be in equilibrium with the atmosphere in sedimentary aquifer systems. In addition to being inert and stable, solubility of atmospheric noble gases is also temperature dependent [*Weiss,* 1970, 1971; *Clever,* 1979]. Because atmospheric noble gases are conservative tracers and their concentrations in groundwater are temperature dependent, noble gas temperatures (NGTs) have long held out the promise of providing reliable information on absolute values of paleotemperature. In principle, NGTs are assumed to closely record the mean annual air temperature at the water table in sedimentary aquifer systems [*Stute and Sonntag*, 1992; *Stute and Schlosser*, 1993] and consequently, NGTs have been widely used to reconstruct the past climate in continental areas [e.g., *Mazor,* 1972; *Stute et al*., 1992, 1995; *Aeschbach-Hertig et al.*, 2002; *Kipfer et al.,* 2002; *Ma et al.,* 2004; *Castro et al*., 2012]. NGTs are calculated from the ASW component of noble gases dissolved in groundwater based on a small set of assumptions. These assumptions include: a) solubility equilibrium between noble gases and

water; b) noble gas partial pressures as determined by standard atmospheric values for the altitude of recharge; c) 100% relative humidity at the air-water interface, and; d) temperature dependent noble gas solubilities determined by ground temperature at the time of recharge. *Heaton and Vogel* [1981] found that in addition to a temperature-dependent ASW component, groundwater also incorporates an "excess air" (EA) component caused by incorporation and subsequent dissolution of trapped air bubbles in groundwater due to hydrostatic pressure increase caused by water table fluctuations. Because the concentrations of atmospheric noble gases in the recharge areas of groundwater systems are determined by a small number of physical properties, NGTs have been regarded as a robust indicator of past climate [e.g., *Stute and Schlosser*, 1993; *Kipfer et al.*, 2002; *Aeschbach-Hertig et al.*, 2002].

Consequently, for over four decades, NGT paleoclimate reconstructions have been carried out extensively in sedimentary aquifer systems throughout the world [e.g., *Andrews and Lee*, 1979; *Stute et al.*, 1992, 1995; *Aeschbach-Hertig et al.*, 2002; *Ma et al.*, 2004; *Castro et al.*, 2007a; *Varsányi et al.*, 2011]. More specifically, most NGT studies have focused on identifying major climatic events and, in particular, the contrast in temperatures between the Last Glacial Maximum (LGM; ~18 kyrs BP) and present time [e.g., *Kipfer et al.*, 2002]. However, the use of NGTs to identify abrupt climate shifts still remains rare [*Ma et al.*, 2004, *Castro et al.*, 2007a]. This is because it is generally assumed that in sedimentary groundwater flow systems, high-frequency noble gas climatic signals from abrupt climatic events are severely diminished or lost due to the effect of dispersion [*Stute and Schlosser*, 1993]. However, through a comparative analysis of both the impact of dispersion on high frequency climatic signals and assumptions underlying competing NGT models, *Castro et al.*

[2007a] showed that a number of hydrologic systems do have the ability to preserve short term (100–200 yrs) climatic fluctuations archived by noble gases.

Thus, one of the goals of this dissertation is to expand the present use of NGTs in sedimentary aquifer systems to identify abrupt climatic shifts. A thorough understanding of the abrupt variability of past climate is critical to fully understand our present climate and to predict future climate evolution.

Although noble gas studies have been systematically conducted in sedimentary aquifer systems throughout the world for four decades [e.g., *Stute et al.*, 1992, 1995; *Ma et al.*, 2004; *Castro et al.*, 2007a; *Varsányi et al.*, 2011], very few studies have been conducted in fractured and karstic groundwater systems, i.e., systems in which rapid water infiltration occurs. Indeed, fractured groundwater regions typically have complex internal structures and challenging access, are often poorly characterized with respect to groundwater resources and frequently suffer from freshwater scarcity and/or groundwater contamination problems. Two critical aspects to achieving an in depth and overall understanding of the hydrogeology of these systems are the identification of recharge areas and timing of recharge, commonly unknown in these regions. Because many volcanic islands present a steep altitude gradient and thus, a steep temperature gradient, in addition to having a climate characterized by two distinct seasons with markedly distinct average temperature and precipitation values, the atmospheric component of noble gases is expected to provide constraints on both the recharge locations and timing of recharge in these systems. Developing this new NGT application in fractured media is another goal of this dissertation and will be of great societal relevance to fractured groundwater systems as well as systems containing cavities (e.g., karst

environments) with thin soil cover that are present in extensive areas of the United States and throughout the world.

In summary, the goals of this dissertation are: (1) to assess whether or not NGTs can be applied in fractured, basaltic and karstic systems, i.e., in systems where infiltration is rapid to estimate both location and timing of recharge, and; (2) to expand the present use of the NGT proxy in sedimentary aquifer systems to identify abrupt climatic shifts in continental areas. A brief outline of how these goals are investigated is presented below in addition to the aims and scope of each of the chapters included in this dissertation.

To critically investigate whether or not NGTs can be applied in fractured and karstic, flow systems, i.e., in rapid infiltration areas (goal 1), a combined noble gas and stable isotope (δD, $\delta^{18}O$) study was undertaken in the fractured groundwater systems of the Galapagos Islands of Santa Cruz and San Cristobal. Detailed results and discussion of this investigation is presented in Chapter 2. Combined NGTs and stable isotope analyses demonstrate the utility of atmospheric noble gases in identifying recharge areas and timing of recharge in fractured and karstic systems, while providing specific answers with respect to recharge location, timing of recharge and groundwater residence times in these islands. In addition, a number of samples located at high altitudes in these islands display high apparent recharge altitudes, cold apparent temperatures and a unique, previously unknown noble gas pattern of Ne, Kr, and Xe depletion together with relative Ar enrichment. This study further explores various mechanisms to assess their potential at reproducing these patterns including, the impact of fog droplets and mixing of fog droplets and rainwater. However, a complete understanding of this unique noble gas pattern calls for a comprehensive study of noble gas composition in rainwater and is consequently investigated in Chapter 3 of this dissertation, as

described below. The study presented in Chapter 2 represents a benchmark in the development of NGTs in fractured groundwater systems and, more broadly, in rapid infiltration areas. This work was recently published in Water Resources Research [*Warrier et al*., 2012a].

Chapter 3 is aimed at understanding the origin of this previously unknown noble gas pattern in the Galapagos Islands through a comprehensive study of dissolved noble gases and helium isotopic ratios in rainwater samples collected in southeast Michigan during multiple precipitation events over a period of several months. Prior to this study, only four measurements of noble gas concentrations were available in rainwater in the Jordan Rift Valley, Israel [*Mazor*, 1972]. Chapter 3 presents the first comprehensive study of measured noble gas concentrations in rainwater together with multiple weather data at the time of sample collection. Such a combined analysis identifies two groups of rainwater noble gas patterns that are associated with local weather patterns and precipitation characteristics. The first one, associated with low-pressure systems, presence of fog and light rainfall, displays a relative Ar enrichment together with Ne, Kr, and Xe depletion, similar to the noble gas signature present in high-altitude springs in the Galapagos Islands. The second one, associated with the passage of frontal systems, displays a mass-dependent depletion pattern for Ne, Ar, Kr and Xe with respect to surface conditions. Precipitation for the second group of samples is characterized by thunderstorms, heavy rainfall, and high cloud ceiling heights. The origin of noble gases in rainwater is subsequently investigated using a simple diffusion mass-transfer model. Together with this model and measured noble gas concentrations in rainwater, raindrop sizes are derived for individual precipitation events. Time estimates for rainwater noble gas concentrations to re-equilibrate at the surface using actual rainwater

measurements are also provided in this study. Results indicate that complete re-equilibration of rainwater with surface conditions should occur within hours and suggest that rainwater noble gas patterns are not likely to be recorded in sedimentary aquifer systems which typically have thicker unsaturated zones and longer infiltration times. This, in turn, allows the use of noble gases in paleoclimatic reconstructions and leads to the second goal of this dissertation. This comprehensive study of noble gases in rainwater is critical to improving our understanding of the noble gas thermometer in paleoclimate studies as well as to expand the use of noble gases as tracers of groundwater circulation in fractured and karstic environments. This work has been submitted to *Geophysical Research Letters* [*Warrier et al.,* in revision].

To develop a detailed paleoclimate NGT record in southern Michigan and expand the present use of the NGT proxy in sedimentary aquifer systems to identify abrupt climatic shifts (goal 2), groundwater samples were collected from the shallow, sedimentary Saginaw aquifer in the Michigan Basin. Groundwater samples were analyzed for dissolved noble gases, stable (δD, $\delta^{18}O$) and carbon ($\delta^{13}C$ and ^{14}C activity) isotopes as well as major elements. Noble gas concentrations, stable isotope ratios and groundwater ages indicate two groups of samples. The first group displays groundwater ages from modern to younger than the LGM (~0-~18 kyr BP), stable isotope ratios close to values for modern Michigan rain and moderate noble gas excesses (~26-60% Ne excess) with respect to modern recharge conditions. These samples display robust NGT fits and are suited for a paleoclimatic reconstruction presented in Chapter 4. In contrast, the second group of samples, all of which are located in the main discharge area of the Michigan Basin, display ages beyond the LGM (~26.6 kyr- >50 kyr), extremely depleted δD, $\delta^{18}O$ values similar to values for modern

groundwater resulting directly from snowmelt and unusually high (~80%-120%) atmospheric noble gas excesses which result in poor NGT fits. Mechanisms leading to unusually large atmospheric noble gas excesses for these samples are investigated in detail in Chapter 5.

Chapter 4 presents a new ~13.1 kyr paleoclimatic record based on NGT, excess air and the stable isotope record derived from the Saginaw aquifer in southern Michigan. Together with the previous NGT record from the underlying Marshall aquifer [*Ma et al*., 2004], new aspects of late-Pleistocene and Mid-Holocene climate shifts in southern Michigan are revealed. Based on groundwater ages and the entire Saginaw stable isotope record, new constraints on the timing and sources of subglacial meltwater contributions to this system are also provided. This study highlights the utility of atmospheric noble gases in identifying abrupt climatic oscillations. This work was recently published in Geophysical Research Letters [*Castro et al*., 2012].

Chapter 5 systematically investigates the origin of unusually large atmospheric noble gas excesses in Saginaw aquifer samples located in the Saginaw Bay discharge area in the Michigan Basin. Through a step-by-step analysis and through comparison with the noble gas patterns of an aquifer system in southeast Wisconsin [*Klump et al*., 2008], this study first shows that large atmospheric noble gas excesses do not result from commonly observed water table fluctuations or development of ice cover but instead, are the result of sources external to the aquifer. Subsequently, this study shows that the large excesses of atmospheric noble gases found in the discharge area are likely the remnants of a previously identified past thermal event in the Michigan Basin and are compatible with Rayleigh type elemental fractionation controlled by diffusion or solubility related mechanisms. This study highlights the use of atmospheric noble gases in subsurface fluids to trace the thermal history of stable

tectonic regions. This work is currently in review in *Earth and Planetary Science Letters* [*Warrier et al*., in review].

A summary of major results and conclusions of this dissertation as well as future research questions motivated by this work is provided in Chapter 6. This dissertation has important societal relevance in fractured groundwater regions, which typically have scarce freshwater resources that are highly stressed. Results from this dissertation can contribute to improved water resource management plans in these regions through a better understanding of the hydrogeology of these systems. This dissertation also has important scientific implications in the fields of meteorology, paleoclimatology, hydrogeology and tectonics.

References

Aeschbach-Hertig, W., M. Stute, J. F. Clark, R. F. Reuter, and P. Schlosser (2002), A paleotemperature record derived from dissolved noble gases in groundwater of the Aquia Aquifer (Maryland, USA), *Geochim. Cosmochim. Acta*, 66(5), 797–817.

Andrews, J. N., and D. J. Lee (1979), Inert gases in ground water from the Bunter Sandstone of England as indicators of age and palaeoclimatic trends., *J. Hydrol.*, *41*, 233-252.

Andrews, J. N., I. S. Giles, R. L. F. Kay, D. J. Lee, J. K. Osmond, J. B. Cowart, P. Fritz, J. F. Barker, and J. Gale (1982), Radioelements, radiogenic helium and age relationships for groundwaters from the granites at Stripa, Sweden, *Geochim. Cosmochim. Acta*, *46*, 1533–1543.

Castro, M. C., A. Jambon, G. d. Marsily, and P. Schlosser (1998a), Noble gases as natural tracers of water circulation in the Paris Basin. 1. Measurements and discussion of their origin and mechanisms of vertical transport in the basin, *Water Resources Research*, *34*(10), 2443-2466.

Castro, M. C., P. Goblet, E. Ledoux, S. Violette, and G. d. Marsily (1998b), Noble gases as natural tracers of water circulation in the Paris Basin. 2. Calibration of a groundwater flow model using noble gas isotope data, *Water Resources Research*, *34*(10), 2467-2483.

Castro, M. C., D. Patriarche, and P. Goblet (2005), 2-D numerical simulations of groundwater flow, heat transfer and 4He transport – implications for the He terrestrial budget and the mantle helium-heat imbalance, *Earth and Planetary Science Letters*, *237*, 893-910.

Castro, M. C., C. M. Hall, D. Patriarche, P. Goblet, and B. R. Ellis (2007a), A new noble gas paleoclimate record in Texas – basic assumptions revisited, *Earth and Planetary Science Letters*, *257*, 170-187.

Castro, M. C., D. Patriarche, P. Goblet, L. Ma, and C. M. Hall (2007b), 4He/heat flux ratios as new indicators of past thermal and tectonic events — new constrains on the tectonothermal history of the Michigan Basin., in *The 4th Mini Conference on Noble Gases in the Hydrosphere and in Natural Gas Reservoirs*, edited, GFZ Potsdam.

Castro, M. C., L. Ma, and C. M. Hall (2009), A primordial, solar He-Ne signature in crustal fluids of a stable continental region, *Earth and Planetary Science Letters*, *279*(3-4), 174-184.

Castro, M. C., R. B. Warrier, C. M. Hall, and K. C. Lohmann (2012), A late Pleistocene-Mid-Holocene noble gas and stable isotope climate and subglacial record in southern Michigan, *Geophys. Res. Lett.*, *39*(19), L19709.

Clever H. L., ed. (1979) Krypton, Xenon, and Radon-Gas Solubilities. *Solubility Data Series 2*, International Union of Pure and Applied Chemistry (IUPAC). Pergamon.

Heaton, T. H. E., and J. C. Vogel (1981), "Excess air" in groundwater, *Journal of Hydrology*, *50*, 201-216.

Kipfer, R., W. Aeschbach-Hertig, F. Peeters, and M. Stute (2002), Noble Gases in Lakes and Ground Waters, *Reviews in Mineralogy and Geochemistry*, *47*(1), 615-700.

Klump, S., T. Grundl, R. Purtschert, and R. Kipfer (2008), Groundwater and climate dynamics derived from noble gas, 14C, and stable isotope data, *Geology*, *36*(5), 395-398.

Ma, L., M. C. Castro, and C. M. Hall (2004), A late Pleistocene-Holocene noble gas paleotemperature record in southern Michigan, *Geophys. Res. Lett.*, *31*(23), L23204.

Ma, L., M. C. Castro, and C. M. Hall (2009a), Crustal noble gases in deep brines as natural tracers of vertical transport processes in the Michigan Basin, *Geochem. Geophys. Geosyst.*, *10*(6), Q06001.

Ma, L., M. C. Castro, and C. M. Hall (2009b), Atmospheric noble gas signatures in deep Michigan Basin brines as indicators of a past thermal event, *Earth and Planetary Science Letters*, *277*(1-2), 137-147.

Mazor, E. (1972), Paleotemperatures and other hydrological parameters deduced from noble gases dissolved in groundwaters; Jordan Rift Valley, Israel, *Geochimica et Cosmochimica Acta*, *36*(12), 1321-1336.

Ozima, M., and F. A. Podosek (2002), *Noble gas geochemistry*, xiv, 286 p. pp., Cambridge University Press, Cambridge, UK ; New York.

Porcelli, D., C. J. Ballentine, and R. Wieler (2002), *Noble gases in geochemistry and cosmochemistry*, 844 pp.

Stute, M., and C. Sonntag (1992), Paleotempertures derived from noble gases dissolved in groundwater and in relation to soil temperature. In: Isotopes of Noble Gases as Tracers in Environmental Studies, paper presented at Proceedings of a consultants meeting on isotopes of noble gases as tracers in environmental studies, IAEA, Vienna, May 29 to June 2, 1989.

Stute, M., P. Schlosser, J. F. Clark, and W. S. Broecker (1992), Paleotemperatures in the southwestern United States derived from noble gases in ground water, *Science*, 256(5059), 1000–1001.

Stute, M., and P. Schlosser (1993), Principles and applications of the noble gas paleothermometer, in Climate Change in Continental Isotopic Records, *Geophys. Monogr. Ser.*, edited by P. K. Smart et al., vol. 78, pp. 89–100, AGU, Washington, D. C.

Stute, M., M. Forster, H. Frischkorn, A. Serjo, J. F. Clark, P. Schlosser, W. S. Broecker, and G. Bonani (1995), Cooling of tropical Brazil (5°C) during The Last Glacial Maximum, Science, 269(5222), 379–383.

Varsányi, I., L. Palcsu, and L. Ó. Kovács (2011), Groundwater flow system as an archive of palaeotemperature: Noble gas, radiocarbon, stable isotope and geochemical study in the Pannonian Basin, Hungary, *Applied Geochemistry*, *26*(1), 91-104.

Warrier, R. B., M. C. Castro, and C. M. Hall (2012), Recharge and source-water insights from the Galapagos Islands using noble gases and stable isotopes, *Water Resour. Res.*, *48*(3), W03508.

Weiss R. F. (1970) The solubility of nitrogen, oxygen and argon in water and seawater. *Deep-Sea Res.* 17, 721–735.

Weiss R. F. (1971) Solubility of helium and neon in water and seawater. *J. Chem. Eng.* Data 16, 235–241.

CHAPTER 2

RECHARGE AND SOURCE-WATER INSIGHTS FROM THE GALAPAGOS ISLANDS USING NOBLE GASES AND STABLE ISOTOPES [1]

Abstract

Through a combined noble gas and stable isotope study carried out in the Galapagos Islands of Santa Cruz and San Cristobal, we demonstrate the utility of atmospheric noble gases in identifying recharge areas and timing of recharge in fractured, basaltic systems. Timing of recharge obtained through noble gas temperatures (NGTs) for all samples is corroborated by stable isotopes. Except for one sample, combined NGTs and stable isotope analyses point to recharge during the hot season for all low altitude (<~420 m) spring samples from San Cristobal and all basal aquifer samples in Santa Cruz. Stable isotope comparisons also indicate that San Cristobal springs located at high altitudes (>420 m a.s.l) are recharged during both the "garúa" and hot seasons. Preservation of seasonality independently recorded by NGTs and stable isotopes is further reinforced by estimated young water ages.

[1] Citation: Warrier R. B., M. C. Castro, and C. M. Hall (2012), Recharge and source-water insights from the Galapagos Islands using noble gases and stable isotopes, *Water Resour. Res.*, 48, W03508, doi:10.1029/2011WR010954

Samples located at high altitude display systematic deviations of dissolved noble gases from expected air saturated water values and lead to inconsistent recharge altitudes and temperatures using standard NGT models. Existing degassing models are unable to account for the observed noble gas pattern for most samples. We explore various mechanisms to assess their potential at reproducing the observed noble gas signature. In particular, the potential impact of fog droplets during the cooler "garúa" season on dissolved noble gas concentrations in groundwater and the effect of mixing high-altitude (≥1500 m) rainwater with low-altitude (~400 m) fog droplets is explored. This mixing hypothesis is capable of explaining Ne and Xe concentrations for most high altitude samples.

2.1 Introduction

Among the numerous applications of noble gas geochemistry, the study of noble gases (He, Ne, Ar, Kr, and Xe) dissolved in groundwater can enhance our understanding of surface and groundwater dynamics by providing us with indications about flow paths, connectivity between aquifers, and water residence times [e.g., *Andrews and Lee*, 1979; *Andrews et al.*, 1982; *Bottomley et al.*, 1984; *Torgersen and Ivey*, 1985; *Stute et al.*, 1992; *Castro et al.*, 1998a; *Castro et al.*, 1998b; *Bethke et al.*, 1999; *Castro et al.*, 2005; *Castro et al.*, 2007]. In addition, because Ne, Ar, Kr, and Xe are conservative tracers and their concentrations in the recharge areas of groundwater systems are typically considered to be simply a function of temperature (T), pressure (P) (altitude of recharge area), salinity (S), and excess air (EA), noble gas temperatures (NGTs) have commonly been regarded as a potentially robust indicator of past climate [e.g., *Stute and Schlosser*, 1993; *Kipfer et al.*, 2002; *Sun et al.*, 2010].

For over four decades, noble gas studies in groundwater have been carried out extensively in sedimentary systems. However, to this day, few studies have been conducted in volcanic, fractured groundwater flow systems. These include the Cascades Volcanic Arc [*James et al.*, 2000, *Saar et al.*, 2005], Yellowstone [*Mazor, and Fournier*, 1973, *Mazor*, 1977, *Kennedy et al*., 1985, 1988, *Lowenstern and Hurwitz*, 2008, *Gardner et al.*, 2010], Cape Verde Islands [*Heilweil et al.*, 2009], the Azores archipelago [*Jean-Baptiste et al.*, 2009], and the Reunion [*Marty et al.*, 1993]. So far, however, none of these studies has taken advantage of information provided by NGTs. Unlike the islands of Santa Cruz and San Cristobal in the Galapagos, in which no volcanic and/or hydrothermal activity is present, most of these volcanic systems are extremely active and thus, are not comparable to our study area. Volcanic systems and equatorial and tropical basaltic islands in particular, typically have complex internal structures and challenging access, are often poorly characterized with respect to groundwater resources and frequently suffer from freshwater scarcity and/or groundwater contamination problems. The Galapagos Archipelago, a UNESCO World Heritage site, famous for its unique fauna and flora, is one example of such a region, and has historically been regarded as an inhospitable land due to a lack of this vital resource [e.g., *d'Ozouville*, 2007]. Development of a comprehensive long term freshwater exploitation and management plan will ensure preservation of natural habitats while providing the required potable water needs for the island's inhabitants. Such an exploitation and management plan requires an in-depth and overall understanding of the hydrogeology of these islands [e.g., *Adelinet et al.*, 2008; *d'Ozouville et al.*, 2008a; *d'Ozouville et al.*, 2008b; *Auken et al.*, 2009]. Two critical aspects to achieving such a goal are the identification of recharge areas as well as the timing of recharge, currently unknown in these systems.

Noble gases have previously been used to provide constraints on recharge locations and/or timing of recharge in different systems [e.g., *Aeschbach-Hertig et al.*, 1999; *Manning and Solomon*, 2003]. Because many basaltic islands present a steep altitude gradient and thus, a steep temperature gradient, in addition to having a climate characterized by two distinct seasons with markedly distinct average temperature and precipitation values, the atmospheric component of Ne, Ar, Kr, and Xe is expected to provide constraints on both recharge locations and timing of recharge in these systems. This last decade has seen a surge of studies dedicated to improving NGT estimation techniques as well as studies aimed at better understanding the behavior of noble gases in the unsaturated zone and at the water table/soil air interface in sedimentary systems [*Mercury et al.*, 2003, 2004, *Peeters et al.*, 2002, *Hall et al.*, 2005; *Castro et al.*, 2007; *Aeschbach-Hertig et al.*, 2008; *Cey et al.*, 2008; *Sun et al.*, 2008; *Cey et al.*, 2009; *Sun et al.*, 2010]. All these recent studies have led to an in-depth level of understanding of physical processes in sedimentary systems capable of affecting the atmospheric component of noble gases and thus, estimated NGTs, far greater than previously achieved. Similar studies in basaltic areas, however, have not yet been carried out.

Here, through a combined noble gas and stable isotope study carried out in the Galapagos Islands of Santa Cruz and San Cristobal, we demonstrate the utility of atmospheric noble gases at identifying recharge areas and timing of recharge in basaltic systems, while providing specific answers with respect to recharge location, timing of recharge and groundwater residence times in these islands. Simultaneously, we highlight the need to conduct further in-depth noble gas studies in fractured and basaltic regions in particular, to enhance our understanding of processes capable of impacting NGTs in these systems and, in particular, capable of leading to the unexpected relative Ar excess and

simultaneous depletion of Ne, Kr, and Xe observed in a number of our samples.

2.2 Geological, Hydrogeological and Climate Regional Settings

The Galapagos Islands, located on the equator in the eastern Pacific Ocean, about 1000 km off the coast of Ecuador (Figures 2.1a and 2.1b) emerge from a shallow submarine platform which forms the western part of the East-West trending Carnegie Ridge on the Nazca plate [e.g., *Geist et al.*, 1988; *White et al.*, 1993]. Santa Cruz and San Cristobal (Figure 2.1b), two of the oldest islands (~1.3Ma and ~2.35Ma, respectively) [*Geist et al.*, 1986; *White et al.*, 1993], are located in the central and eastern most portion of the archipelago. Although *White et al.* [1993] comment that Santa Cruz and San Cristobal can both be considered (theoretically) active, so far as we know, neither has erupted in the past 10,000 years. Also, neither has an active geothermal system, and the youngest basalts on both are very primitive, making a shallow magma body unlikely [*Geist et al.*, 1986]. In practice, both islands can be considered inactive (L. Siebert and T. Simkin, Volcanoes of the world: An illustrated catalog of Holocene volcanoes and their eruptions, available online at http://www.volcano.si.edu/world, 2002; D. J. Geist, personal communication, 2011).

Studies of Santa Cruz and San Cristobal hydrogeological systems have recently intensified, with generation of digital elevation models, field based hydrological instrumentation, as well as extensive coverage by helicopter-borne electromagnetic prospecting [*d'Ozouville*, 2007; *d'Ozouville et al.*, 2008a; *d'Ozouville et al.*, 2008b; *Auken et al.*, 2009]. These studies identified: (1) a basal aquifer, which appears to be continuous, surrounds the islands and penetrates at least 9 km inland; and (2) perched aquifers on the southern, windward portion of both islands. Unlike San Cristobal, direct access to the basal

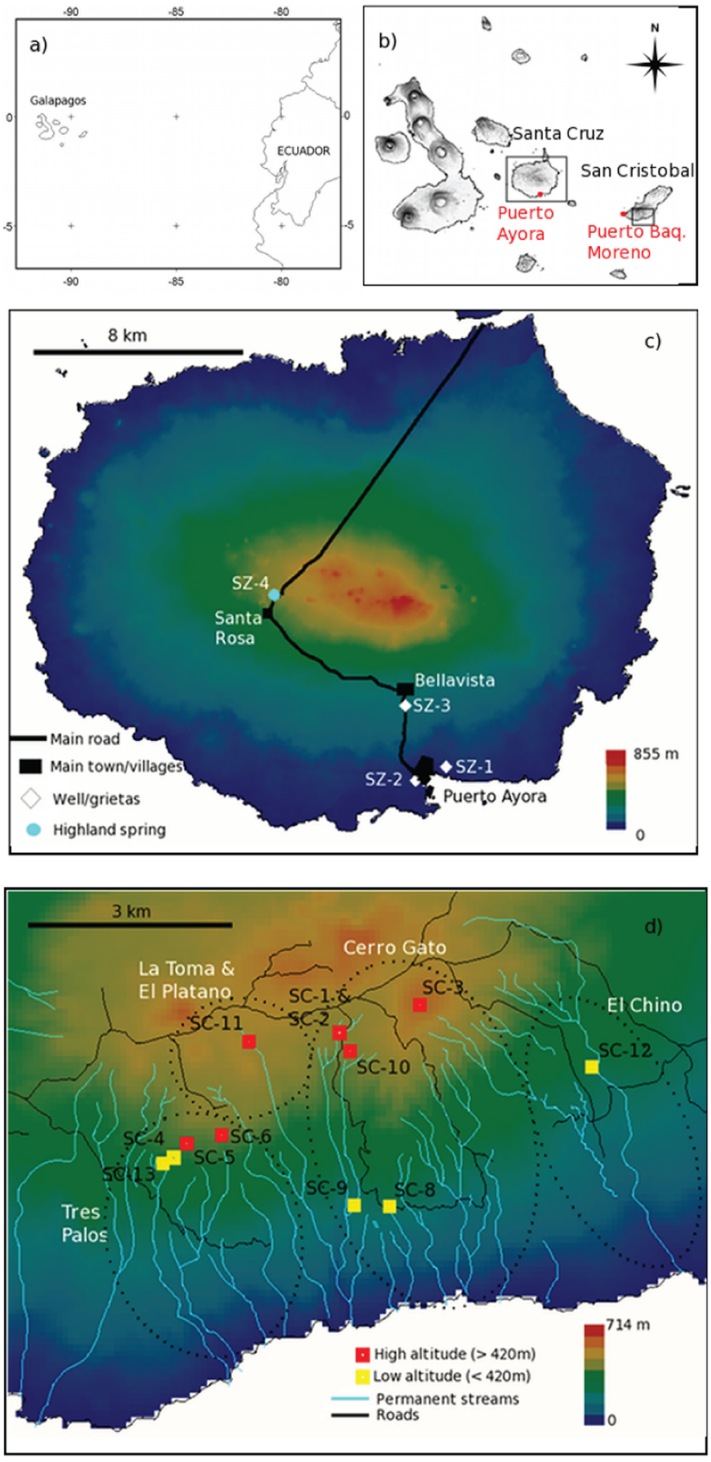

Figure 2.1 (a) Location of Galapagos Islands off the coast of Ecuador; **(b)** location of Santa Cruz and San Cristobal islands and the main inhabited towns; **(c)** Santa Cruz Island elevation from SRTM (Shuttle Radar Topography Mission) [*d'Ozouville et al.,* 2008b] data and sampled locations are indicated; **(d)** San Cristobal Islands elevation from SRTM data and location of springs sample (southern windward slope) are indicated. Springs are distinguished as high (>420 m) versus low altitude (<420 m).

aquifer in Santa Cruz is possible through "grietas" (open fractures) in the vicinity of the coastline. The latter basal aquifer was also intercepted at a depth of ~160 m near Bellavista [*Proctor and Redfern International Limited*, 2003] (Figure 2.1c) and is now locally exploited. Only one perennial spring is known in Santa Cruz; it is the outlet of a small perched aquifer located in a volcanic cone at Santa Rosa. An extensive (50 km^2) continuous hidden perched aquifer with no visible outcrops was also identified in Santa Cruz, while a series of discontinuous perched aquifers leading to multiple water spring alignments and the presence of perennial streams was identified in San Cristobal (Figure 2.1d) [*d'Ozouville*, 2007; *d'Ozouville et al.*, 2008a]. The presence of a perennial hydrographic system is unique to San Cristobal. A perennial lake located in the crater of a volcanic cone, El Junco, is also found in San Cristobal at 690 m of elevation.

Climate in the Galapagos Islands is characterized by a cool "garúa" season from June to December, and a rainy, hot season from January to May (Figure 2.2a) [*Trueman and d'Ozouville*, 2010]. Average "garúa" temperatures are 22.6±3.4°C (see http://www.darwinfoundation.org/datazone/darwin_weather) and 23.5±3.4°C (Figure 2.2; see http://www7.ncdc.noaa.gov/CDO/cdo) at sea level in Santa Cruz and San Cristobal respectively. During the "garúa" season, a stable, inversion cloud layer is present between ~300 m and the summit of the islands (870 m and 730 m respectively, for Santa Cruz and San Cristobal) [*d'Ozouville*, 2007]. This stable inversion layer brings moisture-laden mist to the upper portion of the islands. The hot, rainy season is characterized by short and intense episodes of precipitation (Figure 2.2a). Average temperatures during this season are 25.9±2.0°C at sea level and 24.9±1.5°C at 180 m in Santa Cruz (see http://www.darwinfoundation.org/datazone/darwin_weather) and 26.5±2.7°C at sea level in

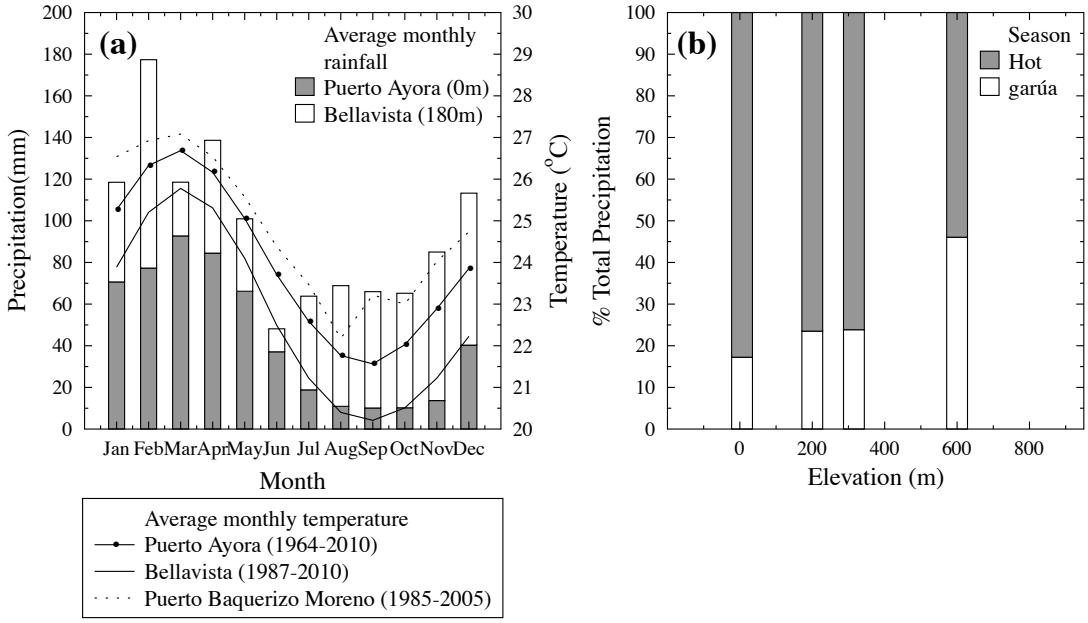

Figure 2.2 Meteorological information for Santa Cruz and San Cristobal **(a)** Monthly mean temperature and precipitation measurements from land weather stations located at Puerto Ayora (0 m a.s.l) and Bellavista (180 m a.s.l) in Santa Cruz, as well as Puerto Baquerizo Moreno (~0 m a.s.l), in San Cristobal. Monthly mean temperatures are indicated and averaged over extended time periods for each station as available. Monthly average precipitations obtained for Puerto Ayora and Bellavista for the same time period are indicated as bars. Monthly average precipitation at sea level (solid grey bars) in Santa Cruz is less than that observed at Bellavista (solid white bars, 180 m) throughout the year. **(b)** Measured % contribution of precipitation during each season in 1969 at different altitudes in Santa Cruz. Percent contribution from the hot season (Jan-May) is indicated by grey bars while contribution from the "garúa" season (Jun-Dec) is indicated by white bars. Percent contribution from the "garúa" season increases with altitude increase.

San Cristobal (Figure 2.2; see http://www7.ncdc.noaa.gov/CDO/cdo). These distinct seasonal temperature variations yield an average annual temperature of 24.0±3.9°C (see http://www.darwinfoundation.org/datazone/darwin_weather) and 24.8±4.3°C (see http://www7.ncdc.noaa.gov/CDO/cdo) at sea level in Santa Cruz and San Cristobal respectively.

In addition to seasonal variations in temperature and precipitation, temperature and precipitation also vary as a function of altitude. While annual average temperatures vary with a gradient of -0.8°C /100m [*d'Ozouville*, 2007] in Santa Cruz, average annual rainfall increases with altitude increase (see, e.g., Figure 2.2a). Precipitation-altitude patterns also indicate a greater contribution of "garúa" precipitation to the total annual precipitation with increasing altitude (Figure 2.2b). Indeed, while precipitation during the "garúa" season represents only ~17% of total annual precipitation at an elevation of 6 m above sea level (asl), it accounts for up to 46% of total annual precipitation at an elevation of 600 m asl [*Kramer and Black*, 1970]. In addition, preliminary estimations point to a non-negligible component of fog contribution to groundwater recharge during the "garúa" season at high altitude [*Dominguez et al.*, 2011]. A similar distribution of rainfall with altitude is observed in Santa Cruz [*d'Ozouville et al.*, 2008b]. While annual and monthly average temperatures and precipitations reflect available data over multiple years, large temperature and precipitation variations do occur from year to year. Such variations are particularly marked between El Nino and La Nina events [*d'Ozouville et al.*, 2008a] and need to be considered and discussed for comparison purposes.

2.3 Sampling and Analytic Methods

29 water samples were collected for analysis of noble gases at 16 different locations in

Santa Cruz and San Cristobal in October 2007, on the windward (southward), inhabited portion of the islands (Figures 2.1c and 2.1d). These include six samples collected in Santa Cruz at four locations (Figure 2.1c), five samples in the basal aquifer, three near Puerto Ayora at sea level, and two near Bellavista, in addition to one sample collected from the spring of Santa Rosa. In addition, 23 samples were collected in San Cristobal at 12 locations (Figure 2.1d) of which 21 samples are from springs located in the El Chino, Cerro Gato, La Toma, El Platano and the Tres Palos watershed areas (~200-570 m), and two samples are from the El Junco lake (690 m).

All samples were analyzed for He, Ne, Ar, Kr and Xe in the Noble Gas Laboratory at the University of Michigan. Sampling and analytical procedures are briefly described below and can be found in more detail in *Ma et al.* [2004], *Saar et al.* [2005], and *Castro et al.* [2009]. Water samples were also collected from each of the 16 sampling sites (Figures 2.1c and 2.1d) for measurement of δD and $\delta^{18}O$ in the Stable Isotope Laboratory at the University of Michigan following procedures described elsewhere [*Ma et al.*, 2004].

Water samples for noble gas analyses were collected in copper tubes (i.e., standard refrigeration grade 3/8" Cu tubing) and water was allowed to flow through for ~10 minutes. While the water flushed through the system, absence of gas bubbles that could potentially contaminate or phase fractionate the samples was checked through a transparent plastic tube mounted at the end of the copper tube. Copper tubes were then sealed by stainless steel pinch-off clamps [*Weiss*, 1968]. The copper tubes were subsequently attached to a vacuum extraction system and noble gases were quantitatively extracted for inletting into a MAP-215 mass spectrometer. Noble gases were transported using water vapor as a carrier gas through two constrictions in the vacuum system, purified, and sequentially allowed to enter a MAP-

215 mass spectrometer using a cryo-separator. The complete measurement procedure comprises measurement of He, Ne, Ar, Kr, and Xe concentrations, and their respective isotopic ratios, with standard errors for concentration measurements of 1.5, 1.3, 1.3, 1.5 and 2.2%, respectively. Noble gas concentrations are based on masses 4, 20, 36, 84 and 132 for He, Ne, Ar, Kr and Xe respectively.

2.4 Results and Discussion

2.4.1 Noble gas patterns

Sample names, location, altitude, water temperatures and electrical conductivity are provided in Table 2.1. Measured noble gas concentrations together with He and Ar isotopic ratios are given in Table 2.2. Noble gas concentrations in air saturated water (ASW) in equilibrium with the atmosphere for a temperature of 20ºC and altitudes of 0 and 421 m, are also indicated for comparison. 421 m corresponds to the average altitude of all spring samples. Figure 2.3 shows all samples normalized to ASW at average sampling elevations of 0 m (basal aquifer) and 421 m (springs) for an average temperature of 20ºC. This temperature value falls close to the range ($\pm 1\sigma$) of annual average temperature values at both sea level and 421 m in both islands. Annual average temperature values at 421 m were extrapolated from measured annual average temperatures at sea level in San Cristobal using the annual average temperature gradient of -0.8ºC/100m.

Results show excess He and Ar concentrations in many samples from both the basal aquifer and springs with respect to ASW (Figure 2.3). He excesses in all basal aquifer samples range from 7 to 49% that of ASW, while He excesses of up to 22% are observed for most of the spring samples. The origin of these He excesses are constrained through measured R/R_a values (Table 2.2, where R is the measured $^3He/^4He$ ratio, and R_a is the

Table 2.1 Sample numbers, Location, Altitude, Measured Water Temperature and Electrical Conductivity for All Samples

Sample No.	Latitude	Longitude	Altitude	Electrical conductivity	Water Temperature
	GWS.84 (South)	GWS.84 (West)	m (asl)	μScm^{-1} at 25℃	(°C)
			Santa Cruz		
sz1-1[a]	0.738	90.302	0	8810	22.8
sz2-1[a]	0.7462	90.3194	0	4140	16
sz2-2[a]	"	"	0	4140	"
sz3-1[a]	0.704	90.326	160	2550	22.5
sz3-2[a]	"	"	160	2550	"
sz4-1	0.641	90.403	500	129	18.7
			San Cristobal		
sc1-1	0.9002	89.4919	519	96	18.2
sc1-2	"	"	519	96	"
sc2-1	"	"	519	131	18.4
sc2-2	"	"	519	131	"
sc3-1	0.896	89.48	690	30	19
sc3-2	"	"	690	30	"
sc4-1	0.9172	89.5158	427	50	21.6
sc4-2	"	"	427	50	"
sc5-1	0.9154	89.514	447	35	20.4
sc5-2	"	"	447	35	"
sc6-1	0.9142	89.5089	463	57	18.8
sc6-2	"	"	463	57	"
sc8-1	0.9241	89.4848	229	86	21.4
sc9-1	0.9238	89.4898	229	91	21.7
sc9-2	"	"	229	91	"
sc10-1	0.9025	89.4904	417	38	20.3
sc10-2	"	"	417	38	"
sc11-1	0.9012	89.505	572	39	21.2
sc11-2	"	"	572	39	"
sc12-1	0.9048	89.4586	295	144	18.8
sc12-2	"	"	295	144	"
sc13-1	0.9181	89.5174	382	75	21.8
sc13-2	"	"	382	75	"

[a]Basal aquifer; With the exception of Lake El Junco (sc3-1,3-2) and samples collected in the basal aquifer all other samples correspond to springs from perched aquifers.

Table 2.2 Measured He, Ne, Ar, Kr and Xe Elemental Concentrations and He and Ar isotope ratios for All Samples[a]

Sample No.	He	Ne	Ar	Kr	Xe	R/R_a[b]	($^{38}Ar/^{36}Ar$)	($^{40}Ar/^{36}Ar$)
	10^{-8} cm^3 STP/g	10^{-7} cm^3 STP/g	10^{-4} cm^3 STP/g	10^{-8} cm^3 STP/g	10^{-9} cm^3 STP/g	(±1σ)	(±1σ)	(±1σ)
			Santa Cruz					
sz1-1	4.68	1.67	2.65	5.88	8.04	1.18 (0.03)	0.1858 (0.0028)	294.5 (1.75)
sz2-1	5.17	1.71	2.62	5.72	7.57	1.86 (0.05)	0.1879 (0.0021)	295.2 (0.86)
sz2-2	5.08	1.69	3.06	6.02	8.33	1.85 (0.06)	0.1877 (0.0049)	292.0 (1.04)
sz3-1	5.63	1.57	2.90	6.46	8.69	3.15 (0.08)	0.1835 (0.0033)	296.8 (0.96)
sz3-2	6.67	1.77	2.70	6.49	7.97	3.02 (0.09)	0.1882 (0.0024)	296.9 (0.96)
sz4-1	4.26	1.49	2.80	6.42	8.58	0.95 (0.04)	0.1920 (0.0044)	296.5 (1.36)
			San Cristobal					
sc1-1	4.49	1.65	3.21	6.80	9.13	1.02 (0.02)	0.1905 (0.0038)	293.8 (0.99)
sc1-2	4.53	1.63	3.38	6.89	9.52	1.03 (0.02)	0.1849 (0.0008)	291.8 (1.81)
sc2-1	3.93	1.49	2.60	5.76	8.12	1.01 (0.03)	0.1898 (0.0037)	295.6 (1.15)
sc2-2	4.60	1.61	3.13	6.86	9.53	0.97 (0.03)	0.1892 (0.0017)	296.2 (1.38)
sc3-1	4.38	1.59	2.81	6.09	8.37	0.97 (0.02)	0.1876 (0.0031)	294.8 (1.53)
sc3-2	4.42	1.55	2.83	4.93	6.35	0.99 (0.02)	0.1845 (0.0015)	291.1 (0.94)
sc4-1	4.45	1.63	2.62	5.49	7.30	1.04 (0.03)	0.1875 (0.0015)	293.8 (0.76)
sc4-2	4.22	1.53	2.90	6.30	8.27	1.01 (0.03)	0.1903 (0.0040)	295.5 (1.11)
sc5-1	5.18	1.72	2.87	5.57	7.40	0.96 (0.03)	0.1868 (0.0023)	294.4 (0.62)
sc5-2	4.72	1.58	2.78	5.56	7.65	1.13 (0.08)	0.1850 (0.0024)	293.4 (1.11)
sc6-1	4.47	1.51	2.62	5.46	7.29	1.05 (0.10)	0.1921 (0.0038)	292.6 (2.40)
sc6-2	3.84	1.48	2.20	4.50	6.17	1.02 (0.02)	0.1935 (0.0025)	296.1 (0.84)
sc8-1	4.52	1.67	2.86	5.69	7.46	0.99 (0.02)	0.1948 (0.0033)	294.5 (0.91)
sc9-1	4.92	1.81	2.97	5.99	8.27	0.98 (0.01)	0.1927 (0.0033)	294.5 (0.97)
sc9-2	5.03	1.86	2.87	5.89	8.24	0.98 (0.03)	0.1857 (0.0016)	295.6 (0.74)
sc10-1	4.25	1.66	3.05	6.38	8.41	0.98 (0.02)	0.1850 (0.0016)	295.5 (0.84)
sc10-2	4.68	1.62	2.99	6.34	8.89	1.16 (0.08)	0.1901 (0.0049)	293.5 (0.98)
sc11-1	4.60	1.74	2.80	5.82	7.87	1.00 (0.02)	0.1869 (0.0016)	296.8 (1.49)
sc11-2	4.82	1.67	2.96	7.04	8.66	1.09 (0.07)	0.1833 (0.0027)	294.2 (1.03)
sc12-1	4.47	1.45	3.11	7.06	9.55	1.00 (0.03)	0.1822 (0.0041)	297.0 (1.18)
sc12-2	4.59	1.74	3.01	6.32	8.51	1.01 (0.02)	0.1855 (0.0024)	296.5 (0.80)
sc13-1	4.57	1.66	2.85	5.98	8.09	1.01 (0.03)	0.1864 (0.0032)	295.0 (1.07)
sc13-2	4.48	1.67	3.07	5.72	7.61	1.00 (0.03)	0.1855 (0.0024)	293.3 (0.70)
ASW at 20°C, 0M NaCl, 0% excess air,0m altitude	4.48	1.85	3.12	6.98	9.57		0.1880	295.5
ASW at 20°C, 0M NaCl, 0% excess air,421m altitude	4.26	1.76	2.96	6.63	9.09			

[a]Measurement errors of noble gas concentrations are ±1.5%, ±1.3%, ±1.3%, ±1.5%, ±2.2% for He, Ne, Ar, Kr and Xe respectively.

[b]Helium isotope ratios, $R=^3He/^4He$, are normalized by the atmospheric value of $R_a=1.384 \times 10^{-6}$.

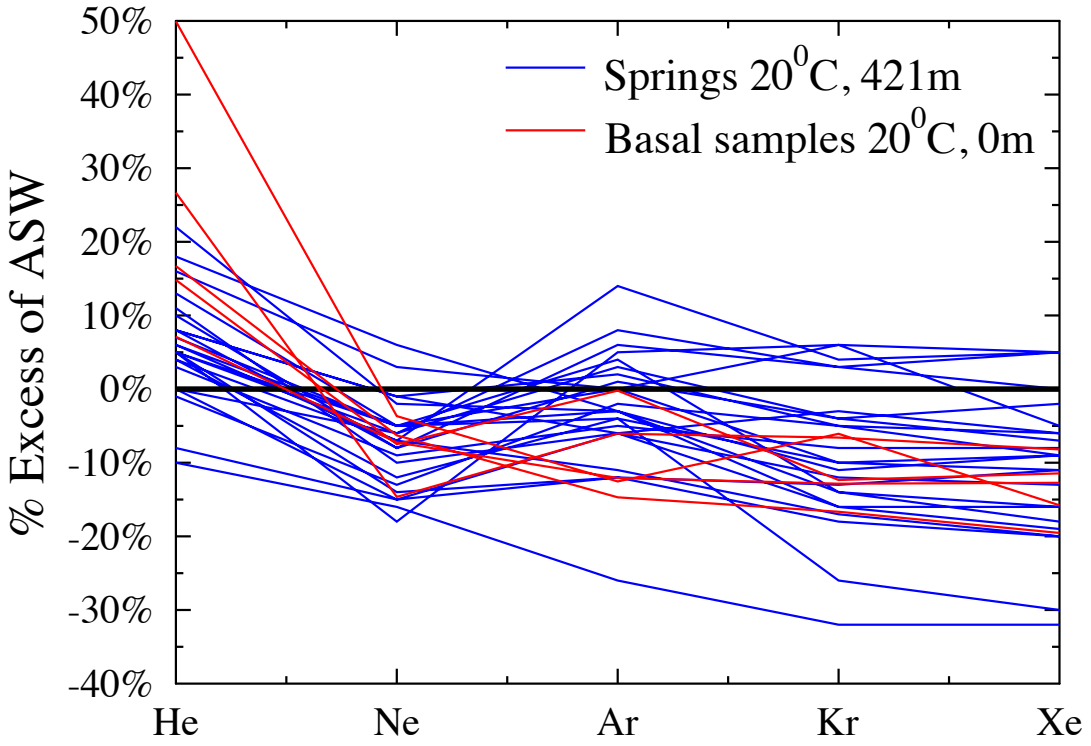

Figure 2.3 Measured noble gas concentrations relative to ASW at 20°C for all spring and basal aquifer samples from Santa Cruz and San Cristobal. Average altitude of 421 m and 0 m asl is assumed for all spring and basal aquifer samples respectively. Noble gas concentrations with no addition or loss of dissolved gases as compared to ASW are indicated by a solid black line.

atmospheric $^{3}He/^{4}He$ ratio of 1.384×10^{-6}) [*Clarke et al.,* 1976] and discussed below. Measured R/R_a for all spring samples vary between 0.095 ± 0.036 and 1.156 ± 0.082 while R/R_a for all basal aquifer samples vary between 1.176 ± 0.033 and 3.146 ± 0.075, respectively. In particular, measured R/R_a in as many as 13 out of 24 spring samples fall within $\pm 1\sigma$ error of the atmospheric value ($R/R_a = 1$), while the remaining 11 spring samples fall within $\pm 2\sigma$ error of the atmospheric value. Because R/R_a displays, for all spring samples, a value close to that of the atmospheric value ($R/R_a \approx 1$), the presence of a significant magmatic He component ($R/R_a \approx 8 \pm 1$) [*Farley and Neroda,* 1998] can be ruled out. Indeed, the slight He excesses observed in springs (~0% - 22%) can be readily explained by the addition of tritiogenic ^{3}He resulting from the β-decay of natural and bomb ^{3}H [see e.g., *Schlosser et al.*, 1988, 1989]. Excess of tritiogenic ^{3}He in spring samples together with measured tritium concentrations in precipitation allows estimation of groundwater residence times for these springs (cf. section 2.6). By contrast, R/R_a for all basal aquifer samples (Santa Cruz) are significantly higher than the atmospheric value ($> \pm 2\sigma$) and point to the presence of a significant mantle component. He component separation analyses of the Santa Cruz basal aquifer samples (not shown) [see e.g., *Castro et a.l*, 2000, *Castro*, 2004] indicates mantle He contributions between ~20 % and ~70% with respect to total He excesses. The presence of a significant mantle He component in the basal aquifer and its simultaneous absence in springs from perched aquifers suggests that springs represent shallow groundwater with short residence times (cf. section 2.6) that are shielded by the influx of external mantle He by the deeper basal aquifer. Mantle He excesses in the basal aquifer samples will be discussed in detail elsewhere. Excess Ar concentrations of up to 14% (measurement precision is 1.3%) with respect to ASW are observed in spring samples. Measured $^{38}Ar/^{36}Ar$ and $^{40}Ar/^{36}Ar$ ratios

(Table 2.2) for all samples (including basal aquifer samples) vary between 0.1882 ± 0.0041 and 0.1948 ± 0.0033 and 291.1 ± 0.94 and 297 ± 1.18, respectively. Ar isotopic ratios for all spring and basal aquifer samples are indistinguishable from ASW ($^{38}Ar/^{36}Ar$=0.1880; $^{40}Ar/^{36}Ar$=295.5) and indicate that the observed Ar excesses are of atmospheric origin. The presence of Ar excesses is discussed in detail below (section 2.7). While excesses are observed in He for most of the samples and Ar for many of the samples, the opposite is true for Ne, Kr, and Xe concentrations with most of the samples displaying a strong depletion with respect to ASW (Figure 2.3). While maximum observed Ne depletion with respect to ASW in springs and basal aquifer samples are 18% and 15% respectively, a much stronger depletion of the heavier noble gases Kr and Xe is observed. Maximum Kr depletion of up to 32% and 18% and Xe depletion of up to 32% and 21% with respect to ASW are observed for springs and basal aquifer samples, respectively (Figure 2.3). While this stronger Kr and Xe depletion might be an artifact of the chosen ASW temperature, it is apparent from Figure 2.3 that Ne, Kr and Xe deviations from ASW values are systematic. Such systematic noble gas deviations from the expected ASW values cannot be due to atmospheric contamination during sampling or noble gas measurements. In particular, Ne concentrations dissolved in water would be expected to increase if air contamination had taken place [see e.g., *Kipfer et al.*, 2002]. In addition to the observed systematic Ne, Kr and Xe depletion for a significant subset of samples, multiple samples (e.g. Sc5-1, 5-2) collected at the same location within half-an-hour to one-hour time intervals display varying measured noble gas concentrations. Although we do not have at the moment a definitive explanation for these varying concentrations, we have no reasons to believe that these result from a sampling artifact, at least for most samples. In particular, if this were to be the case, this would have rendered

impossible the identification of any patterns in our samples.

2.4.2 Preliminary estimate of recharge altitudes and equilibration temperatures

Concentrations of atmospheric noble gases dissolved in water record various physical parameters (e.g., temperature, excess air, altitude, salinity) at which final equilibration takes place. While concentrations of all atmospheric noble gases dissolved in water decrease with temperature increase, their sensitivity to temperature increases with increasing atomic mass [*Mazor*, 1972]. Thus, while Xe concentrations are the most sensitive to temperature of equilibration, Ne concentrations are the least. Hence, Ne concentrations normalized to Xe concentrations (Ne/Xe) will be independent of recharge altitude and mostly sensitive to temperature of equilibration. On the other hand, 1/Xe will depend on both temperature and recharge altitude of equilibration. Indeed, an increase in recharge altitude proportionally decreases concentrations of all dissolved noble gases due to a decrease in partial pressures of noble gases in the atmosphere.

Such a plot of 1/Xe vs. Ne/Xe can be used to estimate an initial range of altitude and temperature of equilibration for all our Galapagos water samples by comparing measured Ne and Xe concentrations along with loci of calculated expected values for ASW (Figure 2.4). Such a simplified comparison with ASW does not account for the addition of the excess air (A) component resulting from dissolution of small air bubbles due to rapid water table fluctuations [*Heaton and Vogel*, 1981]. Because the presence of Ne in water is particularly indicative of the addition or loss of excess air [*Herzberg and Mazor*, 1979], any addition of excess air will move samples to the right hand side of the diagram as indicated in Figure 2.4, while any excess air loss will move samples in the opposite direction.

Figure 2.4 shows all samples together with 1/Xe and Ne/Xe calculated for ASW at

altitudes varying between 0 and 3000 m and temperatures varying between 0 and 35°C. With the exception of one sample from San Cristobal (Sc12-1), which points to a recharge altitude >2000 m and a temperature of 10°C, comparison between measured data and calculated ASW values suggests that recharge altitudes of all samples from both Santa Cruz and San Cristobal vary from 0 m to 2000 m for temperatures varying between ~15°C and ~30°C. It is thus apparent that many samples, more specifically 16 samples, are recording equilibration recharge altitudes and temperature conditions that are not consistent with conditions on the ground. In sections 2.5, 2.6 and 2.7, these 16 samples are referred to as "inconsistent". In particular, some of these recharge altitudes are far greater than the summits of both Santa Cruz (870 m) and San Cristobal (730 m), and some of the temperatures are too low to be observed within the islands during either the "garúa" or the hot season. The unexpected observed relative Ar excess as well as depletion of Ne, Kr and Xe in inconsistent Galapagos samples points to unique equilibration processes that do not conform to key assumptions of the noble gas thermometer and NGT calculations [e.g., *Ballentine and Hall*, 1999; *Aeschbach-Hertig et al.*, 2000]. These mechanisms and, in particular, samples that display these unexpected noble gas patterns, are discussed later in this chapter (cf. section 2.7). Below we discuss results for all noble gas samples that display recharge altitudes and temperatures consistent with those in place in the islands, and show how NGTs and stable isotopes can be used to provide constraints both on recharge location and timing of recharge. These samples are referred to as "consistent" samples. Both consistent and inconsistent samples are clearly indicated in Figure 2.4. In addition, by using R/R_a ratios for all spring samples together with tritium measurements in precipitation, we place constraints on groundwater residence times for the perched aquifers of both islands (cf., section 2.6).

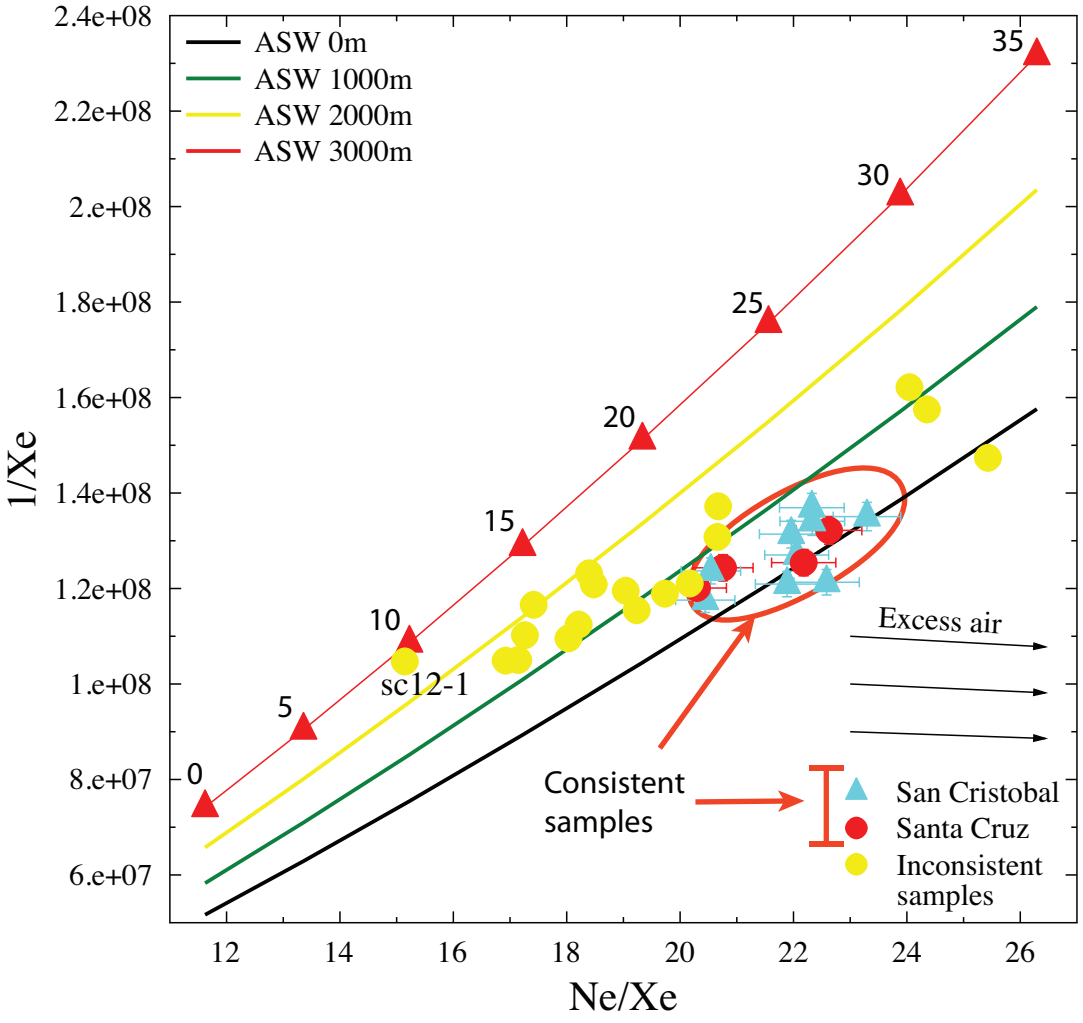

Figure 2.4 Preliminary estimate of recharge altitude and temperature by comparing measured 1/Xe vs. Ne/Xe for all consistent and inconsistent San Cristobal and Santa Cruz samples with theoretical ASW values. Y axis is a function of temperature and pressure (altitude) and X axis depends only on temperature. Solid lines indicate ASW values at altitudes between 0-3000 m and solid markers indicate temperatures between 0-35℃. Addition of excess air moves samples in the direction indicated.

2.5 Constraining recharge areas and timing of recharge

2.5.1 Noble Gas Temperatures (NGTs)

Noble gas temperatures (NGTs) derived from groundwater are generally assumed to reflect the mean annual air temperature (MAAT) and pressure conditions at the base of the aerated zone [*Stute and Sonntag*, 1992]. While this assumption has been verified through field experiments in sedimentary systems [*Klump et al.*, 2007], this might not be the case in mountain groundwater flow systems [*Manning and Solomon*, 2003]. Because of the presence of preferential flow paths in basaltic systems (e.g., fractures, lava tunnels), it is plausible that recharge water in these systems might reflect the temperature of the ground surface at the precise time of infiltration rather than the mean annual air temperature value as commonly assumed in sedimentary systems. Temperatures and altitudes at the time of recharge can be inferred using a standard unfractionated air (UA) model [*Stute and Schlosser*, 1993]. While the UA model provides an unbiased estimate of recharge altitude, the closed system equilibration (CE) model [*Aeschbach-Hertig et al.*, 2008] estimates recharge altitudes that are biased to high values [see, e.g., *Sun et al.*, 2010].

The UA model is the simplest lumped-parameter noble gas model that quantitatively accounts for both ASW and the presence of excess air in groundwater. Excess air is compositionally similar to atmospheric air [*Klump et al.*, 2007] and is lumped into a single parameter (A), representing the total volume of excess air per volume of water. Since the UA model assumes complete dissolution of excess air, final dissolved concentrations ($C_{i,final}$) for each noble gas *i* in water are given by the sum of air saturated water ($C_{i,eq}$) and excess air (A) as follows:

$$C_{i,final} = C_{i,eq}(1+AH_i) \quad \textbf{(2.1)}$$

where H_i represents the Henry's constant for noble gas *i*. Measured final dissolved concentrations of all four noble gases (Ne, Ar, Kr and Xe) are inverted for NGTs and constrained excess air ($A \geq 0$) assuming a particular recharge altitude value [cf., *Ballentine and Hall*, 1999]. While inverse problems that simultaneously estimate NGTs, excess air and recharge altitude using only measured Ne, Ar, Kr and Xe are ill posed, unique values for NGTs and excess air are obtained if recharge altitudes are known [*Manning and Solomon*, 2003]. UA model NGTs were calculated for all consistent water samples assuming various recharge altitudes, varying from sampling/spring altitude, which represents the minimal possible recharge altitude, up to 1000 m (Figures 2.5a and 2.5b) for successive 50 m increments (cf. Appendix A). Because a non-negative constraint is imposed on excess air, NGTs were derived only from those recharge altitudes that yielded zero or positive excess air values. Hence, a minimum recharge altitude for each sample was derived as the sampling altitude with non-negative excess air or lowest altitude beyond the sampling altitude with zero excess air. Figure 2.5 shows the results of all consistent samples calculated NGTs for individual water samples as a function of altitude compared with all possible altitude and temperature values within both islands. NGTs for individual water samples were first compared with extreme temperature-altitude relationships in Santa Cruz (Figure 2.5a) and San Cristobal (Figure 2.5b) as described in Appendix 1 at the end of this chapter (section 2.9).

Comparison between calculated sample NGTs and corresponding altitudes with extreme temperature-altitude transects in these islands clearly show that four Santa Cruz samples (sz1-1, 2-1, 2-2, 3-2) and nine San Cristobal samples (sc4-1, 5-1, 8-1, 9-1, 9-2, 11-1, 12-2, 13-1, 13-2) point to recharge occurring at temperatures and altitudes which are

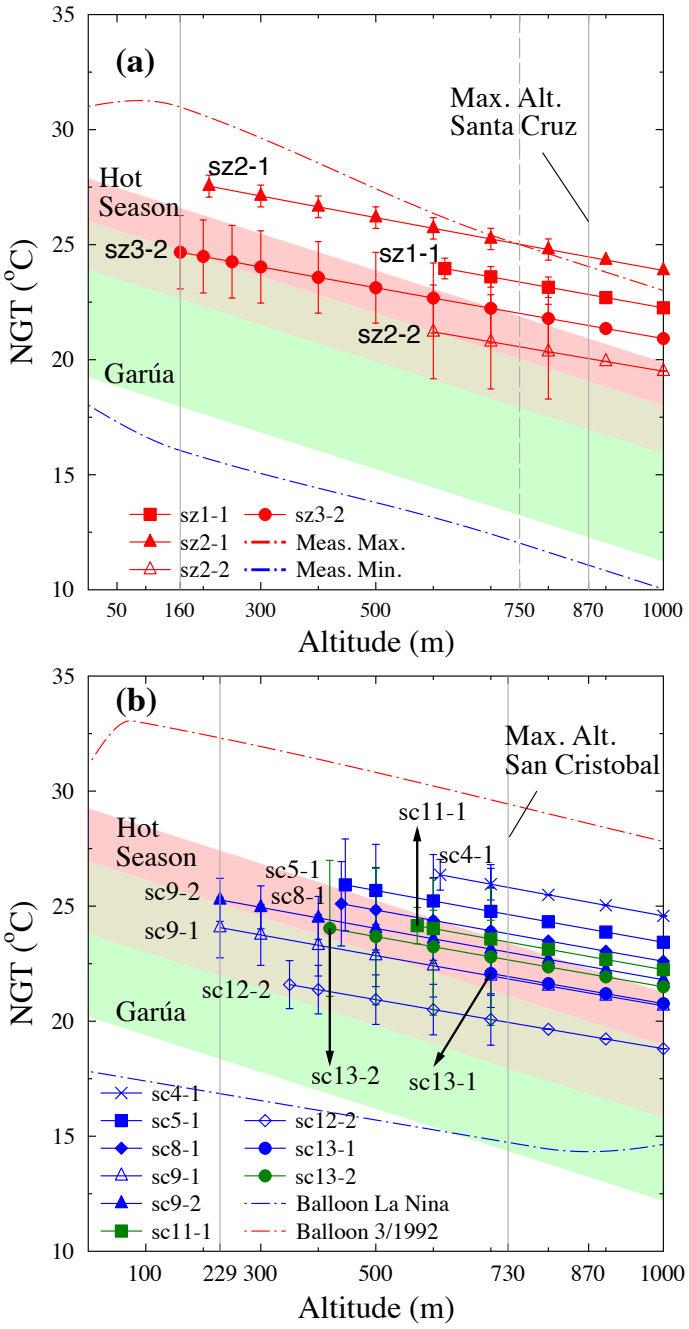

Figure 2.5 NGTs calculated assuming recharge altitudes for samples that fall within expected temperature and altitude ranges **(a)** Santa Cruz NGTs compared with monthly-mean maximum and minimum temperatures during (3/1992) and (9/2007) at Puerto Ayora and Bellavista. Shaded regions are average (1965 to 2010) "garúa" and hot season temperatures at Puerto Ayora ±1σ. Maximum, minimum and shaded average seasonal temperatures extrapolated using average gradient of -0.8°C/100m. **(b)** San Cristobal NGTs compared with monthly mean measured weather balloon temperatures during La Nina (9/2007) for extreme minimum and El Nino (3/1992) plus mean diurnal variation (7.15°C) for extreme maximum temperatures. Shaded regions indicate average (1985 to 2005) "garúa" and hot season temperatures at Puerto Baquerizo Moreno ±1σ, extrapolated using a gradient of -0.8°C/100m.

consistent with those in place in the islands (Figures 2.5a and 2.5b). Overall, it is apparent that recharge altitudes between 160 and 870 m and temperatures between 20.05±2.07°C and 27.54±0.47°C are found for Santa Cruz basal aquifer samples (Figure 2.5a) while recharge altitudes between 229 and 730 m and temperatures of 19.95±1.13°C and 26.36±0.66°C are found for San Cristobal spring samples (Figure 2.5b), suggesting that these are the altitude and temperature range values at which recharge occurs in these two islands, respectively. In addition, the minimum possible recharge altitude for four San Cristobal samples (Sc5-1, 9-1,9-2,11-1) and one Santa Cruz sample (Sz3-2) are the same as their sampling altitudes suggesting that some local recharge water may also contribute to these springs and basal aquifer. Maximum possible recharge altitudes for 12 out of 13 consistent samples from both San Cristobal and Santa Cruz correspond to the peak altitude of the islands as shown in Figure 2.5. However, sz2-1 points to a maximum recharge altitude of 750 m as corresponding NGTs beyond 750 m are greater than the extreme maximum temperature transect (cf. Figure 2.5a).

NGTs for consistent individual water samples are also compared with average seasonal temperatures in Santa Cruz and San Cristobal to constrain timing of recharge. Shaded regions indicate average seasonal temperatures ±1σ (Figure 2.5, dark green and pink for “garúa” and hot season respectively, light green, transition between the two). Average seasonal temperature versus altitude in Santa Cruz was derived by extrapolating the average (1964 - 2010) “garúa” (22.63±3.39°C) and hot season (25.9±1.98°C) temperatures in Puerto Ayora, by assuming a temperature gradient of -0.8°C/100m. Average seasonal temperature versus altitude in San Cristobal was derived by extrapolating the average (1985-2005) “garúa” (23.57±3.38°C) and hot season (26.53±2.72°C) temperature in Puerto Bacquerizo

Moreno (7.9 m a.s.l), assuming a temperature gradient similar to that of Santa Cruz.

Our NGT comparison for consistent water samples in Santa Cruz with the derived average seasonal temperature (Figure 2.5a) points unequivocally to dominant recharge during the hot season. All these samples are located in the basal aquifer. In addition, with the exception of one spring sample (Sc12-2), all other spring samples in San Cristobal (which display expected altitude and temperatures) point also to recharge occurring predominantly during the hot season (Figure 2.5b). It is of relevance to note that all these spring samples are located at low altitudes (<~420 m a.s.l). Based on these results, we can thus conclude that low altitude perched aquifers are also dominantly recharged during the hot season. Sc12-2, on the other hand, indicates likely recharge during both the "garúa" and the hot season.

As shown above, noble gases can be used as an effective tool to identify recharge areas as well as timing of recharge in fractured areas in general and basaltic aquifer systems in particular. Our NGT comparison for consistent water samples with expected altitude and temperature patterns points to recharge of all our basal aquifer samples in Santa Cruz and all low altitude springs (except sc12-2) in San Cristobal predominantly during the hot season. As seen below, NGT derived results on timing of recharge are corroborated by stable isotope analyses obtained for these same samples.

2.5.2 Stable isotopes

Stable isotope analyses of all Santa Cruz samples yield δD and $\delta^{18}O$ values between -13.5‰ and -8.85‰, and -3.1‰ and -2.13‰, respectively (Table 2.3, Figure 2.6a). Springs in San Cristobal yield δD and $\delta^{18}O$ between -11.46‰ and -5.96‰, and -2.74‰ and -1.95‰, respectively (Table 2.3, Figure 2.6a). While most samples lie either on the Global Meteoric Water line (GMWL) [*Craig*, 1961] or show deuterium excess [*Dansgaard*, 1964], Santa Cruz

Table 2.3 Measured stable isotope composition of water samples along with sample numbers.

Sample No.	$\delta^{18}O$ (‰)	±1σ	δD (‰)	±1σ
Santa Cruz				
sz1	-2.13	0.06	-8.85	0.52
sz2	-2.55	0.09	-10.06	0.41
sz3	-2.60	0.06	-10.57	0.67
sz4	-3.10	0.06	-13.50	1.03
San Cristobal				
sc1	-2.31	0.08	-7.13	0.62
sc2	-2.10	0.07	-6.81	0.71
sc3	0.89	0.07	6.54	0.69
sc4	-2.74	0.08	-11.46	0.52
sc5	-2.07	0.06	-6.04	0.71
sc6	-1.95	0.06	-6.40	0.73
sc8	-2.69	0.07	-8.71	0.90
sc9	-2.63	0.09	-8.76	0.50
sc10	-2.22	0.06	-5.96	0.96
sc11	-2.38	0.06	-7.72	0.88
sc12	-2.30	0.07	-7.91	1.04
sc13	-2.60	0.06	-9.70	0.90

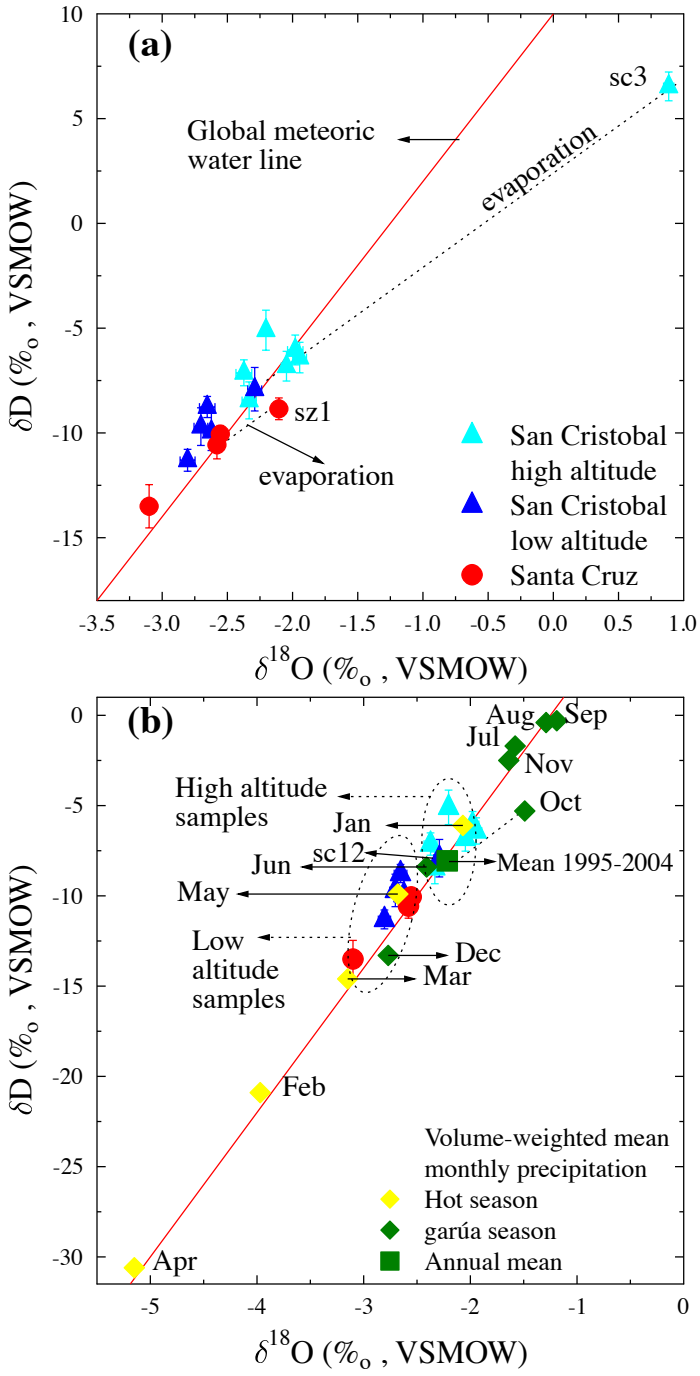

Figure 2.6 (a) Measured δD and $\delta^{18}O$ values of all water samples from San Cristobal (triangles) and Santa Cruz (circles) compared with the global meteoric water line [*Craig*, 1961]. Samples with possible evaporation effects are indicated by dashed lines. $\delta^{18}O$ excess values are calculated assuming an evaporation slope of 4.5 **(b)** Stable isotope ratios of all water samples compared with volume-weighted mean (1995-2004) monthly values for rainfall at Bellavista (diamonds). Mean monthly values from hot season (yellow diamonds) are less enriched than those from the "garúa" season (green diamonds). Ellipses indicate high- and low-altitude sample clusters. High-altitude (>~420 m) samples are more enriched than low-altitude samples and are indicated.

basal aquifer sample sz1 and San Cristobal El Junco lake sample sc3 in particular, lie to the far right of GMWL (Figure 2.6a) and display significant $\delta^{18}O$ excess (~0.5‰ and ~3‰, respectively) assuming an evaporation slope of 4.5. Such $\delta^{18}O$ excess is likely the result of kinetic fractionation during evaporation [*Dansgaard*, 1964]. As a result, both sz1 and lake El Junco are thus excluded from the discussion below. In the discussion that follows, all other water samples from both San Cristobal and Santa Cruz are compared with volume-weighted monthly mean rainfall isotopic composition in order to constrain timing of recharge.

Volume-weighted mean monthly values of stable isotopic composition in rainfall were obtained from the closest available isotope monitoring station (International Atomic Energy Agency/World Meteorological Organization, Global Network of Isotopes in Precipitation, The GNIP Database, available at http://www.iaea.org/water, 2006), located in Bellavista, Santa Cruz, at an elevation of 194 m between 1995 and 2004 (Figure 2.6b, diamonds). Because peak altitudes of both islands are not very high and the progress of the trade-wind generated rainout process of atmospheric vapor, which induces the altitude effect, is halted at the base of the stable inversion layer at an elevation of ~300 m, mean monthly rainfall isotopic composition during the "garúa" season was not corrected for the altitude effect [*Gonfiantini et al.*, 2001]. With the exception of October, all other mean monthly isotopic composition (Figure 2.6b) lie next to the global meteoric water line (GMWL) [*Craig*, 1961]. Mean monthly October isotopic composition deviates to the right of the GMWL, and displays an excess in $\delta^{18}O$ of 0.94‰ which might be an indication of lower humidity conditions generally observed during this month [*Dansgaard*, 1964; *Gonfiantini et al.*, 2001].

Except for the mean monthly isotopic concentrations of transition months between

both seasons, January and December, between the "garúa" and the hot season, and June, transition from hot to the "garúa" season, all other mean monthly rainfall values for both the "garúa" (July–November) and the hot season (February-May) display very distinct, marked signatures as compared to the annual mean value of precipitation (Figure 2.6b). While December and June show significant depletion in stable isotopic composition compared to precipitation during the "garúa" season, January shows significant enrichment compared to storm rain samples from the hot season. Excluding the transition months, precipitation during the hot season is more depleted than the annual mean value of precipitation while precipitation during the "garúa" season is more enriched than the annual mean value of precipitation (Figure 2.6b). Similar isotope observations of precipitation during the hot season compared to the dry season have been reported in a number of tropical regions [*Scholl et al.*, 1996; *Gonfiantini et al.*, 2001; *Scholl et al.*, 2002] and have been attributed to the amount effect [*Dansgaard*, 1964]. This distinct seasonality in isotopic composition of rainfall between the "garúa" and the hot season months as compared to the annual mean is used to identify the timing of recharge for all water samples.

All our water samples fall well within the monthly average rainfall isotopic end members, April (δD= -5.15‰, $\delta^{18}O$ = -30.6‰) for the hot season, and September (δD= -1.19‰, $\delta^{18}O$= -0.3‰) for the "garúa" season (Figure 2.6b). Specifically, Santa Cruz samples (sz2, 3, 4) fall within the domain of depleted precipitation during the hot season indicating likely recharge during this season. These stable isotope comparisons reaffirm our NGT results for basal aquifer samples from Santa Cruz that recharge occurs predominantly during the hot season. Similarly, four spring samples from San Cristobal (sc4, 8, 9, 13) also lie closer to the more depleted rain water samples from intense precipitation events during the

hot season. Of relevance is the fact that all these spring samples which lie closer to the hot season isotopic signature, belong to the same subset of low altitude spring samples observed using NGTs (Figure 2.6b). Similar to observations based on NGTs, isotopic compositions of low altitude spring samples also indicate that recharge might predominantly occur during the hot season. In contrast, seven (sc1, 2, 5, 6, 10, 11, 12) spring samples (Table 2.3) are more enriched than rain water samples from the hot season. These spring samples lie between the subset of enriched "garúa" rainfall samples and the depleted hot season rainfall samples indicating that recharge during both seasons might potentially be important for these springs. More importantly, all seven of these enriched samples (except sc12) are also located at high altitudes (>~420 m).

Results obtained using NGTs and stable isotope analyses thus lead to a common conclusion, i.e., samples predominantly recharged during the hot season are found at lower altitudes (<~420 m a.s.l), while samples pointing to recharge during both seasons appear to be located at higher altitudes (>420 m a.s.l). This suggests that the composition of recharge water at different altitudes follows the distribution of rainfall rather closely as shown in Figure 2.2b. These results are in agreement with previous findings based on the distribution of effective rainfall (Figure 2.2b) [*d'Ozouville et al.*, 2008a], which show that precipitation during the "garúa" season is more prevalent at higher altitudes (cf. section 2.2).

It is interesting to note that the high altitude samples, which point to recharge during both seasons using stable isotopes are precisely those displaying inconsistent recharge altitudes and temperatures using noble gases. In section 2.7, we explore various mechanisms to explain the unexpected relative Ar enrichment and Ne, Kr and Xe depletion observed in 16 inconsistent samples out of a total of 29 water samples, which lead to inconsistent recharge

altitudes and temperatures using standard NGT models. Below, through measured He isotopic ratios in springs together with tritium measurements in precipitation we place constrains in the groundwater residence times. These are fairly young and further reinforce the notion that NGTs do indeed record seasonality in fractured systems rather than the MAAT commonly assumed in sedimentary systems. *Thoma et al.* [2011] have recently come to a similar conclusion.

2.6 Tritium/^{3}He Groundwater residence times

Our combined NGTs and stable isotope analyses independently record seasonal climatic signals for all samples from San Cristobal and Santa Cruz. Among other factors, preservation of seasonal climatic signals is dependent on the presence of a shallow water table and short groundwater residence times [e.g., *Stute and Schlosser*, 1993, *Thoma et al.*, 2011]. Below, we provide a first-order estimate of groundwater residence times for all spring samples based on the presence of marginal He excesses in springs (cf. section 2.4.1) derived from β-decay of natural and bomb ^{3}H and verify that all springs indeed display young groundwater ages. Estimation of groundwater residence times for the basal aquifer samples based on tritiogenic He are not possible due to a significant presence of mantle He which complicates the tritiogenic vs mantle ^{3}He separation (cf. section 2.4.1) [see also *Schlosser*, 1989].

Tritiogenic ^{3}He concentrations for each spring are calculated from measured R/R_a ratios (Table 2.2) and measured ^{4}He concentrations (^4He_m, Table 2.4) following *Schlosser et al*. [1988], assuming ^{4}He concentrations in equilibrium with the atmosphere (ASW). ^{4}He concentrations in equilibrium with the atmosphere corresponding to a wide range of

Table 2.4 Tritiogenic ^{3}He required for He excesses in all springs along with ^{3}H/^{3}He ages for different assumed ^{3}H maximums.

Sample	^4He_m	±1σ	$^3He/^4He$	±1σ	$^3He_{required}$ (±1σ)	$^3H/^3He$ ages 02/2004*	mean 2004¶	10/1999§
	10^{-8} cm^3 STP/g	10^{-10} cm^3 STP/g	$\times10^{-6}$	$\times10^{-6}$	(TU)	(yrs ±1σ)	(yrs ±1σ)	(yrs ±1σ)
sc1-1	4.49	6.74	1.409	0.032	0.84 (0.57)	1.21 (0.81)	1.69 (1.14)	2.66 (1.82)
sc1-2	4.53	6.79	1.430	0.033	1.22 (0.61)	1.74 (0.84)	2.41 (1.18)	3.75 (1.90)
sc2-1	3.93	5.89	1.398	0.044	0.61 (0.70)	0.89 (1.00)	1.24 (1.39)	1.96 (2.20)
sc2-2	4.60	6.90	1.338	0.039	-0.46 (0.72)	-0.69 (1.12)	-0.99 (1.61)	-1.63 (2.72)
sc3-1	4.38	6.57	1.348	0.030	-0.24 (0.54)	-0.37 (0.82)	-0.52 (1.17)	-0.86 (1.94)
sc3-2	4.42	6.63	1.363	0.029	0.02 (0.52)	0.03 (0.77)	0.04 (1.09)	0.07 (1.76)
sc4-2	4.22	6.34	1.402	0.037	0.69 (0.63)	1.01 (0.90)	1.41 (1.26)	2.23 (2.00)
sc5-2	4.72	7.08	1.563	0.104	3.78 (1.97)	4.91 (2.30)	-	9.72 (4.40)
sc6-1	4.47	6.71	1.453	0.137	1.63 (2.46)	2.29 (3.25)	3.16 (4.39)	4.86 (6.52)
sc6-2	3.84	5.75	1.406	0.032	0.73 (0.49)	1.06 (0.70)	1.48 (0.98)	2.34 (1.58)
sc10-1	4.25	6.38	1.349	0.025	-0.20 (0.43)	-0.31 (0.65)	-	-0.71 (1.53)
sc10-2	4.68	7.01	1.600	0.113	4.45 (2.13)	5.66 (2.40)	7.55 (3.13)	11.01 (4.52)
sc11-2	4.82	7.24	1.506	0.096	2.75 (1.85)	3.70 (2.29)	5.03 (3.04)	7.56 (4.47)
sc12-1	4.47	6.71	1.390	0.035	0.49 (0.62)	0.72 (0.90)	1.00 (1.25)	1.60 (1.99)
sc4-1	4.45	6.67	1.442	0.036	1.43 (0.64)	2.02 (0.89)	2.79 (1.24)	4.32 (2.01)
sc5-1	5.18	7.76	1.323	0.044	-0.88 (0.92)	-1.36 (1.50)	-1.96 (2.20)	-3.28 (3.90)
sc8-1	4.52	6.78	1.372	0.033	0.16 (0.60)	0.24 (0.89)	0.34 (1.25)	0.55 (2.01)
sc9-1	4.92	7.38	1.356	0.018	-0.16 (0.36)	-0.24 (0.54)	-0.34 (0.77)	-0.55 (1.26)
sc9-2	5.03	7.55	1.349	0.042	-0.31 (0.84)	-0.47 (1.29)	-0.67 (1.85)	-1.09 (3.07)
sc11-1	4.60	6.91	1.381	0.030	0.34 (0.56)	0.50 (0.82)	0.70 (1.15)	1.12 (1.83)
sc12-2	4.59	6.89	1.398	0.030	0.64 (0.56)	0.94 (0.80)	1.31 (1.12)	2.08 (1.79)
sc13-1	4.57	6.85	1.402	0.040	0.72 (0.74)	1.04 (1.05)	1.46 (1.45)	2.30 (2.29)
sc13-2	4.48	6.72	1.384	0.044	0.39 (0.80)	0.57 (1.16)	0.80 (1.62)	1.28 (2.56)
sz4-1	4.26	6.39	1.320	0.050	-0.71 (0.85)	-1.09 (1.36)	-1.56 (1.98)	-2.59 (3.45)

* ^{3}H/^{3}He age calculated assuming ^{3}H peak of 14.55 ± 1.4 TU in 02/2004

¶ ^{3}H/^{3}He age calculated assuming mean of ^{3}H peak in 2004 of 10.11 ± 3.07 TU

§ ^{3}H/^{3}He age calculated assuming ^{3}H peak of 7.66 ± 0.41 TU in 10/1999

possible temperatures and altitudes on both islands were used to estimate tritiogenic ^{3}He concentrations and subsequently tritium ages in each spring sample (cf. Appendix A). Because tritiogenic ^{3}He concentrations and derived tritium ages for all spring samples are insensitive to the chosen equilibrium conditions (cf. section 2.6.1), below, we discuss only results obtained by assuming ^{4}He equilibrium at maximum possible altitudes and their corresponding MAATs.

Table 2.4 shows the results of calculated tritiogenic ^{3}He in tritium units (TU; 1 TU=2.5×10^{-15} cm^3 STP/g ^{3}He) for each spring sample along with its error ($\pm 1\sigma$). Tritiogenic ^{3}He errors were calculated using a propagation of errors from estimated analytical error estimates. Results show that, within error, the amount of tritiogenic ^{3}He (in TU) required to account for the marginal ^{3}He excesses observed in many spring samples (cf. sec. 2.4.1) varies between ~0 TU and 4.45 ± 2.13 TU (Table 2.4). The calculated amount of ^{3}He excess for each spring sample is then compared with available historical records of ^{3}H in local precipitation. ^{3}H in precipitation was measured continuously between 1995 and 2007 at Bellavista, Santa Cruz (Fig. 2.7; International Atomic Energy Agency/World Meteorological Organization, online, 2006). The ^{3}H record for precipitation at Bellavista shows a background ^{3}H of 1.02 TU with two ^{3}H peaks corresponding to 7.66 ± 0.41 TU in 10/1999, which only lasted for a month, and a subsequent peak in 02/2004 with a maximum of 14.55 ± 1.4 TU, which lasted the entire year, yielding an annual average ^{3}H value in 2004 of 10.11 ± 3.07 TU. Excess ^{3}He added to the groundwater by the decay of each of the above three ^{3}H maximum values (7.66± 0.41 TU, 14.55 ± 1.4 TU and 10.11 ± 3.07 TU) until the sampling date (October, 2007) can be estimated based on its half-life of 12.43 years (Fig. 2.8a). It should be noted that the amount of ^{3}He available from the decay between 10/1999 and

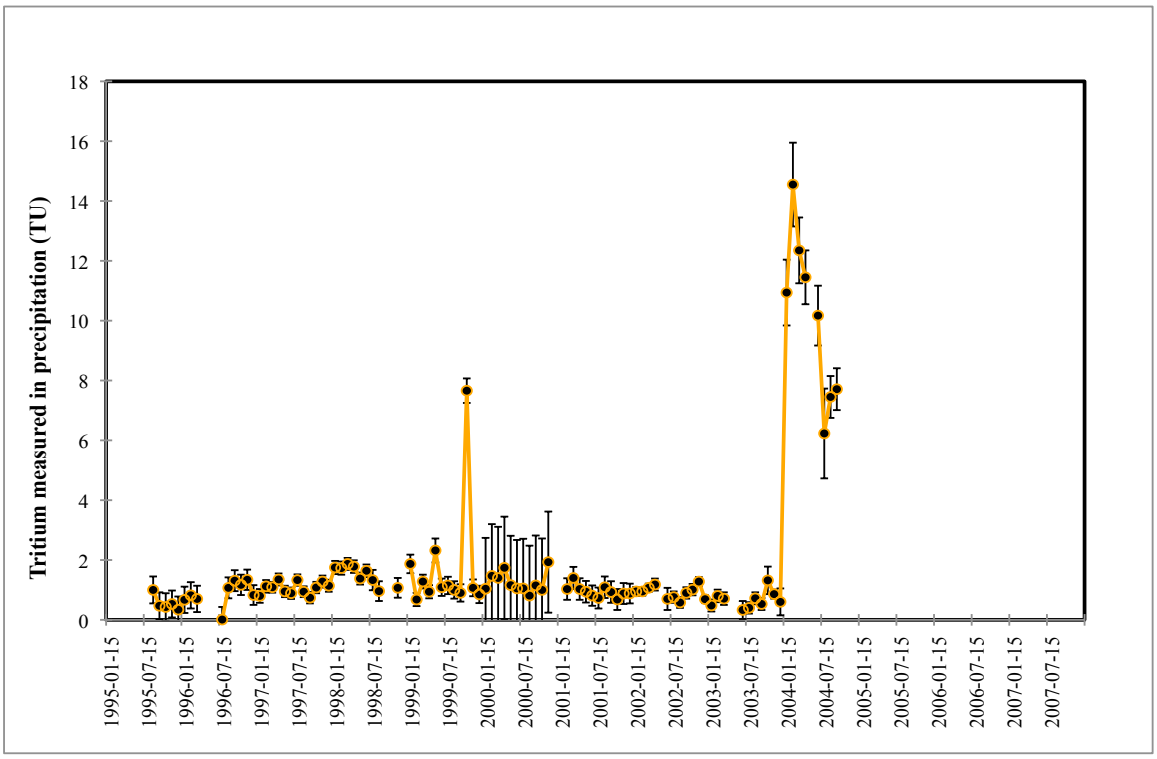

Figure 2.7 Historical record of tritium measurements in precipitation (IAEA/WMO, 2006) between 1995 and 2007 at Bellavista, Santa Cruz. Background tritium measurement of 1.02 TU along with two identifiable 3H peaks corresponding to 7.66 ± 0.41 TU in 10/1999, which only lasted for a month, and a subsequent peak in 02/2004 with a maximum of 14.55 ± 1.4 TU, which lasted the entire year is observed. Tritium measurements in 2004 yield an annual average of 10.11 ± 3.07 TU.

10/2007 (green line, Fig. 2.8.a) would yield the highest ^{3}He availability because of the combined addition of ^{3}He from the decay of ^{3}H maximum in 10/1999 and 2004. Comparison of the amount of estimated tritiogenic ^{3}He (blue triangles, Fig. 2.8. a) with the amount of tritiogenic ^{3}He available from decay of ^{3}H in precipitation (green, red and blue lines, Fig. 2.8a.) shows that within errors, both the amount of tritiogenic ^{3}He available in 10/2007 from decay of ^{3}H between 10/1999 and 10/2007 (green line, Fig. 2.8) as well as between 02/2004 and 10/2007 (red line, Fig. 2.8a) are sufficient to account for the estimated tritiogenic ^{3}He for all spring samples. It is relevant to note that decay of ^{3}H between the 2004 annual average of 10.11 ± 3.07 TU and 10/2007 can account for the tritiogenic ^{3}He for all samples except sc5-2 and sc10-1 and tritium ages are not estimated for those samples. Apparent tritium ages were calculated following:

$$t = \frac{12.43}{\ln 2} \times \ln\left(1 + \frac{[^3He]}{[^3H]}\right) \qquad \textbf{(2.2)}$$

where, t is tritium age in years, [^{3}He] is the calculated amount of tritiogenic ^{3}He in spring samples and [^{3}H] is the measured tritium concentration of groundwater. Although no tritium measurements are available for our groundwater samples, as a first-order approximation, it is assumed that present tritium concentrations in our spring samples result from the decay of one of the above ^{3}H maximums. Such an assumption is expected to yield an upper limit to tritium ages for all springs because the presence of additional tritium from previous unrecorded maximums, if any, would yield younger ages according to equation (2.2). Because the calculation of tritium ages is based on the assumption that ^{3}H maximums can account for the measured amount of tritiogenic ^{3}He in all samples, tritium ages were not calculated for samples sc5-2 and sc10-1 using the annual average maximum ^{3}H peak in

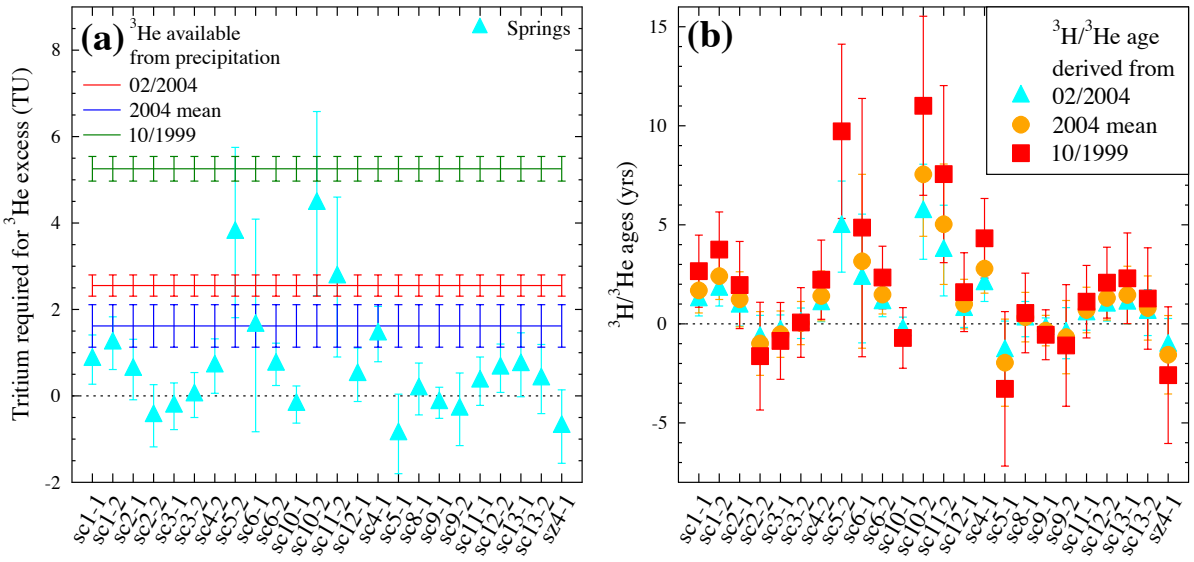

Figure 2.8 Tritium/^{3}He analysis of all springs from San Cristobal and Santa Cruz **(a)** Comparison of ^{3}He excess for all springs with ^{3}He available from precipitation assuming decay of ^{3}H peaks on 10/1999, 02/2004 and mean 2004 **(b)** Tritium/^{3}He ages derived from ^{3}He excess for each spring and assuming tritium concentration in groundwater resulting from the decay of ^{3}H maximums on 10/1999, 02/2004 and mean 2004.

2004 (Table 2.4). For all other springs, tritium ages were calculated assuming a tritium concentration in groundwater that results from the decay of each of the three ^{3}H maximums, thus yielding a range of tritium ages for each sample. Table 2.4 shows tritium ages calculated for all spring samples assuming ^{3}H maximums in 10/1999, 02/2004 as well as the 2004 ^{3}H annual average. Our results show that maximum tritium ages are obtained for all spring samples assuming the 10/1999 ^{3}H maximum while minimum tritium ages are obtained for all spring samples assuming the 02/2004 ^{3}H maximum (Figure 2.8b). However, irrespective of assumed ^{3}H maximums, all springs yield groundwater ages that are very young. Within error, tritium ages for all springs vary between ~0 and 11 ± 4.5 years with a mean age of 2.03 years (corresponding to the 10/1999 maximum). In particular, all consistent spring samples correspond to a mean age 0.75 ± 7.25 years (corresponding to 10/1999 maximum) while the remaining inconsistent springs correspond to a mean age of 2.8 ± 12.4 years. However, poor age uncertainties associated with all spring samples presently do not allow for a definitive age resolution between consistent and inconsistent springs.

Although derived tritium ages for all springs represents a first-order approximation, it is apparent that all spring samples, irrespective of assumption and measured tritium values used, are very young with short groundwater residence times. Short groundwater residence times associated with these springs corroborates results from NGTs and stable isotopes, which independently suggest preservation of seasonal climatic signals. As discussed earlier, high altitude samples display unique noble gas patterns (cf. section 2.4.1) and yield inconsistent recharge altitudes and temperatures using noble gases (cf. section 2.4.2), while simultaneously pointing to recharge during both the “garúa” and hot season using stable isotopes (cf. section 2.5.2). Below, we explore various mechanisms to explain the unexpected

noble gas patterns, particularly, relative Ar enrichment and Ne, Kr and Xe depletion observed in all inconsistent samples.

2.7 Potential gas loss mechanisms in fractured environments

Samples that display inconsistent recharge altitudes and temperatures with respect to those in place in Santa Cruz and San Cristobal using standard noble gas models [e.g., *Stute and Schlosser*, 1993, *Ballentine and Hall*, 1999, *Aeschbach-Hertig et al.*, 1999] also show systematic deviations of dissolved noble gases from expected ASW values. Figures 2.9a and 2.9b show the observed noble gas patterns for all 16 inconsistent samples normalized to ASW at average sampling elevations and temperatures in place in both islands (cf., section 2.4.1). For 11 out of the 16 samples, a common pattern emerges in which Ar excess relative to all other gases is observed (Figure 2.9a). The remaining five samples display varying signatures without similar trends (Figure 2.9b). In particular, sample sc6-2 (Figure 2.9b) shows an excess of the lighter noble gases Ne and Ar relative to the heavier noble gases Kr and Xe, a pattern similar to that predicted by standard noble gas models that account for the addition of excess air [*Aeschbach-Hertig et al.*, 2008]. By contrast, all other four samples show a pronounced loss of Ne over all other noble gases. In addition, samples sc11-2, sc12-1 and sz4-1 display also an excess of Kr relative to all other gases.

Below we explore various mechanisms to assess their potential at reproducing the observed noble gas patterns, and, in particular, the observed relative Ar excess. Specifically, we test the extent of noble gas loss through existing degassing models, in addition to assessing the potential impact of fog droplets ("garúa" dew) on dissolved noble gas concentrations in groundwater and the effect of mixing between noble gas depleted rainwater

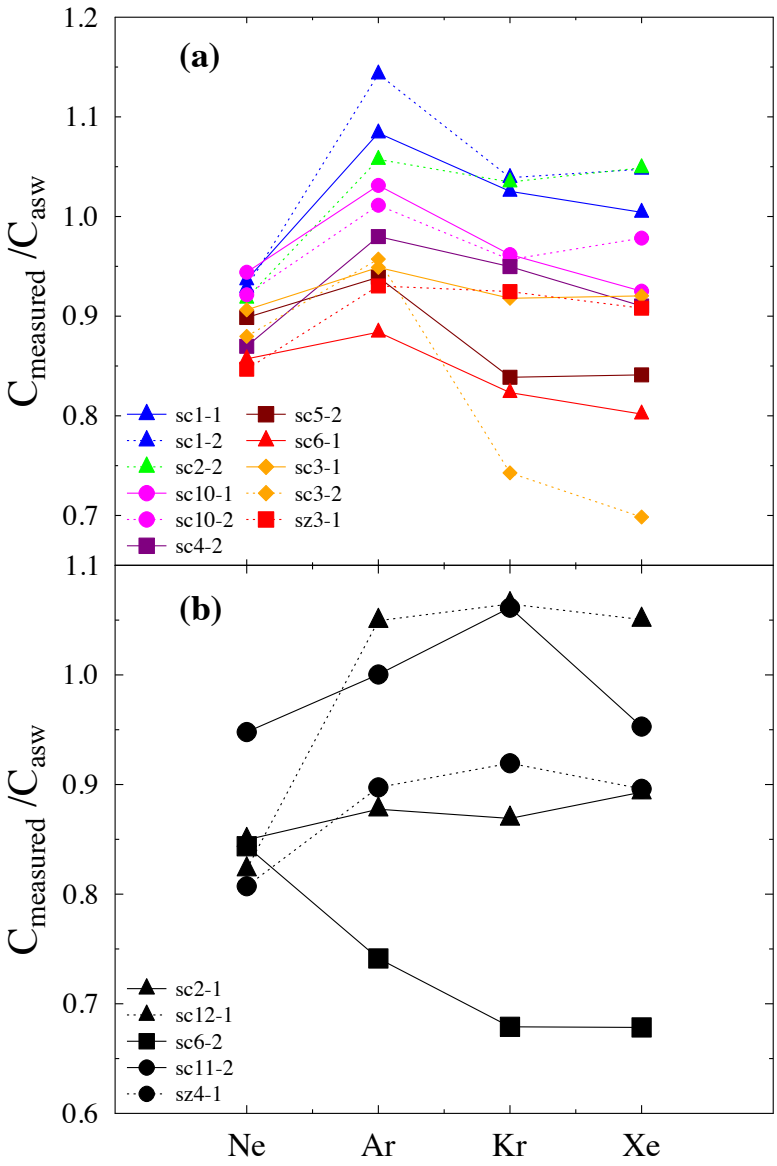

Figure 2.9 Measured Ne, Ar, Kr and Xe patterns for 16 inconsistent water samples normalized to air saturated water (ASW) at sea level and 421 m for all basal aquifer and spring samples respectively. All samples were also normalized to average temperature of 20°C **(a)** Samples with a unique excess of non-radiogenic Ar relative to the concentrations of Ne, Kr and Xe. **(b)** Samples with systematic depletion (triangle) and excess (square) of lighter noble gases as compared to the heavier noble gases. Samples with a Kr "bump" are also shown (circles).

formed in the atmosphere at high-altitude (≥1500 m) and low-altitude (>400 m) fog droplets. Such degassing models have never been tested in fractured, basaltic environments and the effect of mixing high-altitude rainwater with low-altitude fog droplets is an entirely untested process.

2.7.1 Modeling loss of dissolved noble gases through existing degassing models

Groundwater degassing by partitioning of dissolved noble gases into an initially noble gas-free bubble has recently been observed in a number of environments including an ultra deep mine [*Lippmann et al.*, 2003], a hydrocarbon contaminated site [*Amos et al.*, 2005] and agricultural areas [*Visser et al.*, 2007; *Cey et al.*, 2008]. Existing degassing models describe the partitioning mechanisms involved in loss of dissolved noble gases as either a solubility equilibrium process (e.g., closed equilibration (CE) model of *Aeschbach-Hertig et al.* [2008]; 1-step degassing (SD) model of *Brennwald et al.* [2003]), or as a diffusion dominated process (e.g., partial re-equilibration (PR) model of *Stute* [1989]; partial degassing (PD) model of *Stute et al.* [1995]). Here, we use inverse fitting procedures by *Ballentine and Hall* [1999] to fit NGTs, excess air and appropriate degassing parameters from measured noble gas concentrations for each of the 16 inconsistent samples at their sampling altitudes using the CE, SD, PR and PD models. Any particular model is assumed to explain the observed dataset only if the χ^2 test between modeled and measured concentrations yields a probability $p > 0.01$ [see, e.g., *Aeschbach-Hertig et al.*, 2008].

Results of inverse fitting NGTs, excess air and fractionation parameter (F) for the CE model as well as NGTs and degassing volume, B for the SD model are provided in Appendix A. While only three (sc2-1, sz3-1 and sz4-1) out of the 16 samples satisfy the established χ^2

test probability ($p>0.1$; $\chi^2(1) = 6.63$) using the CE model, three samples from San Cristobal (sc2-1, sc3-1, sc6-2) and two samples from Santa Cruz (sz3-1, sz4-1) satisfy the χ^2 test probability ($p>0.1$; $\chi^2(2) < 9.21$) for the SD model. Three out of five samples that can be fit using the SD model (sc2-1, sc6-2, sz4-1) display either a greater depletion of the lighter noble gases relative to the heavier ones (sc2-1, sz4-1) or a greater depletion of the heavier noble gases relative to the lighter ones (sc6-2). Both patterns have previously been shown to be predicted by the CE model [*Aeschbach-Hertig et al.*, 2008]. However, solubility controlled models fail to achieve the established probability criteria ($p>0.01$) for most inconsistent samples.

Inverse fitting dissolved noble gas concentrations using the PR model show that only four out of 16 samples (sc3-1, sc3-2, sc5-2, sc10-2) converge to a global minimum with the non-negative excess air constraint in place. For samples that converge, best-fit χ^2 values result in poor fits ($\chi^2(1) > 6.63$). The PR model has been shown to require large amounts of initial dissolved excess air [*Kipfer et al.*, 2002], which is lacking in all our inconsistent samples and might thus explain the poor fits obtained. Inverse fitting using the alternate diffusion-based PD model shows that none of the 16 samples converge to a global minimum. Lack of convergence of these samples to a global minimum does not necessarily negate diffusion as the underlying process. Instead, it highlights the numerical instability of noble gas models with one degree of freedom [see e.g., *Ballentine and Hall*, 1999].

Existing solubility and diffusion controlled degassing models tested in this study are only able to account for a small subset of all inconsistent samples. Both solubility and diffusion based degassing models favor the loss of lighter noble gases such as He and Ne over the heavier noble gases Kr and Xe. While diffusion based degassing models naturally

favor the loss of Ne over Xe due to its higher diffusion coefficient, solubility based degassing models favor the loss of Ne over Xe due to Xe's greater solubility. Therefore, both solubility and diffusive degassing models are more likely to fit samples that display a progressive depletion of lighter noble gases as compared to the heavier ones or vice versa. By contrast, most of our samples (Figure 2.9a) display a unique depletion pattern with relative Ar excess compared to all other noble gases. Such patterns are possibly caused by processes unique to fractured environments, as investigated below. It is also relevant to note that our noble gas data, unlike data from active volcanic environments [e.g., *Gardner et al.*, 2010] are not compatible with the presence of a hydrothermal gas phase, and thus, with the occurrence of a Rayleigh type of degassing that might lead to the observed pattern of our inconsistent samples. Indeed, only samples located at high altitude, which are referred here as "inconsistent" could possibly point to the presence of a mantle gas phase. However, if that were the case, all the "consistent" samples, which point to the presence of a closed system and absence of a gas phase, should also display the impact of a mantle gas phase, and this is not the case. Indeed, all consistent samples are located at low altitude and samples from the basal aquifer are "consistent", i.e., their signature is that expected for a closed system and thus, incompatible with the presence of a hydrothermal gas phase and possible occurrence of a Rayleigh degassing hypothesis.

2.7.2 Dissolution of noble gases in fog droplets ("garúa" dew)

As many as 14 out of 16 inconsistent water samples are located at high altitudes (>~420 m) where the presence of fog is prominent during the "garúa" season. Fog droplets generally form under conditions that significantly deviate from the standard noble gas

assumption of equilibration at the unsaturated-water table interface at standard atmospheric pressure (Figure 2.10). Fog droplets suspended in oversaturated air represent an anisobaric system since water pressure within the droplet is greater than the surrounding atmospheric pressure ($P_{water} > P_{air}$) due to its curvature [*Mercury et al.*, 2003]. Due to this increase in water pressure within the droplet, noble gases will move from within the droplet to the surrounding air. Consequently, if infiltration of droplets is too fast so as to prevent re-equilibration of the droplets with the soil air at the water table, noble gas composition at recharge might reflect the particular meta-stable conditions under which these droplets formed. Although we do not expect the effect of curvature of fog droplets to independently explain the observed noble gas depletion pattern with relative Ar excess, a combination of this effect with other processes and in particular mixing with high-altitude rain is partially capable of reproducing the observed noble gas patterns as shown below. Thus, we first explore the sole effect of curvature on the dissolution of noble gases within fog droplets.

Dissolution of noble gases in fog droplets was investigated using a framework described by *Mercury et al.* [2004] for positive pressure values of droplet curvature. The increase in water pressure due to curvature of the droplet can be calculated using the Laplace equation of capillarity and the Kelvin equation [*Thomson*, 1871]. An increase in water pressure, dP, decreases the solubility of the noble gas considered through a modification of its Henry's constant k_i. This decrease in solubility of the noble gas 'i' at constant temperature 'T' is given by [*Mercury et al.* 2004]:

$$\ln \frac{k_i(T,P)}{k_i(T,1)} = \frac{1}{RT} \int_1^P V^0_{solute} \bullet dP \qquad (\mathbf{2.3})$$

where, R is the universal gas constant and V^0_{solute} is the volume of noble gas 'i' in solution [*Mercury et al.*, 2003], which can be calculated using thermodynamic constants

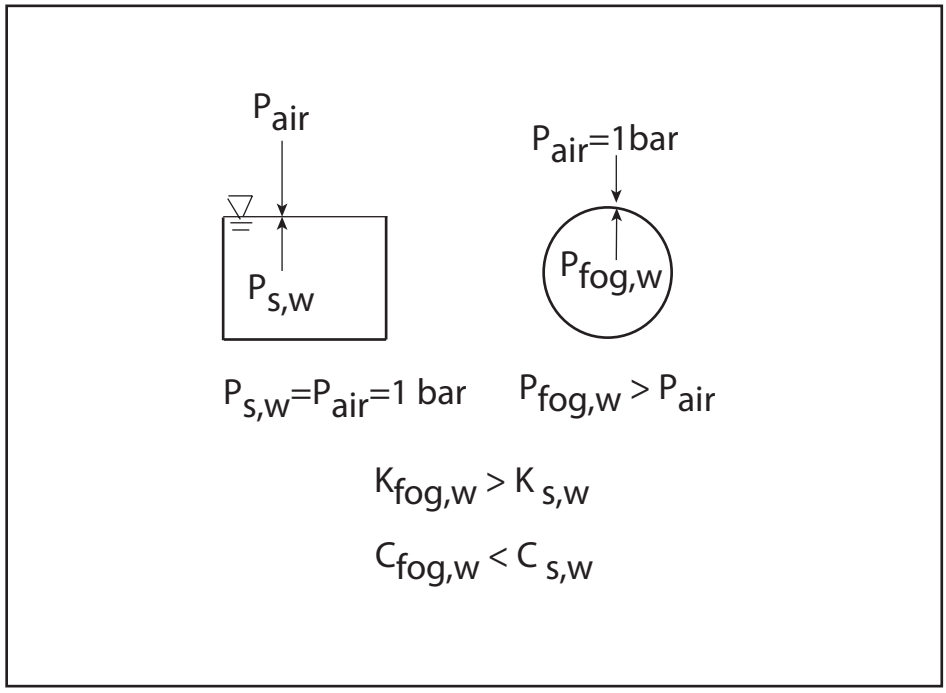

Figure 2.10 Comparison of noble gases within fog droplets and on a plane water surface (s, w). Water pressure within fog droplet, $P_{fog,w}$ is greater than atmospheric pressure P_{air} due to effect of curvature. Increased water pressure increases dimensionless Henry's constant, $K_{fog,w}$ for noble gases thereby decreasing dissolved noble gas concentrations within fog droplets,$C_{fog,w}$ as compared to plane surface water, $C_{s,w}$

in *Mercury et al.* [2004] (additional details for this calculation are provided in Appendix A). The effect of changing pressure on noble gas solubility was incorporated into a UA model framework [cf. *Ballentine and Hall*, 1999] to calculate NGTs and excess air (constrained by non-negativity) for different assumed recharge altitudes, from the sampling altitude up to 3000 m with 50 m increments, and positive water pressures corresponding to droplet sizes of 0.3, 1 and 10 microns. These droplet sizes represent the theoretical diameter of aerosols that can be activated to become fog droplets (see Appendix A for a discussion on droplet sizes) for a typical maximum supersaturation of 0.1% observed in fog in the Galapagos Islands [cf., *Seinfeld and Pandis*, 2006; *Collins and Bush*, 2010]. The validity of the model at a specific altitude and droplet size is evaluated through a chi squared (χ^2) test. The model is assumed to explain the observed dataset only if the χ^2 test yields a probability $p > 0.01$ (χ^2 (2) < 9.2) at that specific altitude and droplet size [*Aeschbach-Hertig et al.*, 2008].

Minimum recharge altitudes obtained for all 16 inconsistent samples using different droplet sizes with non-negative excess air constraint and $\chi^2 < 9.2$ are higher than the peak altitude of the islands. However, for samples with $\chi^2 < 9.2$, minimum recharge altitudes obtained through this model were lower by up to 50 m for a 1 micron droplet as compared to the minimum recharge altitudes obtained using the UA model and thus, move altitudes in the expected direction. NGTs obtained through this model, however, are not significantly different.

Although these results are encouraging as they bring some of our samples closer to the expected altitudes and temperatures, it can be concluded that the magnitude of the effect of curvature based on the chosen size of fog droplets is, by itself, insufficient to explain the observed depletion of noble gas pattern in the inconsistent samples. Below, we discuss in

more detail our proposed hypothesis of mixing between high altitude rainwater and fog droplets to account for the pattern of the 11 inconsistent samples that cannot be explained by existing solubility and diffusion controlled degassing models.

2.7.3 Effect of mixing high-altitude rainwater with low-altitude fog droplets

Apparent high recharge altitudes and cold temperatures displayed by many samples (cf. section 2.4.2) suggest that the available time for rainwater to re-equilibrate with the soil air of the islands might be insufficient due to rapid water infiltration through fractures commonly seen in basaltic settings. Figure 2.11 shows the 11 inconsistent Galapagos samples (yellow circles) along with measured noble gases in rainfall (green circles) and theoretical (modeled) fog concentration (blue square) plotted as F(Xe) vs F(Ne) where $F(i)=([i]/[Ar])_{sample}/([i]/[Ar]_{asw})$, "i" represents any noble gas and "asw" is the air saturated water value at 20˚C. Such a plot of F(Xe) vs F(Ne) is commonly used to study noble gas fractionation patterns in groundwater [e.g., *Kennedy et al., 1985, Gardner et al., 2010*]. Rain samples were collected in Michigan (cf. Appendix A) while the fog droplet concentration is the expected theoretical concentration corresponding to a droplet size of 10 microns at 20˚C (cf. section 2.7.2). Also shown are theoretical values for ASW at different temperatures (solid line) along with expected patterns for Rayleigh degassing [*Porcelli et al*., 2002] at different temperatures (dashed lines). Comparison of rainfall in Michigan and ASW values (Figure 2.11) shows that noble gases in rainfall deviate from expected ASW values. In particular, the rainwater samples show noble gas patterns similar to a Rayleigh style degassing at temperatures of approximately 16˚C and 34˚C, temperatures far higher than the measured surface air temperatures of 10˚C and 25˚C at the time of their respective sample

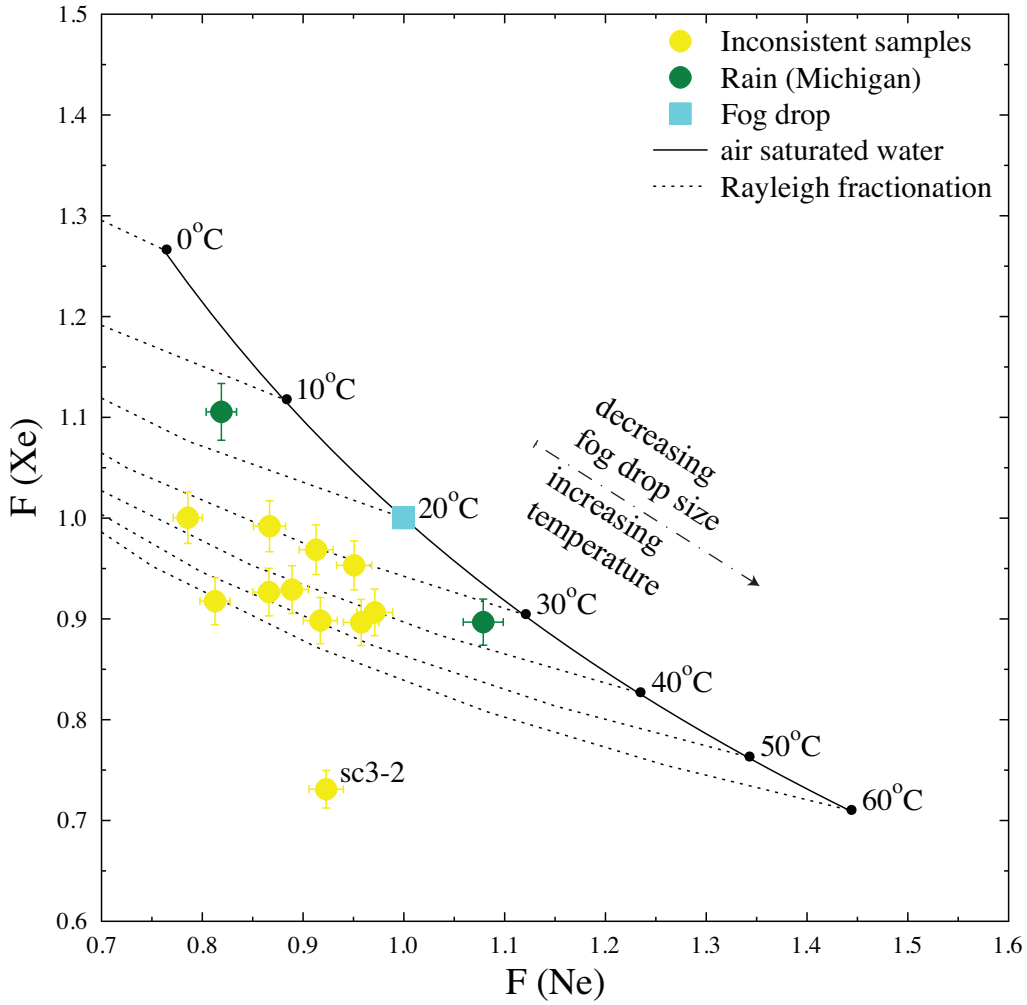

Figure 2.11 F(Xe) vs F(Ne) for 11 inconsistent Galapagos samples (yellow circles) along with measured rain (green circles) and theoretical fog droplet (blue square) concentration at 20˚C and 10micron size. Also shown are values for air saturated water (solid line) and expected Rayleigh style degassing pattern (dashed line) at different temperatures. Rain sampels indicate Rayleigh style degassing at higher temperatures while decreasing fog droplet size is expected to correspond to apparent increase in temperature

collection. Similar deviations of measured noble gas concentrations in rainfall with respect to surface conditions were previously observed in the Jordan Rift Valley [*Mazor*, 1972]. Although the nature of this deviation remains poorly understood, it is apparent that rainwater, independent of geographic location, is not always in equilibrium with ground surface conditions.

In addition to the deviation of rainfall from expected ASW values, fog droplets suspended in oversaturated air are expected to contain lower dissolved noble gases compared to ASW at similar altitudes and temperatures (section 2.7.2). Noble gas solubility within fog droplets decreases with fog droplet size in a non-linear fashion (equation 2.3, section 2.7.2). Because of decreased noble gas solubility within the fog droplet, noble gases point to an apparent increase in temperature (dashed arrow line, Figure 2.11) and altitude (shown below) as compared to ASW values. It is thus apparent that both fog droplets and rainwater are not in equilibrium with ground surface conditions and it is possible that mixing between these two components might reproduce the noble gas pattern observed in these 11 inconsistent Galapagos samples as discussed below.

Figure 2.12 shows 1/Xe vs Ne/Xe for 11 inconsistent Galapagos samples (yellow circles) along with rainwater equilibrated at different altitudes and temperatures mixing with fog droplets of 0.3, 1 and 10 microns at 421m and 20˚C. Condensation altitudes and temperatures during the hot season were obtained by analyzing radio sonde measured dew point differences at different elevations between 1967 and 2010 for San Cristobal (see http://www.ncdc.noaa.gov/oa/climate/igra/). Condensation (dew point difference <0.5°C) occurs mostly at elevations of 850mbar (~1500 m a.s.l) and 700mbar (~3100 m) at temperatures between 12.2 and 19.2°C and 5.8 and 10.8°C respectively.

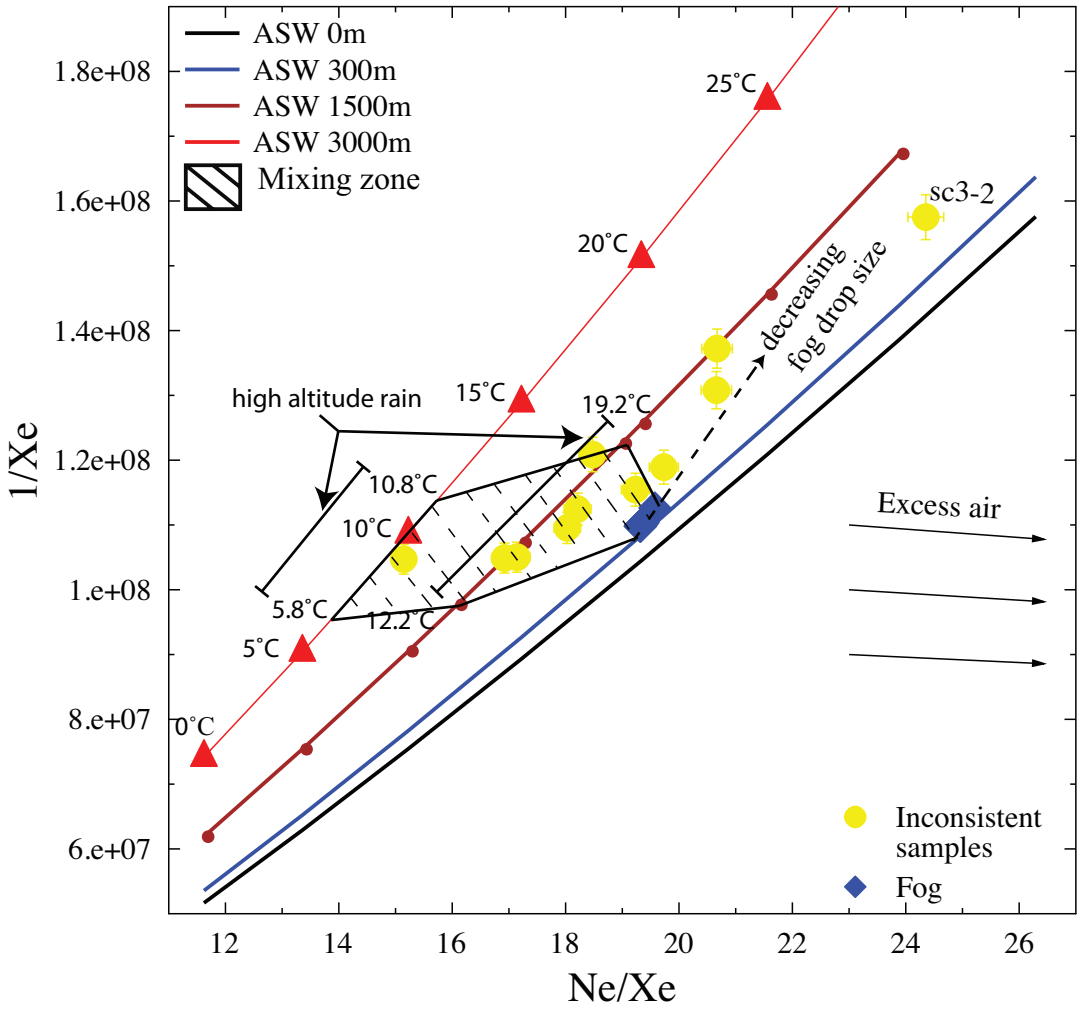

Figure 2.12 1/Xe vs Ne/Xe for 11 inconsistent Galapagos samples (yellow circles) along with high altitude rain water and theoretical fog concentrations (blue diamonds) for drop sizes at 0.3, 1 and 10microns at 421m and 20˚C. Decreasing fog drop size corresponds to an apparent increase in altitude and temperature. Zone of mixing between high altitude rain water and fog droplets is indicated by the shaded region.

Mixing between rainwater that equilibrated at high altitudes and fog droplets of various droplet sizes will produce a mixture that is different in composition from either source (shaded region, Figure 2.12). As many as seven out of eleven inconsistent samples (yellow circles) fall within this zone of mixing and have thus, the potential to explain the observed noble gas patterns in these samples. Three samples that fall outside of the shaded area (excluding sc3-2 which underwent evaporation, cf. section 2.5.2) would require fog droplet sizes <0.3 microns. Because currently measured fog droplet sizes are ≥0.1 microns (see Appendix A), these three samples are not considered in the analysis below. Because Figure 2.12 can evaluate only two (Ne, Xe) out of four (Ne, Ar, Kr, Xe) measured noble gases, below, we evaluate, through a statistical analysis, the mixing hypothesis using all four noble gases simultaneously for the 7 inconsistent samples located within the shaded mixing area (Figure 2.12), assuming high-altitude rainfall and fog droplet end members as discussed above.

High altitude rain water was mixed in different proportions (0-100%) with fog water of varying droplet size (0.3, 1, 10 micron) at an average elevation of 400 m and a mean temperature of 19.4°C extrapolated from measured mean "garúa" temperature at Puerto Ayora using a gradient of -0.8°C/100m. For each of the above combinations, χ^2 values were calculated as the sum of the ratio of the squared concentration differences between measured and hypothetical noble gas mixture for all four noble gases, divided by their respective squared measurement uncertainties. For each of the 7 inconsistent samples, a best mixing combination was then identified as the mixture combination with the least χ^2 value. Minimum χ^2 values thus found for many samples after mixing were lower than those for either end members. Minimum χ^2 values obtained through this mixing hypothesis also show a

significant improvement over the constrained CE ($0<F<1$) and UA models. However, a χ^2 test ($p < 0.01$; $\chi^2(4) = 13.28$) considered simultaneously for all four noble gases for this hypothesis is unsuccessful.

Although our mixing hypothesis readily explains Ne and Xe concentrations for all 7 samples (Figure 2.12), our statistical analysis based simultaneously on all four noble gases is unsuccessful. This suggests that our model parameter estimates for either end members may not be accurate. Among these are condensation altitudes and temperatures, as well as initial fog equilibration conditions. Measurements of noble gases in fog are currently non-existent and are very scarce in rainfall [*Mazor*, 1972, this study]. Such measurements together with measurement of rates of noble gas equilibration during surface runoff and within fractures should provide better constraints on the above model parameters and need to be carried out in future studies.

2.8 Conclusions

NGTs are successfully used to identify recharge areas and timing of recharge in basal and perched aquifers in the fractured, baslatic hydrologic systems of Santa Cruz and San Cristobal in the Galapagos Archipelago. Specifically, recharge altitudes between 160 and 870 m and temperatures between 20.05±2.07°C and 27.54±0.47°C are found for the basal aquifer in Santa Cruz, while recharge altitudes between 229 and 730 m and temperatures of 19.95±1.13°C and 26.36±0.66°C are found for springs in San Cristobal. Timing of recharge obtained through NGTs for all samples are also corroborated by stable isotope results. Except for one sample, combined NGT and stable isotope analyses points to recharge during the hot season for all low altitude (<~420 m) spring samples from San Cristobal and all basal aquifer

samples in Santa Cruz. Stable isotope analyses also indicate that San Cristobal springs located at high altitudes (>420 m a.s.l) are recharged during both the "garúa" and hot seasons. These results suggest that the composition of recharge water at different altitudes follows the distribution of rainfall closely, as previously suggested for Santa Cruz [*d'Ozouville et al.*, 2008a]. Robust agreement on timing of recharge between NGTs and stable isotopes also suggests that seasonal variations in temperature are likely to be preserved by noble gases dissolved in groundwater in basaltic environments in the presence of fractures or where soil cover is thin. Groundwater residence times for all springs derived from measured R/R_a values and tritium content in precipitation all yield young ages (<11 ± 4.5 years) and further reinforce the notion that NGTs and stable isotopes in this system are indeed recording seasonality as opposed to the commonly assumed MAAT in sedimentary systems.

Samples located at high altitude (>~420 m) display systematic deviations of dissolved noble gases from expected ASW values and lead to equilibration recharge altitudes and temperature conditions that are not consistent with conditions on the ground using standard NGT models. Most inconsistent samples indicate a unique noble gas pattern with relative Ar excess together with a strong depletion of Ne, Kr and Xe. Existing degassing models are only able to account for the observed noble gas pattern for 5 out of 16 inconsistent samples. The impact of fog droplets ("garúa" dew) on dissolved noble gas concentrations in groundwater on the highlands was explored. Although the effect of fog droplets brings some inconsistent samples closer to the expected altitudes and temperatures, such mechanism, by itself, is insufficient to reproduce the observed noble gas patterns. On the other hand, the effect of mixing high-altitude atmosphere rainwater with fog droplets readily explains Ne and Xe

concentrations for many of the inconsistent samples. However, a statistical analysis conducted of the mixing hypothesis based simultaneously on all four noble gases is unsuccessful, and suggests that our model parameter estimates are ill constrained. A full understanding of this unique noble gas signature is out of the scope of this study and will be the object of future investigations.

2.9 Appendix 1

Extreme temperature value transects were computed by combining available weather data measured using weather balloons and land stations during the hottest month (March) in an El Nino (1992) year and during the coldest month (September) in a La Nina (2007) year for each of the islands. Weather balloons are launched at sea level daily at 6am in San Cristobal and measure air temperatures at different elevations (these compare well with minimum surface temperature measurements observed at the land station in Puerto Bacquerizo Moreno (7.9 m asl; http://www7.ncdc.noaa.gov/CDO/cdo). Because weather balloons record only minimum temperatures, the extreme maximum temperature-altitude transect (Figure 2.5, red dashed line) is calculated based on maximum diurnal temperature variations computed from available land station data. Because weather records on diurnal temperature variation during the hottest month (March) in the El Nino (1992) year are unavailable, extreme maximum temperatures in San Cristobal were calculated by combining weather balloon data for March, 1992 (http://www.ncdc.noaa.gov/oa/climate/igra/) with the mean monthly observed diurnal temperature variation (±7.15°C) for the closest available diurnal temperature dataset (March, 1993) (http://www7.ncdc.noaa.gov/CDO/cdo). Extreme minimum temperatures (Figure 2.5, blue dashed line) in San Cristobal are those of weather

balloon temperatures (always recorded at 6am; http://www.ncdc.noaa.gov/oa/climate/igra/) for the coldest month (September) in a La Nina year (2007). Maximum and minimum temperatures recorded for weather stations in Puerto Ayora and Bellavista for the same extreme events (http://www.darwinfoundation.org/datazone/darwin_weather) were used along with the established annual temperature gradient (-0.8°C/100m) [*Auken et al.*, 2009] to estimate extreme maximum and minimum temperature transects in Santa Cruz.

Acknowledgements

We thank J. Selker and the Associate Editor for the editorial handling of this manuscript, as well as three anonymous reviewers for their insightful and thorough reviews. We thank Noémi d'Ozouville and Sophie Violette for field sampling and logistics with local authorities through the Galapagos Islands Integrated Water Studies project. We are also thankful to the Galapagos National Park Service, the Charles Darwin Foundation, the Municipalities of Santa Cruz and San Cristobal, and the Galapagos National Institute for local collaboration and logistics. Financial support by the National Geographic Society award #8452-08 and the National Science Foundation CAREER award EAR-0545071 is greatly appreciated.

References

Adelinet, M., Fortin, J., d'Ozouville, N., Violette, S. (2008), The relationship between hydrodynamic properties and weathering of soils derived from volcanic rocks, Galapagos Islands (Ecuador). *Environmental geology* 56, 45-58.

Aeschbach-Hertig, W., F. Peeters, U. Beyerle, Kipfer, R. (1999) Interpretation of dissolved atmospheric noble gases in natural waters. *Water Resources Research* 35, 2779-2792.

Aeschbach-Hertig, W., F. Peeters, U. Beyerle, Kipfer, R. (2000) Paleotemperature reconstruction from noble gases in ground water taking into account equilibration with entrapped air. *Nature* 405, 1040–1044.

Aeschbach-Hertig, W., El-Gamal, H., Wieser, M., Palcsu, L. (2008) Modeling excess air and degassing in groundwater by equilibrium partitioning with a gas phase. *Water Resour. Res.*, 44, W08449, doi:10.1029/2007WR006454.

Amos, R.T., K.U. Mayer, B.A. Bekins, G.N. Delin, Williams, R.L. (2005) Use of dissolved and vapor-phase gases to investigate methanogenic degradation of petroleum hydrocarbon contamination in the subsurface, *Water Resources Research,* 41, W02001,doi:10.1029/2004WR03433.

Andrews, J.N., Lee, D.J. (1979) Inert gases in ground water from the Bunter Sandstone of England as indicators of age and palaeoclimatic trends, *J. Hydrol.* 41, 233-252.

Andrews, J.N., Giles, I.S., Kay, R.L.F., Lee, D.J., Osmond, J.K., Cowart, J.B., Fritz, P., Barker, J.F., Gale, J. (1982) Radioelements, radiogenic helium and age relationships for groundwaters from the granites at Stripa, Sweden, *Geochim. Cosmochim. Acta*, 46, 1533–1543.

Auken, E., Violette, S., d'Ozouville, N., Deffontaines, B., Sørensen, K.I., Viezzoli, A., de Marsily, G. (2009) An integrated study of the hydrogeology of volcanic islands using helicopter borne transient electromagnetic: Application in the Galápagos Archipelago, *Comptes Rendus Geosciences,* 341, 899-907.

Ballentine, C.J., Hall, C.M. (1999) Determining paleotemperature and other variables using noble gas concentrations in water. *Geochim. Cosmochim. Acta.*, 63, 2315-2336.

Bethke, C.M., Zhao, X., Torgersen, T. (1999) Groundwater flow and the 4He distribution in the Great Artesian Basin of Australia, *Journal of Geophysical Research* 104, 12999-13011.

Bottomley, D.J., Ross, J.D., Clarke, W.B. (19840 Helium and neon isotope geochemistry of some ground waters from the Canadian Precambrian Shield, *Geochim. Cosmochim Acta*, 48, 1973-1985.

Brennwald, M.S., Hofer, M., Peeters, F., Aeschbach-Hertig, W., Strassmann, K., Kipfer, R.,

Imboden, D.M. (2003) Analysis of dissolved noble gases in the pore water of lacustrine sediments, *Limnology and Oceanography: Methods*, 1, 51-62.

Castro, M.C., Jambon, A., Marsily, G.d., Schlosser, P. (1998a) Noble gases as natural tracers of water circulation in the Paris Basin. 1. Measurements and discussion of their origin and mechanisms of vertical transport in the basin, *Water Resources Research*, 34, 2443-2466.

Castro, M.C., Goblet, P., Ledoux, E., Violette, S., Marsily, G.d. (1998b) Noble gases as natural tracers of water circulation in the Paris Basin. 2. Calibration of a groundwater flow model using noble gas isotope data. *Water Resources Research*, 34, 2467-2483.

Castro, M.C., Stute, M., Schlosser, P. (2000) Comparison of ^{4}He ages and ^{14}C ages in simple aquifer systems: implications for groundwater flow and chronologies. *Applied Geochemistry*, 15, 1137-1167.

Castro, M.C. (2004) Helium sources in passive margin aquifers--new evidence for a significant mantle ^{3}He source in aquifers with unexpectedly low in situ ^{3}He/^{4}He production, *Earth and Planetary Science Letters*, 222, 897-913.

Castro, M.C., D. Patriarche, Goblet, P. (2005) 2-D numerical simulations of groundwater flow, heat transfer and 4He transport – implications for the He terrestrial budget and the mantle helium-heat imbalance, *Earth and Planetary Science Letters,* 237, 893-910.

Castro, M.C., Hall, C.M., Patriarche, D., Goblet, P., Ellis, B.R. (2007) A new noble gas paleoclimate record in Texas – basic assumptions revisited, *Earth and Planetary Science Letters*, 257, 170-187.

Castro, M.C., Ma, L., Hall, C.M. (2009) A primordial, solar He-Ne signature in crustal fluids of a stable continental region, *Earth and Planetary Science Letters,* 279, 174-184.

Cey, B.D., Hudson, G.B., Moran, J.E., Scanlon, B.R. (2008) Impact of Artificial Recharge on Dissolved Noble Gases in Groundwater in California, *Environmental Science & Technology*, 42, 1017-1023.

Cey, B.D., Hudson, G.B., Moran, J.E., Scanlon, B.R. (2009) Evaluation of Noble Gas Recharge Temperatures in a Shallow Unconfined Aquifer, *Ground Water*, 47, 646-659.

Clarke, W. B., W. Jenkins, and Z. Top (1976), Determinations of tritium by mass-spectrometric measurement of ^{3}He, *Int. J. Appl. Radiat. Is.*, 27(9), 515–522.

Collins, A., Bush, M.B. (20100 An analysis of modern pollen representation and climatic conditions on the Galápagos Islands, *Holocene*, 21, 231-250.

Craig, H. (1961) Isotopic variations in meteoric waters, *Science*, 133, 1702-1703.

d'Ozouville, N. (2007) Étude du fonctionnement hydrologique dans les îles Galápagos : caractérisation d'un milieu volcanique insulaire et préalable à la gestion de la ressource. Université Pierre et Marie Curie, France, p. 471 p.

d'Ozouville, N., Auken, E., Sorensen, K., Violette, S., de Marsily, G., Deffontaines, B., Merlen, G. (2008a) Extensive perched aquifer and structural implications revealed by 3D resistivity mapping in a Galapagos volcano, *Earth and Planetary Science Letters*, 269, 518-522.

d'Ozouville, N., Deffontaines, B., Benveniste, J., Wegmüller, U., Violette, S., de Marsily, G. (2008b) DEM generation using ASAR (ENVISAT) for addressing the lack of freshwater ecosystems management, Santa Cruz Island, Galapagos. *Remote Sensing of Environment*, 112, 4131-4147.

Dansgaard, W. (1964) Stable isotopes in precipitation, *Tellus*, 16, 436-468.

Dominguez, C., Pryet, A., Pilar Fuente-Tomai, Violette, S., Villacís, M. and d'Ozouville, N. (2011) Fog interception and redistribution of rainfall by vegetation as controlling factors of recharge rates: a case-study in Galápagos Islands, *Geophysical Research Abstracts*, Vol. 13, EGU2011-2683-2, 2011

Farley, K. A., and Neroda, E. (1998) Noble gases in the Earth's mantle, *Annu. Rev. Earth Planet. Sci. Lett.*, 26, 189–218.

Gardner, W.P., Susong, D.D., Solomon, D.K., Heasler, H.P. (2010) Using noble gases measured in spring discharge to trace hydrothermal processes in the Norris Geyser Basin, Yellowstone National Park, U.S.A. *Journal of Volcanology and Geothermal Research*, 198, 394-404.

Geist, D.J., McBirney, A.R., Duncan, R.A. (1986) Geology and petrogenesis of lavas from San Cristobal Island, Galapagos Archipelago. *Geological Society of America Bulletin*, 97, 555-566.

Geist, D.J., White, W.M., Mcbirney, A.R. (1988) Plume-asthenosphere mixing beneath the Galapagos archipelago, *Nature*, 333, 657-660.

Gonfiantini, R., Roche, M.-A., Olivry, J.-C., Fontes, J.-C., Zuppi, G.M. (2001) The altitude effect on the isotopic composition of tropical rains, *Chemical Geology*, 181, 147-167.

Hall, C.M., Castro, M.C., Lohmann, K.C., Ma, L. (2005) Noble gases and stable isotopes in a shallow aquifer in southern Michigan: Implications for noble gas paleotemperature reconstructions for cool climates, *Geophys. Res. Lett.*, 32, L18404.

Heaton, T.H.E., Vogel, J.C. (1981) "Excess air" in groundwater, *Journal of Hydrology,* 50, 201-216.

Heilweil, V., Solomon, D., Gingerich, S., Verstraeten, I. (2009) Oxygen, hydrogen, and

helium isotopes for investigating groundwater systems of the Cape Verde Islands, West Africa, *Hydrogeology Journal,* 17, 1157-1174.

Herzberg, O., Mazor, E. (1979) Hydrological applications of noble gases and temperature measurements in underground water systems: Examples from Israel, *Journal of Hydrology*, 41, 217-231.

IAEA/WMO (2006) Global Network of Isotopes in Precipitation., The GNIP Database. Accessible at: http://www.iaea.org/water.

James, E.R., Manga, M., Rose, T.P., Hudson, G.B. (2000) The use of temperature and the isotopes of O, H, C, and noble gases to determine the pattern and spatial extent of groundwater flow, *Journal of Hydrology*, 237, 100-112.

Jean-Baptiste, P., Allard, P., Coutinho, R., Ferreira, T., Fourré, E., Queiroz, G., Gaspar, J.L. (2009) Helium isotopes in hydrothermal volcanic fluids of the Azores archipelago, *Earth and Planetary Science Letters,* 281, 70-80.

Kennedy, B.M., Lynch, M.A., Reynolds, J.H., Smith, S.P. (1985) Intensive sampling of noble gases in fluids at Yellowstone: I. Early overview of the data; regional patterns, *Geochimica et Cosmochimica Acta*, 49, 1251-1261.

Kennedy, B.M., Reynolds, J.H., Smith, S.P. (1988) Noble gas geochemistry in thermal springs, *Geochimica et Cosmochimica Acta*, 52, 1919-1928.

Kipfer, R., Aeschbach-Hertig, W., Peeters, F., Stute, M. (2002) Noble Gases in Lakes and Ground Waters, *Reviews in Mineralogy and Geochemistry*, 47, 615-700.

Klump, S., Tomonaga, Y., Kienzler, P., Kinzelbach, W., Baumann, T., Imboden, D.M., Kipfer, R. (2007) Field experiments yield new insights into gas exchange and excess air formation in natural porous media, *Geochimica et Cosmochimica Acta*, 71, 1385-1397.

Kramer, P., Black., J. (1970) Scientific and Conservation Report No. 21. Charles Darwin Research Station, Galapagos, Ecuador.

Lippmann, J., Stute, M., Torgersen, T., Moser, D.P., Hall, J.A., Lin, L., Borcsik, M., Bellamy, R.E.S., Onstott, T.C. (2003) Dating ultra-deep mine waters with noble gases and ^{36}Cl, Witwatersrand Basin, South Africa, *Geochimica et Cosmochimica Acta,* 67, 4597-4619.

Lowenstern, J. B. and Hurwitz, S. (2008) Monitoring a supervolcano in repose: Heat and volatile flux at the Yellowstone Caldera, *Elements*, 4:35–40.

Ma, L., Castro, M.C., Hall, C.M. (2004) A late Pleistocene noble gas paleotemperature record in southern Michigan, *Geophys. Res. Lett.,* 31, L23204, doi:10.1029/2004GL021766.

Manning, A.H., Solomon, D.K. (2003) Using noble gases to investigate mountain-front recharge, *Journal of Hydrology*, 275, 194-207.

Marty, B., Meynier, V., Nicolini, E., Griesshaber, E., Toutain, J.P. (1993) Geochemistry of gas emanations: A case study of the Reunion Hot Spot, Indian Ocean, *Applied Geochemistry*, 8, 141-152.

Mazor, E. (1972) Paleotemperatures and other hydrological parameters deduced from noble gases dissolved in groundwaters; Jordan Rift Valley, Israel, *Geochimica et Cosmochimica Acta,* 36, 1321-1336.

Mazor, E. and Fournier, R.O. (1973) More on noble gases in Yellowstone National Park hot waters, *Geochimica et Cosmochimica Acta*, 37:515–525.

Mazor, E. (1977) Geothermal tracing with atmospheric and radiogenic noble gases, *Geothermics*, 5(1-4):21 – 36.

Mercury, L., Azaroual, M., Zeyen, H., Tardy, Y. (2003) Thermodynamic properties of solutions in metastable systems under negative or positive pressures, *Geochimica et Cosmochimica Acta,* 67, 1769-1785.

Mercury, L., Pinti, D.L., Zeyen, H. (2004) The effect of the negative pressure of capillary water on atmospheric noble gas solubility in ground water and palaeotemperature reconstruction, *Earth and Planetary Science Letters,* 223, 147-161.

Peeters, F., Beyerle, U., Aeschbach-Hertig, W., Holocher, J., Brennwald, M.S., Kipfer, R. (2002) Improving noble gas based paleoclimate reconstruction and groundwater dating using $^{20}Ne/^{22}Ne$ ratios, *Geochimica et Cosmochimica Acta*, 67, 587-600.

Porcelli, D., Ballentine, C.J., Wieler, R. (2002) An Overview of Noble Gas Geochemistry and Cosmochemistry, *Reviews in Mineralogy and Geochemistry*, 47, 1-19.

Proctor and Redfern International Limited (2003) Actualizacion del Estudio de Factibiliad del Sistema de Agua y Saneamiento de Puerto Ayora, Reporte Final, project report (PO-PPF-1172/0C-EC), Proctor & Redfern International Ltd., Don Mills, Ontario, Canada.

Saar, M.O., Castro, M.C., Hall, C.M., Manga, M., Rose, T.P. (2005) Quantifying magmatic, crustal, and atmospheric helium contributions to volcanic aquifers using all stable noble gases: Implications for magmatism and groundwater flow, *Geochem. Geophys. Geosyst.*, 6, Q03008, doi:10.1029/2004GC000828.

Schlosser, P., Stute, M., Dörr, H., Sonntag, C., Münnich, K.O. (1988) Tritium/^{3}He dating of shallow groundwater, *Earth and Planetary Science Letters*, 89, 353-362.

Schlosser, P., Stute, M., Sonntag, C., Otto Münnich, K. (1989) Tritiogenic ^{3}He in shallow groundwater, *Earth and Planetary Science Letters,* 94, 245-256.

Scholl, M.A., S. E. Ingebritsen, C. J. Janik, and J. P. Kauahikaua (1996) Use of precipitation and groundwater isotopes to interpret regional hydrology on a tropical volcanic island: Kilauea volcano area, Hawaii, *Water Resour. Res.*, 32, 3525-3538.

Scholl, M.A., Gingerich, S.B., Tribble, G.W. (2002) The influence of microclimates and fog on stable isotope signatures used in interpretation of regional hydrology: East Maui, Hawaii, *Journal of Hydrology*, 264, 170-184.

Seinfeld, J.H., Pandis, S.N. (2006) Atmospheric chemistry and physics: from air pollution to climate change. Wiley, Hoboken, N.J.

Stute, M. (1989), Edelgase im Grundwasser—Bestimmung von Paläotemperaturen und Untersuchung der Dynamik von Grundwasserfliesssystemen. . Universität Heidelberg, Heidelberg.

Stute, M., Sonntag, C. (1992) Paleotempertures derived from noble gases dissolved in groundwater and in relation to soil temperature. In: Isotopes of Noble Gases as Tracers in Environmental Studies, Proceedings of a consultants meeting on isotopes of noble gases as tracers in environmental studies. IAEA, Vienna, p. 305

Stute, M., Schlosser, P., Clark, J.F., Broecker, W.S. (1992) Paleotemperatures in the Southwestern United States Derived from Noble Gases in Ground Water, *Science,* 256, 1000-1003.

Stute, M., Schlosser, P. (1993) Principles and applications of the Noble gas paleothermometer: in Climate Change in Continental Isotopic Recors, in: P.K. Smart, K.C. Lohmann, J. McKenzie, Savin, S. (Eds.), Geophysical Monograph. AGU, Washington, D. C., pp. 89– 100.

Stute, M., Forster, M., Frischkorn, H., Serejo, A., Clark, J.F., Schlosser, P., Broecker, W.S., Bonani, G. (1995) Cooling of Tropical Brazil (5°C) During the Last Glacial Maximum, *Science*, 269, 379-383.

Sun, T., Hall, C.M., Castro, M.C., Lohmann, K.C., Goblet, P. (2008) Excess air in the noble gas groundwater paleothermometer: A new model based on diffusion in the gas phase, *Geophys. Res. Lett.*, 35, L19401, doi:10.1029/2008GL035018.

Sun, T., Hall, C.M., Castro, M.C., 2010. Statistical properties of groundwater noble gas paleoclimate models: Are they robust and unbiased estimators? *Geochem. Geophys. Geosyst.,* 11, Q02002, doi:10.1029/2009GC002717.

Thoma, M.J., McNamara, J.P., Gribb, M.M., Benner, S.G. (2011) Seasonal recharge components in an urban/agricultural mountain front aquifer system using noble gas thermometry, *Journal of Hydrology*, 409, 118-127.

Thomson, W. (1871) On the equilibrium of vapor at a curved surface of liquid, *Philos. Mag.* 42, 448-452.

Torgersen, T., Ivey, G.N. (1985) Helium accumulation in ground water, II: A model for the

accumulation of the crustal 4He degassing flux, *Geochim Cosmochim Acta*, 49, 2445-2452.

Trueman, M, d'Ozouville, N. (2010) Characterizing the Galapagos Terrestrial Climate 1965-2009: a baseline for comparing future possible climate change, *Galapagos Research*, 67. P. 26-37.

Visser, A., Broers, H.P., Bierkens, M.F.P. (2007) Dating degassed groundwater with $^{3}H/^{3}He$, *Water Resour. Res.*, 43, W10434.

Weiss, R.F. (1968) Piggyback sampler for dissolved gas studies on sealed water samples. *Deep Sea Research and Oceanographic Abstracts*, 15, 695-699.

White, M.W., McBirney, A.R., Duncan, R.A. (1993) Petrology and geochemistry of the Galapagos Islands: Portrait of a Pathological Mantle Plume. *J. Geophys. Res.,* 98 (B11), 19533-19563, doi:10.1029/93JB02018.

CHAPTER 3

NOBLE GAS COMPOSITION IN RAINWATER AND ASSOCIATED WEATHER PATTERNS [2]

Abstract

A comprehensive study of noble gases in rainwater was carried out in southeast Michigan. Results show that all rainwater samples are in disequilibrium with surface conditions and present atmospheric He excesses up to 29%. Two noble gas patterns are identified. The first one, associated with low pressure systems, presence of fog and light rainfall, displays a relative Ar enrichment together with Ne, Kr, and Xe depletion, similar to a pattern first identified in high-altitude springs in the Galapagos Islands [*Warrier et al.*, 2012]. The second one, associated with the passage of frontal systems, displays a mass-dependent depletion pattern for Ne, Ar, Kr and Xe with respect to surface conditions. Precipitation is characterized by thunderstorms, heavy rainfall, and high cloud ceiling heights. A diffusion mass-transfer model suggests that noble gas patterns originate from ice. Complete re-equilibration of Kr and Xe with surface conditions should occur within hours.

3.1 Introduction

The atmospheric component of noble gases (He, Ne, Ar, Kr and Xe) dissolved in the

[2] Warrier, R. B., Castro, M. C., Hall, C. M., and K. C. Lohmann (2012), Noble gas composition in rainwater and associated weather patterns, submitted to *Geophys. Res. Lett.*

recharge area of groundwater systems is considered to be mainly a function of the ground air temperature, the mean local atmospheric pressure (altitude of the recharge area) and excess air (EA) [*Hall et al.*, 2012]. Consequently, noble gas temperatures (NGTs) are generally assumed to record the mean annual air temperature (MAAT) and have been regarded as a robust indicator of past climate [*Kipfer et al.*, 2002; *Aeschbach-Hertig et al.,* 2002*; Sun et al.*, 2010; *Castro et al.*, 2012]. Calculation of NGTs assumes that rainwater at the water table, commonly referred to as air saturated water (ASW), is in equilibrium with ground air. Lack of noble gas equilibration with respect to surface conditions, however, was recently observed in a study of high-altitude springs in the Galapagos Islands [*Warrier et al.*, 2012]. More specifically, the presence of a previously unknown noble gas pattern was identified, with relative Ar enrichment, together with Ne, Kr and Xe depletion. In addition, all samples displayed atmospheric He excesses. *Warrier et al*. [2012] hypothesized that this previously unknown noble gas pattern resulted from mixing between high altitude (≥1.5km) rainwater and low-altitude (~400m) fog droplets.

Only a few measurements of noble gas concentrations in rainwater are currently available, four in the Jordan Rift Valley, Israel [*Mazor,* 1972], and two in southeast Michigan, USA [*Warrier et al*., 2012]. Independent of geographic location, it is apparent that these scarce currently available measured noble gas concentrations in rainfall are not in equilibrium with surface conditions, and show significant deviations from expected ASW values. To present, no comprehensive study of noble gas composition in rainwater has been carried out. Such studies are critical to further develop the use of the noble gas thermometer in paleoclimate studies, as well as to expand the use of noble gases as tracers of groundwater circulation in fractured and karstic environments, where rainwater infiltration is rapid.

To understand the origin of the unique noble gas pattern in the Galapagos Islands [*Warrier et al.*, 2012], rainwater samples were collected in southeast Michigan in 2011 during multiple precipitation events over a period of several months, and analyzed for noble gas concentrations and helium isotopic ratios. We first show that all rainwater samples, without exception, are in disequilibrium with surface conditions and display two distinct noble gas patterns. One of these patterns is similar to the previously unknown noble gas pattern observed in high-altitude Galapagos springs. Subsequently, measured noble gas patterns in rainwater are analyzed together with multiple weather data at the time of sample collection and are shown to be associated with local weather conditions. The origin of noble gases in rainwater is subsequently investigated using a simple diffusion mass-transfer model. Together with this model and measured noble gas concentrations in rainwater, raindrop sizes are derived for individual precipitation events. Time estimates for rainwater noble gas concentrations to re-equilibrate at the surface using actual rainwater measurements are also provided in this study.

3.2 Regional Setting and Climate

Located in Midwestern United States (Fig. B1, Appendix B), southeast Michigan has a continental type of climate with warm summers (May-Sep; mean=19.5±1.7˚C; Fig. B2.a, Appendix B) and cold winters (Oct-Apr; mean=2.7±0.9˚C; Fig. B2.a, Appendix B). Regional precipitation (Fig. B2.b, Appendix B) is strongly influenced by the movement of high and low-pressure systems across the North-American continent. Although precipitation is reasonably well distributed throughout the year, peak precipitation occurs during summer months mostly as thunderstorms under the influence of southerly air masses from the Gulf of

Mexico. By contrast, cold air masses from the northwest Pacific and Canada are stronger from mid-autumn to late spring [*Shadbolt et al.*, 2006]. In addition, prevailing westerly winds bring some lake effect precipitation to the area during late fall and early winter.

3.3 Sample Collection and Measurements

Nineteen rainwater samples were collected from Ann Arbor (42.28˚N, 83.77˚W) and Milan (42.08˚N, 83.68˚W) in southeast Michigan between May and September 2011 (Figure B1; Table B1, Appendix B). Most rainwater samples were collected as runoff from rooftops in bottles and/or jugs. A few samples were collected directly from rainfall. Rainwater samples were subsequently transferred into copper tubes for analyses of noble gases. He, Ne, Ar, Kr and Xe concentrations as well as He isotopic ratios were measured at the University of Michigan following analytical procedures described in *Hall et al.* [2012].

3.4 Noble Gas Patterns and Associated Weather Data

Noble gas concentrations for all Michigan rainwater samples (black squares, Fig. 3.1a) deviate from expected ASW values ($C/C_{ASW}=1$) corresponding to measured surface air temperature and altitude at the time and location of sampling. Specifically, all rainwater samples present He excesses (1%-29%) with respect to ASW that are atmospheric in origin as indicated by the measured He isotopic ratios (Table B1, Appendix B). Similar atmospheric He excesses (≤22%) are observed in springs in the Galapagos [*Warrier et al*., 2012]. In contrast, Ne, Ar, Kr and Xe concentrations for most samples are depleted with respect to ASW (black squares, Fig. 3.1a). Specifically, while Ne concentrations display a maximum depletion of 11%, Ar, Kr and Xe display maximum depletions of 26%, 33% and 36% with

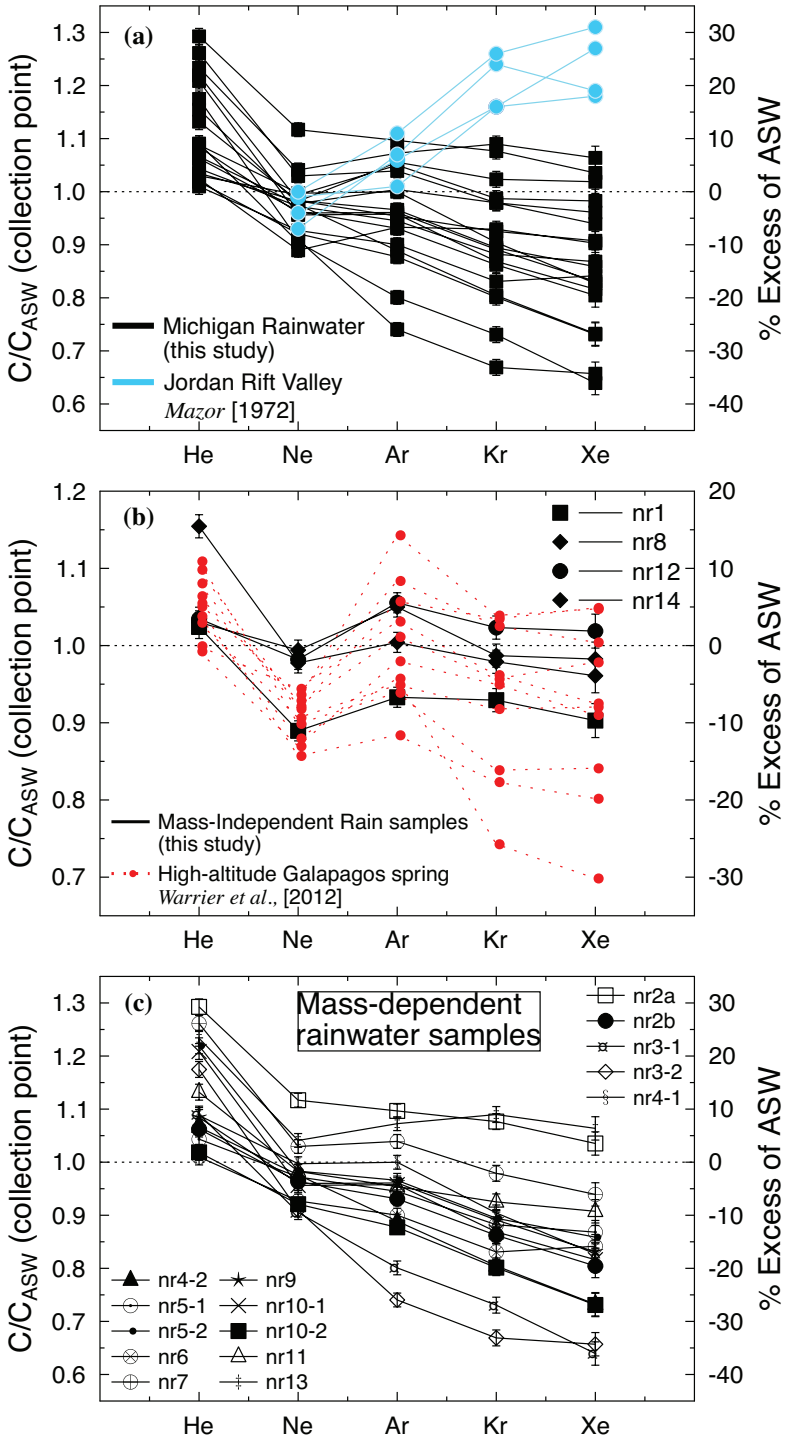

Figure 3.1 Measured noble gas concentrations in rainfall normalized to air saturated water corresponding to measured surface air temperature and altitude at the time and location of sampling. Right Y axis represents normalized values as % excess relative to ASW **(a)** Measured noble gas patterns in rainwater for all samples collected in southeast Michigan (black lines, this study) and samples from Jordan Rift Valley, Israel (blue lines, *Mazor* [1972]) **(b)** Mass-independent subset of noble gas patterns in Michigan rainfall and **(c)** Mass-dependent subset of noble gas patterns observed in rainwater from Michigan.

respect to ASW. Deviations of measured concentrations from expected ASW values indicate that Michigan rainwater is not in equilibrium with surface conditions. Lack of rainwater equilibration with surface conditions had previously been observed in the Jordan Rift Valley in Israel [*Mazor,* 1972]. However, noble gas patterns observed in this study are distinct from those previously observed by *Mazor* [1972]. While He was not reported and Ne concentrations were shown to be depleted (≤-7%) in the Jordan Rift Valley as also observed in Michigan, Ar, Kr and Xe concentrations in rainfall were in excess of ASW for all samples by up to 11%, 26% and 31%, respectively (blue circles; Fig. 3.1a; *Mazor,* 1972). Depleted Ar, Kr and Xe concentrations in rainwater in southern Michigan are thus in sharp contrast to excesses observed for these same gases in Israel, and indicate that noble gas concentrations in rainfall are not uniform throughout the world. These observations further suggest that the mechanism of incorporation of noble gases in rainwater at these two locations is distinct. Overall, two groups of rainwater samples can be identified in Michigan: a) a group displaying mass-independent noble gas patterns with relative Ar enrichment and Ne, Kr, and Xe depletion represented by samples nr1, 8, 12 and 14 (black markers, Fig. 3.1b); b) a group displaying a mass-dependent pattern with greater depletion of the heavier noble gases Kr and Xe as compared to the lighter ones Ne and Ar (Fig. 3.1c) represented by all the remaining samples.

Distinct noble gas patterns collected from rainfall at the same location suggests a likely association with local weather conditions. Mass-independent patterns with relative Ar enrichment and Ne, Kr, and Xe depletion displayed by southern Michigan rainwater samples are remarkably similar to the previously unknown pattern observed in high-altitude spring samples in the Galapagos Islands (red circles, Fig. 3.1b). *Warrier et al.* [2012] previously

showed that mixing between rainwater that equilibrated at high altitudes (≥1.5km) in the atmosphere together with low-altitude (~400m) fog droplets is at least partially capable of producing the observed noble gas patterns in these samples. A combined analysis of multiple weather data at the time of sample collection for all four rainwater samples displaying mass-independent patterns point to the presence of mist/fog, light to moderate rainfall and low cloud ceiling heights (~300m) under a low-pressure system (section B2 in Appendix B). Strikingly similar noble gas patterns observed in two distinct geographic locations specifically during the occurrence of fog and light rain suggest that dissolved noble gas concentrations in fog might be at least partly responsible for this unique noble gas pattern of relative Ar enrichment, together with Ne, Kr and Xe depletion. Noble gas measurements in fog have never been carried out. We thus lack an understanding of the underlying physical processes in these systems leading to disequilibrium and mass-independent patterns. Nevertheless, gas/aqueous-phase concentrations of pollutant species in fogs such as low molecular weight organic acids, ammonia, H_2O_2, sulfur S(IV) and nitrite are also observed to be in phase disequilibrium (both super- and under-saturated) with surface conditions based on Henry's law [e.g., *Munger et al*., 1983]. Inhomogeneous pH among individual fog drops [*Pandis and Seinfeld,* 1991], vertical in-cloud variation of gas phase concentrations [*Bott and Carmichael*, 1993], and mass transport limitations due to the presence of organic films [*Moore et al*., 2004] are some of the processes proposed to account for deviations from instantaneous phase equilibrium in fog with respect to ASW. This active area of research highlights the complexity of processes involved in gas phase dissolution of fog, and suggests that a full understanding of noble gas patterns in rainwater will also require a comprehensive understanding of noble gas behavior in fog.

In contrast, samples with mass dependent patterns (Fig. 3.1c) were collected during the passage of more active systems such as cold, warm or stationary fronts. Precipitation was characterized by thunderstorms, heavy rainfall, and high cloud ceiling heights (>1km; section B2 in Appendix B). Except for collection of sample nr5-1, during which some brief initial fog activity existed during a thunderstorm approach, total absence of fog was registered during collection of all samples displaying mass-dependent noble gas patterns for which precipitation characteristics were available (section B2 in Appendix B). As discussed above, in addition to other weather attributes, presence or absence of fog might thus be a critical parameter in determining observed noble gas patterns in rainwater. In addition to fog, these weather attributes include rainfall intensity and cloud ceiling heights. In turn, these distinct weather attributes relate to microphysical aspects of precipitation, including drop size distribution [e.g., *Marshall and Palmer,* 1948], droplet growth mechanism (diffusional condensation vs. collision and coalescence, e.g., *Rogers and Yau*, 1989), and dominant mass-transfer processes within raindrops (convective diffusion vs. turbulent mixing, e.g., *Amokrane and Caussade*, 1999). While a detailed analysis of raindrop microphysics is out of the scope of the current manuscript, a simple first order model is utilized below to explain the origin of some of the observed noble gas patterns in mass-dependent rainwater samples.

3.5 Origin of Noble Gases in Raindrops

Noble gas patterns for rainwater sample nr4-2 from Michigan (this study) and sample 2 from Israel [*Mazor*, 1972] (closed black triangles and blue circles, respectively, Fig. 3.2) are compared with expected noble gas patterns if liquid rainwater had equilibrated at higher altitudes (500 – 2000m; red circles, Fig. 3.2) assuming a surface temperature of 18˚C [*Mazor*,

1972] and an average lapse rate of 6.5˚C/km [*Moore*, 1956]. Because of lower pressures at high altitude, He and Ne concentrations are lower than ASW values at the surface as these gases are mostly sensitive to pressure. In contrast, the heavier noble gases Ar, Kr and Xe are particularly sensitive to temperature and the impact of low temperatures at altitude dominates over that of low pressures leading to expected concentrations at higher altitudes higher than surface ASW values (red circles, Fig. 3.2). Expected Ar, Kr and Xe patterns for liquid rainwater in approximate equilibrium with air for altitudes varying between 1500 and 2000m are similar to the pattern displayed by sample 2 in Israel (red and blue circles, Fig. 3.2) and suggest that precipitation in-cloud in this region originates as liquid water in equilibrium with the atmosphere at these high altitudes. However, such an origin cannot explain the simultaneous atmospheric He excesses and depletion of Ne, Ar, Kr and Xe observed in most rainwater samples from southeast Michigan (black squares; Fig. 3.1a, this study). It is possible that the Wegener-Bergeron-Findeisen process of rain formation, originating as ice crystals in mixed phase clouds, is responsible for our observed noble gas patterns [*Wegener,* 1911; *Bergeron,* 1935; *Findeisen,* 1938]. Indeed, the presence of hail and high altitude condensation levels below freezing recorded for most of our rainwater samples strongly suggest that precipitation in southeast Michigan starts as ice (section B2 in Appendix B). While noble gas concentrations in ice within clouds have not been measured, overall mass-dependent noble gas patterns in Michigan rainwater (Fig. 3.1c) are very similar to average measured noble gas patterns in Antarctica ice (*Malone et al.*, 2010; green triangles, Fig. 3.2). In particular, average noble gas composition in ice is enriched in He and depleted in Ne by 38% and 18%, respectively, while the heavier noble gases Ar, Kr and Xe are extremely depleted, by 90%, 94% and 95% with respect to equilibrium conditions, respectively (green

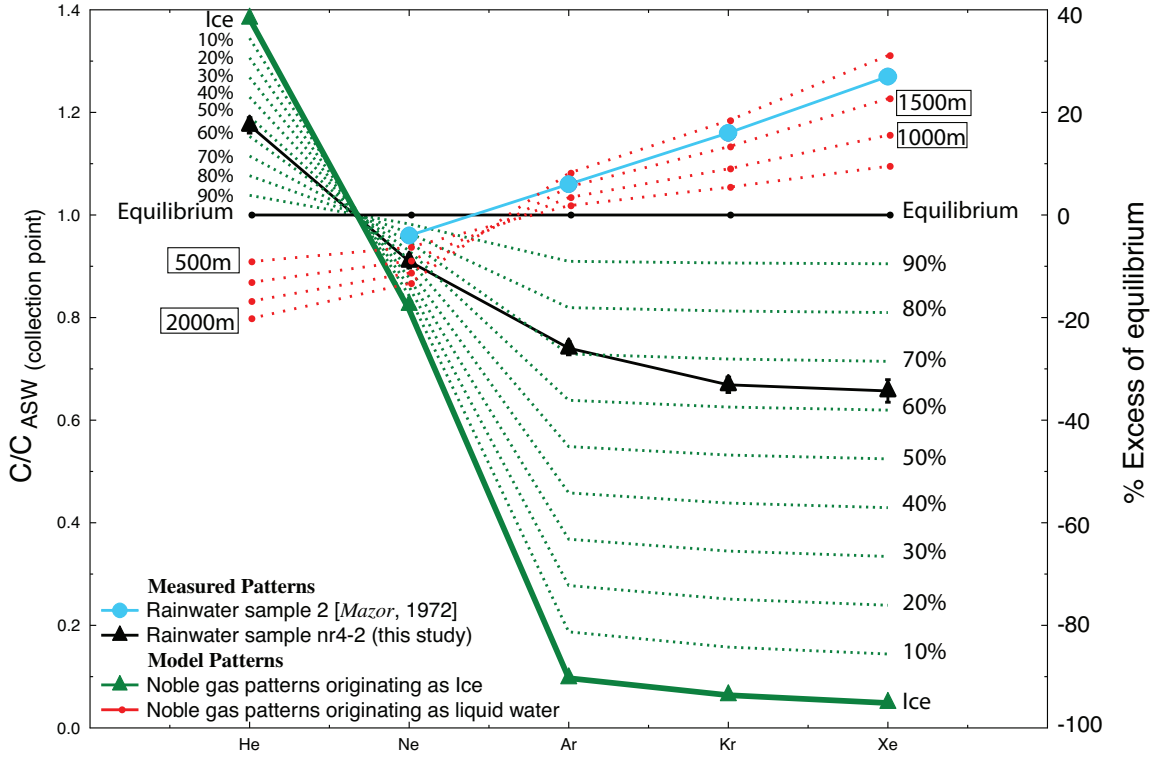

Figure 3.2 Comparison of measured noble gas patterns in rainwater from Michigan (nr4-2, this study, black triangle) and Israel (sample 2 of *Mazor* [1972], blue circle) together with expected rainwater patterns originating as a liquid in equilibrium at higher altitudes (red circles) and ice (green triangles). Both rainwater samples are normalized to ASW at respective measured surface conditions. Expected noble gas patterns during various stages (0-100%) of isothermal equilibrium in a raindrop (green dotted lines) are also indicated.

triangles, Fig. 3.2, ASW at 0˚C, *Malone et al*., 2010). Laboratory experiments show that the unique noble gas patterns observed in ice are due to the ability of smaller atoms such as He to be incorporated into the ice structure as freezing progresses, as opposed to larger atoms such as Ar, Kr and Xe which are entirely excluded from the ice structure, while Ne remains in ice at low concentrations [*Top et al.*, 1988].

A simple mass-transfer model (section B4 in Appendix B) involving diffusion in a sphere (raindrop) was used to investigate whether noble gas patterns in Michigan rainwater can originate from ice, assuming that noble gas concentrations in ice crystals within clouds are similar to those of Antarctic ice. Expected noble gas patterns corresponding to different stages of isothermal disequilibrium starting from ice and assuming ASW at 0˚C as diffusive mass transfer proceeds within a raindrop, are shown (green dotted lines, Fig.3.2). Comparison of expected and measured noble gas patterns suggests that such a model is capable of reproducing the various degrees of atmospheric He excesses together with Ne, Ar, Kr and Xe depletion levels observed in our Michigan rainwater samples. For example, sample nr4-2 indicates measured He and Ne concentrations within 50%-60% of equilibrium with the atmosphere while Ar, Kr and Xe point to equilibration values between 60% and 70% (Fig. 3.2). Ar, Kr and Xe point to greater equilibration values than He and Ne due to increased dissolution of the heavier noble gases in rainwater resulting from heat transfer, a process which is not accounted for in our simple diffusive mass-transfer model (cf. section B4 in Appendix B). Indeed, evaporation of a falling raindrop lowers the droplet's surface temperature compared to it's surroundings leading to greater dissolution of the more temperature sensitive heavier noble gases Ar, Kr and Xe [see, e.g., *Elperin et al.*, 2007]. A comprehensive treatment of

transient, coupled heat and mass transfer of noble gases within a falling raindrop is out of the scope of the present manuscript. However, our simple diffusion mass transfer model shows that mass-dependent noble gas patterns are expected in rainwater if the latter is assumed to start as ice. This, in turn, strongly suggests that ice is the starting point of rainwater formation in southeast Michigan.

3.6 Calculation of droplet sizes based on measured noble gas concentrations in rainfall

Measured noble gas concentrations for rainwater samples displaying mass-dependent depletion are used to provide a range of droplet sizes for corresponding rainfall events assuming that: a) noble gas concentrations in raindrops start as ice and; b) noble gas concentrations of ice crystals within clouds have a composition similar to the average ice concentrations measured in Antarctica by *Malone et al.* [2010]. This method is briefly described below for rainwater sample nr4-2 (Fig. 3.3; see also section B5 in Appendix B).

The total amount of noble gases transferred in or out of a raindrop from initial ice values are first calculated based on measured concentrations for nr4-2. The corresponding time 't' taken to achieve measured noble gas concentrations from initial ice concentrations is subsequently calculated using a diffusive mass transfer model in a raindrop for a range of assumed droplet diameters (0.019-10mm; red lines, Fig. 3.3, section B5 in Appendix B). The time 't' to achieve measured noble gas concentrations in rainwater is then compared with the time 't_z' taken for a raindrop to fall from a cloud base between 0.5 and 5kms for a similar range of assumed droplet sizes (blue lines, Fig.

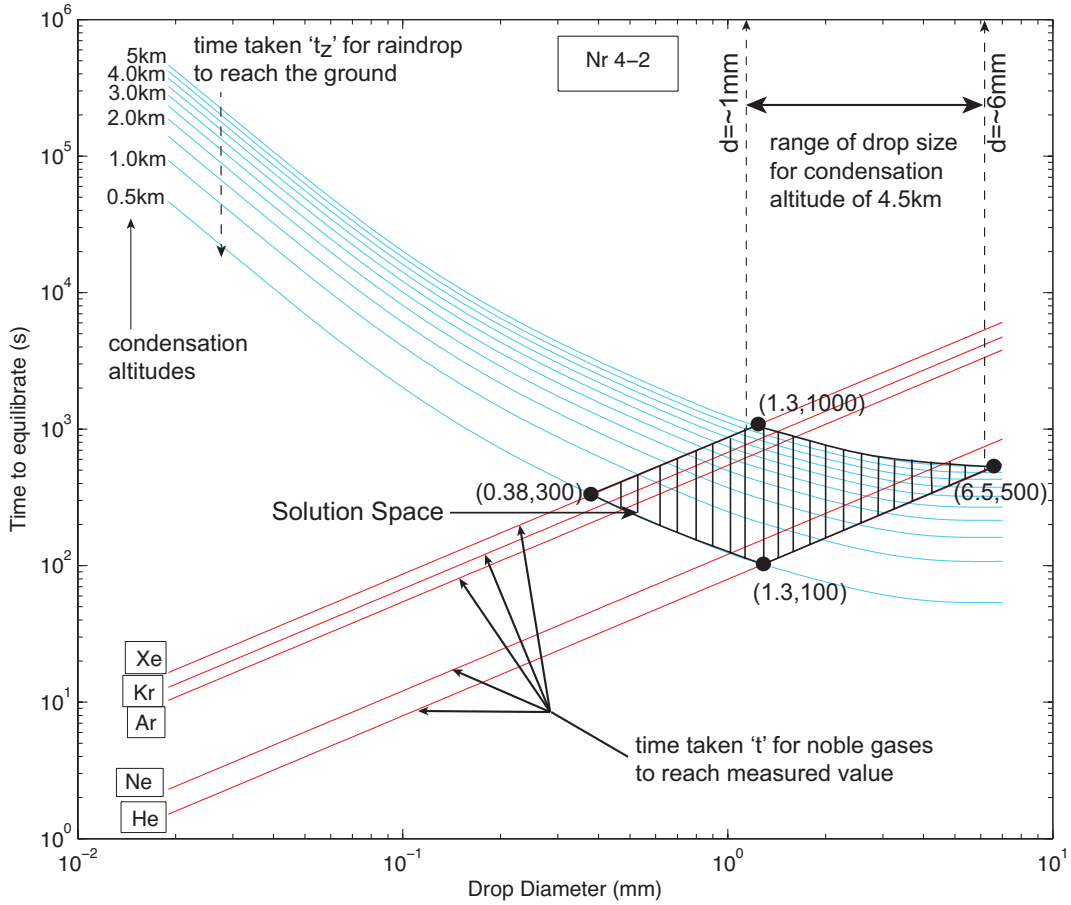

Figure 3.3 Calculation of raindrop sizes for precipitation event corresponding to sample nr4-2. Comparison of time (y-axis) taken by noble gases to reach measured values in raindrops of different sizes (x-axis) and time taken for a drop to fall from cloud base to ground surface yields a solution space (shaded area) of time and droplet diameters. Range of droplet sizes constrained by observed condensation altitude for this precipitation event is also indicated.

3.3) yielding a solution space (shaded area, Fig. 3.3) defined by equilibration times of 100, 300, 500 and 1000 seconds and droplet sizes of 0.38, 1.3 and 6.5mm diameter. Because weather sounding data for nr4-2 indicates a condensation altitude of ~4.5km (Table B3 in Appendix B), drop sizes are further constrained to be between 1 and 6mm. Drop sizes for other mass-dependent rainwater samples are similarly calculated and yield large values, between 0.45 and 10mm in diameter (Table B3 in Appendix B). Calculated drop sizes fall within the range of raindrop sizes observed in nature, which, depending on the amount of airstream turbulence, is usually between 6-8mm but may reach diameters as large as 10mm [*Rogers and Yau*, 1989]. Because large drop sizes are generally associated with heavy rainfall [e.g., *Marshall and Palmer,* 1948], our results indicate that heavy rainfall is expected for samples displaying mass-dependent depletion. Heavy rainfall for samples displaying mass-dependent depletion is corroborated both by direct observations at the time of collection as well as by weather stations' data (section B2 in Appendix B).

3.7 Time estimates for noble gases in rainwater to re-equilibrate at the surface

Our study shows that all rainwater samples, without exception, are in disequilibrium with surface conditions. Although noble gases in rainwater are typically assumed to re-equilibrate at surface conditions on the order of a few minutes, a detailed analysis using actual rainwater measurements is lacking (section B5, Appendix B). Time taken for measured maximum deviations of noble gases in Michigan rainwater (Fig. 3.1) to re-equilibrate at the surface is calculated using a diffusive mass-transfer model in a sheet of water considering a realistic water depth of 1cm and an average surface air

temperature of 25˚C (section B5, Appendix B). Our results show that maximum atmospheric He excesses of 29% in rainwater would take ~15 minutes to reach equilibrium, while maximum deviations of -11%, -26%, -33% and -36% for Ne, Ar, Kr and Xe would take ~3.3mins, ~34mins, ~72mins and ~108mins (~2 hours), respectively. Faster re-equilibration of He and Ne as compared to Ar, Kr and Xe is observed due both to their higher diffusion coefficients and lower initial disequilibrium with respect to surface conditions. Our calculations show that the typical assumption of rainwater re-equilibration occurring within minutes is more applicable for lighter noble gases and smaller water depths (<1cm) while heavier noble gases and greater water depths require re-equilibration time on the order of hours. Noble gas patterns in rainfall will thus be recorded in groundwater systems if time to re-equilibrate with surface conditions is greater than the time taken to reach the water table. This is likely the case in the Galapagos Islands where rapid water infiltration due to the presence of fractures and thin soil cover [*Warrier et al*., 2012] allows little time for noble gas re-equilibration at the water table.

3.8 Concluding Remarks

Studies of noble gases in fog and rainwater are non-existent, yet, these are critical to improving our understanding of the noble gas thermometer in paleoclimate studies. These will also expand the use of noble gases as tracers of groundwater circulation in fractured and karstic environments, where rainwater infiltration is rapid. Here, a comprehensive study of noble gases in rainwater in southeast Michigan is presented. It is shown that rainwater is consistently in disequilibrium with surface conditions and present

systematic atmospheric He excesses. Two distinct noble gas patterns emerge, one associated with the presence of fog and light rainfall, the other associated with the presence of thunderstorms, heavy rainfall, and high cloud ceilings. Noble gas patterns are likely to originate from ice and complete re-equilibration with surface conditions should occur within hours.

References

Aeschbach-Hertig, W., M. Stute, J. F. Clark, R. F. Reuter, and P. Schlosser (2002), A paleotemperature record derived from dissolved noble gases in groundwater of the Aquia Aquifer (Maryland, USA), *Geochim. Cosmochim. Acta*, 66(5), 797-817.

Amokrane, H., and B. Caussade (1999), Gas Absorption into a Moving Spheroidal Water Drop, *Journal of the Atmospheric Sciences*, 56(12), 1808-1829.

Bergeron, T. (1935) On the physics of clouds and precipitation. Proces Verbaux de l'Association de Météorologie, *International Union of Geodesy and Geophysics*, 156–178.

Bott, A., Carmichael, G.R. (1993) Multiphase chemistry in a microphysical radiation fog model—a numerical study. *Atmospheric Environment* 27A, 503–522.

Castro, M. C., R. B. Warrier, C. M. Hall, and K. C. Lohmann (2012), A late Pleistocene-Mid-Holocene noble gas and stable isotope climate and subglacial record in southern Michigan, *Geophys. Res. Lett.*, *39*(19), L19709.

Elperin, T., A. Fominykh, and B. Krasovitov (2007), Evaporation and Condensation of Large Droplets in the Presence of Inert Admixtures Containing Soluble Gas, *Journal of the Atmospheric Sciences*, *64*(3), 983-995.

Findeisen, W. (1938) Kolloid-meteorologische Vorgänge bei Neiderschlags-bildung. *Meteor. Z.*, 55, 121–133.

Hall, C. M., M. C. Castro, K. C. Lohmann, and T. Sun (2012), Testing the noble gas paleothermometer with a yearlong study of groundwater noble gases in an instrumented monitoring well, *Water Resour. Res.*, *48*(4), W04517.

Kipfer, R., W. Aeschbach-Hertig, F. Peeters, and M. Stute (2002), Noble Gases in Lakes and Ground Waters, *Reviews in Mineralogy and Geochemistry*, *47*(1), 615-700.

Malone, J. L., M. C. Castro, C. M. Hall, P. T. Doran, F. Kenig, and C. P. McKay (2010), New insights into the origin and evolution of Lake Vida, McMurdo Dry Valleys, Antarctica - A noble gas study in ice and brines, *Earth and Planetary Sci. Lett.*, *289*(1-2), 112-122.

Marshall, J. S., and W. M. Palmer (1948), The distribution of raindrops with size, *J. Meteorol.*, 5, 165–166.

Mazor, E. (1972), Paleotemperatures and other hydrological parameters deduced from noble gases dissolved in groundwaters; Jordan Rift Valley, Israel, *Geochimica et Cosmochimica Acta*, *36*(12), 1321-1336.

Moore, J. (1956), The tropospheric temperature lapse rate, *Meteorology and Atmospheric Physics*, *9*(4), 468-470.

Moore, K. F., D. Eli Sherman, J. E. Reilly, M. P. Hannigan, T. Lee, and J. L. Collett Jr (2004), Drop size-dependent chemical composition of clouds and fogs. Part II:Relevance to interpreting the aerosol/trace gas/fog system, *Atmospheric Environment*, *38*(10), 1403-1415.

Munger, J. W., D. J. Jacob, J. M. Waldman, and M. R. Hoffmann (1983), Fogwater Chemistry in an Urban Atmosphere, *J. Geophys. Res.*, *88*(C9), 5109-5121.

Pandis, S. N., and J. H. Seinfeld (1991), Should Bulk Cloudwater or Fogwater Samples Obey Henry's Law?, *J. Geophys. Res.*, *96*(D6), 10791-10798.

Rogers, R. R., and M. K. Yau (1989), *A short course in cloud physics*, xiv, 290 p. pp., Butterworth-Heinemann, Oxford ; Boston.

Shadbolt, R. P., E. A. Waller, J. P. Messina, and J. A. Winkler (2006), Source regions of lower-tropospheric airflow trajectories for the lower peninsula of Michigan: A 40-year air mass climatology, *J. Geophys. Res.*, *111*(D21), D21117.

Sun, T., C. M. Hall, and M. C. Castro (2010), Statistical properties of groundwater noble gas paleoclimate models: Are they robust and unbiased estimators?, *Geochem. Geophys. Geosyst.*, *11*(Q02002).

Top, Z., S. Martin, and P. Becker (1988), A laboratory study of dissolved noble gas anomaly due to ice formation, *Geophys. Res. Lett.*, *15*(8), 796-799.

Warrier, R. B., M. C. Castro, and C. M. Hall (2012), Recharge and source-water insights from the Galapagos Islands using noble gases and stable isotopes, *Water Resour. Res.*, *48*(3), W03508.

Wegener, A. (1911) Thermodynamik der Atmosphäre. Leipzig, 331pp.

CHAPTER 4

A LATE PLEISTOCENE - MID-HOLOCENE NOBLE GAS AND STABLE ISOTOPE CLIMATE AND SUBGLACIAL RECORD IN SOUTHERN MICHIGAN [3]

Abstract

Stable isotopes (δD, $\delta^{18}O$) and ^{14}C derived ages in the Saginaw aquifer in southern Michigan suggest subglacial meltwater contributions from the Laurentide Ice Sheet of up to 36% in the late Pleistocene, following the Last Glacial Maximum. Contributions of up to 74% from previous glaciation periods are observed. Together with the Marshall record [*Ma et al.*, 2004], noble gas temperatures (NGTs) and excess air (EA) from the Saginaw aquifer capture, for the first time, the onset of the Younger Dryas (~12,9kyrs BP) with a ~3.3˚C cooling accompanied by drier conditions. Mid-Holocene (MH) climatic shifts are also identified, with warming (~2.9˚C), increased aridity starting at ~5.4kyrs BP followed by reversal to cooler, humid conditions at ~4.1kyrs BP. Except for the last MH reversal, the stable isotope record mimics the NGT and EA records. Contrasting trends displayed by $\delta^{18}O$ and deuterium-excess in the last MH reversal suggests enhanced vapor transport from the Gulf of Mexico.

---

[3] Castro, M. C., R. B. Warrier, C. M. Hall, and K. C. Lohmann (2012), A late Pleistocene-Mid-Holocene noble gas and stable isotope climate and subglacial record in southern Michigan, *Geophys. Res. Lett.*, 39, L19709, doi:10.1029/2012GL053098.

4.1 Introduction

The noble gas temperature (NGT) proxy is regarded as a robust indicator of past climate [*Kipfer et al.*, 2002; *Sun et al.*, 2010]. Unlike other continental proxies, it provides a direct measure of the ground air temperature at the water table [*Mazor*, 1972]. This is because the solubility of atmospheric noble gases (Ne, Ar, Kr, Xe) in groundwater is dependent on the ground air temperature, the mean local atmospheric pressure (altitude of the recharge area) and excess air (EA). The latter is incorporated in groundwater through dissolution of air bubbles due to water table fluctuations [*Heaton and Vogel*, 1981]. High EA values have been linked to significant fluctuations in water table levels due to discrete episodes of intense rainfall typical of arid climates while low EA values have been linked to humid climatic regimes (warm or cool) with shallow water table levels and continuous recharge [*Castro et al.*, 2007, Hall et al., 2012; see also *Aeschbach-Hertig et al.*, 2002]. Similarly, $\delta^{18}O$ is expected to reflect the mean annual air temperature (MAAT) in mid-latitude regions, while the deuterium-excess (d-excess) parameter is indicative of non-equilibrium processes [*Dansgaard*, 1964]. In particular, the high relative humidity of air masses overlying oceans [*Merlivat and Jouzel*, 1979] and high evaporation during precipitation typical of drier conditions [*Dansgaard*, 1964] lead to lower d-excess values. Temperature and humid versus arid climatic regimes derived from NGTs and EA can thus be independently compared with corresponding $\delta^{18}O$ and d-excess trends, respectively, to achieve an in-depth understanding of abrupt climatic events.

NGTs have been commonly used to identify major contrasting trends between Pleistocene and present time, and the Last Glacial Maximum (LGM) in particular [*Kipfer et*

al., 2002]. Their use to identify abrupt climate shifts, however, remains rare [*Ma et al.*, 2004, *Castro et al.*, 2007]. These are critical to understand current climate patterns, and to provide additional constraints to general circulation models. The NGT study by *Ma et al.* [2004] carried out in the Marshall aquifer in southern Michigan, a region covered by the Laurentide Ice Sheet (LIS) during the LGM and early deglaciation periods, first identified the Bølling-Allerød (BOA) warming event through NGTs.

Here, we present a new ~13.1kyrs paleoclimatic reconstruction based on the NGT, EA and stable isotope record derived from the overlying Saginaw aquifer in southern Michigan. Together with the original *Ma et al.* [2004] Marshall aquifer record, new aspects of late Pleistocene and Mid-Holocene climate shifts in southern Michigan are revealed. Based on groundwater ages and the entire stable isotope Saginaw record, which goes beyond the LGM, new constraints on the timing and sources of subglacial meltwater contributions to this system are also provided.

4.2 Regional Setting

The Saginaw aquifer, a major groundwater flow system composed mostly of sandstones, is located in the central portion of the Michigan Basin, in the Lower Peninsula of Michigan (Figure 4.1). It is underlain by the Bayport-Michigan confining units, which, in turn, overlies the Marshall aquifer [*Mandle and Westjohn*, 1989]. These formations subcrop at an altitude of ~275-300m and are overlain by the unconfined Glacial Drift aquifer. In the Saginaw aquifer, groundwater flows gravitationally from the south and north to the NE and SE, respectively, into the Saginaw lowlands (SL) region and Lake Huron, where it discharges (Figure 4.1). In the Marshall aquifer in southern Michigan, groundwater flows gravitationally

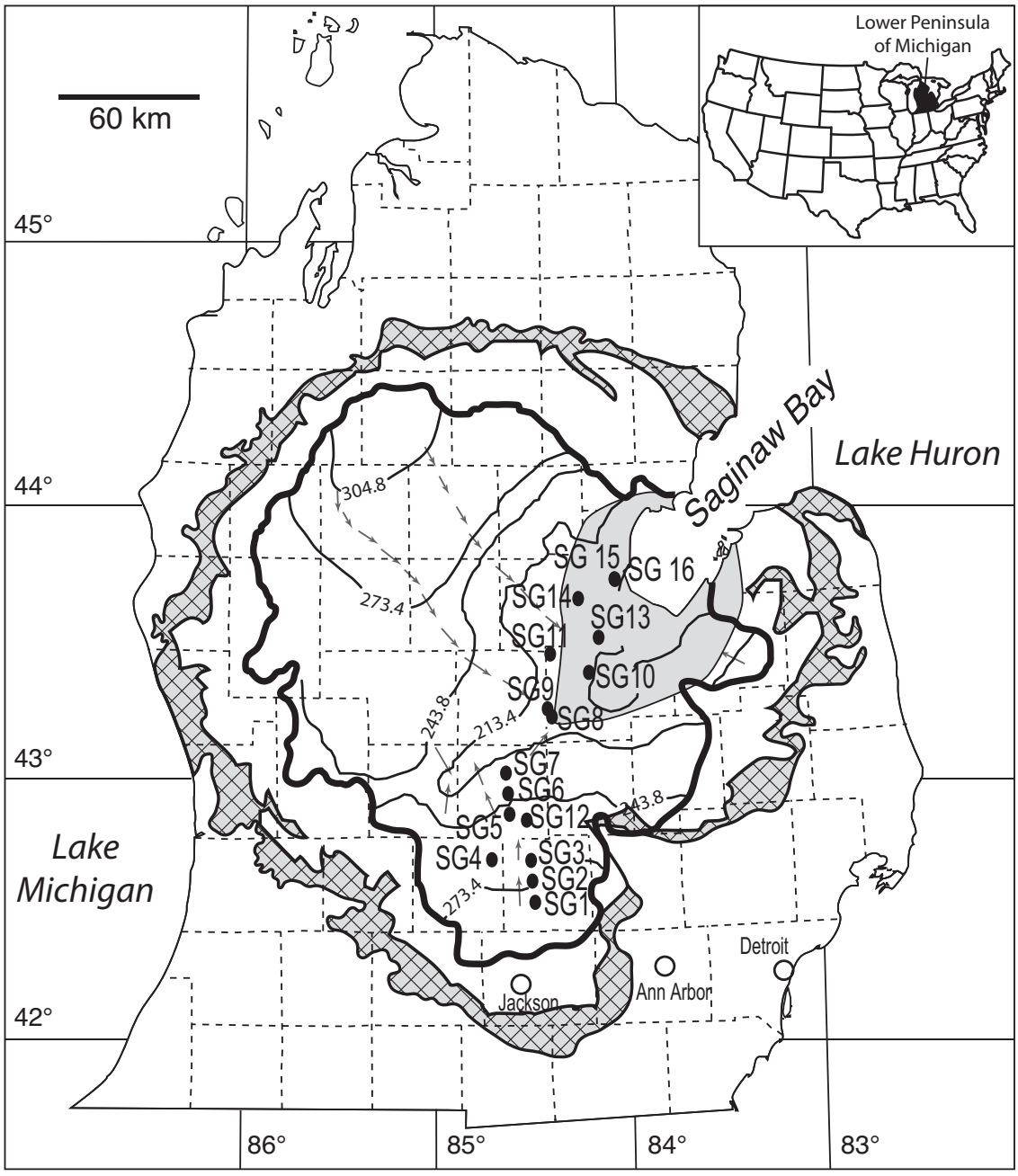

Figure 4.1 Detailed study area and location of Saginaw aquifer samples in southern Michigan [adapted from *Mandle and Westjohn*, 1989]. Bold contour represents the Saginaw subcrop, gray contour with grid represents the Marshall subcrop. Equipotential line (contour lines) values are shown in meters together with main groundwater flow directions (arrows). Gray area corresponds to the Saginaw lowlands.

to the NW and NE, and discharges into Lake Michigan and Lake Huron (SL area), respectively.

4.3 Sample Collection and Measurements

Groundwater samples were collected from 16 wells in the Saginaw aquifer along a main groundwater flow path, from the recharge area in southern Michigan, toward the Saginaw Bay area, in Lake Huron (Figure 4.1). Samples were analyzed for noble gases (Ne, Ar, Kr and Xe), stable (δD, $\delta^{18}O$) and carbon ($\delta^{13}C$ and ^{14}C activity) isotopes as well as major elements (Tables C1-C3 in Appendix C). Noble gas concentrations, stable isotope ratios and major elements were measured at the University of Michigan following analytical procedures described in *Hall et al.* [2012]. NGTs and EA were calculated from measured noble gas concentrations using the unfractionated air (UA) model [*Kipfer et al., 2002*] (section C2 and Table C4 in Appendix C).

Groundwater ages for all samples are calculated from ^{14}C activities measured at the AMS facility at Woods Hole Oceanographic Institution. Model corrected ^{14}C ages for all Saginaw (this study) and Marshall [*Ma et al.*, 2004] samples were subsequently converted into calibrated calendar ages (sec. C3 and Table C2 in Appendix C). Calibrated calendar ages are referred to hereafter simply as ages.

4.4 Groundwater Ages and Stable Isotope Record – Timing and Source of Subglacial Meltwater Contributions

Saginaw groundwater samples range in age from modern to >50kyrs BP and yield a large range of δD and $\delta^{18}O$ values varying between -124.03‰ and -59.17‰, and -17.48‰ and -8.49‰, respectively (Figure 4.2, Table C2 in Appendix C). It is apparent that δD and

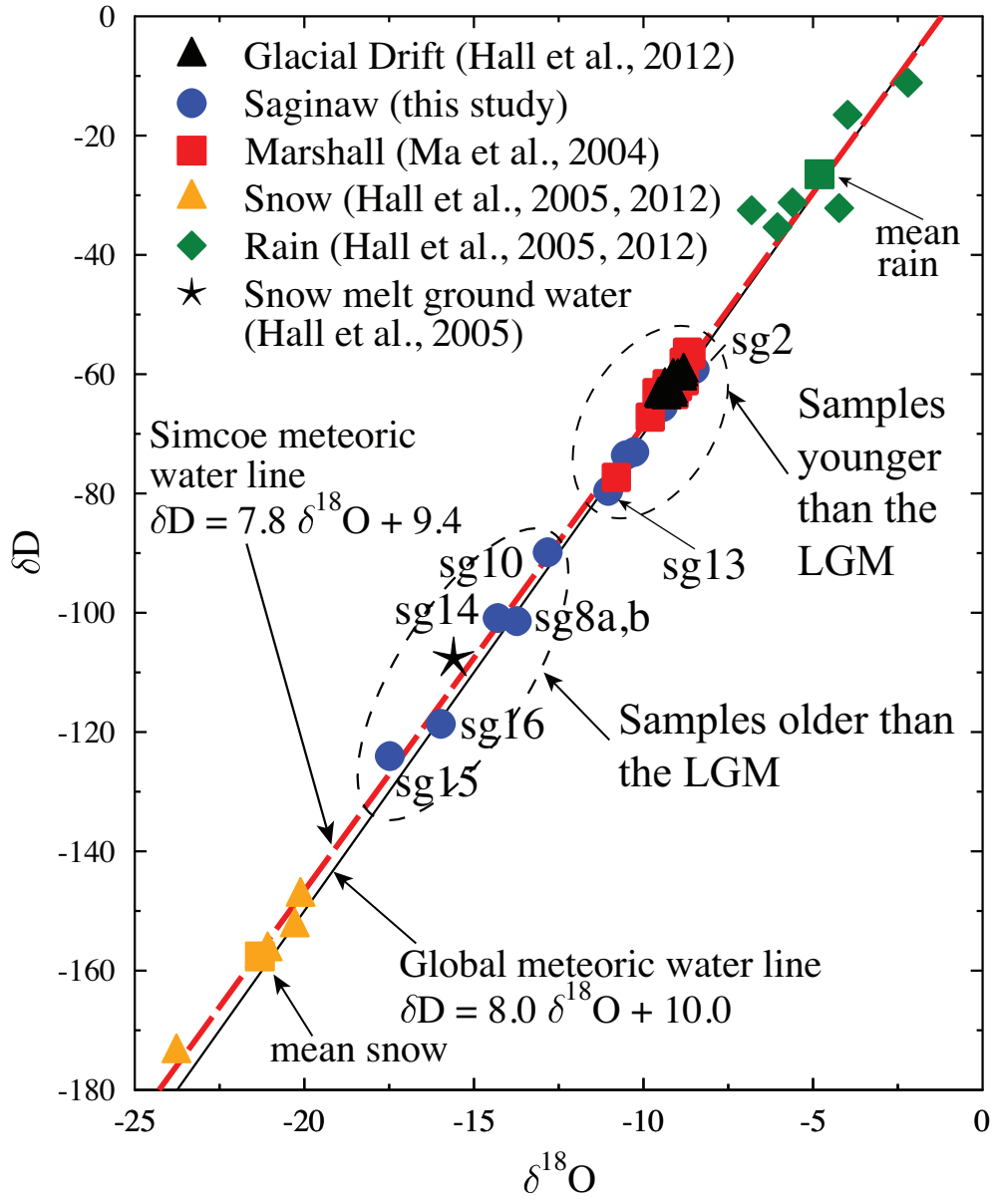

Figure 4.2 Plot of δD vs. $\delta^{18}O$ for all Saginaw (blue circles), Marshall (red squares) and Glacial Drift (black triangles) aquifer samples. Also shown are stable isotope ratios for modern rainfall (green diamonds), snow (yellow triangles) and groundwater from snow meltwater (black star) in southern Michigan. The Global Meteoric Water line as well as the local Simcoe meteoric water line (http://isohis.iaea.org) are also shown.

$\delta^{18}O$ from the Saginaw (this study), the Marshall [*Ma et al.*, 2004] and the Glacial Drift [*Hall et al.*, 2012] aquifers fall close to the Global Meteoric Water Line [*Craig*, 1961] as well as the local meteoric water line in Simcoe, Ontario, Canada (Figure 4.2), suggesting that δD and $\delta^{18}O$ were not significantly modified by water-rock interactions within these aquifers. Samples from all three aquifers fall between mean values for modern rainwater (δD= -26.48‰, $\delta^{18}O$= -4.81‰) and snow (δD= -157.61‰, $\delta^{18}O$= -21.31‰) in southern Michigan (Figure 4.2). In particular, all Glacial Drift, Marshall and Saginaw samples that range in age from modern to younger than the LGM (~0 - ~18kyrs B.P) display δD and $\delta^{18}O$ values closer to values for modern rain (Figure 4.2). By contrast, with the exception of sample sg13, all Saginaw samples located in the SL region (Figure 4.1) display ages beyond the LGM and yield extremely depleted δD (<-89.86‰) and $\delta^{18}O$ (<-12.83‰) values, similar to values for modern groundwater resulting directly from snowmelt and closer to snow values (Figure 4.2). The percentage contribution of modern snow to total recharge for all Saginaw samples was calculated assuming that groundwater recharge is simply a binary mixture between mean modern rain and snow (Figure 4.2, Table C5 in Appendix C). Because the stable isotopic composition in the past has changed, these values should be taken as a first order indication. Snowmelt contribution for modern Saginaw samples (sg1, sg2) varies between 26% and 29%, a value similar to that of modern Glacial Drift samples (Table C5 in Appendix C). This is expected as the Saginaw aquifer is recharged through the Glacial Drift aquifer. As samples get older (≤~13kyrs BP), the percentage of snowmelt contribution increases up to 36%. Such an increase might be due to: a) a climate cooler than present at that time as also shown by our NGT record (below) where the presence of a thicker and longer winter snow cover was likely in place; or b) contribution of LIS subglacial meltwater as the deglaciation proceeded [see,

e.g., *Ma et al.*, 2004] and as also previously suggested [e.g., *Hoaglund et al.,* 2004*; McIntosh et al.*, 2011]. In contrast, except for sample sg13, snow contributions for samples in the SL area (sg8, sg10, sg14, sg15, sg16), all of which display ages beyond the LGM (~26.6 kyrs - >50kyrs;), are much greater (48% to 74%) than observed for modern groundwater recharge. Unlike younger samples, however, late Pleistocene (following the LGM) LIS subglacial meltwater contribution to the Saginaw aquifer in the SL area is not supported by our newly estimated groundwater ages, as previously suggested by *Hoaglund et al.* [2004]. Indeed, our ^{14}C measurements and subsequently derived calendar ages point instead to subglacial meltwater contributions from previous glacial ice advances or deglaciation periods. Alternatively, it is also possible that ^{14}C activity has been reduced due to mixing with older groundwaters from the Marshall aquifer or the Bayport-Michigan confining unit [see, e.g., *Ma et al.*, 2005]. Indeed, as shown by *Castro and Goblet* [2005], mixing with older groundwaters can lead to apparently older ^{14}C ages. At present it is not possible to ascertain whether or not ^{14}C ages in this area are providing entirely accurate information. In addition to extremely depleted δD and $\delta^{18}O$ values, most of these samples with ages beyond the LGM display also unusually high (~80% - 120%) atmospheric noble gas excesses (Table C1 in Appendix C) which result in poor NGT fits using existing NGT models (Sec.C2 in Appendix C). Mechanisms leading to unusually large atmospheric noble gas excesses for these samples are discussed in detail elsewhere (Warrier, R. B. et al., Evidence for a thermal event in the Michigan Basin through near-surface atmospheric noble gas signatures in the Saginaw Bay discharge area, submitted to *Earth and Planetary Science Letters*, 2012). While a number of these older samples in the SL area present poor model fits and thus poorly constrained NGT estimates, most Saginaw samples with ages <LGM display robust NGT fits and are thus

suited for a paleoclimatic reconstruction (sec.C2, Appendix C). These are the results discussed below. The focus is thus on climatic events during the late Pleistocene, mid-Holocene (MH) and present time.

4.5 NGTs, Excess Air, $\delta^{18}O$ and d-excess – Younger Dryas and Mid-Holocene climatic oscillations record

Saginaw samples younger than the LGM range in age from modern to ~13.1kyrs and yield NGTs varying between 8.0 ± 0.8˚C and 1.6 ± 0.9˚C (Figure 4.3a, Tables C2 and C4 in Appendix C]. Our modern Saginaw sample (sg2) displays the highest NGT of the entire set of samples (8.0 ± 0.8˚C) pointing to an overall warming trend in southern Michigan since the late Pleistocene, and, more broadly, since the LGM (Figure 4.3a). While our modern Saginaw sample displays a NGT value close to the MAAT of 9.1 ± 0.8˚C of southern Michigan (Figure 4.3a), the mean of modern samples from the Marshall (m1, 6, 7, 8, 9) of 6.3 ± 0.8˚C (Figure 4.3a) [*Ma et al*., 2004] displays a strong bias to low NGTs. However, as pointed out by *Ma et al.* [2004], some of these "modern" samples could possibly be hundreds of years old and representative of a cooler period instead. Other Marshall modern samples are likely recording specific recharge conditions at the time they were sampled rather than true soil temperature. Indeed, field observations and noble gas measurements strongly suggest that at least part of this bias is due to net depletion of O_2 in the soil air due to biological processes without corresponding build-up of CO_2, leading to higher noble gas partial pressures [*Hall et al.*, 2005, *Sun et al., 2008*]. Our modern Saginaw NGT value shows that soil air noble gases partial pressures are similar to standard air and suggest that recharge conditions for this sample are distinct from those of the Marshall modern samples (sec.C2 in

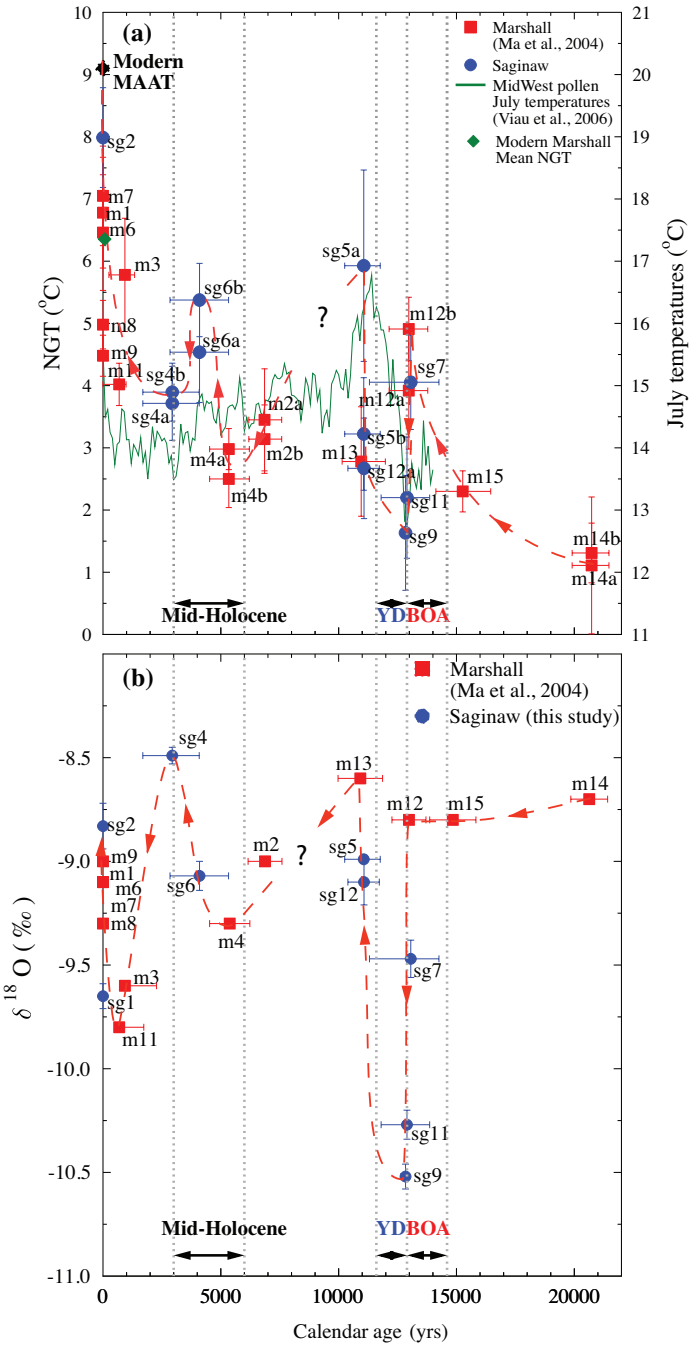

Figure 4.3. Comparison of **a)** NGTs and **b)** $\delta^{18}O$ as a function of groundwater ages for the Saginaw and Marshall aquifers. July high-resolution temperature reconstruction (Y right axis) from pollen in the Midwest [*Viau et al.*, 2006; World Data Center for Paleoclimatology http://www.ncdc.noaa.gov/paleo/recons.html] is also shown. We are only able to compare temperature differences for both the pollen and NGT records rather than absolute temperatures. The temperature differences recorded by both methods are comparable for both the YD and MH climate variations. MAAT is also indicated together with time periods corresponding to the BOA, YD and MH climatic events. Also shown is a schematic line (red dashed line), similar to the moving average, for visualization of climatic trends.

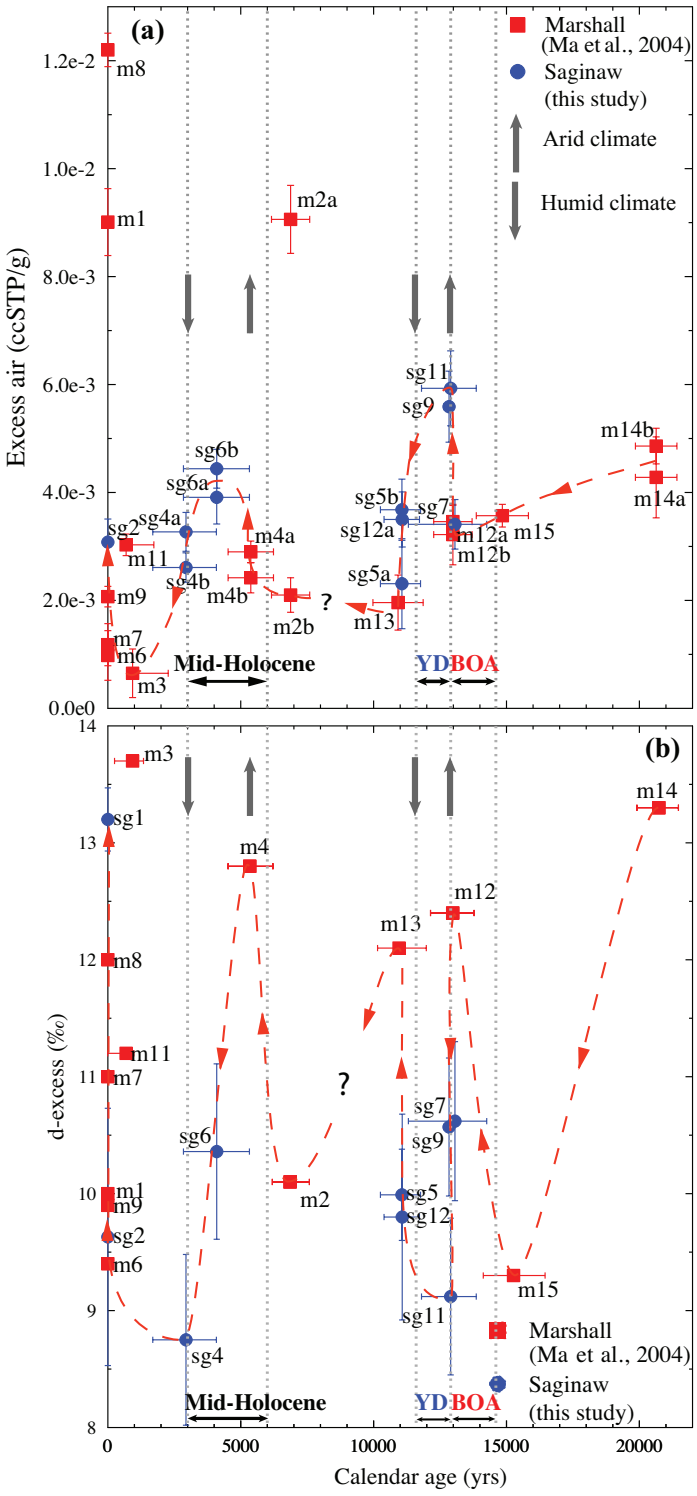

Figure 4.4 Comparison of **a)** EA and **b)** d-excess as a function of groundwater ages for the Saginaw and Marshall aquifers. Also shown are the time periods corresponding to the BOA, YD and MH climatic events. A schematic line (red dashed line) similar to the moving average is also indicated for visualization of climatic trends. Upward and downward arrows indicate change into arid and humid regimes, respectively.

Appendix C). *Hall et al.* [2012] have shown that large precipitation events such as Hurricane Ike can significantly modify recharge conditions within aquifer systems and bring O_2 depleted soil air back to standard conditions, with simultaneous incorporation of high levels of EA at the water table. Sample sg2's EA value is at a level similar to that measured in the Glacial Drift aquifer following Hurricane Ike suggesting the occurrence of a major storm event prior to recharge. In contrast, modern Marshall samples are compatible with conditions prior to Hurricane Ike [*Hall et al.*, 2012]. It is thus possible that modern NGTs are reflecting mostly recharge conditions rather than the MAAT. The study of *Hall et al.* [2012] suggests, however, that the NGT temperature proxy should be viewed as an average of recharge conditions over several years. It is possible that once averaged over several years, such bias might vanish. However, in the event that such a bias to low NGTs in the Marshall recharge area would apply to all the Marshall NGT record, all the main conclusions of this study (below) would still apply (cf. sec.C2 in Appendix C).

Particularly relevant aspects of our combined Saginaw and Marshall NGT paleoclimatic reconstruction are the abrupt climatic oscillations recorded both in the late Pleistocene and Mid-Holocene within the overall warming trend observed since the LGM (Figure 4.3a, cf. sec.C4 in Appendix C). A dispersion analysis of both events indicates that these climatic records should be well preserved in both the Saginaw and Marshall aquifers (sec.C5 in Appendix C). Rapid climatic oscillations in northeast US began with warming at the onset of the Bølling/Allerød (BOA) event at ~14,6kyr BP and were followed by a rapid climatic reversal to cooler conditions during the Younger Dryas (YD) at ~12,9kyrs BP [*Shuman et al.*, 2002]. Although *Ma et al.* [2004] were able to identify overall climatic trends associated with the occurrence of the BOA and YD events, the onset and termination of the

YD were almost entirely missed. Our new NGT record in the Saginaw aquifer has now allowed us to close this gap by capturing for the first time both the onset and termination of the YD. Indeed, our combined Saginaw and Marshall NGT record identifies statistically distinct rapid climatic variations (sec.C4 in Appendix C) both at the onset (m12b, sg7, m12a, sg11, sg9) and termination (sg9, sg12a, m13, sg5b, sg5a) of the YD. More specifically, our NGT record points to a cooling of ~3.3 ± 1˚C (m12b-sg9, Figure 4.3a) at the onset of the YD which is comparable with regional cooling estimates of 3-4˚C obtained through pollen temperature proxies (Figure 4.3a) [*Viau et al*., 2006], macrofossils and fish remains [*Peteet et al.*, 1993] as well as endogenic lake calcite in northeastern USA [*Zhao et al.*, 2010]. Some proxies in Midwest lakes, however, indicate a greater regional cooling (5-5.6˚C; [*Hou et al.*, 2007; *Yu*, 2007]). It is possible that our slightly lower (~1˚C) NGT estimates may partly be due to increased duration of snow cover during the YD. Snow cover has an insulating effect which might lead to an overestimation of NGTs and thus, an underestimation of the MAAT cooling [*Cey*, 2009]. Transition from warm BOA to cool YD NGTs is also corroborated by a sudden decrease in our $\delta^{18}O$ record of 1.7‰ (m12-sg9, Figure 4.3b). Such depletion is also consistent with a $\delta^{18}O$ decrease of 1.5‰ observed in carbonates from a lake in Southern Ontario [*Yu*, 2000]. The onset of the YD recorded by both NGTs and $\delta^{18}O$ (Figures 4.3a and 4.3b) is also accompanied by a distinct increase in EA (m12b-sg9, 11; Figure 4.4a) and a simultaneous decrease in d-excess (MI12-sg9, 11, Figure 4.4b) of 3.3‰ indicating a transition from a warm, humid (BOA) environment to a cool, arid one (YD). Transition from a warm, humid climate at the peak of BOA to cold, arid conditions during the YD were also previously recorded through vegetation changes [e.g., *Shuman et al.*, 2002] and low lake levels [*e.g., Webb*, 1990] in the Great Lakes region.

Termination of the YD at ~11,6kyrs BP was marked by rapid (~50 yrs) warming in eastern North America [*Peteet et al.*, 1993; *Viau et al.*, 2006]. Our combined NGT record displays a general warming trend (sg9, sg12a, m13, sg5b, sg5a; sec.C2 in Appendix C) within this time period of 4.3 ± 1.8˚C (sg9-sg5a, Figure 4.3a), a value comparable to regional warming estimates from pollen data (~4˚C, *Viau et al*., 2006) and lake carbonates (5.4-8˚C; *Hou et al*., 2007). Our NGT increase is accompanied by a 1.9‰ $\delta^{18}O$ increase (Figure 4.3b), in excellent agreement with a 2‰ increase recorded by *Yu* [2000] in southern Ontario. Termination of the YD is also accompanied by a strong decrease in EA (Figure 4.4a) as well as an increase in d-excess of ~3‰ (Figure 4.4b) suggesting a return to a warmer, humid climate immediately following the YD.

Our Saginaw samples have also recorded, for the first time, the MH climatic oscillations through NGTs. Unlike previous climatic events (e.g., BOA, YD), the timing and magnitude of MH climatic oscillations varied regionally [*e.g., Bartlein et al.*, 2011]. Numerous proxies in the Midwest, including fossil pollen [*Winkler et al.*, 1986; *Viau et al.*, 2006] and speleothems [*Dorale et al.*, 1992] show evidence for a temperature increase of ~0.5-4˚C between ~6kyrs and ~3kyrs BP [e.g., *Kirby et al.*, 2002] followed by a rapid cooling of ~4˚C up to ~2.5kyrs [e.g., *Dorale et al.*, 1992]. Our combined NGT record points to the MH warming onset at ~5.4 kyrs (m4b) peaking at ~4.1 kyrs BP with a corresponding NGT increase of 2.9 ± 0.8˚C (sg6b; Figure 4.3a). This warming period is followed by a rapid NGT cooling of 1.7 ± 0.9˚C between ~4.1kyrs and ~2.9kyrs BP (sg6b, sg4a; Figure 4.3a). The timing and magnitude of MH climatic oscillations observed through NGTs generally correlates well with regional proxies. Corresponding EA variations are observed. Specifically, increased EA values between the onset of the MH warming at ~5.4kyrs BP

(m4b, Figure 4.4a) and its peak at ~4.1 kyrs (sg6b, Figure 4.4a), a sign of increasing aridity within a warmer climate, followed by return to low EA values (sg4b, Figure 4.4a) and thus, a return to greater humidity levels in a cooler environment. This change in arid versus humid climatic regimes is also well documented through a host of regional studies including vegetation changes [*Bartlein et al.*, 2011; *Baker et al.*, 1998] and low lake levels [*e.g., Winkler et al.*, 1986]. As shown by the NGT and EA record, transition from cool, humid conditions to warm, drier conditions at the peak of the MH are also corroborated by enriched $\delta^{18}O$ values accompanied by decreasing d-excess values (m4-sg6, Figures 4.3b and 4.4b). In contrast, cooling and the return to more humid conditions at the end of the MH climatic event (sg6b-sg4a, Figures 4.3a and 4.4a) are not reflected in the $\delta^{18}O$ and d-excess record. More specifically, $\delta^{18}O$ and d-excess values are more enriched and lower, respectively, at the termination of the MH cooling period at ~2.9kyrs BP (sg4, Figures 4.3b and 4.4b). Previous studies have hypothesized a change in air-mass distribution over the Great Lakes region during the MH [*Krishnamurthy et al.*, 1995]. An increase in vapor transport from the Gulf of Mexico would lead to enriched $\delta^{18}O$ values [see, e.g., *Ma et al.*, 2004, *Hall et al.*, 2012] as well as lower d-excess values due to expected higher relative humidity at the Gulf of Mexico ocean source as compared to other moisture sources in the Midwest [*Shadbolt et al.*, 2006]. Our $\delta^{18}O$ and d-excess results from the late MH are consistent with this hypothesis.

4.6 Concluding remarks

NGTs and EA hold great potential in identifying rapid climatic shifts both, in terms of actual temperature changes (NGTs) and humid versus arid climatic regimes (EA). Here, for the first time, the onset and termination of the YD and MH oscillations are identified through

NGTs and EA and further strengthened by direct correlation of $\delta^{18}O$ and d-excess signatures for most of the record. Together with groundwater age information, the stable isotope record (δD, $\delta^{18}O$) also places new constraints on timing and sources of subglacial meltwater contributions from the LIS both prior and following the LGM.

Acknowledgements

We thank constructive comments by two anonymous reviewers. Financial support by the National Science Foundation CAREER award EAR-0545071 is greatly appreciated.

References

Aeschbach-Hertig W., U. Beyerle, J. Holocher, F. Peeters, R. Kipfer, Excess air in groundwater as a potential indicator of past environmental changes, Study of Environmental Change using Isotope Techniques, IAEA, Vienna, 2002, 174-183.

Baker, R. G., L. A. Gonzalez, M. Raymo, E. A. Bettis, M. K. Reagan, and J. A. Dorale (1998), Comparison of multiple proxy records of Holocene environments in the midwestern United States, *Geology*, *26*(12), 1131-1134.

Bartlein, P., et al. (2011), Pollen-based continental climate reconstructions at 6 and 21 ka: a global synthesis, *Climate Dynamics*, *37*(3), 775-802.

Castro, M. C., and P. Goblet (2005), Calculation of ground water ages - A comparative analysis, *Ground Water*, *43*(3), 368-380.

Castro, M. C., C. M. Hall, D. Patriarche, P. Goblet, and B. R. Ellis (2007), A new noble gas paleoclimate record in Texas – basic assumptions revisited, *Earth and Planetary Science Letters*, *257*, 170-187.

Cey, B. D. (2009), On the accuracy of noble gas recharge temperatures as a paleoclimate proxy, *J. Geophys. Res.*, *114*(D4), D04107.

Craig, H. (1961), Isotopic variations in meteoric waters, *Science*, *133*(3465), 1702-1703.

Dansgaard, W. (1964), Stable isotopes in precipitation, *Tellus*, *16*(4), 436-468.

Dorale, J. A., L. A. Gonzalez, M. K. Reagan, D. A. Pickett, M. T. Murrell, and R. G. Baker (1992), A High-Resolution Record of Holocene Climate Change in Spele, *Science*, *258*(5088), 1626.

Hall, C. M., M. C. Castro, K. C. Lohmann, and L. Ma (2005), Noble gases and stable isotopes in a shallow aquifer in southern Michigan: Implications for noble gas paleotemperature reconstructions for cool climates, *Geophys. Res. Lett.*, *32*(18), L18404.

Hall, C. M., Castro M.C., Lohmann K.C. and Sun T. (2012), Testing the noble gas paleothermometer with a yearlong study of groundwater noble gases in an instrumented monitoring well, *Water Resources Research,* 48, W04517, doi:10.1029/2011WR010951.

Heaton, T. H. E., and J. C. Vogel (1981), "Excess air" in groundwater, Journal of Hydrology, 50, 201-216.

Hoaglund, J.R., III, J.J. Kolak, D.T. Long, and G.J. Larson, Analysis of modern and Pleistocene hydrologic exchange between Saginaw Bay (Lake Huron) and the Saginaw Lowlands area, *Geol. Soc. Am. Bull.*, *116* (1-2), 3-15, 2004.

Hou, J., Y. Huang, W. W. Oswald, D. R. Foster, and B. Shuman (2007), Centennial-scale compound-specific hydrogen isotope record of Pleistocene-Holocene climate transition from southern New England, *Geophys. Res. Lett.*, *34*(19), L19706.

Kipfer, R., W. Aeschbach-Hertig, F. Peeters, and M. Stute (2002), Noble Gases in Lakes and Ground Waters, *Reviews in Mineralogy and Geochemistry*, *47*(1), 615-700.

Kirby, M. E., H. T. Mullins, W. P. Patterson, and A. W. Burnett (2002), Late glacial-Holocene atmospheric circulation and precipitation in the northeast United States inferred from modern calibrated stable oxygen and carbon isotopes, *Geological Society of America Bulletin*, *114*(10), 1326-1340.

Krishnamurthy, R. V., K. A. Syrup, M. Baskaran, and A. Long (1995), Late glacial climate record of midwestern United States from hydrogen isotope ratio of lake organic matter, *Science*, *269*(5230), 1565.

Ma, L., M. C. Castro, and C. M. Hall (2004), A late Pleistocene-Holocene noble gas paleotemperature record in southern Michigan, *Geophys. Res. Lett.*, *31*(23), L23204.

Ma, L., M. C. Castro, C. M. Hall, and L. M. Walter (2005), Cross-formational flow and salinity sources inferred from a combined study of helium concentrations, isotopic ratios, and major elements in the Marshall aquifer, southern Michigan, *Geochem. Geophys. Geosyst.*, *6*(10), Q10004.

Mandle, R. J., and D. B. Westjohn (1989), Geohydrologic framework and ground-water flow in the Michigan Basin, in Regional Aquifer Systems of the United States: Aquifers of the Midwestern Area, AWRA Monogr. Ser., vol. 13, pp. 83– 109, Am. Water Resour. Assoc., Middleburg, Va.

Mazor, E. (1972), Paleotemperatures and other hydrological parameters deduced from noble gases dissolved in groundwaters; Jordan Rift Valley, Israel, *Geochimica et Cosmochimica Acta*, *36*(12), 1321-1336.

McIntosh, J. C., G. Garven, and J. S. Hanor (2011), Impacts of Pleistocene glaciation on large-scale groundwater flow and salinity in the Michigan Basin, *Geofluids*, *11*(1), 18-33.

Merlivat, L., and J. Jouzel (1979), Global Climatic Interpretation of the Deuterium-Oxygen 18 Relationship for Precipitation, *J. Geophys. Res.*, *84*(C8), 5029-5033.

Peteet, D. M., R. A. Daniels, L. E. Heusser, J. S. Vogel, J. R. Southon, and D. E. Nelson (1993), Late-glacial pollen, macrofossils and fish remains in northeastern U.S.A.- The Younger Dryas oscillation: A contribution to the 'North Atlantic seaboard programme' of IGCP-253, 'Termination of the Pleistocene', *Quaternary Science Reviews*, *12*(8), 597-612.

Shadbolt, R. P., E. A. Waller, J. P. Messina, and J. A. Winkler (2006), Source regions of lower-tropospheric airflow trajectories for the lower peninsula of Michigan: A 40-year air mass climatology, *J. Geophys. Res.*, *111*(D21), D21117.

Shuman, B., T. Webb III, P. Bartlein, and J. W. Williams (2002), The anatomy of a climatic oscillation: vegetation change in eastern North America during the Younger Dryas chronozone, *Quaternary Science Reviews*, *21*(16-17), 1777-1791.

Sun, T., C. M. Hall, M. C. Castro, K. C. Lohmann, and P. Goblet (2008), Excess air in the noble gas groundwater paleothermometer: A new model based on diffusion in the gas phase, *Geophysical Research Letters*, *35*(19).

Sun, T., C. M. Hall, and M. C. Castro (2010), Statistical properties of groundwater noble gas paleoclimate models: Are they robust and unbiased estimators?, *Geochem. Geophys.*

Geosyst., *11*(Q02002).

Viau, A. E., K. Gajewski, M. C. Sawada, and P. Fines (2006), Millennial-scale temperature variations in North America during the Holocene, *J. Geophys. Res.*, *111*(D9), D09102.

Webb, R. S. (1990), Late Quaternary water level fluctuations in the northeastern United States, 9101848 thesis, 372 p. pp, Brown University, United States -- Rhode Island.

Winkler, M. G., A. M. Swain, and J. E. Kutzbach (1986), Middle Holocene dry period in the northern Midwestern United States: Lake levels and pollen stratigraphy, *Quaternary Research*, *25*(2), 235-250.

Yu, Z. (2000), Ecosystem response to Lateglacial and early Holocene climate oscillations in the Great Lakes region of North America, *Quaternary Science Reviews*, *19*, 1723-1747.

Yu, Z. C. (2007), Rapid response of forested vegetation to multiple climatic oscillations during the last deglaciation in the northeastern United States, *Quaternary Research*, *67*(2), 297-303.

Zhao, C., Z. Yu, E. Ito, and Y. Zhao (2010), Holocene climate trend, variability, and shift documented by lacustrine stable-isotope record in the northeastern United States, *Quaternary Science Reviews*, *29*(15-16), 1831-1843.

CHAPTER 5

LARGE ATMOSPHERIC NOBLE GAS EXCESSES IN A SHALLOW AQUIFER IN THE MICHIGAN BASIN AS INDICATORS OF A PAST MANTLE THERMAL EVENT[4]

Abstract

Significant atmospheric noble gas excesses in aquifer systems have systematically been linked to increased hydrostatic pressure, either due to increased water table levels or due to the development of ice cover. Measured noble gases (Ne, Ar, Kr, Xe) in the shallow Saginaw aquifer in the Michigan Basin display both moderate (~20-60% Ne excess) and large (~80->120% Ne excess) excesses of atmospheric noble gases with respect to air saturated water for modern recharge conditions. All large atmospheric noble gas excesses are located in the main discharge area of the Michigan Basin, in the Saginaw Lowlands region.

Here, through a step-by-step analysis, with the aide of the closed-system equilibration model of *Aeschbach-Hertig et al.* [2008] we first show that large atmospheric noble gas excesses in the Saginaw aquifer do not result from increased hydrostatic pressure but instead, are the result of sources external to the aquifer. External factors with the potential to account for excess of atmospheric noble gases in the Saginaw aquifer are biological consumption of

[4] Warrier, R. B., Castro, M. C., Hall, C. M., and K. C. Lohmann (2012), Evidence for a thermal event in the Michigan Basin through near-surface atmospheric noble gas signatures in the Saginaw Bay discharge area, submitted to *Earth and Planetary Science Letters*.

soil air O_2 without an equivalent build up of CO_2, and vertical transport of atmospheric noble gases that are believed to have escaped from deep Michigan Basin brines following a past thermal event of mantle origin. We show that atmospheric noble gas excesses due to O_2 depletion of soil air are not substantial enough compared to the total observed atmospheric noble gas excesses in the Saginaw aquifer, in the Saginaw Lowlands region. Subsequently, we show that the atmospheric noble gas pattern of the entire Michigan Basin strata appears to result from two distinct end-members: a) an end-member represented by the deepest, most depleted brines from which most of the atmospheric noble gases escaped; and b) an end-member with excess atmospheric noble gas values above those displayed by the Saginaw samples. The latter is unconstrained due to the dilution effect exerted by recharge water. Using a Rayleigh distillation model we further show that the greater enrichment of lighter relative to heavier noble gases in the Saginaw aquifer in the Saginaw Lowlands area is compatible with either diffusion or solubility related mechanisms. These findings reinforce the notion that a past thermal event is indeed responsible for the atmospheric noble gas excesses found in the Saginaw aquifer in the Saginaw Lowlands area. They are also consistent with and reinforce previous findings with respect to the occurrence of a thermal event of mantle origin.

5.1 Introduction

The study of noble gases (He, Ne, Ar, Kr and Xe) in sedimentary basins has proven to be a powerful tool to investigate the origin and history of crustal fluids [e.g., *Pinti and Marty*, 1995, *Castro et al.*, 1998a,b, *Ballentine and Burnard*, 2002, *Castro and Goblet*, 2003, *Lippmann et al.*, 2003, *Prinzhofer and Battani*, 2003, *Patriarche et al.*, 2004, *Castro et al.*,

2009, *Pinti et al.*, 2011] due to their conservative nature and origin specific isotopic signatures (atmospheric, crustal, mantle).

The atmospheric component of noble gases (^{22}Ne, ^{36}Ar, ^{84}Kr and ^{130}Xe) dissolved in groundwaters is introduced into the subsurface by recharge water and is expected to be in solubility equilibrium with the atmosphere (Air Saturated Water - ASW) at the time of recharge. However, moderate excesses of atmospheric noble gas concentrations with respect to ASW values (~10-60% Ne excess) [*Wilson and McNeill*, 1997] are commonly found in groundwaters and thought to result mostly from incorporation of trapped air bubbles due to water table fluctuations and subsequent dissolution due to increased hydrostatic pressure [*Heaton and Vogel*, 1981]. Although not common, large atmospheric noble gas excesses with respect to ASW (> 80% Ne excess) have also been previously identified in sedimentary aquifer systems in Africa [e.g., *Beyerle et al.*, 2003, *Kulongoski et al.*, 2004), Europe [e.g., *Ingram et al.*, 2007, *Alvarado et al.*, 2011] and North America [e.g., *Klump et al.*, 2008; *Kulongoski et al.*, 2009]. These large atmospheric noble gas excesses were also attributed to increased hydrostatic pressure, either due to increased water table levels [e.g., *Beyerle et al.*, 2003, *Kulongoski et al.*, 2004, 2009] or to the development of ice cover [e.g., *Klump et al.*, 2008, *Alvarado et al.*, 2011].

A recent noble gas study in the shallow Saginaw aquifer in the Michigan Basin (Castro et al., in revision) has also identified both moderate and large excesses of atmospheric noble gases with respect to ASW. Interestingly, all large atmospheric noble gas excesses are located in the main discharge area of the Michigan Basin, in the Saginaw Lowlands (SL) area. The goal of this paper is to investigate the origin of such large excesses of atmospheric noble gases.

Castro et al. [2005] showed that the occurrence of a ^{4}He/heat flux ratio greater than the crustal production ratio can only result from a past mantle thermal event. The presence of a ^{4}He/heat flux ratio higher than the crustal flux ratio was subsequently identified in groundwaters of the underlying Marshall aquifer in the Michigan Basin [*Ma et al*., 2005, *Castro et al.*, 2007a], where unusually high He excesses are present. Analysis of deep (~0.5-3.6Km) brines in the Michigan Basin subsequently revealed the presence of a mantle, solar-like component for both He and Ne [*Castro et al.*, 2009]. In addition, both the crustal and atmospheric noble gas signatures of these deep brines strongly support the occurrence of this mantle thermal event [*Ma et al.*, 2009a, b]. In particular, the atmospheric noble gas component in these deep brines is extremely depleted, up to orders of magnitude lower than those of air saturated seawater/brine under surface conditions. *Ma et al.* [2009a] have shown that this atmospheric noble gas depletion pattern is best explained by a model involving subsurface boiling and steam separation, consistent with the occurrence of a past thermal event of mantle origin as previously indicated by high ^{4}He/heat flux ratios. These findings are also consistent with the presence of elevated temperatures in the Michigan Basin (e.g., ~80-260°C) in the past at shallow depths as suggested by previous thermal studies in the basin [e.g., *Cercone and Lohmann*, 1987, *Luczaj et al.*, 2006]. If excess He produced and released by this thermal event at depth are still making its way to the surface and are present in the shallow Marshall aquifer [*Castro et al.*, 2007; *Ma et al.*, 2005], then it is also expected that heavier atmospheric noble gases (^{22}Ne, ^{36}Ar, ^{84}Kr and ^{130}Xe) that escaped from deep brine formations during the occurrence of this thermal event are present in shallow groundwaters of this system.

Here, we present measured noble gas (Ne, Ar, Kr, Xe) concentrations and isotopic

ratios from the shallow Saginaw aquifer in the Michigan Basin. Through a step-by-step analysis, with the aide of the closed-system equilibration (CE) model of *Aeschbach-Hertig et al.* [2000, 2008] and through comparison with the noble gas patterns of an aquifer system in southeast Wisconsin [*Klump et al.*, 2008], we first show that our large atmospheric noble gas excesses do not result from commonly observed water table fluctuations or development of ice cover but instead, are the result of sources external to the aquifer. Subsequently, we show that the large excesses of atmospheric noble gases found in the SL area are likely the remnants of the previously identified past thermal event in the Michigan Basin and are compatible with Rayleigh type elemental fractionation controlled by diffusion or solubility related mechanisms.

5.2 Geological and Hydrogeologic Background

Located in the northeastern United States, the Michigan Basin is a concentric intracratonic depression floored by crystalline Precambrian basement and consists of a succession of sedimentary rocks that reaches depths over 5km (Fig. 5.1.a, *Dorr and Eschman*, 1970). The entire sedimentary strata (Fig. 5.1b) are covered by thick Pleistocene Glacial Drift sediments and are composed mainly of sandstones (e.g., Marshall and Saginaw aquifers), shales (e.g., Michigan Formation), carbonates (e.g., Traverse Formation) and evaporites (e.g., Salina Group).

An ancient rift zone transects the entire crystalline basement of the Michigan Basin (Fig. 5.1a), and is believed to be part of the Mid-Continent Rift (MCR) system [*Hinze et al.*, 1975; *Van Schmus*, 1992]. Despite its present low geothermal gradient (~19˚C/km; *Vugrinovich*, 1989), a wealth of studies based on a diversity of proxies (e.g.,

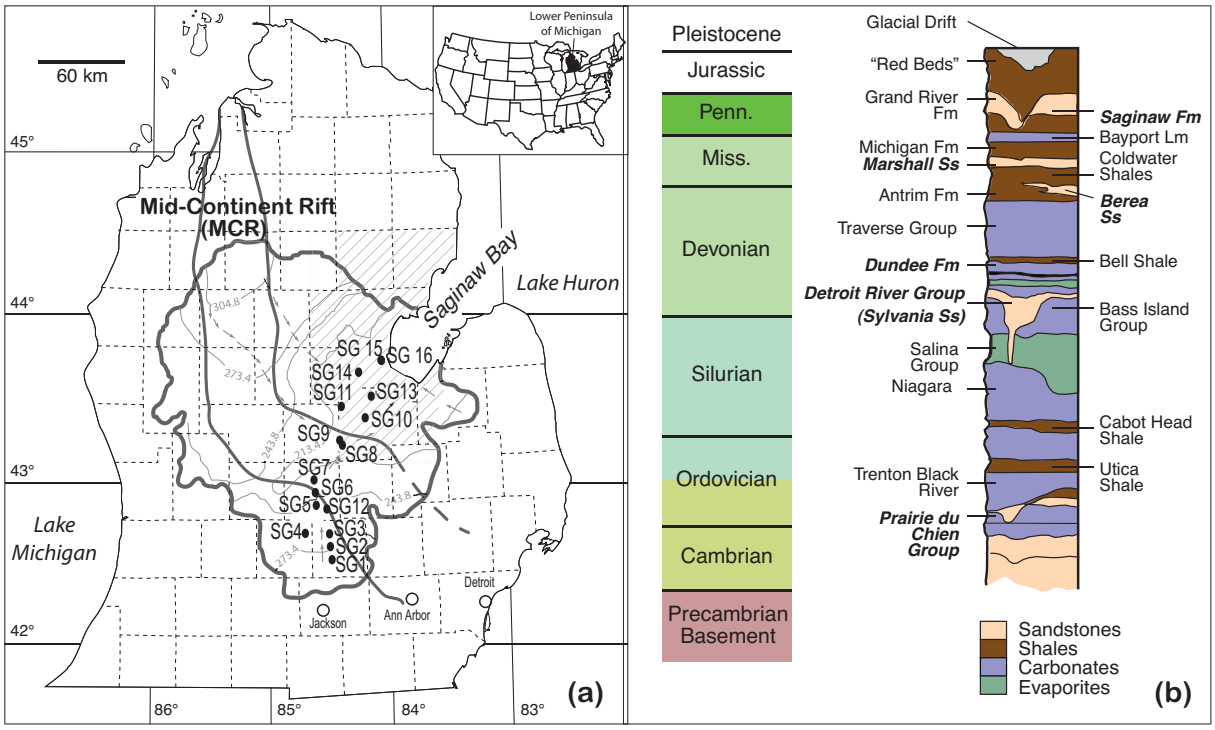

Figure 5.1 a) Location of the Michigan Basin study area in the lower peninsula of Michigan (inset). Location of Saginaw aquifer samples, Mid Continental Rift (MCR) and the Saginaw lowlands region (hatchered area, after Hoaglund et al., 2004) are indicated. Bold contour represents the Saginaw subcrop. Equipotential line values (contour lines) are shown in meters together with main groundwater flow directions (arrows). **b)** Stratigraphic succession of the Michigan Basin together with major lithologies present in the basin are indicated; units for which formation brines were sampled by Ma et al. (2009a) and utilized in this study are highlighted in bold, in addition to the Marshall and Saginaw aquifer.

organic maturity data, stable isotopes, fluid inclusions, authigenic clay minerals) point to the occurrence of past elevated temperatures (e.g., ~80-260°C) in the Michigan Basin [*Cercone*, 1984; *Cercone and Lohmann*, 1987; *Cercone and Pollack*, 1991; *Coniglio et al.*, 2009; *Crowley*, 1991; *Girard and Barnes*, 1995; *Luczaj et al.*, 2006]. Recent reactivation of the MCR is likely at the origin of elevated temperatures. Reactivation of the MCR during the Late Devonian-Mississippian (370-323 Ma) period has been suggested based on formation of authigenic illite in the vicinity of the MCR [*Girard and Barnes*, 1995]. Apatite fission-track ages from drilled basement samples also indicate two additional, more recent periods of thermal activity, during the Triassic (~224 Ma) and Cretaceous (~111-159 Ma), respectively [*Crowley*, 1991]. Major uplift of the basin fault blocks in southern Michigan also occurred at the end of the Mississippian period (~320 Ma), further suggesting reactivation of the MCR [*Fisher et al.*, 1988].

The Saginaw aquifer, located in the central portion of the Michigan Basin (Fig. 5.1a), is underlain by the Bayport-Michigan confining units, which, in turn, overlies the Marshall aquifer [*Mandle and Westjohn*, 1989]. These formations subcrop at an altitude of ~275m and are overlain by the unconfined Glacial Drift aquifer. In the Saginaw aquifer, groundwater flows gravitationally from the south and north to the NE and SE, respectively, into the Saginaw Lowlands (SL) region (Saginaw Bay area), where it discharges (Fig.5.1a). Pre-development freshwater heads [*Barton et al.*, 1996], groundwater flow simulations [*Hoaglund et al.*, 2004], and high helium fluxes in the Marshall aquifer as well as major element data throughout the entire sedimentary strata [*Ma et al.*, 2005] point to the presence of upward cross-formational flow in the SL area. Cross-formation flow appears to be particularly significant in the lower formations and is likely responsible for the presence of

extremely high salinity values (Total Dissolved Solids -TDS ≥ 200g/l) in the Marshall aquifer in this region [*Ma et al.*, 2005].

5.3 Sampling Techniques and Experimental Methods

Groundwater samples were collected from 16 wells in the Saginaw aquifer along a main groundwater flow path, from the recharge area in southern Michigan, towards the SL region (Fig. 5.1. a). Groundwater was sampled in copper tubes (i.e., standard refrigeration grade 3/8" Cu tubing) that were sealed by stainless steel pinch-off clamps [*Weiss*, 1968] at well head pressures after water was allowed to flow through for ~10 minutes to avoid atmospheric contamination. Noble gas concentrations (Ne, Ar, Kr, Xe, Table 5.1) and isotopic ratios (Table D1 in Appendix D) were measured at the University of Michigan as described briefly below and in detail elsewhere [*Saar et al.,* 2005, *Castro et al*., 2009].

Water samples (~14 ml) were attached to a vacuum extraction and purification system and noble gases were extracted for inletting into a MAP-215 mass spectrometer. Noble gases were transported using water vapor as a carrier gas through two constrictions in the vacuum system, purified by a Ti sponge getter, and sequentially allowed to enter the MAP-215 mass spectrometer using a cryo-separator. The cryo-separator temperatures were set at 65, 190, 215, and 270K for analysis of Ne, Ar, Kr, and Xe, respectively.

5.4 Noble Gas Patterns – Results and Discussion

Sample numbers, location, well depth and measured noble gas concentrations (Ne, Ar, Kr and Xe) for all Saginaw aquifer samples are reported in Table 5.1, in addition

Table 5.1 Sample numbers, location, well depth and total measured Ne, Ar, Kr and Xe elemental concentrations[a].

Sample No.	Lat. (deg.)	Long. (deg.)	Well depth (m)	Ne ($x10^{-7}$) cm^3 $STPg^{-1}$	Ar ($x\ 10^{-4}$) cm^3 $STPg^{-1}$	Kr ($x\ 10^{-7}$) cm^3 $STPg^{-1}$	Xe ($x\ 10^{-8}$) cm^3 $STPg^{-1}$
sg1a	42.53	-84.39	99	0.868	2.675	0.726	1.273
sg1b	"	"	"	1.108	3.186	0.891	1.502
sg2	42.6	-84.4	35	2.55	4.246	0.939	1.47
sg3	42.68	-84.41	79	2.642	4.864	1.105	1.426
sg4a	42.68	-84.62	61	2.666	4.786	1.079	1.643
sg4b	"	"	"	2.546	4.669	1.069	1.634
sg5a	42.85	-84.52	55	2.479	4.207	0.994	1.706
sg5b	"	"	"	2.778	4.709	1.096	1.806
sg6a	42.93	-84.53	67	2.753	4.796	1.079	1.532
sg6b	"	"	"	2.835	4.711	1.055	1.515
sg7	43.01	-84.54	61	2.699	4.661	1.061	1.711
sg9	43.24	-84.32	67	3.157	5.146	1.161	1.927
sg11	43.45	-84.31	85	3.168	5.332	1.157	1.727
sg12a	42.83	-84.43	66	2.756	4.771	1.114	1.829
sg12b	"	"	"	1.713	2.729	0.639	1.07
Samples in Saginaw lowlands area							
sg8a	43.21	-84.3	40	3.685	6.251	1.375	2.052
sg8b	"	"	"	3.683	6.311	1.392	2.108
sg10	43.38	-84.11	49	3.75	6.254	1.331	1.575
sg13	43.51	-84.06	98	3.189	5.177	1.175	1.855
sg14	43.65	-84.16	101	4.295	7.236	1.359	1.78
sg15	43.72	-83.97	38	4.418	7.198	1.482	1.673
sg16	43.73	-83.97	78	4.394	7.267	1.545	2.015
ASW 275m, 9.1˚C, 0M NaCl				1.969	3.815	0.906	1.323

[a]Measurement errors of noble gas concentrations are ±1.3%, ±1.3%, ±1.5%, ±2.2% for Ne, Ar, Kr and Xe respectively. All uncertainties are at ±1s level of confidence.

to ASW concentrations for mean modern recharge conditions (9.1ºC, 275 m altitude). With the exception of samples sg3 and sg8a, all samples present isotopic ratios within ±1 or ±2σ errors of the atmospheric value, indicating that any noble gas excesses present in these Saginaw groundwaters are entirely of atmospheric origin (Table D1 in Appendix D). Sample sg3 displays slightly higher Ne isotopic ratios with respect to atmospheric values ($^{20}Ne/^{22}Ne$ = 9.91 ± 0.04; $^{21}Ne/^{22}Ne$ = 0.0299 ± 0.0002), while sample sg8a shows a slightly elevated $^{136}Xe/^{130}Xe$ ratio (2.204 ± 0.011). These Ne and Xe excesses of crustal and mantle origin [see, e.g., *Castro et al*., 2009, *Ma et al.*, 2009b] are, however, entirely negligible with respect to the total measured Ne and Xe concentrations.

Figure 5.2 shows total measured noble gas concentrations for all samples normalized to ASW at mean modern recharge conditions both in absolute (left y-axis) and percentage (right y-axis) values. Except for samples sg1a, b and sg12b, which underwent degassing (green squares, Fig. 5.2), all other samples (blue and red squares, Fig. 5.2) present excess of atmospheric Ne, Ar, Kr and Xe concentrations with respect to ASW (Fig. 5.2). Ne and Ar excesses vary between 26% and 124% and 10% and 91%, respectively, while Kr and Xe excesses vary between 4% and 71% and 8% and 59%, respectively. Two clear subset of samples emerge among those displaying excess atmospheric noble gases: a) a subset which displays moderate noble gas excesses of ~26 - 60% $C_{Ne}/C_{ASW,Ne}$ (blue squares, Fig. 5.2); and, b) a subset of samples displaying extremely high noble gas excesses, between ~80 - 124% $C_{Ne}/C_{ASW,Ne}$ (red squares, Fig. 5.2). Of relevance is the fact that all samples presenting the largest atmospheric noble gas excesses (red squares, Fig. 5.2) are located in the SL region (Fig. 5.1), the main regional discharge area of the Michigan Basin.

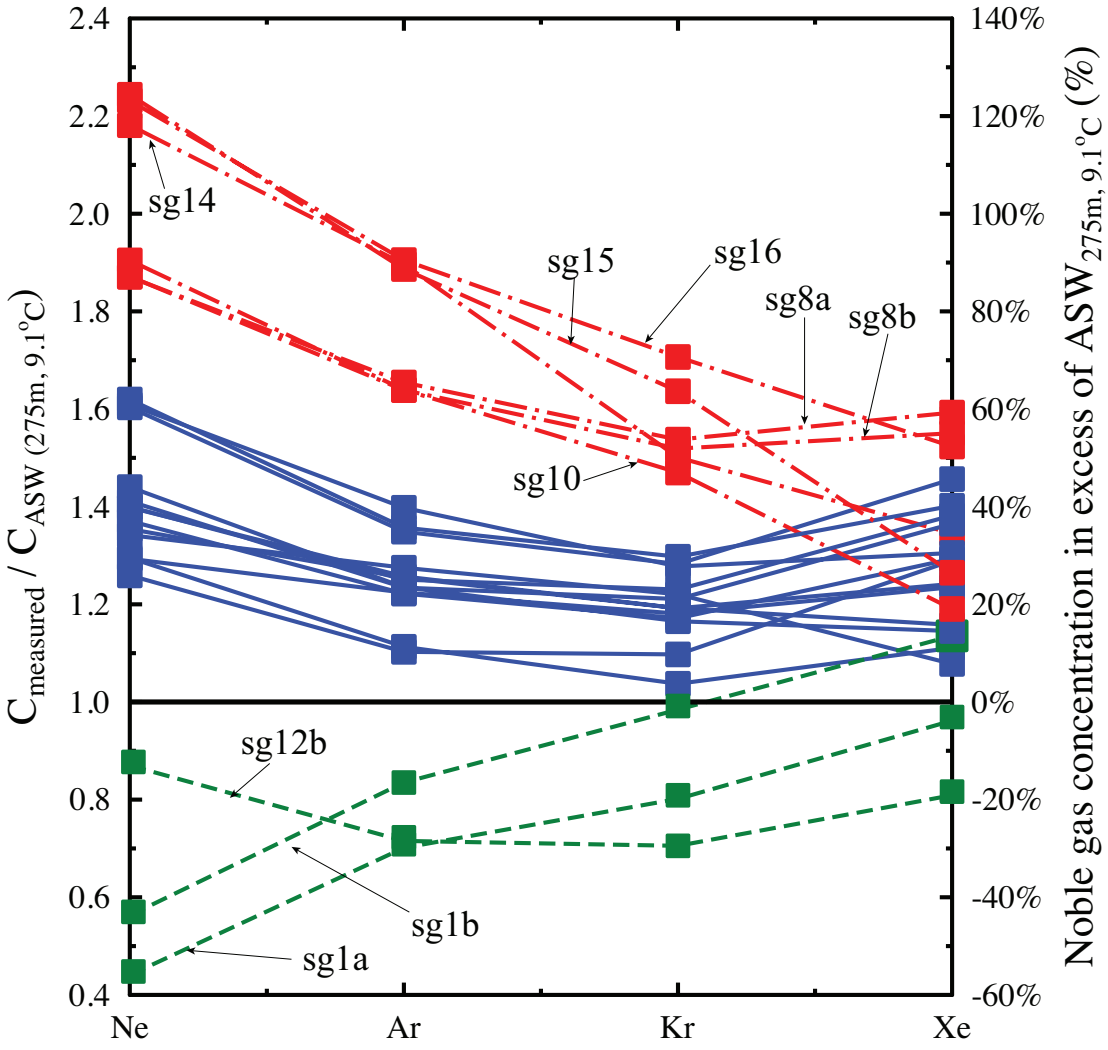

Figure 5.2 Measured Ne, Ar, Kr and Xe concentrations of all samples from the Saginaw aquifer normalized to modern recharge conditions at 275m, 9.1˚C shown as absolute values (left y-axis) and as a percentage (right x-axis). Degassed samples (green squares) and samples with moderate (blue squares) and large (red squares) noble gas excesses are also indicated.

Moderate atmospheric noble gas excesses (~10~60% $C_{Ne}/C_{ASW,Ne}$; *Wilson and McNeill*, 1997) in continental aquifer systems are common and believed to result from incorporation and subsequent dissolution of trapped air bubbles in groundwater due to water table fluctuations [*Heaton and Vogel*, 1981]. Atmospheric noble gas excesses greater than ~80% $C_{Ne}/C_{ASW,Ne}$ are somewhat unusual and not commonly observed in continental aquifer systems. They have been linked to increased water table fluctuations [e.g., *Beyerle et al*., 2003, *Kulongoski et al*., 2009) or to changes in regional hydraulic conditions due to the development of ice cover [e.g., *Klump et al*., 2008]. Noble gas patterns for samples in the SL area display a general mass-dependent trend, with the higher excesses recorded for the lighter noble gases Ne and Ar, and the lowest excesses recorded for the heavier ones, Kr and Xe. Two samples (sg8a, b) among those with the largest excesses (red squares, Fig. 5.2) violate the mass-dependent trend, with Xe excesses greater than those of Kr by 3% and 5%, respectively (Fig. 5.2). These samples are discussed in more detail below (section 5.6.2).

Atmospheric noble gas excesses may also result from external factors. For example, they maybe due to increased noble gas partial pressures in the unsaturated zone due to O_2 depletion without corresponding build up of CO_2 [*Hall et al.*, 2005, *Castro et al.*, 2007b]. It is also possible that such excesses might result from the addition of atmospheric noble gases that were previously released at depth due to a past thermal event and that were subsequently transported to shallow, near-surface areas [see, e.g., *Ma et al.*, 2009a]. The CE model of *Aeschbach-Hertig et al*. [2000, 2008] can be used to investigate whether atmospheric noble gas excesses result from increased hydrostatic pressure or, alternatively, if these are the result of external factors such as those mentioned above. Below, using the CE model, we first show that our high atmospheric noble gas excesses do not result from increased hydrostatic

pressures but rather, are the result of factors external to the aquifer. We also show that O_2 depletion in the unsaturated zone cannot account for these excesses.

5.5 Atmospheric Noble Gas Excesses – Increased Hydrostatic Pressures vs. External Factors

Of particular interest to us are the high atmospheric noble gas excesses observed by *Klump et al.* [2008] in a sedimentary aquifer system in southeast Wisconsin, an area that is relatively close to our study area. More specifically, through a detailed analysis of the CE model parameters [*Aeschbach-Hertig et al.*, 2000, 2008], *Klump et al.* [2008] were able to correlate their observed atmospheric noble gas excesses to increased hydrostatic pressure. Below, by using a similar approach to that of *Klump et al.* [2008] and by comparing their results with those of the Saginaw aquifer, we show that the large atmospheric noble gas excesses of samples located in the SL area do not result from an increase in hydrostatic pressure but rather, are caused by a change in total gas amount ratios due to external factors.

5.5.1 CE Model Parameter Description

The CE model [*Aeschbach-Hertig et al.*, 2000, 2008] allows for an examination of underlying physical causes responsible for noble gas dissolution (or exsolution) through analyses of its model parameters. Dissolved noble gas concentrations (C_w) are described as:

$$C_w = C_{eq}\left(1 + \frac{(1-F)AH_i}{1+FAH_i}\right) \qquad \textbf{(5.1)}$$

where C_{eq} is the ASW component, A is the volume of excess air per volume of water, H_i represents the Henry's constant for gas i and F is a fractionation parameter that describes the

change in trapped gas volume prior to and following bubble dissolution. This fractionation parameter usually varies between $0 \leq F \leq 1$. Such range of values represent the various degrees of dissolution of trapped gas. F=0 represents complete dissolution of all entrapped bubbles, F=1 suggests no bubble dissolution and F>1 indicates sample degassing. *F* can be expressed by the ratio between the total gas amount ratio ν and the hydrostatic gas pressure *q* in the bubbles as:

$$F = \frac{\nu}{q} \quad where, \nu = \frac{\sum_i n_b}{\sum_i n_a}; \; q = \frac{P_b - e}{P_a - e} \tag{5.2}$$

where *P* represents the dry gas pressure of bubbles, *e* is the saturation water vapor pressure, *n* is the amount of noble gas *i* in bubble and subscripts *a* and *b* represent the initial and final equilibrium state of bubbles. Theoretically, for a fixed volume of excess air, increased noble gas dissolution occurs for lower F values (equation 5.1) and may be driven either by a increase in pressure *q*, by a decrease in total gas amount ratio ν, or by a simultaneous increase in *q* and decrease in ν (equation 5.2).

Measured noble gas concentrations for our Saginaw aquifer samples were input into the CE model to obtain the fitted parameters *F*, ν and *q* as well as noble gas temperatures (NGTs), excess air and ΔNe. Here, ΔNe refers to the percentage of measured Ne concentration in excess of model-dependent atmospheric equilibrium, i.e., $\Delta Ne = (Ne_{measured}/Ne_{eq} - 1)*100$ where Ne_{eq} is Ne in equilibrium with ASW [*Aeschbach-Hertig et al*., 2002]. Model results are presented in Table 5.2 and described in detail in section D2 in Appendix D.

5.5.2 CE Model Parameter Analysis

Figure 5.3 compares the CE model derived fractionation factor F with the estimated amount of ΔNe (Table 5.2) for all Saginaw aquifer samples with noble gas excesses (blue circles, Figs. 5.2, 5.3) and acceptable fits (cf. section D2 in Appendix D), and those from groundwaters in southeast Wisconsin (red triangles, Fig. 5.3; *Klump et al*., 2008). Saginaw samples display F values between 0 and 0.66 and ΔNe values between 19% and 53% (blue circles, Fig. 5.3) while Wisconsin samples display F values between 0 and 0.77 and ΔNe values between 12.5% and 73.8% (red triangles, Fig. 5.3). In particular, a subset of Saginaw aquifer samples (sg2, 5b, 7, 9, 12a, 13) and sample DOI from southeast Wisconsin display F=0 (Fig. 5.3), suggesting complete dissolution of trapped noble gases. In contrast, all other samples from the Saginaw aquifer and southeast Wisconsin display a range of positive F values and thus, point to various degrees of excess air dissolution. As previously shown by *Klump et al*. [2008] and as also observed in our Saginaw samples (Fig. 5.3), ΔNe is inversely correlated to the fractionation factor F. More specifically, all samples from both the Saginaw and Wisconsin aquifers with F>0 display a very good inverse correlation between F and ΔNe amounts with correlation coefficients of -0.95 and -0.93 for Saginaw and Wisconsin samples, respectively. This inverse correlation between F and ΔNe suggests that large amounts of dissolved excess air are formed by a more complete dissolution (or lower fractionation level) of entrapped air bubbles, a finding that is consistent with the theoretical formulation (cf. equation 5.1). As mentioned earlier (cf. equation 5.2), increased dissolution of entrapped air bubbles (high ΔNe, low F) can be obtained by: (a) an increase in hydrostatic pressure q; (b) a decrease in the total trapped gas amount ratio ν; or (c) simultaneous increase in q and decrease in ν. Below, we proceed to individually compare parameters q

Table 5.2 CE model results for assumed recharge altitude of 275m.

Sample No.	NGT (±1σ) (°C)	Excess Air (x 10^{-3}) (±1σ) (cm^3 $STPg^{-1}$)	F (±1σ)	ν	q	Δ Ne[a] (%)	χ^2
sg1a	7.0 (1.7)	9.92 (5.73)	3.78 (0.80)	2.32	0.61	< 0	6.75
sg1b	2.5 (0.9)	19.29 (5.97)	2.45 (0.16)	1.91	0.78	< 0	0.1
sg2	8.0 (0.8)	3.08 (0.43)	0.00[b] (0.00)	0.78	1221	22	9.72
sg3			does not converge				
sg4a	4.8 (1.0)	18.17 (14.53)	0.63 (0.11)	0.77	1.23	23	3.16
sg4b	4.6 (0.8)	13.97 (13.51)	0.66 (0.15)	0.81	1.24	19	2.44
sg5a			does not converge				
sg5b	3.2 (0.9)	3.69 (0.57)	0.00[b] (0.00)	0.76	1860	24	14.41
sg6a	6.9 (1.1)	36.37 (17.14)	0.65 (0.04)	0.73	1.13	27	0.01
sg6b	6.9 (0.9)	20.58 (9.28)	0.55 (0.07)	0.71	1.28	29	0.14
sg7	4.1 (0.8)	3.41 (0.46)	0.00[b] (0.00)	0.77	1115	23	10
sg9	1.6 (0.9)	5.59 (0.66)	0.00[b] (0.00)	0.68	2868	32	15.25
sg11	4.4 (1.3)	29.34 (13.74)	0.52 (0.06)	0.65	1.26	35	3.99
sg12a	2.7 (0.8)	3.51 (0.51)	0.00[b] (0.00)	0.77	1164	23	11.83
sg12b			does not converge				
Samples in Saginaw lowlands area							
sg8a	0.2 (0.8)	37.2 (9.23)	0.46 (0.03)	0.59	1.29	41	1.73
sg8b	-0.5 (0.9)	35.35 (10.18)	0.46 (0.04)	0.59	1.3	41	2.56
sg10			does not converge				
sg13	1.7 (0.5)	5.82 (0.38)	0.00[b] (0.00)	0.67	2230	33	5.16
sg14	4.5 (44)	56.5 (463)	0.40 (0.05)	0.5	1.25	50	97.5
sg15			does not converge				
sg16	4.5 (2.0)	112.40 (29.49)	0.42 (0.01)	0.47	1.13	53	0.31

[a] $\Delta Ne=[(Ne_{measured}/Ne_{eq})-1]*100$

[b] F values are infinitesimally small and approximately equal to zero

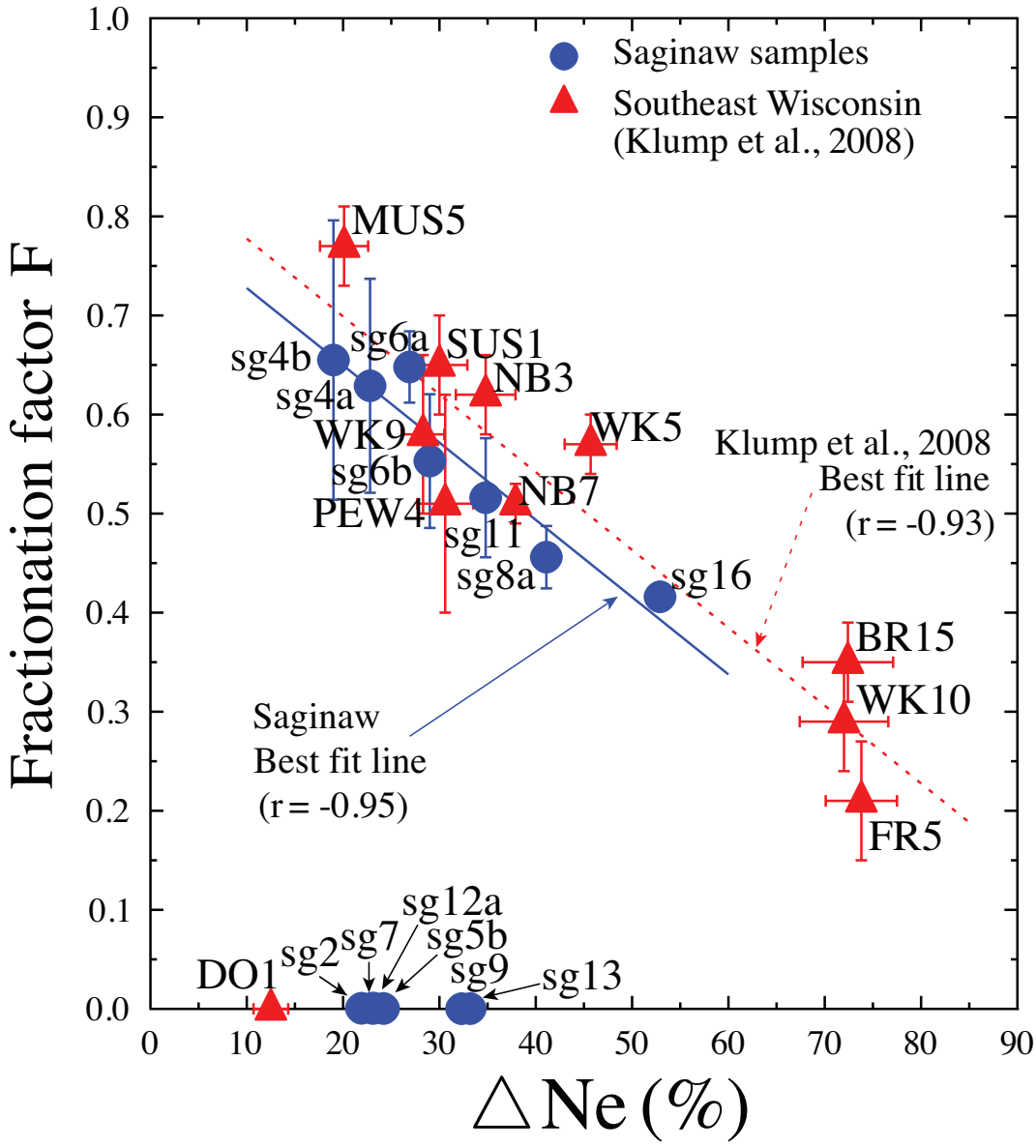

Figure 5.3 Derived CE model fractionation parameter F, as a function of the estimated amount of Ne excess (ΔNe) for samples with acceptable fits from the Saginaw aquifer (this study) and southeast Wisconsin (Klump et al., 2008). Best-fit lines and correlation coefficients r for all samples with 0<F<1 are also indicated.

and ν as a function of ΔNe for all Saginaw and Wisconsin samples with F>0 to see whether Saginaw samples result from increased hydrostatic pressure or external factors.

Figure 5.4 compares the hydrostatic pressure parameter q with the total amount of excess air (ΔNe) for all Saginaw (blue circles) and Wisconsin (red triangles) samples with F>0. Results show that q varies between 1.13 and 1.29 and 1.15 and 1.44 for Saginaw and Wisconsin samples, respectively (cf. Table 5.2). In addition to the larger range in q values displayed by Wisconsin samples compared to our Saginaw samples, Wisconsin samples also present an almost perfect positive correlation (r=0.98) between q and ΔNe (Fig. 5.4). Such a correlation has been previously observed (e.g., *Cey et al*., 2008, *Ingram et al*., 2007) and suggests that an increase in hydrostatic pressure acting on trapped air bubbles leads to increased dissolution of excess noble gases [*Aeschbach-Hertig et al.*, 2002]. Because groundwater ages (20-28ka BP) for Wisconsin samples with high hydrostatic pressures ($q \geq 1.40$) and high ΔNe (Fig. 5.4) correspond to the timing of the Laurentide Ice Sheet (LIS) progression into this area, *Klump et al.* [2008] speculated that large amounts of excess noble gases might be the result of regional hydraulic changes due either to an increase in water table fluctuations or the development of ice cover. In contrast, however, positive correlation between q and ΔNe for Saginaw samples (blue circles; Fig. 5.4) is absent (r=-0.24). Unlike Wisconsin samples, our Saginaw sample with the highest ΔNe (sg16) located in the SL region also displays the lowest q value (~1.1; Fig. 5.4). In addition, the range of q values (1.1-1.3) displayed by Saginaw samples is lower than that displayed by Wisconsin samples and corresponds to typical q values (~1.2) recorded in temperate zone aquifers [*Kipfer et al.*, 2002]. Absence of correlation between q and ΔNe suggests that large excess atmospheric noble gases in Saginaw samples in the SL region are not the result of enhanced water table

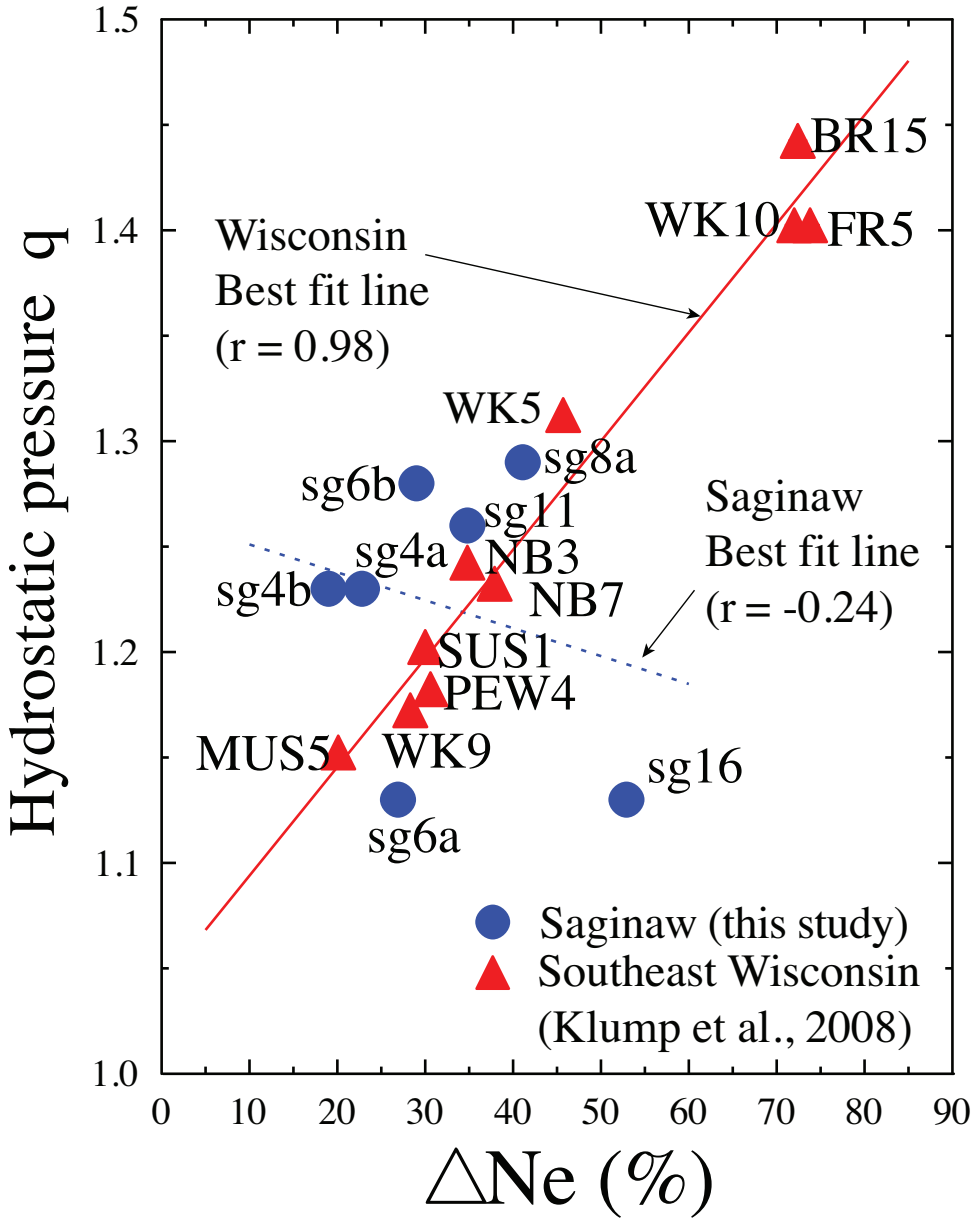

Figure 5.4 Comparison of CE model derived hydrostatic pressure parameter q with amount of Ne excess (ΔNe) for Saginaw (this study) and Wisconsin samples (Klump et al., 2008). Best-fit lines and correlation coefficients r for all samples are also indicated.

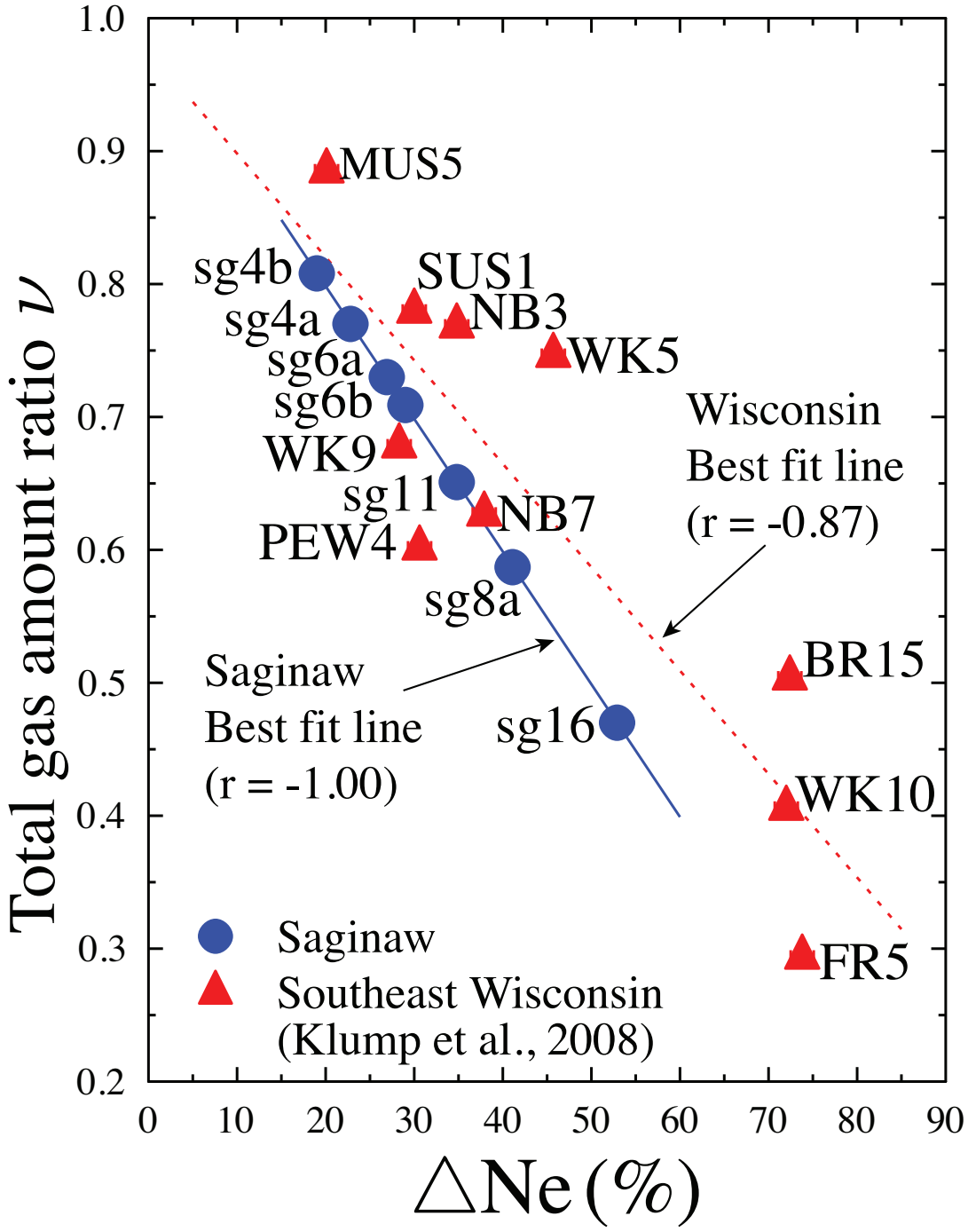

Figure 5.5 Comparison of CE model total gas amount ratio parameter ν with amount of Ne excess (ΔNe) for Saginaw (this study) and Wisconsin samples (Klump et al., 2008). Best-fit lines and correlation coefficients r for all samples are also indicated.

fluctuations. Additionally, if groundwater ages (26.6kyrs - >50kyrs) derived for SL samples with high dissolved excess air are accurate [*Castro et al.*, 2012], groundwater from the SL area was recharged at a time during which the study area was ice-free [*Karrow et al.*, 2000]. Thus, it is also unlikely that large scale regional hydraulic changes following the progression of the LIS led to increased excess air formation in the Saginaw aquifer in the SL area as suggested for groundwater samples from southeastern Wisconsin [*Klump et al.*, 2008]. Alternatively, increased dissolution of entrapped air bubbles (high ΔNe, low F) can be obtained by an apparent decrease in the total trapped gas amount ratio ν following external addition of noble gases as described below.

Figure 5.5 compares the CE model derived total gas amount ratio ν as a function of total excess air (ΔNe) for all Saginaw (blue circles) and Wisconsin (red triangles) samples with F>0. Results display a perfect inverse correlation between ν and ΔNe for the Saginaw aquifer with a correlation coefficient r=-1.00, in addition to a very good correlation also for Wisconsin samples with r=-0.87. Although not previously discussed by *Klump et al.* [2008], good correlation of ΔNe with both q and ν in Wisconsin samples is consistent with their proposed mechanism of increased water table fluctuations during recharge or with progression of the LIS. In particular, it is likely that increased hydrostatic pressure (high q values) lead to increased dissolution of noble gases in groundwater which was likely followed by re-equilibration of the system leading to a decrease in gas amount ratios (low ν). In contrast, due to lack of correlation between q and ΔNe (Fig. 5.4), the observed perfect correlation between fitted ν values and ΔNe in the Saginaw samples cannot be explained by increased water table fluctuations. Simultaneous lack of correlation between q and ΔNe and perfect inverse correlation between ν and ΔNe for Saginaw samples strongly suggests that

increased dissolution of excess air for samples in the SL region results from a decrease in the total trapped gas amount ratio ν without a change in hydrostatic pressure q. This, in turn, strongly suggests that the origin of the large excesses of atmospheric noble gases in the Saginaw aquifer in the SL area is due to external factors and is not related to hydrostatic pressure. *Aeschbach-Hertig et al.* [2008] had previously speculated that a decrease in the total trapped gas amount ratio ν without change in hydrostatic pressure q could occur due to external factors.

External factors with the potential to account for excess of atmospheric noble gases in the Saginaw aquifer include biological consumption of soil air O_2 without an equivalent build up of CO_2 [see, e.g., *Hall et al.,* 2005, *Castro et al*., 2007b] and/or vertical transport of atmospheric noble gases that escaped from deep Michigan Basin brines following a past thermal mantle event [see, e.g., *Castro et al.*, 2005, 2009, *Ma et al*, 2009a, b]. Maximum atmospheric noble gas excesses that could potentially be produced through an O_2 depletion mechanism (26.6%) is minor compared to the total observed amount of atmospheric noble gas excesses for Saginaw samples in the SL region (section D3 in Appendix D). Thus, we are left with the hypothesis that the large observed atmospheric noble gas excesses in the SL area are the remnants of all the atmospheric noble gases that were released from deep Michigan Basin brines during the thermal mantle event (see, e.g., *Ma et al*., 2009a). Below we assess the likelihood of such a scenario.

5.6 Atmospheric Noble Gas Excesses in the Saginaw Lowlands (SL) Area as a Result of a Mantle Thermal Event

5.6.1 Atmospheric Noble Gas Concentrations vs. Depth

Multiple lines of evidence point to the occurrence of a past thermal event of mantle origin in the Michigan Basin, likely related to the recent reactivation of the MCR system (e.g., *Fisher et al*., 1988, *Girard and Barnes*, 1995). Specifically, the occurrence of a ^{4}He/heat flux ratio greater than the crustal production ratio in the Marshall aquifer [*Castro et al.*, 2005, 2007a, *Ma et al*., 2005], the presence of a primordial, solar-like He and Ne component in deep brines of the Michigan Basin [*Castro et al*., 2009], and the extreme depletion of atmospheric noble gases in these brines consistent with the occurrence of subsurface boiling and steam separation [*Ma et al.*, 2009a] are all strongly suggestive of this past thermal event. A wealth of studies based on a diversity of proxies point also to the occurrence of past elevated temperatures (~80-260°C) in the basin [*Cercone*, 1984; *Cercone and Lohmann*, 1987; *Cercone and Pollack*, 1991; *Coniglio et al*., 2009; *Crowley*, 1991; *Girard and Barnes*, 1995; *Luczaj et al*., 2006] and is consistent with the occurrence of such a thermal event.

Unusually high He excesses are found in the shallow Marshall aquifer underlying the Saginaw aquifer. It is thought that such unusually high He excesses are at least partly the result of this past thermal event [*Ma et al.*, 2005, *Castro et al.*, 2007a]. If part of the He released by this thermal event at depth is still making its way to the surface and is present in the shallow Marshall aquifer [*Castro et al*., 2007a; *Ma et al.*, 2005], then it is also expected that all other heavier atmospheric noble gases that escaped from the deepest brine formations during the occurrence of this thermal event are at least partly present in shallow

groundwaters of the Saginaw aquifer and, possibly, also those of the Marshall aquifer.

Atmospheric concentrations of ^{22}Ne, ^{36}Ar, ^{84}Kr and ^{130}Xe are available from nine deep brines located in the SL area [*Ma et al*., 2009a; samples 1, 2, 8, 10, 11, 13, 34, 35, 36]. Noble gas concentrations are also available for one brine sample in the Marshall aquifer (Table D2, Appendix D) in the SL area, which was originally collected for a He isotopic study (sample 16, *Ma et al.,* 2005). In addition, six Saginaw samples, which present large excesses of atmospheric noble gases (red squares, Fig. 5.2) are also located in the SL region.

Figure 5.6 shows measured atmospheric ^{22}Ne, ^{36}Ar, ^{84}Kr and ^{130}Xe for all deep brines (green triangles and circles), the Marshall brine (red square) and Saginaw samples with large excesses (blue circles; Table D3 in Appendix D) located in the SL area as a function of depth. Also indicated for reference are ASW values for modern recharge conditions (275m, 9.1˚C, 0M NaCl), as well as air saturated seawater values at 10˚C and 20˚C. Studies of major elements and stable isotopes suggest that deep Michigan basinal brines originated from ancient seawater [*Long et al.*, 1988; *Wilson and Long*, 1993a, b; *Davisson and Criss*, 1996; *Martini*, 1997; *McIntosh et al*., 2004]. It is apparent that although atmospheric concentrations of all deep basinal brines (green circles, Fig. 5.6) are depleted by orders of magnitude with respect to ASW values for both modern recharge conditions and seawater, our shallow Saginaw samples (blue circles, Fig. 5.6) are largely in excess of ASW values with Ne, Ar, Kr and Xe excesses up to 124%, 91%, 71% and 60% with respect to modern recharge conditions (Fig. 5.6). The Marshall brine sample occupies an intermediate position between these two extremes. More specifically, our Marshall brine displays a ^{22}Ne excess of 24% while ^{36}Ar, ^{84}Kr and ^{130}Xe display increasing depletions of 61%, 81% and 87% with respect to ASW at modern recharge conditions, respectively.

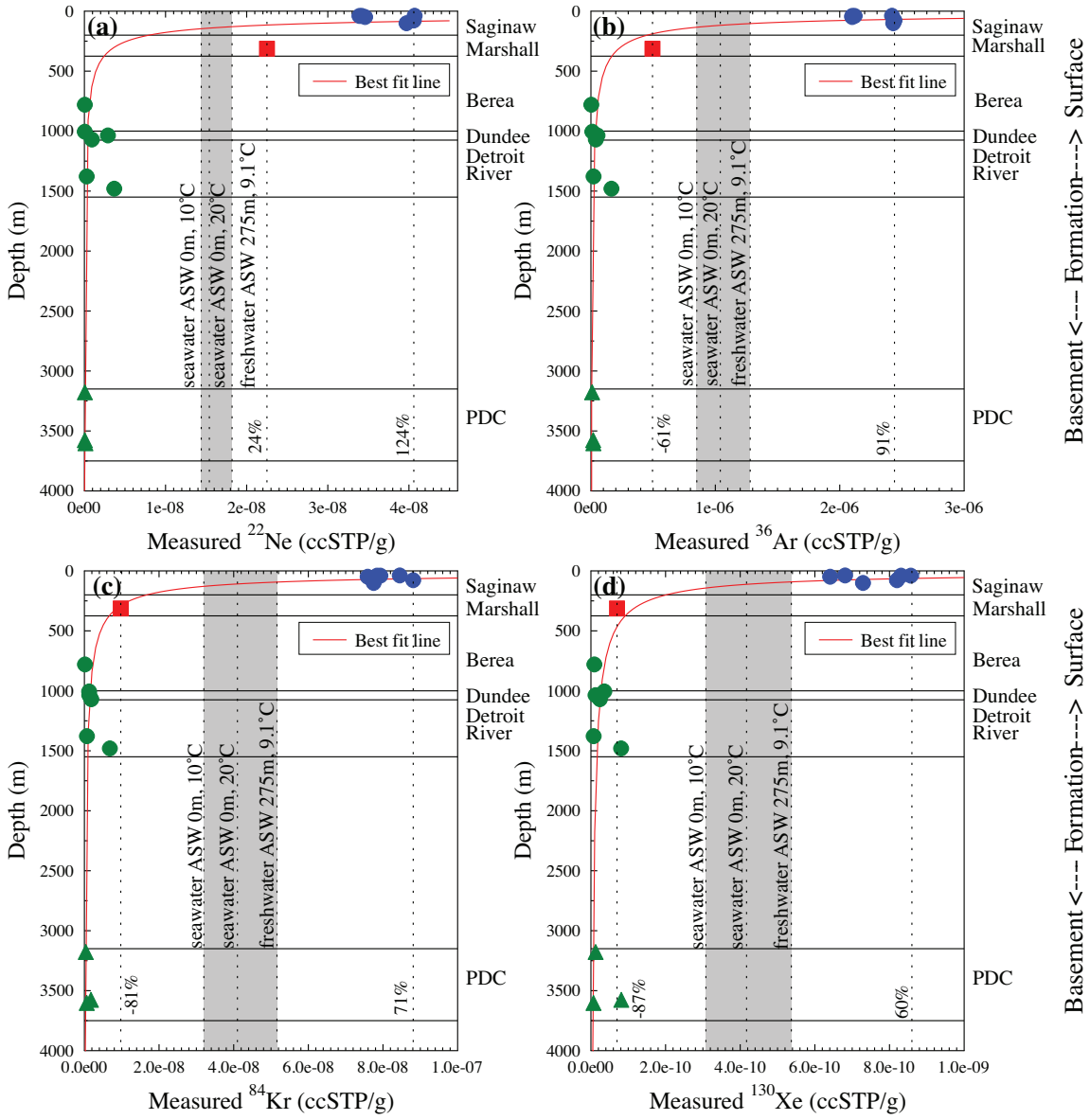

Figure 5.6 Measured atmospheric noble gas concentration-depth profiles for: **a)** ^{22}Ne**; b)** ^{36}Ar**; c)** ^{84}Kr**; d)** ^{130}Xe derived for the Saginaw aquifer samples (blue circles, this study), a brine Marshall sample (red square, Table S2; Ma et al., 2005) and deep brines (green triangle and circles; Ma et al., 2009a) for samples within the Saginaw lowlands region. Shaded areas indicate the range of values between ASW for freshwater at modern recharge conditions (9.1˚C, 275m altitude) and seawater at 10˚C and 20˚C, respectively. Dashed lines indicate various % relative to modern recharge conditions. A best-fit line using a power-law correlation is also indicated for visual purposes.

This noble gas pattern displayed by the Marshall brine is likely reflecting the impact of depleted deep basinal brines (green circles, Fig. 5.6). Indeed, unlike observed in the Saginaw aquifer where impact of cross-formational flow appears to be small as evidenced by the presence of low salinity groundwater in the SL area (TDS<4.5g/l; *Castro et al.*, 2012), impact of upward cross-formational flow in the Marshall aquifer is significant as evidenced by the extremely high salinity values found in this area, and in our Marshall brine sample in particular (TDS=217g/l; Table D2 in Appendix D). Upward transport of deep basinal brines and subsequent mixing with meteoric water has been previously proposed to account for the presence of such high salinity waters in near-surface environments in the Michigan Basin [*Long et al.*, 1988; *Mandle and Westjohn*, 1989; *Weaver et al*., 1995; *Kolak et al*., 1999; *McIntosh et al*., 2004, *Ma et al.,* 2005]. Thus, although it is likely that excess of atmospheric noble gases might still be present in the Marshall, such excesses can no longer be identified due to mixing with depleted basinal brines. In addition, recharge water will also exert a dilution effect on both, excesses of atmospheric noble gases in the Marshall as well as in the Saginaw aquifers. Therefore, although still large, atmospheric noble gas excesses recorded in the Saginaw aquifer in the SL region are likely not representative of the excess atmospheric noble gas end-member component. For visual purposes, Figure 5.6 includes also the best fit lines for a power law correlation which evolves toward two values, an end-member represented by the deepest, most depleted brines (green triangles), and an end-member with values above those displayed by the Saginaw samples (blue circles). This latter end-member is unconstrained due to the dilution effect exerted by recharge water.

Greater relative enrichment of lighter noble gases (^{22}Ne) compared to heavier ones (^{130}Xe) in the shallow Saginaw aquifer in the SL area (Fig. 5.6) can occur due to Rayleigh

type elemental fractionation controlled by diffusion or solubility related mechanisms. Here, we suggest a possible mechanism involving the upward transport of atmospheric noble gases from deep brines toward the surface in which both high He and Ne diffusivities, combined with solubility-controlled processes that might occur when a gas phase is present [*Zartman et al*., 1961; *Bosch and Mazor*, 1988] might lead to the observed fractionation between Ne, Ar, Kr and Xe. While diffusion-controlled processes naturally favors the loss of ^{22}Ne over ^{130}Xe due to its higher diffusion coefficient [*Jähne et al*., 1987, *Bourg and Sposito*, 2008], solubility-controlled processes favor the loss of ^{22}Ne over ^{130}Xe to a gas phase due to ^{130}Xe's greater solubility in liquid water [*Weiss*, 1970, *Crovetto et al*., 1982, *Smith and Kennedy*, 1983]. Thus, both diffusion and solubility related mechanisms are capable of causing enrichment of lighter noble gases with respect to the heavier ones in shallow formations. Below, we utilize a simple Rayleigh fractionation model and measured atmospheric ^{22}Ne, ^{36}Ar, ^{84}Kr and ^{130}Xe concentrations of Saginaw samples from the SL area with large excesses to assess whether such fractionation mechanisms are compatible with our observed noble gas patterns.

5.6.2 Elemental Fractionation Mechanisms

As previously discussed, the observed elemental fractionation might be due to either diffusion or solubility controlled mechanisms. To test this hypothesis, we use a simple model in which fractionated elemental ratios in the escaped phase (into the shallow formations) can be simulated by a Rayleigh Law as follows [*Ma et al.*, 2009b]:

$$\left(\frac{^{22}Ne}{^{36}Ar}\right)_{esc} = \left(\frac{^{22}Ne}{^{36}Ar}\right)_{init} \times \left(\frac{1-f^{\alpha}}{1-f}\right) \qquad \textbf{(5.4)}$$

where, subscripts *esc* and *init* stand for elemental ratios in the escaped and initial phases, respectively, *f* is the fraction of ^{36}Ar remaining in deep formations (residual phase) and *a* is the process-controlled fractionation coefficient. For a diffusion-controlled process, *a* is given by:

$$\alpha = \frac{D_{^{22}Ne}}{D_{^{36}Ar}} \qquad \textbf{(5.5)}$$

where, D_{22Ne} and D_{36Ar} are the noble gas diffusion coefficients in water (*Jähne et al*., 1987, *Bourg and Sposito*, 2008). For a solubility-controlled process, a is given by:

$$\alpha = \frac{K_{^{22}Ne}}{K_{^{36}Ar}} \qquad \textbf{(5.6)}$$

where, K_{22Ne} and K_{36Ar} are the Henry's law constants (*Crovetto et al*., 1982; *Smith and Kennedy*, 1983). Diffusion coefficient values, Henry's law constants and fractionation coefficient *a* used for all gases at reservoir temperatures (40˚C - 120˚C) are given in Table D4 in Appendix D. Model-expected ratios in the escaped phase for diffusion and solubility-controlled processes can be similarly derived for ^{84}Kr/^{36}Ar and ^{130}Xe/^{36}Ar (cf. equation 5.4).

Figure 5.7 compares measured ^{84}Kr/^{36}Ar and ^{130}Xe/^{36}Ar with ^{22}Ne/^{36}Ar for Saginaw samples with large excesses of atmospheric noble gases (blue circles) with values for air-saturated seawater at various temperatures (0˚C - 20˚C; solid line) and excess air amounts (dashed lines), assuming complete bubble dissolution. Sea water in equilibrium with the atmosphere represents the initial composition of the deep brines prior to the occurrence of the past thermal event [*Ma et al*., 2009a, b]. Because deep reservoir conditions prior to the thermal event are poorly constrained, a wide range of initial reservoir conditions (ASW between 10˚C - 20˚C, 0.6M salinity) and modern reservoir temperature estimates (40˚C - 120˚C) were modeled [cf. *Ma et al.*, 2009a, b]. More specifically, Rayleigh model ratios for

diffusion-dominated fractionation at 40˚C (red line) and solubility-controlled fractionation at 120˚C (green line) are shown. Varying degrees of gas loss (Equation 5.4; (1-f) = $\%^{36}Ar$ lost from brines) between these two scenarios fall within the shaded region.

Comparison of $^{84}Kr/^{36}Ar$ and $^{22}Ne/^{36}Ar$ shows that all samples fall within the domain of expected diffusion or solubility controlled Rayleigh model elemental ratios in the escaped phase (shaded area, Fig. 5.7.a). Similarly, $^{130}Xe/^{36}Ar$ and $^{22}Ne/^{36}Ar$ ratios show that most samples (sg10, 14, 15, 16) also fall within the domain of Rayleigh model elemental ratios in the escaped phase (shaded region, Fig. 5.7.b). In contrast, and as previously indicated (cf. Section 5.4), samples sg8a, b display relative Xe concentrations greater than those of Kr and deviate from the mass dependent fractionation trend displayed by all other samples. Cold water (e.g., 0˚C) will be more enriched in Xe with respect to the lighter noble gases. It is thus possible that some of the Xe concentrations in excess of those expected from our Rayleigh model are the result of mixing between the escaped excess atmospheric noble gas phase from deep brines and colder water. All other samples fall entirely within the domain of our Rayleigh model expected ratios and indicate that the source of such high excesses of atmospheric noble gases are very likely the deepest Michigan Basin brines. It further reinforces the notion that a past thermal event is indeed responsible for the large excess atmospheric noble gases found in the Saginaw aquifer in the SL area.

Because initial reservoir conditions are poorly constrained (shaded area, Fig. 5.7), a dominant fractionation mechanism (diffusion vs. solubility-controlled) cannot presently be established for these samples. While $^{130}Xe/^{36}Ar$ vs. $^{22}Ne/^{36}Ar$ for most samples (sg10, 14, 15) appear to suggest diffusion-controlled noble gas fractionation at 40˚C (red line, Fig. 5.7. b), sample sg16 points to a solubility-controlled noble gas fractionation at 120˚C (green line,

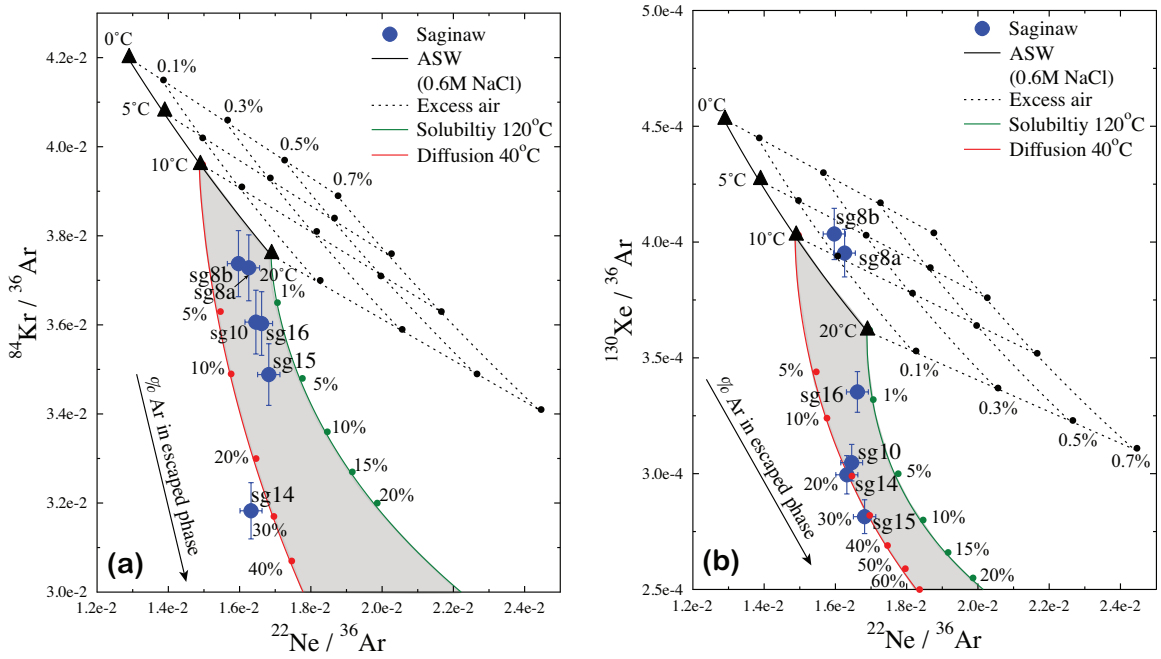

Figure 5.7 Comparison of measured: **a)** $^{84}Kr/^{36}Ar$ and $^{22}Ne/^{36}Ar$; **b)** $^{130}Xe/^{36}Ar$ and $^{22}Ne/^{36}Ar$ for all Saginaw samples with large atmospheric noble gas excesses (red squares, Fig. 2). Also shown are values for ASW for seawater (solid line) and excess air (dotted lines), assuming complete excess air dissolution. Rayleigh model expected patterns assuming both diffusion (red line) and solubility-controlled (green line) processes are also indicated. Arrow indicates % Ar loss from deep brines (escaped phase) corresponding to (1-f) as described in equation 4.

Fig. 5.7.b). These noble gas fractionation mechanisms place constraints on the amount of noble gases transported to shallow formations. In particular, while a diffusion-controlled process yields a maximum upward Ar transport of ~30% with respect to the initial total amount, a solubility-controlled process yields an upward Ar transport between ~1% and ~20% (Figs. 5.7.a, b). These upward noble gas transport estimates cannot account for the total loss of atmospheric noble gases in the deepest brines, which, for most brines and most noble gases is over 95% [*Ma et al*., 2009a]. It is possible that the unaccounted for excess atmospheric noble gases that escaped from deep brines that are missing in the Saginaw aquifer have already moved through the Saginaw aquifer into the Glacial Drift aquifer and possibly into the atmosphere. Alternatively, part of these excesses might be still present in the Marshall aquifer but are no longer identifiable due to dilution by depleted deep brines moving upward through cross-formational flow. In addition, as mentioned earlier, part of the atmospheric noble gas excesses in the Saginaw Lowlands area have likely been diluted by recharge water and thus, can no longer be identified.

To assess whether or not part of the escaped atmospheric noble gases are present at shallower levels will require sampling the Glacial Drift aquifer in the SL area and we plan to do so in the near future. Alternatively, slow transport of crustal heavier noble gases through low permeability formations was previously observed in the Michigan Basin [*Ma et al.*, 2009b]. It is thus conceivable that part of the atmospheric noble gases might be found in one of the confining units below the Saginaw aquifer. Such a mechanism can be verified through groundwater flow modeling coupled with vertical He transport in the SL area [e.g., *Patriarche et al*., 2004].

5.7 Conclusions

Measured noble gases (Ne, Ar, Kr, Xe) in the shallow Saginaw aquifer in the Michigan Basin display both moderate (~20-60% Ne excess) and large (~80->120% Ne excess) excesses of atmospheric noble gases with respect to ASW for modern recharge conditions. All large atmospheric noble gas excesses are located in the main discharge area of the Michigan Basin, in the Saginaw Lowlands (SL) region. Moderate atmospheric noble gas excesses are common and thought to result mostly from incorporation and subsequent dissolution of trapped air bubbles in groundwater due to water table fluctuations. Although not common, large atmospheric noble gas excesses have also been observed in other continental aquifer systems and have been linked to increased hydrostatic pressure, either due to increased water table levels or to the development of ice cover.

Here, with the aide of the closed-system equilibration (CE) model of *Aeschbach-Hertig et al*. [2008] and through comparison with the noble gas patterns of an aquifer system in southeast Wisconsin [*Klump et al.*, 2008], we show that our large atmospheric noble gas excesses do not result from increased hydrostatic pressure but instead, are the result of sources external to the aquifer. External factors with the potential to account for excess of atmospheric noble gases in the Saginaw aquifer are biological consumption of soil air O_2 without an equivalent build up of CO_2, and/or vertical transport of atmospheric noble gases that escaped from deep Michigan Basin brines following a past thermal event of mantle origin [e.g., *Castro et al*., 2005, 2009, *Ma et al*, 2009a, b]. We show that the maximum atmospheric noble gas excesses that could potentially be produced through an O_2 depletion mechanism are not substantial (26.6%) compared to the total observed atmospheric noble gas excesses in the Saginaw aquifer in the SL region. Using the atmospheric noble gas

composition of deep brines [*Ma et al*., 2009a], a brine from the Marshall aquifer and water samples from the Saginaw aquifer, all located in the SL area, we subsequently show that the atmospheric noble gas pattern of the entire Michigan Basin strata appears to result from two distinct end-members: a) an end-member represented by the deepest, most depleted brines from which most of the atmospheric noble gases escaped; and b) an end-member with excess atmospheric noble gas values above those displayed by the Saginaw samples. The latter is unconstrained due to the possible dilution effect exerted by recharge water. Using a Rayleigh distillation model we further show that the greater relative enrichment of lighter noble gases compared to the heavier ones in the Saginaw aquifer in the SL area is compatible with diffusion or solubility related mechanisms. These findings reinforce the notion that a past thermal event is indeed responsible for the large atmospheric noble gas excesses found in the Saginaw aquifer in the SL area. They are also consistent with and reinforce previous findings with respect to the occurrence of a thermal event of mantle origin [*Castro et al.*, 2009, *Ma et al*., 2009a, b].

Acknowledgements

We thank all homeowners for access to their wells and P. Hojnacki for his assistance in the field. Financial support by the National Science Foundation CAREER award EAR-0545071 is greatly appreciated.

References

Aeschbach-Hertig, W., Peeters, F., Beyerle, U., Kipfer, R., 2000. Palaeotemperature reconstruction from noble gases in ground water taking into account equilibration with entrapped air. Nature 405, 1040-1044.

Aeschbach-Hertig, W., U. Beyerle, J. Holocher, F. Peeters, Kipfer, R., 2002. Excess air in groundwater as a potential indicator of past environmental changes, in Study of Environmental Change using Isotope Techniques, pp. 174–183, Int. At. Energy Agency, Vienna.

Aeschbach-Hertig, W., El-Gamal, H., Wieser, M., Palcsu, L., 2008. Modeling excess air and degassing in groundwater by equilibrium partitioning with a gas phase. Water Resour. Res. 44.

Alvarado, J.A.C., Leuenberger, M., Kipfer, R., Paces, T., Purtschert, R., 2011. Reconstruction of past climate conditions over central Europe from groundwater data. Quaternary Science Reviews 30, 3423-3429.

Ballentine, C.J., Burnard, P.G., 2002. Production, release and transport of noble gases in the continental crust. Rev. Mineral. Geochem. 47, 481–538.

Barton, G.J., Mandle, R.J., Baltusis, M.A., 1996. Predevelopment freshwater heads in the glaciofluvial, Saginaw, and Marshall aquifers in the Michigan Basin, Open-File Report, - ed. U.S. Geological Survey ; Branch of Information Services [distributor], pp. iv, 15 p. :ill., maps ;28 cm.

Battani, A., Sarda, P., Prinzhofer, A., 2000. Basin scale natural gas source, migration and trapping traced by noble gases and major elements: the Pakistan Indus basin. Earth and Planetary Science Letters 181, 229-249.

Beyerle, U., Rueedi, J., Leuenberger, M., Aeschbach-Hertig, W., Peeters, F., Kipfer, R., Dodo, A., 2003. Evidence for periods of wetter and cooler climate in the Sahel between 6 and 40 kyr BP derived from groundwater. Geophys. Res. Lett. 30, 1173.

Bosch, A., Mazor, E., 1988. Natural gas association with water and oil as depicted by atmospheric noble gases: case studies from the southeastern Mediterranean Coastal Plain. Earth and Planetary Science Letters 87, 338-346.

Bourg, I.C., Sposito, G., 2008. Isotopic fractionation of noble gases by diffusion in liquid water: Molecular dynamics simulations and hydrologic applications. Geochimica et Cosmochimica Acta 72, 2237-2247.

Brennwald, M.S., Kipfer, R., Imboden, D.M., 2005. Release of gas bubbles from lake sediment traced by noble gas isotopes in the sediment pore water. Earth and Planetary Science Letters 235, 31-44.

Castro, M.C., Jambon, A., Marsily, G.d., Schlosser, P., 1998a. Noble gases as natural tracers of water circulation in the Paris Basin. 1. Measurements and discussion of their origin and mechanisms of vertical transport in the basin. Water Resources Research 34, 2443-2466.

Castro, M.C., Goblet, P., Ledoux, E., Violette, S., Marsily, G.d., 1998b. Noble gases as

natural tracers of water circulation in the Paris Basin. 2. Calibration of a groundwater flow model using noble gas isotope data. Water Resources Research 34, 2467-2483.\

Castro M.C., and Goblet P. (2003), Noble Gas Thermometry and Hydrologic ages: Evidence for Late Holocene Warming in Southwest Texas, Geophys. Res. Lett., 30 (24), 2251, doi:10.1029/2003GL018875.

Castro, M.C., D. Patriarche, Goblet, P., 2005. 2-D numerical simulations of groundwater flow, heat transfer and 4He transport – implications for the He terrestrial budget and the mantle helium-heat imbalance. Earth and Planetary Science Letters 237, 893-910.

Castro, M.C., Patriarche, D., Goblet, P., Ma, L., Hall, C.M., 2007a. 4He/heat flux ratios as new indicators of past thermal and tectonic events — new constrains on the tectonothermal history of the Michigan Basin., The 4th Mini Conference on Noble Gases in the Hydrosphere and in Natural Gas Reservoirs, GFZ Potsdam.

Castro, M.C., Hall, C.M., Patriarche, D., Goblet, P., Ellis, B.R., 2007b. A new noble gas paleoclimate record in Texas - Basic assumptions revisited. Earth and Planetary Science Letters 257, 170-187.

Castro, M.C., Ma, L., Hall, C.M., 2009. A primordial, solar He-Ne signature in crustal fluids of a stable continental region. Earth and Planetary Science Letters 279, 174-184.

Castro, M. C., R. B. Warrier, C. M. Hall, and K. C. Lohmann (2012), A late Pleistocene-Mid-Holocene noble gas and stable isotope climate and subglacial record in southern Michigan, *Geophys. Res. Lett.*, *39*(19), L19709.

Cercone, K.R., 1984. Thermal history of Michigan Basin. AAPG Bulletin 68, 130-136.

Cercone, K.R., Lohmann, K.C., 1987. Late burial diagenesis of Niagaran (Middle Silurian) pinnacle reefs in Michigan Basin. AAPG Bulletin 71, 156-166.

Cercone, K.R., Pollack, H.N., 1991. Thermal maturity of the Michigan Basin. Special Paper - Geological Society of America 256, 1-11.

Cey, B.D., Hudson, G.B., Moran, J.E., Scanlon, B.R., 2008. Impact of Artificial Recharge on Dissolved Noble Gases in Groundwater in California. Environmental Science & Technology 42, 1017-1023.

Coniglio, M., Sherlock, R., Williams-Jones, A.E., Middleton, K., Frape, S.K., 2009. Burial and Hydrothermal Diagenesis of Ordovician Carbonates from the Michigan Basin, Ontario, Canada, Dolomites. Blackwell Publishing Ltd., pp. 231-254.

Crovetto, R., Fernandez-Prini, R., Japas, M.L., 1982. Solubilities of inert gases and methane in H2O and in D2O in the temperature range of 300 to 600 K. The Journal of Chemical Physics 76, 1077-1086.

Crowley, K.D., 1991. Thermal History of Michigan Basin and Southern Canadian Shield From Apatite Fission Track Analysis. J. Geophys. Res. 96, 697-711.

Davisson, M.L., Criss, R.E., 1996. Na–Ca–Cl relations in basinal fluids. Geochim. Cosmochim. Acta 60, 2743–2752.

Dorr, J.A., Eschman, D.F., 1970. Geology of Michigan, first ed. Univ. of Michigan Press, Ann Arbor, Michigan.

Fisher, J.H., Barratt, M.W., Droste, J.B., Shaver, R.H., 1988. Michigan Basin. In: Sloss, L.L. (Ed.), Sedimentary Cover — North America Craton, vol. D-2. Geological Society of America, pp. 361–382.

Girard, J.-P., Barnes, D.A., 1995. Illitization and paleothermal regimes in the Middle Ordovician St. Peter Sandstone, central Michigan Basin; K-Ar, oxygen isotope, and fluid inclusion data. AAPG Bulletin 79, 49-69.

Hall, C.M., Castro, M.C., Lohmann, K.C., Ma, L., 2005. Noble gases and stable isotopes in a shallow aquifer in southern Michigan: Implications for noble gas paleotemperature reconstructions for cool climates. Geophysical Research Letters 32.

Heaton, T.H.E., Vogel, J.C., 1981. "Excess air" in groundwater. Journal of Hydrology 50, 201-216.

Hinze,W.J., Kellogg, R.L., O, ' Hara, N.W., 1975. Geophysical studies of basement geology of Southern Peninsula of Michigan. AAPG Bull. 59, 1562–1584.

Hoaglund, J.R., III, Kolak, J.J., Long, D.T., Larson, G.J., 2004. Analysis of modern and Pleistocene hydrologic exchange between Saginaw Bay (Lake Huron) and the Saginaw Lowlands area. Geological Society of America Bulletin 116, 3-15.

Ingram, R.G.S., Hiscock, K.M., Dennis, P.F., 2007. Noble Gas Excess Air Applied to Distinguish Groundwater Recharge Conditions. Environmental Science & Technology 41, 1949-1955.

Jähne, B., Heinz, G., Dietrich, W., 1987. Measurements of the diffusion coefficients of sparingly soluble gases in water. J. Geophys. Res. 92, 10767-10776.

Karrow, P.F., Dreimanis, A., Barnett, P.J., 2000. A Proposed Diachronic Revision of Late Quaternary Time-Stratigraphic Classification in the Eastern and Northern Great Lakes Area. Quaternary Research 54, 1-12.

Kipfer, R., Aeschbach-Hertig, W., Peeters, F., Stute, M., 2002. Noble Gases in Lakes and Ground Waters. Reviews in Mineralogy and Geochemistry 47, 615-700.

Klump, S., Grundl, T., Purtschert, R., Kipfer, R., 2008. Groundwater and climate dynamics derived from noble gas, 14C, and stable isotope data. Geology 36, 395-398.

Kolak, J.J., Long, D.T., Matty, J.M., Larson, G.J., Sibley, D.F., Councell, T.B., 1999. Ground-water, large-lake interactions in Saginaw Bay, Lake Huron: A geochemical and isotopic approach. Geological Society of America Bulletin 111, 177-188.

Kulongoski, J.T., Hilton, D.R., Selaolo, E.T., 2004. Climate variability in the Botswana Kalahari from the late Pleistocene to the present day. Geophys. Res. Lett. 31, L10204.

Kulongoski, J.T., Hilton, D.R., Izbicki, J.A., Belitz, K., 2009. Evidence for prolonged El Nino-like conditions in the Pacific during the Late Pleistocene: a 43ka noble gas record from California groundwaters. Quaternary Science Reviews 28, 2465-2473.

Lippmann, J., Stute, M., Torgersen, T., Moser, D.P., Hall, J.A., Lin, L., Borcsik, M., Bellamy, R.E.S., Onstott, T.C., 2003. Dating ultra-deep mine waters with noble gases and 36Cl, Witwatersrand Basin, South Africa. Geochimica et Cosmochimica Acta 67, 4597-4619.

Long, D.T., Wilson, T.P., Takacs, M.J., Rezabek, D.H., 1988. Stable-isotope geochemistry of saline near-surface ground water: East-central Michigan basin. Geological Society of America Bulletin 100, 1568-1577.

Luczaj, J.A., Harrison, W.B., Smith Williams, N., 2006. Fractured hydrothermal dolomite reservoirs in the Devonian Dundee Formation of the central Michigan Basin. AAPG Bulletin 90, 1787-1801.

Ma, L., Castro, M.C., Hall, C.M., Walter, L.M., 2005. Cross-formational flow and salinity sources inferred from a combined study of helium concentrations, isotopic ratios, and major elements in the Marshall aquifer, southern Michigan. Geochem. Geophys. Geosyst. 6, Q10004.

Ma, L., Castro, M.C., Hall, C.M., 2009a. Atmospheric noble gas signatures in deep Michigan Basin brines as indicators of a past thermal event. Earth and Planetary Science Letters 277, 137-147.

Ma, L., Castro, M.C., Hall, C.M., 2009b. Crustal noble gases in deep brines as natural tracers of vertical transport processes in the Michigan Basin. Geochem. Geophys. Geosyst. 10, Q06001.

Mandle, R. J., and Westjohn, D. B., 1989. Geohydrologic framework and ground-water flow in the Michigan Basin, in Regional Aquifer Systems of the United States: Aquifers of the Midwestern Area, AWRA Monogr. Ser., vol. 13, pp. 83– 109, Am. Water Resour. Assoc., Middleburg, Va.

Martini, A.M., 1997. Hydrogeochemistry of saline fluids and associated water and gas, Ph.D. dissertation, Univ. of Michigan, Ann Arbor.

McIntosh, J.C., Walter, L.M., Martini, A.M., 2004. Extensive microbial modification of formation water geochemistry: Case study from a Midcontinent sedimentary basin, United States. Geological Society of America Bulletin 116, 743-759.

Ozima, M., Podosek, F.A., 2002. Noble gas geochemistry. Cambridge University Press, Cambridge, UK ; New York.

Patriarche, D., Castro, M.C., Goblet, P., 2004. Large-scale hydraulic conductivities inferred from three-dimensional groundwater flow and 4He transport modeling in the Carrizo aquifer, Texas. Journal of Geophysical Research-Solid Earth 109. doi:10.1029/2004JB003173.

Pinti, D.L., Marty, B., 1995. Noble gases in crude oils from the Paris Basin, France: implications for the origin of fluids and constraints on oil–water–gas interactions. Geochim. Cosmochim. Acta 59, 3389–3404.

Pinti, D.L., Beland-Otis, C., Tremblay, A., Castro, M.C., Hall, C.M., Marcil, J.S., Lavoie, J.Y., Lapointe, R., 2011. Fossil brines preserved in the St-Lawrence Lowlands, Quebec, Canada as revealed by their chemistry and noble gas isotopes. Geochimica et Cosmochimica Acta 75, 4228-4243.

Prinzhofer, A., Battani, A., 2003. Gas isotopes tracing: an important tool for hydrocarbons exploration. Oil Gas Sci. Technol.-Rev. IFP 58, 299–311.

Saar, M.O., Castro, M.C., Hall, C.M., Manga, M., Rose, T.P., 2005. Quantifying magmatic,

crustal, and atmospheric helium contributions to volcanic aquifers using all stable noble gases: Implications for magmatism and groundwater flow. Geochem. Geophys. Geosyst. 6, Q03008.

Smith, S.P., Kennedy, B.M., 1983. The solubility of noble gases in water and in NaCl brine. Geochimica et Cosmochimica Acta 47, 503-515.

Van Schmus, W.R., 1992. Tectonic setting of the Midcontinent Rift system. Tectonophysics 213, 1–15.

Vugrinovich, R., 1986. Patterns of regional subsurface fluid movement in the Michigan Basin, Open File Rep. 86-6. Geol. Surv. Div. Mich. Dep. Of Nat. Resour., Lansing.

Vugrinovich, R., 1989. Subsurface temperatures and surface heat flow in the Michigan Basin and their relationships to regional subsurface fluid movement. Mar. Pet. Geol. 6, 60–70.

Weaver, T.R., Frape, S.K., Cherry, J.A., 1995. Recent cross-formational fluid flow and mixing in the shallow Michigan Basin. Geological Society of America Bulletin 107, 697-707.

Weiss, R.F., 1968. Piggyback sampler for dissolved gas studies on sealed water samples. Deep Sea Research and Oceanographic Abstracts 15, 695-699.

Weiss, R.F., 1970. The solubility of nitrogen, oxygen and argon in water and seawater. Deep Sea Research and Oceanographic Abstracts 17, 721-735.

Wilson, G.B., McNeill, G.W., 1997. Noble gas recharge temperatures and the excess air component. Applied Geochemistry 12, 747-762.

Wilson, T.P., Long, D.T., 1993a. Geochemistry and isotope chemistry of Michigan Basin brines: Devonian formations. Appl. Geochem. 8, 81–100.

Wilson, T.P., Long, D.T., 1993b. Geochemistry and isotope chemistry of CaNaCl brines in Silurian strata, Michigan Basin, U.S.A. Applied Geochemistry 8, 507-524.

Zartman, R.E., G. J. Wasserburg, Reynolds, J.H., 1961. Helium, Argon, and Carbon in Some Natural Gases. J. Geophys. Res. 66, 277–306.

CHAPTER 6

SUMMARY AND CONCLUSIONS

This final chapter of the dissertation summarizes major results from each chapter and provides brief concluding remarks of the overall work presented.

6.1 Summary of Major Results

Chapter 2: Noble gas temperatures (NGTs) were successfully used to identify recharge areas and timing of recharge in basal and perched aquifers in the fractured, basaltic hydrologic systems of Santa Cruz and San Cristobal in the Galapagos Archipelago. Specifically, recharge altitudes between 160 and 870 m and temperatures between 20.05±2.07°C and 27.54±0.47°C are found for the basal aquifer in Santa Cruz, while recharge altitudes between 229 and 730 m and temperatures of 19.95±1.13°C and 26.36±0.66°C are found for springs in San Cristobal. Timing of recharge obtained through NGTs for all samples are also corroborated by stable isotope results and points to recharge during the hot season for all low altitude (<~420 m) spring samples from San Cristobal and all basal aquifer samples in Santa Cruz. Stable isotope analyses also indicate that San Cristobal springs located at high altitudes (>420 m a.s.l) are recharged during both the "garúa" and hot seasons. Robust agreement on

the timing of recharge between NGTs and stable isotopes also suggests that seasonal variations in temperature are preserved by noble gases dissolved in groundwater in basaltic environments in the presence of fractures or where soil cover is thin. Preservation of seasonality independently recorded by NGTs and stable isotopes is further reinforced by estimated young water ages (<11 ± 4.5 years). Samples located at high altitude (>~420 m) display inconsistent recharge altitudes and temperatures and indicate a unique noble gas pattern with relative Ar excess together with a strong depletion of Ne, Kr and Xe. Existing degassing models are unable to account for the observed noble gas pattern for most samples. The impact of fog droplets ("garúa" dew) on dissolved noble gas concentrations in groundwater on the highlands was explored but such a mechanism, by itself, is insufficient to reproduce the observed noble gas patterns. On the other hand, the effect of mixing high-altitude (≥1500 m) atmosphere rainwater with low-altitude (~400 m) fog droplets readily explains Ne and Xe concentrations for most inconsistent samples. However, a statistical analysis conducted of the mixing hypothesis based simultaneously on all four noble gases is unsuccessful, and suggests that model parameter estimates are ill constrained. A full understanding of this unique noble gas pattern requires a comprehensive study of noble gas composition in rainwater. This is subsequently investigated in Chapter 3 of this dissertation.

Chapter 3: This chapter presents noble gas concentrations and helium isotopic ratios for rainwater samples collected in southeast Michigan during multiple precipitation events, over a period of several months. Results show that all rainwater samples are in disequilibrium with surface conditions and present atmospheric He excesses up to 29%. In addition, analyses of measured noble gas concentrations in rainwater together with multiple weather

data at the time of sample collection identify two groups of rainwater noble gas patterns. The first group of samples, associated with low-pressure systems, presence of fog and light rainfall, displays a relative Ar enrichment together with Ne, Kr, and Xe depletion, similar to high-altitude springs in the Galapagos Islands (Chapter 2). The second group of samples, associated with the passage of frontal systems, displays a mass-dependent depletion pattern with a greater depletion of the heavier noble gases, Kr and Xe, as compared to the lighter ones, Ne and Ar. Precipitation for the second group of samples is characterized by thunderstorms, heavy rainfall, and high cloud ceiling heights (>1km). A diffusion mass-transfer model strongly suggests that ice is the starting point of rainwater formation in southeast Michigan. Using this model and measured noble gas concentrations in rainwater samples with mass-dependent patterns, raindrop sizes between 0.45 and 10mm in diameter were derived for individual precipitation events and point to the occurrence of heavy rainfall. Complete re-equilibration of rainwater with surface conditions is shown to occur within hours and suggest that rainwater noble gas patterns are not likely to be recorded in sedimentary aquifer systems which typically have thicker unsaturated zones and longer infiltration times. This, in turn, allows the use of noble gases in paleoclimate reconstructions. A detailed paleoclimate NGT record in southern Michigan is presented in Chapter 4.

Chapter 4: This study presents a new ~13.1kyrs paleoclimatic reconstruction based on NGTs, excess air and stable isotope record derived from Saginaw aquifer in southern Michigan. NGTs vary between 8.0 ± 0.8˚C and 1.6 ± 0.9˚C and point to an overall warming trend in southern Michigan since the late Pleistocene, and, more broadly, since the LGM. Together with the Marshall record [*Ma et al.*, 2004], NGTs and EA from the Saginaw aquifer

capture, for the first time, the onset of the Younger Dryas (~12,9kyrs BP) with a ~3.3˚C cooling accompanied by drier conditions. Mid-Holocene (MH) climatic shifts are also identified, with warming (~2.9˚C), increased aridity starting at ~5.4kyrs BP followed by reversal to cooler, humid conditions at ~4.1kyrs BP. Except for the last MH reversal, the stable isotope record mimics the NGT and EA records. Contrasting trends displayed by $\delta^{18}O$ and deuterium-excess in the last MH reversal suggests enhanced vapor transport from the Gulf of Mexico. In addition, stable isotopes (δD, $\delta^{18}O$) and ^{14}C derived ages in the Saginaw aquifer in southern Michigan suggest subglacial meltwater contributions from the Laurentide Ice Sheet (LIS) of up to 36% in the late Pleistocene, following the Last Glacial Maximum (LGM). Contributions of up to 74% from previous glaciation periods are observed. These results place new constraints on timing and sources of subglacial meltwater contributions from the LIS both prior and following the LGM. In addition, samples with groundwater ages prior to the LGM (~26.6 kyr- >50 kyr) are located in the main discharge area of the Michigan Basin and display extremely depleted δD, $\delta^{18}O$ values similar to values for modern groundwater resulting directly from snowmelt as well as unusually high (~80%-120%) atmospheric noble gas excesses. Mechanisms leading to unusually large atmospheric noble gas excesses for these samples were investigated in detail in Chapter 5.

Chapter 5: This study systematically investigates the origin of large atmospheric noble gas excesses (~80 - 124% Ne excess) in Saginaw aquifer samples located in the main discharge area of the Michigan Basin, in the Saginaw lowlands (SL) region. Through a step-by-step analysis, large atmospheric noble gas excesses in the Saginaw aquifer are shown to result from sources external to the aquifer rather than from increased hydrostatic pressure. External

factors with the potential to account for excess of atmospheric noble gases in the Saginaw aquifer are biological consumption of soil air O_2 without an equivalent build up of CO_2 and/or vertical transport of atmospheric noble gases that escaped from deep Michigan Basin brines following a past thermal event of mantle origin. This study shows that the maximum atmospheric noble gas excess that could potentially be produced through an O_2 depletion mechanism is not substantial (26.6%) compared to the total observed atmospheric noble gas excess in the Saginaw aquifer in the SL region. Subsequently, it is shown that the atmospheric noble gas pattern of the entire Michigan Basin strata appears to result from two distinct end-members: a) an end-member represented by the deepest, most depleted brines from which most of the atmospheric noble gases escaped; and b) an end-member with excess atmospheric noble gas values above those displayed by the Saginaw samples. Using a Rayleigh distillation model it is further shown that the greater relative enrichment of lighter noble gases compared to the heavier ones in the Saginaw aquifer in the SL area is compatible with diffusion or solubility related mechanisms. These findings reinforce the notion that a past thermal event is indeed responsible for the large atmospheric noble gas excesses found in the Saginaw aquifer in the SL area. They are also consistent with and reinforce previous findings with respect to the occurrence of a thermal event of mantle origin.

6.2 Concluding Remarks

Chapters 2-5 successfully investigate the two goals of this dissertation and demonstrate (1) the utility of atmospheric noble gases in identifying recharge areas and timing of recharge in fractured, basaltic systems; and (2) the ability of NGTs to identify abrupt climatic shifts in continental areas. This dissertation has focused on dissolved

atmospheric noble gases combined with a diversity of other natural tracers including stable isotopes (δD, $\delta^{18}O$, and $\delta^{13}C$), radiocarbon (^{14}C) and major element chemistry and investigated 29 freshwater spring samples from perched aquifers and basal aquifer samples from the Galapagos Islands of Santa Cruz and San Cristobal, 19 rainwater samples from southeast Michigan and 22 groundwater samples from the Saginaw aquifer in southern Michigan. The study of dissolved atmospheric noble gases in groundwater has provided a powerful tool to investigate groundwater recharge dynamics in fractured, basaltic systems, reconstruct past abrupt climatic records archived in groundwater as well as to trace the thermal history of stable tectonic regions. Dissolved atmospheric noble gases in rainwater also contribute to a better understanding of the noble gas thermometer as well as to expand the use of noble gases as tracers of groundwater circulation in fractured and karstic environments. This dissertation has important societal relevance in fractured groundwater areas, which typically have scarce freshwater resources and can contribute to improved water resource management plans in these regions. This dissertation also has important scientific implications for the fields of meteorology, atmospheric and climate sciences, paleoclimatology, environmental engineering, hydrogeology and tectonics.

References

Ma, L., M. C. Castro, and C. M. Hall (2004), A late Pleistocene-Holocene noble gas paleotemperature record in southern Michigan, *Geophys. Res. Lett.*, *31*(23), L23204.

APPENDICES

Additional text, tables and figures that support the main results presented in chapters 2-5 are provided in Appendices A-D, respectively. Supporting material presented in each appendix are briefly enumerated here and discussed in detail in the corresponding appendix.

Appendix A includes 3 tables (Tables A1-A3), 2 figures (Figures A1 and A2) as well as additional text that support results from chapter 2.

Appendix B provides additional text, 3 tables (Tables B1-B3) and 10 figures (Figures B1-B10) that support main results presented in chapter 3.

Appendix C consists of additional text, 5 tables (Tables C1-C5) and 4 figures (Figures C1-C4), which additionally supports the main results discussed in chapter 4.

Appendix D includes 4 tables (Tables D1-D4) as well as additional text that support the primary results presented in chapter 5.

APPENDIX A : SUPPLEMENTARY MATERIAL FOR CHAPTER 2

A.1 Introduction

Appendix A includes 3 tables (Tables A1-A3), 2 figures (Figures A1 and A2) as well as additional text that support results from chapter 2. Results of inverse fitting 13 consistent samples using the UA model in Table A1 (below). Results of inverse fitting all 16 inconsistent samples using the closed equilibration (CE) model of *Aeschbach-Hertig et al.* [2008], and 1-step degassing (SD) model of *Brennwald et al.* [2003], are shown in Table A2 (below). Discussion of sensitivity analysis of tritium ages to chosen equilibrium altitude and temperature is provided in section A2 (below), while a comparison of tritium ages using different equilibrium altitudes and temperatures is provided in Figure A1 (below).

Fog droplet size is discussed in section A3 (below). Table A3 presents measured noble gas concentrations in rainfall from southern Michigan. Section A4 provides a description of the calculation of volume change along with subroutine for fog droplet (NP) model.

A.2 Description of Table A1

Table A1 provides results of inverse fitting 13 consistent samples using UA model for various assumed recharge altitudes. Column descriptions for Table A1 are provided below.

1. Column "ID", sample name.
2. Column "Elev", assumed recharge elevation in meters.

3 Column "NGT", best fit noble gas temperature, degree C.

4. Column "err_NGT", uncertainty of noble gas temperature, degree C, 1-sigma error.
5. Column "chi2", chi squared, the sum of the squared deviations between the modeled and measured concentrations-weighted with the experimental 1-sigma-errors.
6. Column "A", fitted excess air volume, cm3 STP/g.
7. Column "err_A", uncertainty of excess air volume, cm3 STP/g, 1-sigma error.

Table A1. Results of inverse fitting 13 consistent samples using UA model for various assumed recharge altitudes.

ID	Elev	NGT	err_NGT	chi2	A	err_A
sc4-1	427	27.23	0.63	3.59	-1.54E-04	1.69E-04
sc4-1	477	26.99	0.64	3.73	-1.11E-04	1.73E-04
sc4-1	527	26.76	0.65	3.88	-6.80E-05	1.76E-04
sc4-1	577	26.53	0.66	4.04	-2.60E-05	1.79E-04
sc4-1	627	26.29	0.67	4.2	1.60E-05	1.83E-04
sc4-1	677	26.06	0.68	4.36	5.80E-05	1.86E-04
sc4-1	727	25.83	0.69	4.53	1.00E-04	1.90E-04
sc4-1	777	25.6	0.7	4.71	1.42E-04	1.93E-04
sc4-1	827	25.37	0.72	4.89	1.83E-04	1.97E-04
sc4-1	877	25.14	0.73	5.08	2.24E-04	2.01E-04
sc4-1	927	24.91	0.74	5.27	2.65E-04	2.04E-04
sc4-1	977	24.68	0.75	5.46	3.06E-04	2.08E-04
sc4-1	1027	24.46	0.76	5.66	3.46E-04	2.12E-04
sc5-1	447	25.92	2	37.23	3.99E-04	5.73E-04
sc5-1	497	25.69	2	37.71	4.42E-04	5.77E-04
sc5-1	547	25.47	2.01	38.2	4.85E-04	5.80E-04
sc5-1	597	25.24	2.02	38.7	5.28E-04	5.84E-04
sc5-1	647	25.01	2.03	39.2	5.71E-04	5.88E-04
sc5-1	697	24.79	2.03	39.7	6.13E-04	5.91E-04
sc5-1	747	24.56	2.04	40.21	6.55E-04	5.95E-04
sc5-1	797	24.34	2.05	40.72	6.97E-04	5.98E-04
sc5-1	847	24.11	2.05	41.24	7.39E-04	6.02E-04
sc5-1	897	23.89	2.06	41.76	7.80E-04	6.06E-04
sc5-1	947	23.67	2.07	42.29	8.22E-04	6.09E-04
sc5-1	997	23.44	2.07	42.82	8.63E-04	6.13E-04
sc5-1	1047	23.22	2.08	43.35	9.04E-04	6.16E-04
sc8-1	229	26.07	1.8	30.85	-1.85E-04	5.06E-04
sc8-1	279	25.84	1.81	31.35	-1.40E-04	5.10E-04
sc8-1	329	25.61	1.82	31.85	-9.60E-05	5.14E-04
sc8-1	379	25.38	1.82	32.36	-5.20E-05	5.17E-04
sc8-1	429	25.15	1.83	32.87	-9.00E-06	5.21E-04
sc8-1	479	24.93	1.84	33.39	3.50E-05	5.25E-04
sc8-1	529	24.7	1.85	33.91	7.80E-05	5.29E-04
sc8-1	579	24.47	1.86	34.43	1.21E-04	5.33E-04
sc8-1	629	24.25	1.87	34.96	1.64E-04	5.37E-04
sc8-1	679	24.03	1.88	35.5	2.06E-04	5.41E-04
sc8-1	729	23.8	1.89	36.04	2.49E-04	5.45E-04
sc8-1	779	23.58	1.9	36.59	2.91E-04	5.49E-04
sc8-1	829	23.36	1.9	37.14	3.33E-04	5.53E-04
sc8-1	879	23.14	1.91	37.69	3.74E-04	5.57E-04
sc8-1	929	22.92	1.92	38.26	4.16E-04	5.61E-04
sc8-1	979	22.7	1.93	38.82	4.57E-04	5.65E-04
sc8-1	1029	22.48	1.94	39.39	4.98E-04	5.69E-04
sc9-1	229	24.07	1.32	16.84	4.35E-04	4.04E-04
sc9-1	279	23.84	1.32	17.08	4.80E-04	4.07E-04
sc9-1	329	23.62	1.33	17.34	5.24E-04	4.10E-04

sc9-1	379	23.39	1.33	17.59	5.68E-04	4.13E-04
sc9-1	429	23.17	1.34	17.85	6.12E-04	4.16E-04
sc9-1	479	22.95	1.35	18.12	6.56E-04	4.19E-04
sc9-1	529	22.72	1.35	18.39	6.99E-04	4.22E-04
sc9-1	579	22.5	1.36	18.67	7.43E-04	4.25E-04
sc9-1	629	22.28	1.36	18.95	7.86E-04	4.28E-04
sc9-1	679	22.06	1.37	19.23	8.28E-04	4.31E-04
sc9-1	729	21.84	1.38	19.52	8.71E-04	4.34E-04
sc9-1	779	21.62	1.38	19.82	9.13E-04	4.37E-04
sc9-1	829	21.41	1.39	20.12	9.55E-04	4.40E-04
sc9-1	879	21.19	1.4	20.42	9.97E-04	4.44E-04
sc9-1	929	20.97	1.4	20.73	1.04E-03	4.47E-04
sc9-1	979	20.76	1.41	21.04	1.08E-03	4.50E-04
sc9-1	1029	20.54	1.42	21.36	1.12E-03	4.53E-04
sc9-2	229	25.27	0.94	7.96	7.52E-04	2.86E-04
sc9-2	279	25.04	0.93	7.99	7.96E-04	2.86E-04
sc9-2	329	24.81	0.93	8.03	8.40E-04	2.87E-04
sc9-2	379	24.58	0.93	8.07	8.84E-04	2.88E-04
sc9-2	429	24.36	0.93	8.12	9.28E-04	2.88E-04
sc9-2	479	24.13	0.93	8.17	9.72E-04	2.89E-04
sc9-2	529	23.9	0.93	8.23	1.02E-03	2.90E-04
sc9-2	579	23.68	0.94	8.29	1.06E-03	2.91E-04
sc9-2	629	23.45	0.94	8.36	1.10E-03	2.92E-04
sc9-2	679	23.23	0.94	8.43	1.14E-03	2.93E-04
sc9-2	729	23	0.94	8.5	1.19E-03	2.94E-04
sc9-2	779	22.78	0.94	8.58	1.23E-03	2.96E-04
sc9-2	829	22.56	0.94	8.67	1.27E-03	2.97E-04
sc9-2	879	22.34	0.94	8.76	1.31E-03	2.99E-04
sc9-2	929	22.11	0.95	8.85	1.35E-03	3.00E-04
sc9-2	979	21.89	0.95	8.95	1.39E-03	3.02E-04
sc9-2	1029	21.68	0.95	9.06	1.44E-03	3.03E-04
sc11-1	572	24.15	0.79	6.08	4.06E-04	2.33E-04
sc11-1	622	23.92	0.8	6.25	4.49E-04	2.37E-04
sc11-1	672	23.7	0.81	6.43	4.91E-04	2.40E-04
sc11-1	722	23.47	0.82	6.61	5.34E-04	2.43E-04
sc11-1	772	23.25	0.83	6.8	5.76E-04	2.47E-04
sc11-1	822	23.03	0.84	7	6.17E-04	2.50E-04
sc11-1	872	22.81	0.85	7.2	6.59E-04	2.53E-04
sc11-1	922	22.58	0.86	7.4	7.00E-04	2.57E-04
sc11-1	972	22.36	0.86	7.61	7.42E-04	2.61E-04
sc11-1	1022	22.14	0.87	7.83	7.83E-04	2.64E-04
sc12-2	295	21.83	1.03	11.44	-4.20E-05	3.21E-04
sc12-2	300	21.81	1.03	11.47	-3.80E-05	3.21E-04
sc12-2	350	21.59	1.04	11.78	7.00E-06	3.26E-04
sc12-2	400	21.37	1.06	12.1	5.10E-05	3.30E-04
sc12-2	450	21.15	1.07	12.42	9.50E-05	3.34E-04
sc12-2	500	20.94	1.08	12.74	1.39E-04	3.38E-04
sc12-2	550	20.72	1.09	13.08	1.83E-04	3.43E-04
sc12-2	600	20.5	1.1	13.41	2.26E-04	3.47E-04

sc12-2	650	20.29	1.11	13.75	2.69E-04	3.51E-04
sc12-2	700	20.08	1.12	14.1	3.12E-04	3.56E-04
sc12-2	750	19.86	1.13	14.46	3.55E-04	3.60E-04
sc12-2	800	19.65	1.14	14.81	3.97E-04	3.64E-04
sc12-2	850	19.44	1.15	15.18	4.40E-04	3.69E-04
sc12-2	900	19.23	1.16	15.55	4.82E-04	3.73E-04
sc12-2	950	19.01	1.17	15.92	5.23E-04	3.77E-04
sc12-2	1000	18.8	1.18	16.3	5.65E-04	3.82E-04
sc13-1	382	23.49	0.89	8.1	-2.68E-04	2.59E-04
sc13-1	400	23.41	0.89	8.19	-2.52E-04	2.60E-04
sc13-1	450	23.18	0.9	8.43	-2.08E-04	2.64E-04
sc13-1	500	22.96	0.91	8.67	-1.65E-04	2.67E-04
sc13-1	550	22.74	0.92	8.92	-1.21E-04	2.71E-04
sc13-1	600	22.51	0.93	9.17	-7.80E-05	2.75E-04
sc13-1	650	22.29	0.94	9.43	-3.60E-05	2.79E-04
sc13-1	700	22.07	0.95	9.7	7.00E-06	2.83E-04
sc13-1	750	21.85	0.96	9.97	4.90E-05	2.86E-04
sc13-1	800	21.63	0.97	10.24	9.10E-05	2.90E-04
sc13-1	850	21.42	0.98	10.52	1.33E-04	2.94E-04
sc13-1	900	21.2	0.99	10.81	1.75E-04	2.98E-04
sc13-1	950	20.98	1.01	11.1	2.16E-04	3.02E-04
sc13-1	1000	20.76	1.02	11.4	2.57E-04	3.06E-04
sc13-2	382	24.2	2.95	88.71	-3.10E-05	8.59E-04
sc13-2	400	24.12	2.95	88.99	-1.50E-05	8.60E-04
sc13-2	450	23.9	2.96	89.76	2.90E-05	8.63E-04
sc13-2	500	23.68	2.96	90.54	7.20E-05	8.67E-04
sc13-2	550	23.46	2.97	91.33	1.16E-04	8.70E-04
sc13-2	600	23.24	2.97	92.12	1.59E-04	8.74E-04
sc13-2	650	23.02	2.98	92.91	2.02E-04	8.77E-04
sc13-2	700	22.8	2.98	93.71	2.44E-04	8.81E-04
sc13-2	750	22.58	2.98	94.52	2.87E-04	8.84E-04
sc13-2	800	22.36	2.99	95.33	3.29E-04	8.88E-04
sc13-2	850	22.14	2.99	96.14	3.71E-04	8.91E-04
sc13-2	900	21.93	3	96.96	4.13E-04	8.95E-04
sc13-2	950	21.71	3	97.78	4.54E-04	8.98E-04
sc13-2	1000	21.5	3.01	98.6	4.96E-04	9.02E-04
sz1-1	200	25.91	0.53	2.64	-3.61E-04	1.49E-04
sz1-1	250	25.67	0.51	2.47	-3.17E-04	1.44E-04
sz1-1	300	25.44	0.49	2.31	-2.73E-04	1.39E-04
sz1-1	350	25.21	0.48	2.15	-2.29E-04	1.34E-04
sz1-1	400	24.97	0.46	2	-1.86E-04	1.29E-04
sz1-1	450	24.74	0.46	1.85	-1.42E-04	1.29E-04
sz1-1	500	24.51	0.45	1.71	-9.90E-05	1.29E-04
sz1-1	550	24.28	0.45	1.58	-5.60E-05	1.29E-04
sz1-1	600	24.06	0.45	1.45	-1.40E-05	1.29E-04
sz1-1	650	23.83	0.45	1.33	2.90E-05	1.29E-04
sz1-1	700	23.6	0.45	1.21	7.10E-05	1.29E-04
sz1-1	750	23.37	0.45	1.1	1.13E-04	1.29E-04
sz1-1	800	23.15	0.45	0.99	1.54E-04	1.29E-04

sz1-1	850	22.92	0.44	0.89	1.96E-04	1.29E-04
sz1-1	900	22.7	0.44	0.79	2.37E-04	1.29E-04
sz1-1	950	22.48	0.44	0.7	2.78E-04	1.29E-04
sz1-1	1000	22.25	0.44	0.62	3.19E-04	1.29E-04
sz2-1	200	27.59	0.48	0.72	-2.00E-06	1.33E-04
sz2-1	250	27.35	0.48	0.64	4.20E-05	1.33E-04
sz2-1	300	27.12	0.47	0.57	8.60E-05	1.32E-04
sz2-1	350	26.88	0.47	0.51	1.30E-04	1.32E-04
sz2-1	400	26.64	0.47	0.45	1.73E-04	1.32E-04
sz2-1	450	26.41	0.47	0.4	2.16E-04	1.32E-04
sz2-1	500	26.17	0.47	0.35	2.59E-04	1.32E-04
sz2-1	550	25.94	0.47	0.31	3.02E-04	1.32E-04
sz2-1	600	25.71	0.47	0.27	3.45E-04	1.32E-04
sz2-1	650	25.48	0.47	0.24	3.87E-04	1.32E-04
sz2-1	700	25.25	0.46	0.21	4.29E-04	1.32E-04
sz2-1	750	25.02	0.46	0.19	4.71E-04	1.32E-04
sz2-1	800	24.79	0.46	0.18	5.12E-04	1.32E-04
sz2-1	850	24.56	0.46	0.17	5.54E-04	1.32E-04
sz2-1	900	24.33	0.46	0.16	5.95E-04	1.32E-04
sz2-1	950	24.11	0.46	0.16	6.36E-04	1.32E-04
sz2-1	1000	23.88	0.46	0.17	6.77E-04	1.32E-04
sz2-2	200	22.96	1.99	41.85	-2.96E-04	5.98E-04
sz2-2	250	22.74	2	42.33	-2.51E-04	6.01E-04
sz2-2	300	22.52	2	42.81	-2.06E-04	6.04E-04
sz2-2	350	22.3	2.01	43.3	-1.62E-04	6.07E-04
sz2-2	400	22.08	2.01	43.79	-1.18E-04	6.11E-04
sz2-2	450	21.86	2.02	44.29	-7.40E-05	6.14E-04
sz2-2	500	21.64	2.03	44.79	-3.00E-05	6.17E-04
sz2-2	550	21.43	2.03	45.3	1.40E-05	6.21E-04
sz2-2	600	21.21	2.04	45.81	5.70E-05	6.24E-04
sz2-2	650	20.99	2.04	46.32	1.00E-04	6.27E-04
sz2-2	700	20.78	2.05	46.84	1.43E-04	6.31E-04
sz2-2	750	20.56	2.05	47.37	1.85E-04	6.34E-04
sz2-2	800	20.35	2.06	47.9	2.28E-04	6.37E-04
sz2-2	850	20.14	2.06	48.44	2.70E-04	6.41E-04
sz2-2	900	19.92	2.07	48.98	3.12E-04	6.44E-04
sz2-2	950	19.71	2.08	49.52	3.53E-04	6.47E-04
sz2-2	1000	19.5	2.08	50.07	3.95E-04	6.51E-04
sz3-2	200	24.49	1.59	24.06	6.30E-05	4.74E-04
sz3-2	250	24.26	1.58	23.94	1.08E-04	4.72E-04
sz3-2	300	24.03	1.57	23.83	1.52E-04	4.71E-04
sz3-2	350	23.8	1.56	23.72	1.97E-04	4.70E-04
sz3-2	400	23.58	1.55	23.62	2.41E-04	4.69E-04
sz3-2	450	23.35	1.55	23.52	2.84E-04	4.68E-04
sz3-2	500	23.13	1.54	23.44	3.28E-04	4.67E-04
sz3-2	550	22.9	1.53	23.35	3.71E-04	4.66E-04
sz3-2	600	22.68	1.52	23.28	4.14E-04	4.65E-04
sz3-2	650	22.46	1.52	23.21	4.57E-04	4.64E-04
sz3-2	700	22.24	1.51	23.15	5.00E-04	4.63E-04

sz3-2	750	22.01	1.51	23.09	5.42E-04	4.63E-04
sz3-2	800	21.79	1.5	23.04	5.84E-04	4.62E-04
sz3-2	850	21.57	1.49	23	6.26E-04	4.61E-04
sz3-2	900	21.36	1.49	22.96	6.68E-04	4.61E-04
sz3-2	950	21.14	1.48	22.93	7.09E-04	4.60E-04
sz3-2	1000	20.92	1.48	22.91	7.51E-04	4.60E-04

A.3 Description of Table A2

Table A2 provides results of inverse fitting all inconsistent samples at sampling altitudes using CE and SD model. Column descriptions for Table A2 are provided below.

1. Column "ID", sample name.
2. Column "NGT_CE", best fit noble gas temperature obtained using CE model, °C.
3. Column "err_NGT_CE", uncertainty of noble gas temperature using CE model, °C, 1-sigma error.
4. Column "A_CE", CE model fitted excess air volume, cm^3 STP/g.
5. Column "err_A_CE", CE model uncertainty of excess air volume, cm^3 STP/g, 1-sigma error.
6. Column "F_CE", CE model fractionation parameter.
7. Column "chi2_CE", chi squared, the sum of the squared deviations between the CE model and measured concentrations-weighted with the experimental 1-sigma-errors.
8. Column "NGT_SD", best fit noble gas temperature obtained using SD model, °C.
9. Column "err_NGT_SD", uncertainty of noble gas temperature using SD model, °C, 1-sigma error.
10. Column "B", SD model fitted degassing volume, cm^3 STP/g.
11. Column "B_err", uncertainty in degassing volume, cm^3 STP/g, 1-sigma error.
12. Column "chi2_SD", chi squared, the sum of the squared deviations between the SD model and measured concentrations-weighted with the experimental 1-sigma-errors.

Table A2. Results of inverse fitting all inconsistent samples at sampling altitudes using CE and SD model.

ID	NGT_CE	err_NGT_CE	A_CE	err_A_CE	F_CE	chi2_CE	NGT_SD	err_NGT_SD	B	B_err	chi2_SD
sc1-1	17.45	1.53	2.68E-05	2.39E-05	2.43E+01	2.93E+01	17.45	1.53	6.22E-04	5.54E-04	29.32
sc1-2	16.06	2.1	2.18E-05	2.19E-05	3.76E+01	5.81E+01	16.06	2.1	7.97E-04	8.00E-04	58.05
sc2-1	22.92	1.3	1.25E-02	2.06E-02	1.24E+00	1.33E+00	23.88	0.46	1.22E-03	1.53E-04	2.08
sc2-2	16.97	0.87	2.62E-05	9.28E-06	3.67E+01	9.51E+00	16.97	0.87	9.32E-04	3.29E-04	9.5
sc3-1	17.85	8	1.78E+07	9.38E+15	1.06E+00	2.58E+01	21.2	0.57	4.93E-04	1.84E-04	3.57
sc3-2	28.65	4.1	1.51E-05	3.89E-04	3.72E+00	1.52E+02	28.65	4.09	4.14E-05	1.05E-03	152
sc4-2	21.01	1.16	2.50E-05	8.44E-06	5.06E+01	1.50E+01	21.01	1.16	1.24E-03	4.18E-04	15
sc5-2	25.14	1.62	2.21E-05	2.09E-05	2.46E+01	2.57E+01	25.14	1.62	5.20E-04	4.91E-04	25.66
sc6-1	26.4	1	2.57E-05	8.79E-06	3.63E+01	9.41E+00	26.4	1	9.04E-04	3.09E-04	9.4
sc6-2	35.75	22.79	6.19E+00	5.87E+03	9.60E-01	9.96E+01	35.3	0.96	5.28E-04	2.41E-04	6.65
sc10-1	20.67	1.52	2.32E-05	2.92E-05	1.84E+01	2.61E+01	20.67	1.52	4.01E-04	5.04E-04	26.06
sc10-2	20.18	1.03	2.45E-05	1.19E-05	3.13E+01	1.20E+01	20.18	1.03	7.40E-04	3.58E-04	11.97
sc11-2	18.5	1.33	2.58E-05	2.79E-05	1.75E+01	2.11E+01	18.5	1.33	4.25E-04	4.58E-04	21.1
sc12-1	16.54	1.02	2.61E-05	4.70E-06	1.01E+02	1.35E+01	16.55	1.02	2.60E-03	4.71E-04	13.47
sz3-1	21.35	0.51	2.15E-05	2.93E-06	6.61E+01	2.84E+00	21.35	0.51	1.39E-03	1.91E-04	2.83
sz4-1	20.25	0.43	2.28E-05	2.42E-06	6.81E+01	2.11E+00	20.26	0.43	1.53E-03	1.62E-04	2.1

A.4 Description of Table A3

Table A3 provides measured noble gas concentrations in rainfall from southern Michigan. Column descriptions for Table A3 are provided below.

1. Column "Sample", sample name.
2. Column "He", measured He concentration in ccSTP/g.
3. Column "Ne", measured Ne concentration in ccSTP/g.
4. Column "Ar", measured Ar concentration in ccSTP/g.
5. Column "Kr", measured Kr concentration in ccSTP/g.
6. Column "Xe", measured Xe concentration in ccSTP/g.

Table A3. Measured noble gas concentrations in rainfall from southern Michigan.

Sample	He	Ne	Ar	Kr	Xe
nr1b	4.6748E-08	1.7801E-07	3.6628E-04	8.7038E-08	1.24E-08
nr2a	5.56E-08	1.9394E-07	3.03E-04	6.4950E-08	8.3390E-09

A.5 Discussion of sensitivity analysis of tritium ages to chosen equilibrium altitude and temperature

Following procedures described in *Schlosser et al.* [1988], calculation of trtiogenic ^{3}He from measured total He requires assumption of equilibrium ^{4}He concentrations corresponding to a specific recharge altitude and temperature. Calculated tritiogenic ^{3}He values are then used to estimate tritium ages as discussed in section 2.6. A wide range of temperatures and altitudes possible on both Santa Cruz and San Cristobal were used to derive tritiogenic ^{3}He concentrations and subsequently tritium ages in each spring sample.

Recharge altitudes corresponding to a minimum and maximum altitude were tested for all springs. Minimum altitudes for consistent spring samples correspond to minimum possible altitudes derived in section 2.5.1 while sampling altitudes (Table 2.1) were chosen as minimum possible altitudes for inconsistent springs. Maximum altitudes were chosen as the peak altitude of the islands. Mean annual air temperatures extrapolated using the mean annual temperature gradient of -0.8°C/100m at corresponding minimum and maximum altitudes were used to derive equilibrium ^{4}He concentrations at each specific altitude and temperature for all springs.

Results show that tritiogenic excess ^{3}He calculated by assuming equilibrium ^{4}He concentrations at maximum and minimum recharge altitude yielded values that were very similar as shown in Figure A1. Indeed, comparison of excess ^{3}He derived from maximum and minimum altitudes yield a correlation coefficient of 1 and a slope of 1.0006 confirming that the effect of chosen altitude and temperature of ^{4}He equilibration has minimal effect on calculated excess ^{3}He.The minimal effect of altitude and temperature of ^{4}He equilibration on calculated ^{3}He excess is also reflected in tritium ages derived by assuming tritium peak on

10/1999 (cf. sec. 2.6) as shown in Figure A2. Similar to the observed correlation between excess ^{3}He derived from maximum and minimum recharge altitudes and temperatures, there is very good correlation between tritium ages derived from maximum and minimum recharge altitudes with a correlation coefficient of 1 and slope of 1.0024. The low sensitivity of ^{3}He excess and tritium ages to different recharge altitudes and temperatures might be due to low temperature sensitivity of He. It is thus concluded that the chosen range of altitudes and temperatures has a minimal effect on excess ^{3}He and tritium ages for all springs.

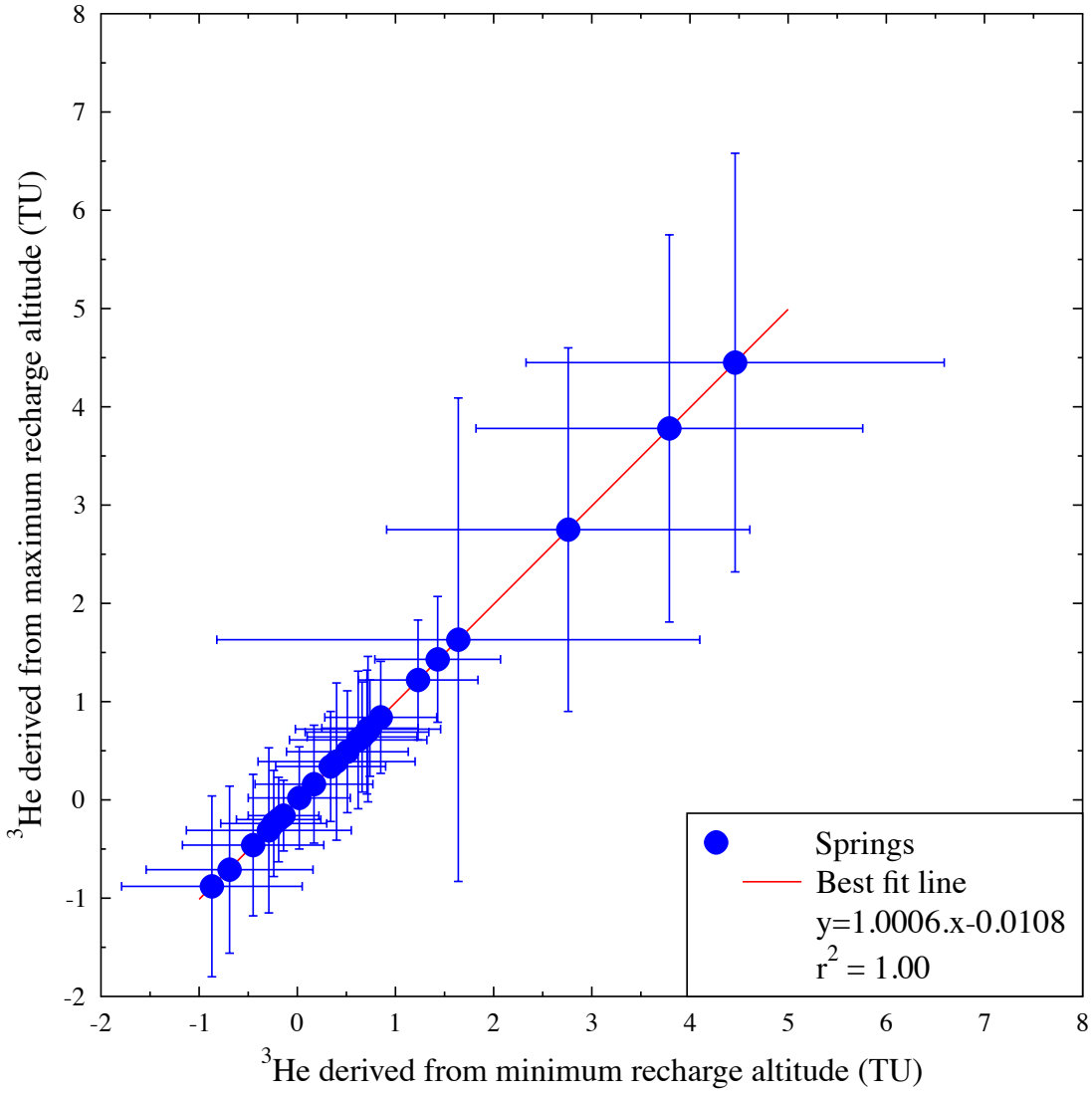

Figure A1. Comparison of ^{3}He derived using different equilibrium altitudes and temperatures.

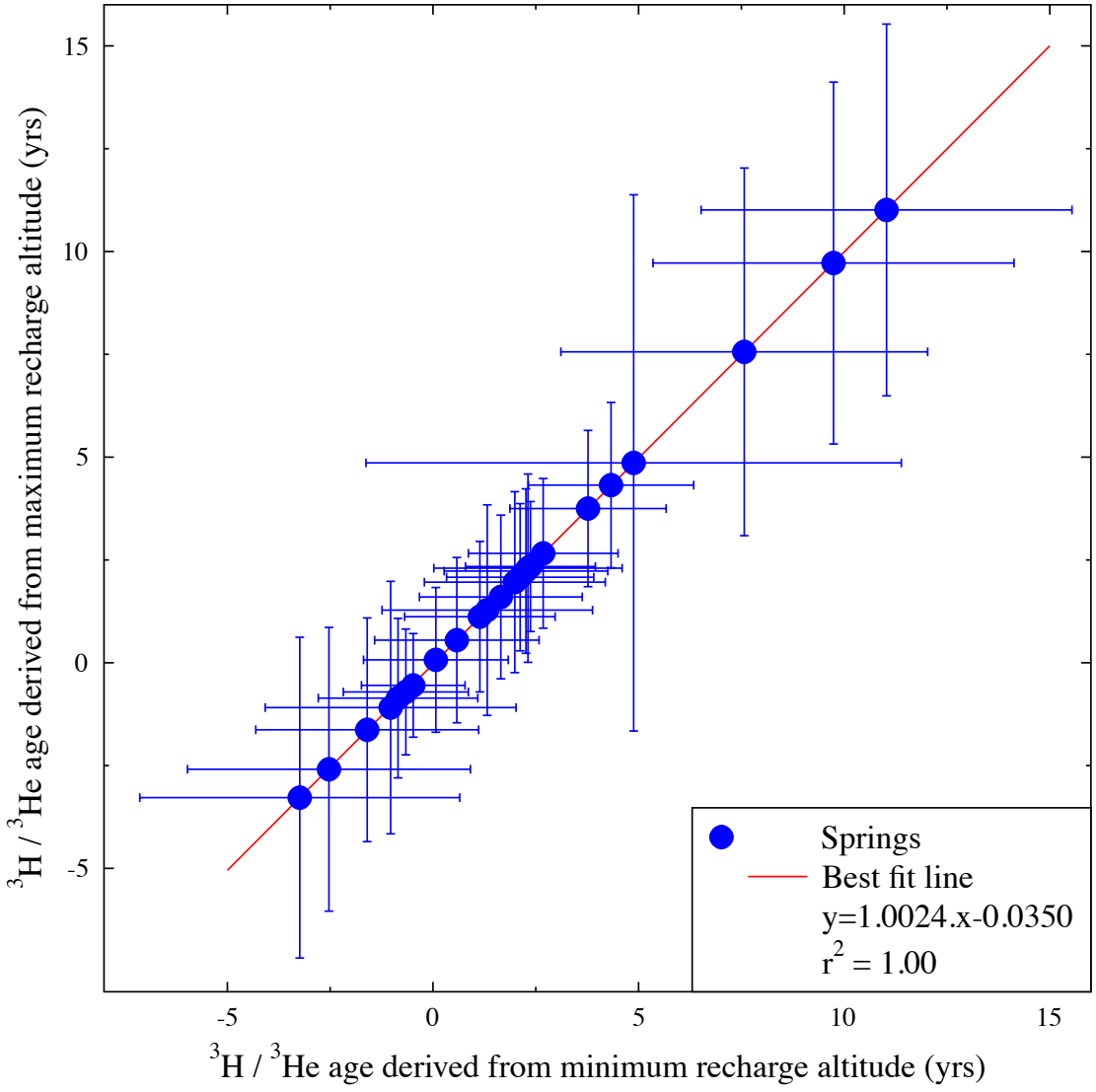

Figure A2. Comparison of tritium ages using different equilibrium altitudes and temperatures corresponding to 10/1999 ^{3}H maximum.

A.6 Discussion of fog droplet size distribution and nucleation of fogs

A.6.1 Theory on formation of fog droplets

Generation of fog droplets begins with nucleation of aerosol particles in the environment. These particles, naturally present in the environment (e.g., sea salt particles) are generally classified into 3 size categories [*Junge et al.*, 1952, 1963]:

1. Particles with dry radii <0.1 micron called Aitken particles
2. Particles with dry radii 0.1-1 micron called large particles
3. R>1micron called giant particles

As the relative humidity in the environment rises, the droplets will grow by slow equilibrium diffusion of water vapor until it reaches a critical supersaturation when it is deemed as active. Once the aerosol is activated, it grows freely by vapor diffusion into a macroscopic cloud drop. The activation of fog droplets occurs at different supersaturations based on different chemical composition and sizes of aerosols. *Hanël* [1976] showed that for a given dry particle radius, the levels of supersaturation required for droplet activation are functions of the soluble substance (chemical composition) as well as on the fraction of soluble to insoluble masses of the particle which is expressed by the Köhler curves [*Seinfeld and Pandis*, 2006]. Based on the Köhler curves, for measured supersaturations of up to 0.1% in fogs in the Galapagos [*Collins and Bush*, 2010] one would expect droplet radius of 0.3 micron to produce a fog droplet in stable equilibrium [*Seinfeld and Pandis*, 2006]. Larger drops may then be formed by collision and coalescence of these smaller, activated droplets.

A.6.2 Some direct fog drop measurement sizes

The range of fog droplets tested in our paper are between 0.3 to 10 microns which

falls within the range of expected fog droplet sizes for measured supersaturations in the Galapagos. These fog droplet sizes are also comparable with directly measured fog droplet sizes in different types of fogs around the world (see, e.g., *Stewart and Essenwanger*, 1982 for a review of measured fog droplet sizes). For example, *Meszaros et al.* [1965] measured fog drop sizes between 0.4 to 10.2 microns in 26 fogs in Budapest, Hungary. Similarly, *Ludwig et al.* [1974] measured droplet sizes in San Joaquin valley in California and found that the most common drop size were less than 1micron.

Given that fog droplets have to necessarily first nucleate from an aerosol particle, which in marine environments can be as small as 0.005microns in radius [*O'Dowd et al.*, 1997], it is not unusual to find varying droplet size distribution in fogs which may be a function of location amongst other factors. It is, however, more likely that one would find non-precipitating liquid droplets in clouds between 0.1 and 50microns based on the cloud type [*Pruppacher and Klett*, 1997]. Fog drop sizes tested in this study (0.3, 1 and 10 microns) fall within the observed range of liquid droplets in clouds.

A.7 Calculation of volume change along with subroutine for fog droplet model

A.7.1 Implementation of the NP Model

The modification of the standard Henry's constant at ~1 bar (atmospheric pressure) can be calculated from the equation for gas solubility as a function of pressure, i.e., equation 6 in *Mercury et al.* [2003], which is given by:

$$\ln \frac{k_H(T,P)}{k_H(T,1)} = \frac{1}{RT} \int_1^P V^\circ_{solute,T} \times dP \qquad (1)$$

Here, V° is given by the TH model shown in equation 2 below (equation 2 in *Mercury et al.*, 2003):

$$V^\circ = a_1 + \frac{a_2}{\varphi + P} + \frac{a_3}{T - \theta} + \frac{a_4}{(\varphi + P)(T - \theta)} - \omega \times Q_{P,T} \quad (2)$$

where, a_1 through a_4, ω, φ and θ are model parameters. For water as the solvent, φ and θ are 2600 bars and 228°K respectively [*Mercury et al.*, 2003] and the other parameters are dependent on the noble gas solute. The values for a_1 through a_4 and ω for each noble gas are listed in Table 1 of *Mercury et al.* [2004]. In equation 2, $Q_{P,T}$ is the Born function and it is defined as:

$$Q_{P,T} = \frac{1}{\varepsilon}\left(\frac{\delta \ln \varepsilon}{\delta P}\right) \qquad (3)$$

where ε is the dielectric constant of water as a function of pressure and temperature. In order to estimate the Born function, an approximation for ε that covers a broad range of P and T from *Bradley and Pitzer* [1979] was used. Their formulation can be written as:

$$\varepsilon = \varepsilon_{1000} + C \ln \frac{B+P}{B+1000} \qquad (4)$$

where,

$$\varepsilon_{1000} = U_1 \exp\left(U_2 T + U_2 T^2\right) \qquad (5)$$

$$C = U_4 + \frac{U_5}{U_6 + T} \qquad (6)$$

$$B = U_7 + \frac{U_8}{T} + U_9 T \qquad (7)$$

The constants U_1 through U_9 are given in *Bradley and Pitzer* [1979]. Applying equations 4 through 7 to equation 3 yields the following approximation to the Born function:

$$Q_{P,T} = \left(\frac{C}{\varepsilon^2 (B+P)} \right) \qquad (8)$$

The above equations were implemented using the following Pascal code. The integral in equation 1 is performed by iterative trapezoid rule numerical quadrature (procedure qtrap from *Press et al.*, 1986). The quadrature routine requires the definition of a function "func". In order to select which noble gas will be used for the integration, the global variable is made equal to one of heparms, neparms, arparms, krparms or xeparms for He, Ne, Ar, Kr or Xe respectively. Note that T is in °K and P is in bars. Note also that in the function v0, the volume has been multiplied by 10. This is because the constants listed in *Mercury et al.* [2004] were converted from calories to joules, but the conversion of all of the a_i and ω factors are too small by precisely a factor of 10. The listed parameters in the code below match those in *Mercury et al.* [2004], but the volume calculated in v0 is multiplied by 10 to give the correct volume in cc. The calculated values using v0 match those given in Table 5 of *Mercury et al.* [2003].

```
type
        parmarr=array[1..5] of double;
```

```
var
currparms:parmarr;
const
u1=3.4279e2;
u2=-5.0866e-3;
u3=9.4690e-7;
u4=-2.0525;
u5=3.1159e3;
u6=-1.8289e2;
u7=-8.0325e3;
u8=4.21452e6;
u9=2.1417;
arparms:parmarr=(2.512,2874.324,12.761,-128156,-128574);
heparms:parmarr=(1.4528,291.5,22.912,-117478,-88826);
neparms:parmarr=(1.871,1311.8,18.902,-121696,-106064);
krparms:parmarr=(2.6242,3151.9,11.67,-129302,-95437);
xeparms:parmarr=(3.146,4426.4,6.661,-134570,-92634);
function born(t,p:double):double;
var
tmp,e1,eps,p1:double;
eps1000,c,b:double;
begin
eps1000:=u1*exp(u2*t+u3*sqr(t));
```

```
c:=u4+u5/(u6+t);
b:=u7+u8/t+u9*t;
eps:=eps1000+c*ln((b+p)/(b+1000));
tmp:=c/((b+p)*sqr(eps));
born:=tmp;
end;
function v0(t,p:double; var a:parmarr):double;
const
psi=2600;
theta=228;
begin
v0:=10.0*(a[1]+a[2]/(psi+p)+a[3]/(t-theta)
+a[4]/((psi+p)*(t-theta))-born(t,p)*a[5]);
end;
FUNCTION func(x: double): double;
begin
func:=v0(temperature,x,currparms);
end;
```

References

Arnott, W. P., Schmitt, C., Yangang Liu, and Hallett, J., 1997. Droplet size spectra and water-vapor concentration of laboratory water clouds: inversion of Fourier transform infrared (500–5000 cm-1) optical-depth measurement," Appl. Opt. 36, 5205-5216.

Bradley, D.J. and Pitzer, K.S., 1979. Thermodynamics of Electrolytes. 12. Dielectric Properties of Water and Debye-Hückel Parameters to 350° C and 1 kbar. J. Phys. Chem., 83, 1599-1603.

Collins, A., Bush, M.B., 2010. An analysis of modern pollen representation and climatic conditions on the Galápagos Islands. The Holocene. Doi: 10.1177/0959684610378874.

Hänel, G., 1976. The Properties of Atmospheric Aerosol Particles as Functions of the Relative Humidity at Thermodynamic Equilibrium with the Surrounding Moist Air. Advances in Geophysics, 19 (C), pp. 73-188.

Junge, C., 1952. Die konstitution des atmospharischen aerosols, Ann. Meteorol. 5, 1-55.

Junge, C. E., 1963. Air Chemistry and Radioactivity, Academic Press, New York.

Mason, B. J., 1971. The Physics of Clouds (Clarendon, Oxford) pp. 93-94.

Mercury, L., Azarouhal, M., Zeyen, H. and Tardy, Y., 2003. Thermodynamic properties of solutions in metastable systems under negative or positive pressures. Geochim. Cosmochim. Acta, 67, 1769-1785.

Mercury, L., Pinti, D.L. and Zeyen, H., 2004. The effect of the negative pressure of capillary water on atmospheric noble gas solubility in ground water and palaeotemperature reconstruction. Earth Planet. Sci. Lett., 223, 147-161.

Mészaros, A., 1965. Concentration et distribution dimensionnelle des gouttelettes de brouillards atmosphériques (in French), J. Rech. Atmos., 2, 53–64.

O'Dowd, C.D., Smith, M.H., Consterdine, I.E., Lowe, J.A., 1997. Marine aerosol, sea-salt, and the marine sulphur cycle: a short review. Atmospheric Environment 31, 73-80.

Press, W.H., Flannery, B.P., Teulosky, S.A. and Vetterling, W.T. 1986. Numerical Recipes. (Cambridge U. Press), Cambridge, 818pp.

Pruppacher, H. R., and Klett, J. D., 1997. Microphysics of Clouds and Precipitation, Kluwer, Dordrecht, The Netherlands.

Schlosser, P., Stute, M., Dörr, H., Sonntag, C., Münnich, K.O., 1988. Tritium/3He dating of shallow groundwater. Earth and Planetary Science Letters 89, 353-362.

Seinfeld, J.H., Pandis, S.N., 2006. Atmospheric chemistry and physics: from air pollution to climate change. Wiley, Hoboken, N.J.

Shock, E.L., Helgeson, H.C. and Sverjensky, D.A., 1989. Calculation of the thermodynamic and transport properties of aqueous species at high pressures and temperatures: Standard partial molal properties of inorganic neutral species. Geochim. Cosmochim. Acta., 53, 2157-2183.

Stewart, D.A., Essenwanger, O.M., 1982. A survey of fog and related optical propagation characteristics. Rev. Geophys. 20, 481-495.

Whiteman, D. N., and S. H. Melfi, 1999. Cloud liquid water, mean droplet radius, and number density measurements using a Raman lidar, J. Geophys. Res., 104(D24), 31, 411–31, 419.

APPENDIX B : SUPPLEMENTARY MATERIAL FOR CHAPTER 3

B.1 Introduction

This appendix provides auxiliary material to chapter 3. Specifically, sample location map of southern Michigan (Figure B1), mean climate summary for Ann Arbor, MI (Figure B2) along with measured noble concentrations and Helium isotope ratios (Table B1) are included. In addition, detailed weather data description for individual rainfall events collected in this study is presented in section B2 along with hourly surface weather station observations included in Table B2. In addition, various weather data products including area forecast discussions for samples nr1, 2, 6 and 12 (section B3), surface analysis maps for nr1, 6, 10 (Figures B3-B5), Doppler radar image for nr2 (Figure B6), SkewT-log P plot of weather balloon measurements for samples nr1, 6, 11 and 12 (Figure B7) and surface weather observations (Figure B8) are provided.

In addition, section B4 discusses in detail diffusive mass transfer of noble gases in a raindrop along with a description of raindrop size estimation. Results of raindrop size estimation are presented in Table B3 along with a plot of terminal velocity as a function of raindrop size (Figure B9) and a plot of noble gas diffusive equilibrium in a raindrop of radius 0.1mm and 5mm (Figure B10). In addition, calculation of the time taken for measured noble gas disequilibrium patterns in rainfall to re-equilibrate at the surface is provided in section B5.

B.2 Detailed weather data description for individual rainwater samples

B.2.1 Introduction to weather products

For each of the precipitation events associated with our sampling collection multiple weather products were analyzed to provide a detailed characterization of each one of these events. Detailed weather information for each sample include: a) synoptic scale weather patterns such as movement of cold/warm fronts and location of high/low pressure ridges/troughs; b) precipitation characteristics such as rainfall intensity (light, moderate, heavy rainfall), presence or absence of thunder, hail, fog; and c) probable condensation altitudes.

Synoptic scale weather features were obtained using surface analyses maps based on station observations issued every three hours by the Hydrometeorological Prediction Center (archived at http://www.hpc.ncep.noaa.gov/html/sfc_archive.shtml). Figures B3, B4 and B5 show examples of such maps corresponding to rainfall events during collection of samples nr1, 6, and the two samples 10-1 and 10-2. Similar maps are used to describe weather features in detail for each rainfall event during collection of all samples (cf., section B.2.2 below). Description of various fronts and boundaries shown on the maps are available at the National Weather Service glossary (http://www.nws.noaa.gov/glossary/). Synoptic scale weather pattern descriptions obtained through surface analysis maps were crosschecked with area forecast discussions issued by the National Weather Service for the Detroit/Pontiac region (archived at http://mesonet.agron.iastate.edu/wx/afos/list.phtml). Section B.3 provides examples of unedited area forecast discussions that are most up to date prior to precipitation events of samples nr1, 2, 6 and 12. Precipitation characteristics for each sampling event were

derived from available surface weather station observations. All weather station records were obtained from the Integrated Surface Hourly database published by the National Climatic Data Center (NCDC; http://gis.ncdc.noaa.gov/web/ish.html). Because an hourly weather station is not available in Milan, MI, the closest available weather stations (cf. Fig. B6) located in Ann Arbor (~15 kms; NCDC WBAN station number: 725374), Willow Run (~19 kms; NCDC WBAN station number: 725376) and Custer (~27 kms; NCDC WBAN station number: 725418) were used to derive precipitation characteristics in Milan. Individual weather station records used for each sampling event are shown in Table B1. All weather records relevant to a particular precipitation event are included in Table B2. Data description for each column in Table B2 including units, abbreviations and weather codes are provided in detail by NCDC (http://hurricane.ncdc.noaa.gov/cdo/3505doc.txt). It should be noted that weather data from a particular weather station was utilized only after ensuring that the specific storm passed through both the sampling location and appropriate weather station at the precise time of sampling by analyzing archived Doppler radar images (available every 5 minutes) for southeast Michigan (NEXRAD available at http://www.ncdc.noaa.gov/oa/radar/radarresources.html). Figure B6 shows an example of a Doppler radar image for the precipitation event during collection of sample nr2. Similar images were obtained for all other samples using the same archive. Condensation altitudes for each sample were estimated from available weather balloon (sounding) data at Detroit, MI (42.695˚N, -83.467˚W; Fig. B1). Similar to weather station records, sounding data from Detroit for a particular rain event was utilized only after ensuring that the specific storm passed through both the sampling location and Detroit (~80 kms and ~70 kms from Milan and Ann Arbor, MI, respectively) at the precise time of sampling by analyzing archived

Doppler radar images for southeast Michigan. Sounding data is available twice daily (at 0 and 12 UTC (Coordinated Universal Time)) from the NOAA/ESRL Radiosonde database (esrl.noaa.gov/raobs) and is plotted in the form of SkewT-logP plots (http://RUCsoundings.noaa.gov), which is a vertical snapshot of temperature, dew point and winds above a point on Earth. Further information about radiosonde (weather balloon) data and SkewT-log P plots is available at the Federal Meteorological handbook at www.ofcm.gov/fmh3/text/default.htm. Figure B7 shows examples of SkewT-log P plots corresponding to samples nr1, 6, 11 and 12. Probable condensation altitudes can be estimated as those altitudes in the SkewT-log P plot at which measured temperature (red lines, Fig. B7) is similar to the dew point (blue line, Fig. B7). This is discussed in detail in section B2.2.

Weather data descriptions obtained by simultaneously analyzing all the above weather products for individual rain events during collection of each sample are provided below. As mentioned above, weather products are available only at specific hours that may or may not necessarily correspond to the precise time of our sampling event (Table B1). However, weather descriptions provided below utilize the most recently available weather products prior to the sampling event and represents our best attempt at describing the weather patterns at the time of sampling. Nevertheless, synoptic weather patterns and precipitation characteristics collectively derived clearly seem to differ vastly between mass independent (nr1, 8, 12, 14) and mass dependent samples as described below. A brief summary comparing the distinct weather patterns observed for mass dependent and mass-independent samples is also provided (Section B4).

B.2.2 Detailed description of weather information for Mass-Independent samples

B.2.2.1 Sample nr1

The surface analysis map (Fig. B3) indicates the presence of a low-pressure trough in the Ohio valley producing precipitation in southeast Michigan. Similar synoptic scale weather patterns were identified in the area forecast discussion (cf. section B3). Surface weather records at Ann Arbor indicate the presence of mist/fog, light to moderate rain and low cloud ceiling heights (~300m) through both manual and automated observations between 15:12 UTC and 15:53 UTC when the sample was collected (Table B2, Figure B8). Available temperature and dew point sounding at 12 UTC visualized in the SkewT-log P plot (Fig. B7) indicates that condensation can occur between ~300m and ~3kms (1000ft and 10,000ft) and probably at higher altitudes (e.g., 3.6kms or ~12,000ft) where air temperatures are below 0˚C. This suggests that in addition to the low clouds/fog observed through surface observations, condensation originating as ice/ice melt from higher condensation altitudes are definitely likely.

B.2.2.2 Sample nr8

The surface analysis map at 18 UTC indicates the presence of a low-pressure trough across the lower peninsula of Michigan. Between 18:34 UTC and 19:34 UTC when nr8 was collected, surface weather observations at Custer weather station indicates the presence of intermittent rain and mist (cf. Table B2). The presence of fog/mist and low altitude clouds was also predicted in the area forecast discussion. SkewT-log P plots of temperature and dew point sounding data at 12 UTC and 24 UTC on August 6th, 2011 indicates the probability of multiple condensation levels in addition to the presence of low altitude clouds. Some of these condensation levels occur at altitudes where temperatures are below 0˚C suggesting that

condensation originating as ice/ice melt are likely.

B.2.2.3 Sample nr12

Area forecast discussion and surface analyses maps at 6 UTC and 9 UTC show that precipitation collected at 7:50 UTC is associated with an upper level low pressure system ahead of a warm front moving in to southern Michigan from the southwest. Surface weather station at Custer observed light continuous rain at 7:53 UTC. While the presence of fog was not reported at this weather station, area forecast discussions had predicted the presence of fog (cf. section B3). In addition, surface temperature and dew points were the same during the period of sample collection indicating the presence of low-altitude clouds/fog (cf. Fig. B8). SkewT-log P plots of temperature and dew point sounding data at 0 UTC and 12 UTC also indicate that low altitude clouds are likely (cf. Fig. B7). In addition, SkewT-log P plots also indicate condensation levels at higher altitudes (~4.5 kms or ~15,000 ft) where temperatures are below 0˚C suggesting that condensation originating as ice/ice melt is likely.

B.2.2.4 Sample nr14

Similar to other samples with mass-independent patterns, both the surface analysis map at 15 UTC and the area forecast discussion suggest that this precipitation event was due to the presence of a low pressure trough south of Michigan in the Ohio Valley. Surface weather records at the Ann Arbor weather station at 15:10 UTC indicates continuous, moderate rain with the presence of mist identified both manually and through automated observations. Low cloud ceiling heights (less than 300m) were observed at the Ann Arbor weather station and previously predicted in the area forecast discussions. However, sounding data is not available for this precipitation event because NEXRAD images do not indicate that the storm passed through both Detroit and Milan at the time of sample collection. Thus,

likely condensation altitudes could not be predicted for this sample.

B.2.3 Detailed description of weather for mass dependent samples

B.2.3.1 Sample nr2

Area forecast discussion and NEXRAD images (Fig. B6) for this precipitation event indicate the occurrence of an isolated thunderstorm due to lake breeze interactions. This isolated thunderstorm misses all available weather stations at the time of sample collection (Fig. B6). Thus, precipitation characteristics and condensation altitudes could not be derived for this sample.

B.2.3.2 Samples nr3-1, nr3-2 and nr4-1, nr4-2

Area forecast discussions predict the occurrence of thunderstorm clusters during the eastward movement of a mesoscale convective complex across southern Michigan during sample collection of nr3-1, 3-2 followed by a second upper level disturbance igniting additional thundershowers during collection of nr4-1, 4-2. While the storm passes through Custer weather station, cloud ceiling height and precipitation characteristics observations were not recorded during the time of sample collection of nr3-1, -2 (cf. Table B1, B2). However, during sample collection of nr4-1, 4-2, the Ann Arbor weather station (cf. Table B2), through which the storm passes, recorded moderate to heavy rain with showers of hail between 21:53 UTC and 22:05 UTC. In addition, SkewT-log P plot at 0 UTC corresponding to nr4-1, 4-2 suggest the presence of multiple condensation levels including at altitude of ~4.5km (~15,000 ft) where temperatures are below 0˚C suggesting that condensation

originating as ice/ice melt is likely.

B.2.3.3 Samples nr5-1 and nr5-2

Surface analyses and area forecast discussions indicate initially a stationary front followed by an advancing warm front that moves east from northern Illinois to southern Michigan bringing with it a thunderstorm complex. Precipitation characteristics recorded at the Ann Arbor weather station initially indicate continuous, moderate rain and mist followed by heavy rain, thunderstorms and hail showers (Table B2). The heavy rain is also captured by the Doppler radar images for these precipitation events. SkewT-log P plot created with temperature and dew point measurements from weather balloons at 0 UTC on July 28th, 2011 indicate that condensation altitudes up to ~4.5kms (~15000 ft) are likely. Because temperatures are ~0˚C at these altitudes, condensation originating as ice/ice melt is probable.

B.2.3.4 Sample nr6

Both the surface analysis map (Fig. B4) and area forecast discussion suggest that this precipitation event occurs due to convection along a stationary front that is positioned in a southwest-northeast direction across the lower peninsula of Michigan. Area forecast discussions further suggest the likelihood of numerous thunderstorms in southeast Michigan. Indeed, surface weather observation at Ann Arbor indicates moderate to heavy rain with showers of hail between 8:13 UTC and 8:51 UTC when sample nr6 was collected (Table B2). In addition, SkewT-log P plot at 0 UTC and 12 UTC (Fig. B7) suggest the presence of multiple condensation levels including altitudes of 1.2km, 2.1km, 4.5km and 6km (or 4000ft, 7000ft, ~15,000ft and 20,000ft). Measured temperatures are below 0˚C above ~4.5 km (red

line, Fig. B7) suggesting that condensation originating as ice/ice melt is likely.

B.2.3.5 Sample nr7

Surface analysis and area forecast discussions suggest heavy rainfall and thunderstorms produced by instability in southern Michigan as indicated by a stationary front. The presence of heavy rain at the time of sample collection is also indicated by Doppler radar images and confirmed by surface weather observations at the Ann Arbor weather station which record heavy rain with hail showers at 7:13 UTC, close to the sample collection instant (Table B2). In addition, cloud base heights recorded at these very same surface weather stations are high (between 1.2km and 2.4km or 4200ft and 8000ft) and suggest multiple condensation levels. Multiple condensation levels at ~1.5km, 3km, 4.5km and 5.4km (or 5000ft, 10,000ft, 15,000ft and 18,000ft) are also evident through SkewT-log P plots at 0 UTC. Condensation at altitudes higher than ~4.5kms where temperatures are below 0˚C suggest that precipitation originating as ice/ice melt is likely.

B.2.3.6 Samples nr9 and nr10-1, 10-2

Surface analysis indicates the movement of a warm front across southern Michigan in a northeast direction producing strong upper level moisture advection generating heavy rain and thunderstorms as also described in the area forecast discussions for nr9. This is followed by a cold front associated with a low pressure system over Ontario, which sweeps across southern Michigan from west to east bringing with it showers and thunderstorms during which nr10-1 and 10-2 are collected (Fig. B5). Surface weather observations in Ann Arbor also indicate moderate to heavy rainfall with thunderstorms and hail showers between 9:33

UTC and 9:36 UTC when nr9 was collected (Table B2). While thunder with rain is reported in the surface analysis map ahead of the cold front during nr10-1 and nr10-2 sample collection, surface weather data is not available at Willow Run station, through which this particular storm passes, to confirm this. However, we have physically observed thunderstorms and hail during sample collection of nr10-1 and 10-2. In addition, we observed a significant drop in temperature (2.8˚C) at the collection site between sampling of 10-1 and 10-2 suggesting that the cold front passed through Milan during that time interval. Sounding plots for both samples indicate multiple condensation level where temperatures are below 0˚C and suggests the likelihood of precipitation originating as ice/ice melt.

B.2.3.7 Sample nr11

Surface analysis map indicates a stationary front slowly moving across southern Michigan from north to south associated with a mid level storm rotating across northern Ohio bringing with it rain and thunderstorms as indicated in the area forecast discussion. Surface weather station at Ann Arbor does not report any particular precipitation characteristic during sample collection (Table B2). Similar to all other samples, multiple condensation levels below 0˚C are possible as indicated by SkewT-log P plots (Fig. B7) suggesting the likelihood of precipitation starting as ice.

B.2.3.8 Sample nr13

Surface analyses maps indicate a stationary front positioned across southern Michigan, which then moves as a cold front across the Lower Peninsula. Area forecast discussion indicates that this will bring clusters of thunderstorms to southeast Michigan. These are

confirmed by surface weather observations at Ann Arbor, which record heavy rain, thunderstorms and showers of hail (Table B2). In addition, sounding plots point to multiple condensation levels and the presence of condensation altitudes below 0˚C.

B.2.4 Summary of weather analyses for mass-independent and mass-dependent samples

Our detailed weather analyses above indicate that all rain samples with mass-independent patterns were collected during precipitation due to the presence of a low-pressure system in the area. Weather records for all samples with mass-independent patterns, without exception, indicate that corresponding precipitation events can be characterized by the presence of fog/mist, light to moderate rain and low cloud ceiling heights (~300m). By contrast, samples with mass-dependent patterns were collected during energetic thunderstorms due either to a stationary front (e.g., nr6), cold front (e.g., nr10-1/10-2) or warm front (e.g., nr9). Surface weather stations confirm this by recording heavy rain, thunderstorms and showers of hail during the time of sample collection. Of particular significance, is the fact that except for some initial fog activity during the approach of the thunderstorm during collection of sample nr5-1, no other surface weather station records the presence of fog or low-level clouds during collection of mass-dependent samples. In addition, all samples, including those displaying mass-dependent and mass-independent patterns indicate the possibility of multiple condensation levels, including altitudes where air temperature is below 0˚C. These results suggest the likelihood of precipitation starting as ice.

B.3 Area forecast discussions for southeast Michigan corresponding to samples nr1, 2, 6 and 12

B.3.1 Introduction

Area forecast discussions (AFDs) provide information on synoptic and mesoscale weather features at the local region where the issuing weather station is located. This supplementary text collates unedited AFDs for southeast Michigan region issued by the National Weather Service in Detroit/Pontiac, MI (archived at http://mesonet.agron.iastate.edu/wx/afos/list.phtml). Because multiple AFDs are issued every day, only the most recent and up-to-date AFD prior to the date and time of rainwater sample collection are included here. For example, on May 15 2011 nr1 was sampled at 15:40 UTC (Coordinated Universal Time). AFDs were issued by the National Weather Service in Detroit/Pontiac at 1:34, 4:50, 7:30, 10:59, 17:24, 18:47 and 23:00 UTC. AFD included in this Supplementary Text corresponds to 10:59 UTC (6:59 AM, EDT) since it is the most up-to-date AFD prior to the occurrence of precipitation event nr1 sampled in this study. Below, we only include AFDs for a few samples (nr1, 2, 6 and 12) for demonstrative purposes. AFDs for all remaining samples are available at the National Weather Service archive listed above.

B.3.2 Sample Area Forecast Discussions

B.3.2.1 Sample nr1

480 FXUS63 KDTX 151059 AFDDTX AREA FORECAST DISCUSSION NATIONAL WEATHER SERVICE DETROIT/PONTIAC MI 659 AM EDT SUN MAY 15 2011

.AVIATION...

WIDESPREAD IFR BASED STRATUS WILL START THE TAF PERIOD AT MANY OF THE TAF SITES. HOWEVER...DRIER AIR BELOW 3K FEET WILL SLOWLY BE ADVANCING IN FROM THE NORTH WHICH HAS ALREADY ADVECTED IN AT MBS. THIS WILL LEAD TO A SLOW BUT STEADY INCREASE IN CEILING HEIGHTS FROM NORTH TO SOUTH DURING THE COURSE OF THE MORNING AND AFTERNOON. THIS WILL OCCUR DESPITE THE INCREASING COVERAGE OF RAINFALL. A STRONG NORTHEASTERLY PRESSURE GRADIENT WILL CONTINUE TO LEAD TO GUSTY WINDS...ESPECIALLY AT MBS WHERE FUNNELING DOWN SAGINAW BAY IS LEADING TO SOME LOCALLY STRONGER WINDS UP TO 40 KNOTS. THE RAIN SHOULD END AT ALL OF THE TAF SITES DURING THE EVENING HOURS WITH VFR CONDITIONS EXPECTED AS LOW PRESSURE PUSHES EAST TOWARDS THE ATLANTIC SEABOARD.

&&

.PREV DISCUSSION...ISSUED 332 AM EDT SUN MAY 15 2011

SHORT TERM...TODAY

A LOW PRESSURE SYSTEM OVER THE EASTERN OHIO VALLEY WILL BEGIN ITS TRACK EASTWARD TOWARDS THE ATLANTIC SEABOARD TODAY. BEFORE IT

MOVES OFF TO THE EAST SHOWERS ARE EXPECTED TO CONTINUE ACROSS MUCH OF THE AREA TODAY UNDER AN 850-500MB DEFORMATION ZONE ON THE COLD SIDE OF THIS LOW. DRY AIR IN PLACE ACROSS THE NORTHERN GREAT LAKES WILL BEGIN TO SINK SOUTHWARD AS THE LOW DEPARTS...SLOWLY SHUTTING OFF THE SHOWERS FROM NORTH TO SOUTH. WHILE THE SOUTHERN CWA WILL REMAIN VERY MOIST WITH CONTINUED SHOWER ACTIVITY ALL OF TODAY...THE SAGINAW VALLEY AND NORTHERN THUMB SHOULD SEE AN END TO THE RAIN BY THE AFTERNOON HOURS AS THIS DRY AIR ADVECTS IN. THE VERY TIGHT PRESSURE GRADIENT ON THE NORTH SIDE OF THIS LOW HAS CREATED VERY GUSTY WINDS ACROSS LAKE HURON EARLY THIS MORNING. THESE WINDS HAVE FUNNELED DOWN SAGINAW BAY AND CHANNELED THESE STRONG WINDS INTO THE SAGINAW VALLEY WITH WIND GUSTS REACHING 50 MPH AT TIMES. WITH THIS FLOW EXPECTED TO LAST FOR MUCH OF TODAY HAVE ISSUED A WIND ADVISORY FOR BAY AND MIDLAND COUNTIES WITH FREQUENT GUSTS OF 40 TO 50 MPH EXPECTED MUCH OF TODAY. WINDS WILL DIE DOWN LATER THIS AFTERNOON AS THE LOW DEPARTS AND WINDS SHIFT TO THE NORTH WITH A LOOSER PRESSURE GRADIENT. WILL TAKE THE ADVISORY THROUGH 4 PM AND CANCEL EARLIER IF WINDS DROP BELOW ADVISORY CRITERIA SOONER. WITH THE REGION ON THE COLD SIDE OF THE LOW PRESSURE SYSTEM AND CLOUDY RAINY CONDITIONS EXPECTED FOR MUCH OF THE DAY WITH MIXING HEIGHTS ONLY TO 925MB THE DIURNAL TEMPERATURE RANGE SHOULD NOT BE VERY LARGE AS HIGHS WILL ONLY BE A FEW DEGREES

WARMER THAN MORNING LOWS.

LONG TERM...

COOL AND BRISK START TO THE WORK WEEK. EXPANSIVE UPPER LEVEL RIDGE AND SURFACE HIGH PRESSURE OVER CENTRAL CANADA WILL DRIFT TO THE SOUTH OVER THE NEXT 48 HOURS AND ENOUGH DRY AIR IS EXPECTED TO FILTER INTO SOUTHEAST MICHIGAN TO ALLOW FOR A DRY MONDAY...AS WEAKENING 500 MB LOW LIFTS NORTH FROM THE EASTERN OHIO VALLEY. SHOWERS WILL LIKELY BE CLOSE BY HOWEVER...ALONG THE US/CANADIAN BORDER. 850 MB TEMPS NOW PROGGED TO FALL SLIGHTLY BELOW ZERO DURING MONDAY...SETTING UP A COLD NIGHT MONDAY NIGHT...IN ADDITION TO TONIGHT. IT APPEARS PRESSURE GRADIENT WILL BE TOO STRONG TO ALLOW WINDS TO DECOUPLE (ESPECIALLY WITH NORTHEAST FLOW OFF LAKE HURON)...AND ALTHOUGH WE ARE LIKELY LOOKING AT MINS IN THE MID 30S ACROSS A PORTION OF SOUTHEAST MICHIGAN...NOT PLANNING ON MENTIONING ANY FROST WITH THE WIND STAYING UP. PLUS...THIS IS NO GUARANTEE CLOUDS ARE GOING TO FULLY CLEAR OUT TONIGHT...AND CLOUDS WILL LIKELY BE RETURNING FOR MONDAY NIGHT. LATEST TRENDS FOR THE SHEARED OUT ENERGY OVER THE DAKOTAS/IOWA IS TO DIVE SOUTHEAST...MUCH FARTHER SOUTH...WITH THE CENTER OF THIS SHORTWAVE HOVERING AROUND FAR EASTERN TENNESSEE OR EVEN NORTHERN GEORGIA MONDAY/TUESDAY. NONE-THE-LESS...THE LARGE SCALE UPPER LEVEL LOW/TROUGH IS QUITE EXTENSIVE...AND GOOD

TAP OF ATLANTIC MOISTURE IS STILL PROGGED TO ADVANCE WESTWARD INTO THE CENTRAL GREAT LAKES ON TUESDAY...WITH LEAD SURGE OF LOW LEVEL WARM ADVECTION...AS 850 MB TEMPS FORECASTED TO CLIMB INTO THE MID SINGLE NUMBERS. BETTER UPPER LEVEL FORCING AS WE HEAD INTO THE MID WEEK PERIOD...AS THE MID/UPPER LEVEL CIRCULATION ADVANCES NORTH INTO THE WESTERN MID ATLANTIC STATES. THE GOOD NEWS IS AN UPPER LEVEL RIDGE IS FORECASTED (PER 00Z GFS/EUROPEAN) TO BUILD INTO THE GREAT LAKES REGION AS WE HEAD INTO THE WEEKEND...SUPPORTING A QUICK WARM UP...WITH TEMPERATURES POTENTIALLY BACK TO 80 DEGREES BY SATURDAY. $$ MARINE... THE PRESSURE GRADIENT WILL CONTINUE TO TIGHTEN AS LOW PRESSURE LIFTS THROUGH THE OHIO VALLEY TO WESTERN PENNSYLVANIA BY MORNING AND HIGH PRESSURE SHIFTS SLOWLY SOUTHEAST TOWARDS THE REGION. THIS SETUP WILL PROVIDE A PROLONGED PERIOD OF NORTHEASTERLY FLOW...WHICH WILL PEAK EARLY THIS MORNING...BUT PERSIST TO SOME DEGREE INTO EARLY NEXT WEEK AS THIS LOW PRESSURE SYSTEM STALLS NEAR THE APPALACHIAN RANGE. NORTHEAST WINDS ARE STILL GUSTING TO GALE FORCE DUE TO THE FUNNELING EFFECT UP SAGINAW BAY AND EXPECT WINDS SPEEDS TO REMAIN AT THESE LEVELS THROUGH THE AFTERNOON HOURS...THEREFORE WILL RETAIN THE GALE WARNING THROUGH ITS CURRENT EXPIRATION. WILL ALSO MAINTAIN THE SMALL CRAFT ADVISORIES FOR THE REMAINDER OF THE LAKE HURON NEAR SHORE WATERS AS WIND SPEEDS SHOULD GENERALLY PEAK CLOSER TO 30 KNOTS

WITHOUT THE HELP OF FUNNELING. FOR THE SAME REASON...WILL CONTINUE TO FORGO A GALE WARNING FOR THE OPEN WATERS AS WINDS GENERALLY REMAIN IN THE LOWER 30 KNOT RANGE. WILL KEEP THE SMALL CRAFT ADVISORIES FOR LAKE ST CLAIR AND FAR WESTERN LAKE ERIE TODAY AS STRONGER NORTHEAST FLOW PENETRATES INTO THESE AREAS AS THE AFOREMENTIONED LOW PRESSURE MOVES EAST OF THE CENTRAL LAKES REGION. WITH THIS LONG PERIOD OF NORTHEAST/NORTH WINDS...WAVES WILL BUILD TO 10 FEET OR MORE OVER PORTIONS OF LAKE HURON TONIGHT INTO SUNDAY AND THEN REMAIN HIGH FOR SEVERAL DAYS THEREAFTER && .DTX WATCHES/WARNINGS/ADVISORIES... MI...WIND ADVISORY...MIZ048-MIZ053...UNTIL 4 PM SUNDAY. LAKE HURON... GALE WARNING...SAGINAW BAY AND THE NEARSHORE WATERS FROM PORT AUSTIN TO HARBOR BEACH...UNTIL 4 PM SUNDAY. SMALL CRAFT ADVISORY...NEARSHORE WATERS FROM HARBOR BEACH TO PORT HURON...UNTIL 8 AM MONDAY. LAKE ST CLAIR... SMALL CRAFT ADVISORY...UNTIL 10 PM SUNDAY. MI WATERS OF LAKE ERIE...SMALL CRAFT ADVISORY...UNTIL 10 PM SUNDAY. && $$ AVIATION.....KURIMSKI SHORT TERM...KURIMSKI LONG TERM....SF MARINE.....KURIMSKI YOU CAN OBTAIN YOUR LATEST NATIONAL WEATHER SERVICE FORECASTS ONLINE AT WWW.WEATHER.GOV/DETROIT (ALL LOWER CASE).

B.3.2.2 Sample nr2a, nr2b

540

FXUS63 KDTX 032319

AFDDTX

AREA FORECAST DISCUSSION

NATIONAL WEATHER SERVICE DETROIT/PONTIAC MI

719 PM EDT SUN JUL 3 2011

.AVIATION...

//DISCUSSION...

JUST EXPECT A FEW SHOWERS TO DOT THE AREA FROM DET/DTW SOUTH AS LAKE BREEZES INTERACT AND HELP RELEASE MINOR LOW LEVEL INSTABILITY FROM DAYTIME HEATING TODAY. OTHERWISE...VFR CONDITIONS ARE EXPECTED WITH LIGHT WINDS AS HIGH PRESSURE REMAINS IN PLACE OVER FROM THE CENTRAL GREAT LAKES TO UPPER MIDWEST.

FOR DTW...MAY SEE AN ISOLATED SHOWER OR TWO EARLY IN THE FORECAST PERIOD AS LAKE BREEZE INTERACTIONS CONTINUE TO PRODUCE LOCALLY ENHANCE LOW LEVEL CONVERGENCE OVER THE REGION.

//DTW THRESHOLD THREATS...

* LOW CONFIDENCE OF CEILINGS AROUND 5000 FEET EARLY IN THE FORECAST FROM ISOLATED SHOWERS.

&&

.PREV DISCUSSION...ISSUED 336 PM EDT SUN JUL 3 2011

SHORT TERM...TONIGHT

MUCH NICER DAY TODAY WITH HIGHS SOLIDLY IN THE 80S ALONG WITH LOWER HUMIDITY. 24 HR CHANGE IN TEMP/DEW PT AVERAGING 10 DEGREES LOWER.

AGITATED BUT DISORGANIZED AND HIGH BASED CU FIELD OVER THE SOUTH HALF OF THIS AFTERNOON AND CANT TOTALLY RULE OUT ISOLATED SHOWER/THUNDERSTORM OVER THE NEXT COUPLE OF HOURS WITH MLCAPES OF 400 TO 800 J/KG...BUT WITH MEAGER SURFACE/LOW LEVEL CONVERGENCE AROUND AND SURFACE DEW PTS EXPECTED TO DROP WITH FURTHER MIXING/ADVECTION PROCESSES...WILL LEAVE THE MENTION OUT. SKIES WILL THEN TREND TO MOSTLY CLEAR/CLEAR OVERNIGHT AS HIGH PRESSURE CONTINUES TO WORK ITS WAY IN FROM THE WEST. FAVORABLE RADIATING NIGHT SHOULD ALLOW FOR A GOOD PORTION OF THE CWA TO

SNEAK INTO THE 50S...WITH WARMER URBAN AREAS IN THE LOWER 60S.

LONG TERM...MONDAY THROUGH NEXT SUNDAY

HIGH PRESSURE WILL BE IN CONTROL OF THE WEATHER FOR THE 4TH OF JULY HOLIDAY. THE HIGH WILL PROVIDE MOSTLY CLEAR SKIES AND LIGHT WINDS AS HIGH TEMPERATURES CLIMB INTO THE 80S. THIS HIGH PRESSURE SYSTEM WILL SLOWLY SINK SOUTH MONDAY NIGHT...AS A LOW PRESSURE SYSTEM TRACKS THROUGH THE GREAT LAKES REGION TUESDAY AND WEDNESDAY. ALTHOUGH RAIN IS NOT EXPECTED ON TUESDAY...THE EFFECTS OF THE APPROACHING LOW WILL STILL BE APPARENT WITH WARMER TEMPERATURES AS WINDS TURN TO THE SOUTHWEST AND INCREASING CLOUDS FROM THE APPROACHING COLD FRONT FROM THE NORTH.

THE FRONT ITSELF IS A RATHER WEAK FEATURE...HOWEVER THE SHORTWAVE COINCIDENT WITH THE FRONT WILL BE THE MAIN DRIVING FORCE BEHIND THE SHOWER AND THUNDERSTORM ACTIVITY TUESDAY NIGHT AND WEDNESDAY. CURRENT MODEL RUNS ARE IN FAIRLY GOOD AGREEMENT ON THE TIMING OF THE ACTIVITY...WITH VERY LITTLE ADJUSTMENT FROM THE PREVIOUS FORECAST.
THE BEST CHANCE FOR RAIN WILL BE ON WEDNESDAY AS THE SHORTWAVE TAKES ADVANTAGE OF MLCAPE VALUES AROUND 1 J/G. DESPITE THE CAPE

VALUES...THE WIND FIELD IS EXPECTED TO BE RATHER WEAK WITH NOT MUCH SHEAR TO SPEAK OF AND FREEZING LEVELS ARE FORECAST TO BE AROUND 13K FT SO SEVERE WEATHER DOES NOT LOOK TO BE A BIG ISSUE AT THIS POINT.

THE MODEL DATA CONTINUES TO LINGER A WEAKER SHORTWAVE ACROSS THE EXTREME SOUTHEASTERN CWA WEDNESDAY EVENING...WARRANTING THE CONTINUATION OF POPS DURING THIS PERIOD. HOWEVER HIGH PRESSURE WILL QUICKLY BUILD IN BEHIND THE DEPARTING FRONT LATER WEDNESDAY NIGHT...PROVIDING DRY AND SLIGHTLY COOLER WEATHER ON THURSDAY.

A SURFACE HIGH OF 1019MB WILL BE CENTERED OVER THE GREAT LAKES FOR FRIDAY AND SATURDAY LEADING TO DRY WEATHER AND TEMPERATURES VERY CLOSE TO THE CLIMO NORMS. NWP GUIDANCE IS MOSTLY WITHIN 3 DEGREES...SO WENT WITH AN OVERALL BLEND OF MOS GUIDANCE. MID RUN GFS
DOES SHOW A WEAK SHORTWAVE MOVING THROUGH MICHIGAN ON SATURDAY THAT COULD SPARK SOME CONVECTIVE SHOWERS...BUT 12Z HAS SINCE SQUASHED THAT NOTION AND WILL PROBABLY JUST GET BY WITH SOME AFTERNOON CU.

MARINE...

TRANQUIL CONDITIONS WILL PERSIST ACROSS AREA WATERS FOR THE REMAINDER OF THE HOLIDAY WEEKEND WITH WINDS EXPECTED TO RANGE FROM 5 TO 10 KNOTS FOR MOST AREAS THROUGH AT LEAST WEDNESDAY WHEN THE A FRONT WILL BRING A BRIEF INCREASE IN WINDS AND THE NEXT CHANCE FOR THUNDERSTORMS LATE TUESDAY INTO WEDNESDAY.

&&

.DTX WATCHES/WARNINGS/ADVISORIES...

MI...NONE.

LAKE HURON...NONE.

LAKE ST CLAIR...NONE.

MI WATERS OF LAKE ERIE...NONE.

AVIATION.....DG

SHORT TERM...SF

LONG TERM....KURIMSKI/MM

MARINE.....SF

B.3.2.3 Sample nr6
043

FXUS63 KDTX 290734

AFDDTX

AREA FORECAST DISCUSSION

NATIONAL WEATHER SERVICE DETROIT/PONTIAC MI

334 AM EDT FRI JUL 29 2011

.SHORT TERM...TODAY

AREAS OF CONVECTION CONTINUE TO FLARE UP ALONG A STALLED FRONTAL BOUNDARY STRETCHING ACROSS THE WESTERN AND CENTRAL GREAT LAKES THIS MORNING. THIS IS BEING ENHANCED BY A COMBINATION OF A MID-LEVEL MCV AND BY A NOCTURNAL LOW-LEVEL JET WHICH IS NOSING UP INTO MICHIGAN. NUMEROUS THUNDERSTORMS ARE EXPECTED SOUTH OF I-69 EARLY THIS MORNING...WITH ACTIVITY STRETCHING FROM SOUTHEAST MICHIGAN BACK TOWARDS THE CHICAGO AREA (THE LATTER OF WHICH WILL AFFECT SOUTHERN LOWER MICHIGAN LATER THIS MORNING). GOOD ELEVATED INSTABILITY LOOKS PRESENT ACROSS THIS AREA PER MODEL CROSS-SECTIONS AND FORECAST SOUNDINGS...POTENTIALLY SUPPORTING UPDRAFTS STRONG ENOUGH FOR STORMS TO BECOME SEVERE. OTHER BIG CONCERN IS THE POTENTIAL FOR FLASH FLOODING AS STRONGER STORMS MAY PRODUCE RAINFALL RATES BETWEEN 1 AND 2 INCHES PER HOUR. MUCH OF THIS RAIN WILL FALL OVER GROUND THAT REMAINS SATURATED FROM RAIN LAST NIGHT.

COLD FRONT WILL DROP ACROSS LOWER MICHIGAN LATER THIS MORNING AS A MID-LEVEL TROUGH PUSHES ACROSS ONTARIO. THIS WILL PUSH SHOWERS AND THUNDERSTORMS OUT OF THE AREA BY LATE AFTERNOON AND ALLOW DEWPOINTS TO FALL SLIGHTLY. THIS FRONT WILL HOWEVER DO LITTLE TO COOL TEMPERATURES.

&&

.LONG TERM...FRIDAY NIGHT THROUGH NEXT WEEK

THE LOW TO MID LEVEL FLOW IS FORECAST TO BE MORE NORTHWESTERLY BY TONIGHT IN THE WAKE OF THE DEPARTING MID LEVEL SHORT WAVE. THIS WILL HELP ADVECT THE MUCH DRIER AIRMASS NOW OBSERVED OVER NORTHERN MINNESOTA INTO SOUTHERN MICHIGAN DURING THE COURSE OF THE NIGHT...ENDING THE RISK FOR ANY ADDITIONAL RAINFALL. WEAK HIGH PRESSURE AND MUCH DRIER AIR WILL BECOME ESTABLISHED OVER SE MI BY SATURDAY...WHICH WILL LEAD TO SUNNY SKIES WITH MORE COMFORTABLE HUMIDITY LEVELS. DESPITE SOME WEAK LOW LEVEL COLD AIR ADVECTION TONIGHT...MODEL SOUNDINGS SUGGEST AMPLE DAYTIME INSOLATION WILL SUPPORT DEEP MIXING HEIGHTS SAT AFTERNOON. THIS SUPPORTS LEANING TOWARD THE HIGH END OF GUIDANCE MAX TEMPS...UPPER 80S TO NEAR 90 WITH SOME MARINE MODIFICATION KEEPING THE THUMB REGION A TOUCH

COOLER.

THE ELONGATED UPPER RIDGE NOW OVER THE SOUTHERN US IS FORECAST TO RETROGRADE BACK INTO THE SOUTH-CENTRAL PLAINS DURING THE COURSE OF THE WEEKEND...WHILE A FAIRLY DEEP MID LEVEL TROUGH SLIDES INTO EASTERN CANADA. THIS WILL LEAD TO SUBSTANTIAL HEIGHT FALLS ACROSS EASTERN CANADA AND NRN NEW ENGLAND BY EARLY NEXT WEEK. ASSOCIATED WITH THIS TROUGH WILL BE A SURFACE FRONT...FORECAST TO DROP INTO SOUTHERN MICHIGAN LATE SUN INTO SUN NIGHT. THERE WILL BE A NARROW RIBBON OF DEEP LAYER MOISTURE ALONG THIS FRONT. INSTABILITY IS FORECAST TO BE SOMEWHAT MARGINAL AT THIS POINT. THE 00Z MODEL SUITE DO HOWEVER SHOW SOME EXIT REGION JET SUPPORT AND FAIRLY DIFFLUENT FLOW ALOFT...WHICH SUPPORTS THE A CHANCE OF CONVECTION LATE SUNDAY THROUGH SUNDAY NIGHT.

THE MEDIUM RANGE SOLUTIONS ALL INDICATE A STRENGTHENING MID LEVEL RIDGE OVER THE SOUTHERN/CENTRAL PLAINS NEXT WEEK...WHICH HAS BEEN THE DOMINATE PATTERN OVER MUCH OF THE SUMMER. THERE WILL BE THE POTENTIAL FOR CONVECTIVE SYSTEM ORIGINATING OVER THE NRN PLAINS/UPPER MIDWEST TO SLIDE INTO LOWER MI UNDER THE NORTHWEST FLOW. TIMING AND PROBABILITY OF THESE SYSTEMS IS QUITE LOW THIS FAR OUT. THE CURRENT FORECAST HAS THE NEXT CHANCE OF

THUNDERSTORMS ON TUES...WHICH IS IN LINE WITH THE RECENT MODEL CONSENSUS. DEPENDING ON TIMING OF ANY CONVECTIVE COMPLEXES...TEMPS ARE EXPECTED TO REMAIN ABOVE SEASONAL NORMS WITH THE GREAT LAKES REGION BEING ON THE FRINGE OF THE STRONG SUBTROPICAL RIDGE.

&&

.MARINE...

SHOWER AND THUNDERSTORM ACTIVITY SHOULD DIMINISH BY MID-AFTERNOON AS A WEAK COLD FRONT DROPS THROUGH THE AREA. HIGH PRESSURE BUILDING INTO THE REGION WILL PROVIDE DRY WEATHER AND LIGHT WINDS FROM THIS EVENING INTO SUNDAY. A COLD FRONT WILL THEN DROP THROUGH THE AREA AS LOW PRESSURE TRACKS ACROSS HUDSON BAY. THIS WILL BRING CHANCES FOR SHOWERS AND THUNDERSTORMS LATE SUNDAY AND SUNDAY NIGHT. WESTERLY WINDS ASSOCIATED WITH THE FRONTAL PASSAGE ARE EXPECTED TO REMAIN BELOW 15 KNOTS.

&&

.AVIATION...ISSUED 1252 AM EDT FRI JUL 29 2011

//DISCUSSION...

A CONVECTIVE COMPLEX WILL CONTINUE TO EVOLVE DURING THE EARLY MORNING HOURS IMPACTING THE FLINT AND PONTIAC TERMINALS MOST DIRECTLY. TRENDS LOOK PRETTY SOLID WITH THE STRONGEST ACTIVITY CONFINED NEAR THE INTERSTATE 69 CORRIDOR EARLY IN THE OVERNIGHT WITH THE PATTERN THEN DEVELOPING TO THE SOUTH AND EAST TOWARD SUNRISE BEFORE EXITING THE AREA BY MID MORNING. FOG WILL TEND TO FORM IN THE TRAILING BOUNDARY LAYER MOISTURE WITH ANY LINGERING SHOWERS AND THUNDERSTORMS MINGLED WITH A PERIOD OF MVFR CEILING ASSOCIATED WITH PASSAGE OF THE SURFACE TROUGH/FRONT. STEADY IMPROVEMENT TO VFR BY AFTERNOON IS THEN EXPECTED AS WEAK HIGH PRESSURE BUILDS INTO THE REGION TOWARD EVENING.

FOR DTW...THUNDERSTORM ACTIVITY WILL TRACK NEARBY TO THE NORTH AND WEST OF THE AIRPORT FOR MUCH OF THE NIGHT BEFORE ACTIVITY TRAILING WESTWARD TOWARD CHICAGO MOVES INTO THE REGION. RELYING ON THE TRAILING ACTIVITY TENDS TO LOWER CONFIDENCE THAT THE AIRPORT WILL BE IMPACTED BUT TRENDS WILL BE MONITORED AND TIMING REFINED DURING THE EARLY MORNING HOURS. WHILE THERE IS SOME UNCERTAINTY ON THUNDERSTORM IMPACTS, CONFIDENCE IS HIGHER ON CEILING TRENDS WITH LESS THAN 5000 FT EXPECTED WITH THE RAIN ALONG WITH A PERIOD OF MVFR CEILING ASSOCIATED WITH THE FRONTAL

PASSAGE THROUGH MID MORNING. STEADY IMPROVEMENT BACK INTO VFR IS THEN EXPECTED FOR THIS AFTERNOON.

//DTW THRESHOLD THREATS...

* MODERATE CONFIDENCE THUNDERSTORMS WILL AFFECT DTW 08Z TO 11Z.

* HIGH CONFIDENCE CEILING BELOW 5000 FT DURING THE MORNING.

&&

.PREV DISCUSSION...ISSUED 1043 PM EDT THU JUL 28 2011

CONVECTIVE TRENDS HAVE SHOWN UP STRONGLY ENOUGH SINCE THE LAST UPDATE TO SUPPORT THE CONTINUATION OF THE FLASH FLOOD WATCH, EVEN FOR METRO DETROIT. THE MCV CROSSING NORTHERN LOWER MICHIGAN WILL CONTINUE TO SUPPORT BACKED FLOW OVER SOUTHERN LOWER MICHIGAN IN THE MIDST OF THE LOW LEVEL MOISTURE AXIS WITH PRECIPITABLE WATER IN THE RANGE OF 2 TO 2.5 INCHES ACCORDING TO HOURLY MESOANALYSIS.
IF ANYTHING, COVERAGE SHOULD INCREASE AS THE MCV SUPPORTS A RAMPED UP LOW LEVEL JET AND ACCELERATED MOISTURE TRANSPORT TO THE SOUTH OF ITS TRACK AND OVER SE MICHIGAN. THIS WILL FUEL

CONVECTION STRONGLY ENOUGH FOR A FEW STORMS TO POSSIBLY APPROACH SEVERE LIMITS, AND THIS WILL BE MONITORED, BUT HEAVY RAINFALL CLEARLY REMAINS THE PRIMARY CONCERN THROUGH THE NIGHT. THE TRACK OF THE MCV AND THE POSITION OF THE LOW LEVEL THETA-E RIDGE STILL FAVOR THE SAGINAW VALLEY AND NORTHERN THUMB, AND THE NORTHERN PORTION OF THE WATCH AREA, FOR THE HEAVIEST RAINFALL BUT COVERAGE WILL BE GREAT ENOUGH TOWARD THE DETROIT AREA TO MAINTAIN THE HEADLINE.

&&

.DTX WATCHES/WARNINGS/ADVISORIES...
MI...FLASH FLOOD WATCH...MIZ053-MIZ060-MIZ061-MIZ062-MIZ063-MIZ068-
MIZ069-MIZ070-MIZ075-MIZ076-MIZ082-MIZ083...UNTIL 11 AM FRIDAY.

LAKE HURON...NONE.

LAKE ST CLAIR...NONE.
MI WATERS OF LAKE ERIE...NONE.

&&

$$

SHORT TERM...HLO

LONG TERM....SC

MARINE.....HLO

AVIATION.....BT

YOU CAN OBTAIN YOUR LATEST NATIONAL WEATHER SERVICE FORECASTS

ONLINE

AT WWW.WEATHER.GOV/DETROIT (ALL LOWER CASE).

B.3.2.4 Sample nr12

433

FXUS63 KDTX 240510

AFDDTX

AREA FORECAST DISCUSSION

NATIONAL WEATHER SERVICE DETROIT/PONTIAC MI

110 AM EDT WED AUG 24 2011

.AVIATION...

//DISCUSSION...

SHOWERS WITH SOME EMBEDDED THUNDERSTORMS WILL PERSIST THROUGH ROUGHLY DAYBREAK...ASSOCIATED WITH AN UPPER LEVEL LOW PRESSURE SYSTEM WHICH WILL BE ROTATING ACROSS LOWER MI EARLY THIS MORNING.
RECENT VAD WIND PROFILE DATA ALONG WITH 00Z MODEL SOUNDINGS INDICATE STRENGTHENING WINDS ABOVE THE NOCTURNAL INVERSION THIS MORNING...PROMPTING A MENTION OF LOW LEVEL WIND SHEAR THROUGH 13Z.
WITH THE EXPECTATION THAT AMPLE LOW LEVEL MOISTURE WILL BE IN PLACE BELOW THIS INVERSION SHORTLY AFTER DAYBREAK...WILL CONTINUE TO CARRY A BRIEF PERIOD OF MVFR BASED STRATUS LATER THIS MORNING. THERE IS A CHANCE OF STRONG THUNDERSTORMS ALONG A COLD FRONT FORECAST TO MOVE ACROSS THE REGION LATE THIS AFTERNOON/EVENING.

FOR DTW...A LITTLE MORE ROBUST INSTABILITY IS NOW FORECAST TO MOVE INTO METRO DETROIT IN THE 08Z TO 12Z TIME PERIOD...WHICH LOOKS TO GIVE DTW A GOOD SHOT AT SOME THUNDERSTORMS EARLY THIS MORNING. GUSTY SOUTH-SOUTHWEST WINDS WILL THEN DEVELOP BY AFTERNOON IN ADVANCE OF A COLD FRONT. WIND GUSTS MAY APPROACH OR EXCEED 30

KNOTS MID TO LATE WED AFTERNOON.

//DTW THRESHOLD THREATS...

* HIGH CONFIDENCE IN THUNDERSTORM CHANCES PRIOR TO 12Z.

* MEDIUM CONFIDENCE IN CLOUD BASES BELOW 5000 FT LATE THIS MORNING.

* HIGH CONFIDENCE SOUTHWEST WIND GUSTS WILL EXCEED 25 KNOTS THIS AFTERNOON.

* MEDIUM CONFIDENCE IN STRONG THUNDERSTORM DEVELOPMENT THIS EVENING.

&&

.PREV DISCUSSION...ISSUED 946 PM EDT TUE AUG 23 2011

UPDATE...

A CLUSTER OF SHOWERS AND SCATTERED THUNDERSTORMS HAVE DEVELOPED OVER SW LOWER MI OVER THE LAST COUPLE OF HOURS. THIS

CONVECTION IS A RESULT OF WARM AIR ADVECTION ON THE NOSE OF STRENGTHENING LOW LEVEL INFLOW. THIS IS ALL IN ADVANCE OF A POTENT MID LEVEL TROUGH OVER NE WISCONSIN. THIS SYSTEM WILL INVOKE PRETTY DECENT MID LEVEL HEIGHT FALLS ACROSS LOWER MI TONIGHT AS IT TRACKS EAST. CONTINUED LOW-MID LEVEL THETA E ADVECTION IN THE PRESENCE OF THIS FORCING SHOULD ALLOW DECENT COVERAGE OF SHOWERS TO CONTINUE TO PUSH EAST INTO THE FORECAST AREA DURING THE REMAINDER OF THE NIGHT. THE 00ZDTX SOUNDING SHOWED NO INSTABILITY OVER SE MI...WHICH EXPLAINS WHY THE THUNDERSTORMS HAVE THUS FAR BEEN UNABLE TO MAKE THE TRIP INTO SE MI. MID LEVEL COOLING WILL HOWEVER STEEPEN THE LAPSE RATES DURING THE COURSE OF THE NIGHT...WHICH WILL ALLOW ENOUGH ELEVATED INSTABILITY TO POSE THE RISK OF SOME THUNDERSTORM DEVELOPMENT...ESPECIALLY LATE. OVERALL...THE GOING FORECAST LOOKS IN GOOD SHAPE. THUS AN UPDATE WILL BE ISSUED STRICTLY TO REMOVE THE TIMING OF SHOWERS AS THEY ARE VIRTUALLY ON THE DOORSTEP.

PREV DISCUSSION...ISSUED 400 PM EDT TUE AUG 23 2011

SHORT TERM... TONIGHT

A BATCH OF SHOWERS AND THUNDERSTORMS HAVE BEEN IMPACTING NORTHERN ILLINOIS THROUGH MUCH OF THE DAY...SLIGHTLY

IMPACTING/DELAYING MOISTURE SURGE INTO LOWER MICHIGAN...AS SURFACE DEW PTS REMAIN IN THE COMFORTABLE MID 50S TO AROUND 60 RANGE ACROSS MOST OF SOUTHEAST MICHIGAN THROUGH 2 PM. HOWEVER...AS THUNDERSTORM COMPLEX CONTINUES TO HEAD SOUTH...SOME OF THAT DEEPER MOISTURE OVER THE MIDWEST (IOWA) WILL WORK INTO SOUTHERN LOWER MICHIGAN. MOISTURE TRANSPORT VECTORS/THETA-E FIELDS SHOW MID LEVEL MOISTURE (700 MB) ARRIVING AROUND 00Z...WITH LOW LEVEL MOISTURE (850 MB) AROUND 6Z. EXPECTATIONS ARE CONVECTION WILL RE-ORGANIZE OVER WISCONSIN LATER TODAY...CLOSE/UNDERNEATH THE MID LEVEL CIRCULATION. THIS MID LEVEL WAVE WILL BE BOOTED TO THE EAST TONIGHT...AS DYNAMIC...CLIPPER LIKE SYSTEM COMES OUT OF SOUTHERN SASKATCHEWAN. THE 850-700 MB THETA-E RIDGE AXIS LOOKS TO BE GETTING PINCHED OFF AS IT MOVES INTO OUR AREA...WITH CORRESPONDING INSTABILITY WEAKENING (SEE SHOWALTER INDICES). NONE-THE-LESS...WITH MID LEVEL CIRCULATION TRACKING OVER/CLOSE TO THE STRAIGHTS OVERNIGHT AND SUBSEQUENT MODEST HEIGHT FALLS EXTENDING SOUTH...ALONG WITH THE 850 THETA-E MOISTURE/CONVERGENCE...EXPECTING NUMEROUS SHOWERS AND EMBEDDED THUNDERSTORMS...JUST NOT AS CONCERNED WITH THE HEAVY RAIN DUE TO THE PROGRESSIVE NATURE AND LESS INSTABILITY. LEFT INHERITED MINS INTACT...MID 60S WITH THE WARM ADVECTION PATTERN AND HIGHER DEW PTS MOVING IN...IN LINE WITH LATEST MAV GUIDANCE.

LONG TERM... WEDNESDAY THROUGH NEXT TUESDAY

THANKS TO THE ACCOMPANYING SHORT WAVE, NOCTURNAL CONVECTION AND ASSOCIATED CLOUD COVER WILL BE TO OUR EAST BY MID WEDNESDAY MORNING.
THIS WILL OPEN THE DOOR ON SURFACE HEATING FOR THE NEXT ROUND OF STORMS AS THE PREFRONTAL TROUGH/COLD FRONT MOVES THROUGH SE MICHIGAN. THERE IS SOME RESIDUAL BOUNDARY LAYER MOISTURE INDICATED THAT COULD TRANSLATE INTO SOME STRATUS FOR A WHILE BUT THIS APPEARS OVERDONE IN THE MODEL DATA BASED ON SATELLITE IMAGERY OVER THE MIDWEST DURING THE MORNING. SHOULD LOW CLOUD COVER BE ABLE TO MATERIALIZE, IT WILL MIX OUT QUICKLY AS SURFACE HEATING AND SOUTHWEST WINDS RAMP UP BY AFTERNOON. SEVERE WEATHER POTENTIAL AND TIMING THEN BECOME THE MAIN PROBLEM IN THE FORECAST FOR WEDNESDAY AFTERNOON AND EVENING.

THE BIG THING, WHICH WAS DOCUMENTED THOROUGHLY IN THE EARLY MORNING FORECAST PACKAGE, IS THE INCREASE IN THE MODEL WIND FIELD AND INSTABILITY PARAMETERS FOR WEDNESDAY AFTERNOON AND EVENING. THIS HAS CARRIED OVER INTO THE 12Z FORECAST CYCLE ADDING CONFIDENCE TO THE POTENTIAL FOR SEVERE CONVECTION. THE LATEST FORECAST SOUNDINGS FROM THE NAM AND GFS SPORT 0-1KM MLCAPE OF 2000-2500 J/KG BY LATE AFTERNOON VS 1500 COMPARED TO YESTERDAYS

DATA. THIS APPEARS TO BE THE RESULT OF A BETTER HANDLE ON THE EML MIGRATING INTO THE MIDWEST FROM THE PLAINS. THERE IS ALSO CONSIDERABLY GREATER SHEAR IN THE LOW LEVELS OF THE WIND PROFILE, DUE TO EXTRA DEEPENING OF THE SURFACE LOW IN NORTHERN ONTARIO, WITH 0-3KM HELICITY RANGING FROM 250-300 M2/S2 COMPARED TO VALUES CLOSER TO 150 YESTERDAY. THE DATA IN YESTERDAY'S MODEL RUNS DEPICTED A SCENARIO SUFFICIENT FOR SEVERE WEATHER, ESPECIALLY WITH REGARD TO LINEAR CONVECTIVE MODES, BUT THE NUMBERS THAT HAVE PERSISTED INTO TODAY'S MODEL DATA INTRODUCE AN EXTRA LAYER OF POTENTIAL THAT INCLUDES SUPERCELL MODES CAPABLE OF LARGE HAIL AND TORNADO DEVELOPMENT. THE MOST CHALLENGING ASPECT OF THE FORECAST WILL BE IDENTIFYING THE TIMING AND LOCATION FOR STORM INITIATION. THIS IS COMPLICATED BY THE LOW TO MID LEVEL CAPPING INVERSION THAT DEVELOPS ON THE HEELS OF THE EARLY MORNING ACTIVITY AND STRENGTHENED BY THE INCREASING SOUTHWEST LOW LEVEL FLOW DURING THE EARLY AFTERNOON. AT THIS POINT, PREFER TO EXPECT THE CAP TO HOLD INTO THE LATE AFTERNOON/AROUND 21Z. AFTER THAT, SURFACE CONVERGENCE ALONG THE PREFRONTAL TROUGH WILL COMBINE WITH MAX TEMPS NEAR 90 AND THE APPROACH OF THE UPPER TROUGH TO INITIATE STORMS. BY THEN, HOWEVER, THE ACTIVITY WILL LIKELY DEVELOP RIGHT OVER SE MICHIGAN BEFORE MOVING OFF TO THE EAST BY MID EVENING. THIS WOULD RESULT IN VERY LITTLE ADJUSTMENT TO EARLIER EXPECTATIONS FOR SEVERE WEATHER OTHER THAN POSSIBLY

SPARING US THE MORE MATURE ASPECTS OF SQUALL LINE DEVELOPMENT IN OUR AREA.

A BROAD EXPANSE OF HIGH PRESSURE WILL THEN SETTLE OVER THE GREAT LAKES FOR THE END OF THE WEEK. THIS WILL BRING COOLER AND LESS HUMID CONDITIONS BACK INTO SE MICHIGAN FOR THURSDAY AND FRIDAY. DRY CONDITIONS WILL BE PUNCTUATED BY LOW TEMPERATURES MAKING A RUN BACK DOWN INTO THE UPPER 40S IN THE TYPICALLY COOLER LOCATIONS IN OUR AREA. THE BROAD HIGH PRESSURE SYSTEM IS ALSO SHOWN TO CONTINUE GUARDING US AGAINST MUCH MOISTURE RETURN AHEAD OF THE NEXT COLD FRONT DUE BY SATURDAY AFTERNOON.

THE LARGE SCALE PATTERN IN THE WESTERLIES IS SHOWN IN THE LATEST GLOBAL MODELS TO PRESERVE SOME TROUGHINESS IN THE UPPER LEVEL PATTERN OVER EASTERN NORTH AMERICA BY THE BEGINNING OF NEXT WEEK.
THERE IS VERY LITTLE AMPLIFICATION UPSTREAM, HOWEVER, SO WE CONTINUE TO EXPECTED A SUPPLY OF SHORT WAVES FROM THE EASTERN PACIFIC AND WESTERN CANADA INTO THE GREAT LAKES. A FAIRLY LARGE SHORT WAVE IS INDICATED IN THE GREAT LAKES AROUND MONDAY BUT WITH TIMING AND TRACK COMPLICATIONS EXPECTED BY THE PRESENCE OF "IRENE", EVEN THOUGH IT WILL REMAIN LARGELY TO OUR EAST THROUGH TUESDAY.

MARINE...

SOUTHWEST WINDS WILL BE RAMPING UP TONIGHT...BUT ESPECIALLY TOMORROW AHEAD OF A COLD FRONT...WITH FREQUENT GUSTS OF 20 TO 30 KNOTS EXPECTED ACROSS THE MARINE AREAS. A SMALL CRAFT ADVISORY HAS BEEN ISSUED FOR ALL NEARSHORE WATERS. SCATTERED THUNDERSTORMS ARE EXPECTED TO BE AROUND TONIGHT AS WARM FRONT MOVES THROUGH. THESE STORMS ARE NOT EXPECTED TO BE SEVERE. OF MORE CONCERN ARE THE THUNDERSTORMS WHICH DEVELOP ALONG THE COLD FRONT LATE TOMORROW...WHICH WILL HAVE THE POTENTIAL TO PRODUCE WINDS OF 50 KNOTS OR GREATER. WINDS BEHIND THE COLD FRONT WILL SHIFT TO THE NORTHWEST...AND WILL REMAIN STRONG OVER THE NORTH HALF OF THE LAKE HURON WEDNESDAY NIGHT INTO THURSDAY. WINDS WILL DIMINISH ON FRIDAY AS HIGH PRESSURE RETURNS.

&&

.DTX WATCHES/WARNINGS/ADVISORIES...

MI...NONE.

LAKE HURON...

SMALL CRAFT ADVISORY...NEARSHORE WATERS FROM PORT AUSTIN TO

PORT

HURON INCLUDING SAGINAW BAY...FROM 8 AM WEDNESDAY TO 8 PM WEDNESDAY.

LAKE ST CLAIR...

SMALL CRAFT ADVISORY...FROM 8 AM WEDNESDAY TO 8 PM WEDNESDAY.

MI WATERS OF LAKE ERIE...

SMALL CRAFT ADVISORY...FROM 8 AM WEDNESDAY TO 8 PM WEDNESDAY.

&&

$$

AVIATION.....SC

UPDATE.....SC

SHORT TERM...SF

LONG TERM....BT

MARINE.....SF

YOU CAN OBTAIN YOUR LATEST NATIONAL WEATHER SERVICE FORECASTS ONLINE AT WWW.WEATHER.GOV/DETROIT (ALL LOWER CASE).

B.4 Diffusive mass transfer of noble gases in a raindrop and calculation of average raindrop sizes from measured noble gases in rainwater

B.4.1 Introduction

Overall mass-dependent noble gas patterns for rainwater samples from southeast Michigan display simultaneous atmospheric He excesses and Ne, Ar, Kr and Xe depletion with respect to ASW (Fig. 3.1c). As mentioned in section 3.5, these patterns cannot originate from liquid rainwater that equilibrated at higher altitudes. Instead, they can be accounted for if precipitation originates as ice (cf. Section 3.5, Fig. 3.2). Multiple lines of weather evidence, including observations of hail during sample collection as well as examination of probable condensation altitudes (cf. Text B2) suggest that precipitation originating as ice is likely in southeast Michigan. Below, we first describe a simple mass-transfer model involving diffusion in a sphere (raindrop), which is used to investigate whether noble gas patterns in Michigan rainwater samples might originate from ice (Fig. 3.2, section 3.5). Subsequently, using this model and measured noble gas concentrations, a procedure for estimating average rain drop sizes corresponding to precipitation events for our collected rainwater samples is outlined.

B.4.2 Diffusive mass transfer in raindrop model description and calculation of isothermal equilibrium stages of noble gases in a raindrop

Diffusion of noble gases into a raindrop can be simulated using a simple mass-transfer model in a sphere. The total amount of noble gases diffusing into or out of a sphere is given by the infinite series solution [*Crank*, 1975]:

$$F_i = 1 - \frac{6}{\pi^2}\sum_{n=1}^{\infty}\frac{1}{n^2}\exp\left(-n^2\pi^2 X\right) \qquad (1)$$

or,

$$F_i = 6X^{0.5}\left\{\pi^{-0.5} + 2\sum_{n=1}^{\infty} ierfc\frac{n}{\sqrt{X}}\right\} - 3X \quad , \text{if } X<0.182873063 \quad (2)$$

where F_i is the fraction of noble gas 'i' (where, 'i'=He, Ne, Ar, Kr and Xe) transferred at any given time 't', parameter $X=Dt/a^2$, where 'a' is the radius of raindrop, 'D' is the diffusion coefficient of noble gases and 'n' is the n^{th} term of the infinite series solution. Equations (1) and (2) provide the basis to calculate diffusive mass transfer in a raindrop of a particular size. If one assumes that: a) noble gas concentrations in raindrops start as ice (see section 3.5) and; b) noble gas concentrations of ice crystals within clouds are similar to the average ice concentrations in Lake Vida, Antarctica [see section 3.5*, Malone et al.*, 2010], expected noble gas patterns as mass transfer proceeds within a raindrop starting from ice and reaching different stages of isothermal equilibrium (=1; assuming ASW at 0˚C) can be calculated (Fig. 3.2) by:

$$F_i = \frac{\left(C_m/C_{eq} - C_{ice}/C_{eq}\right)}{\left(1 - C_{ice}/C_{eq}\right)} \qquad (3)$$

where F_i is the fraction of noble gas 'i' as defined earlier (equations 1, 2), C_m, C_{eq}, C_{ice} are the measured, equilibrium and average ice noble gas concentrations. Using equation (3), model expected noble gas patterns (C_m/C_{eq}; green dotted lines, Fig. 3.2) can be calculated for various stages of equilibration (F_i values between 0-100%) using initial average ice concentrations, C_{ice}/C_{eq} equal to 1.383, 0.825, 0.097, 0.064 for He, Ne, Ar, Kr and Xe (solid

green line, Fig. 3.2; *Malone et al.*, 2010). For example, to derive the expected noble gas patterns for 50% equilibrium (green dotted lines, Fig. 3.2), C_{ice}/C_{eq} values from *Malone et al.* [2010] is used for each noble gas with F_i=0.5 in equation (3) to calculate (C_m/C_{eq}). This yields model values (C_m/C_{eq}) of 1.192, 0.913, 0.549, 0.532 and 0.525 for He, Ne, Ar, Kr and Xe respectively and is plotted as the 50% equilibrium line (green dotted lines, Fig. 3.2). Model expected noble gas patterns are similarly derived for various stages of equilibration assuming initial average ice concentrations from *Malone et al.* [2010] and F_i values between 0-100%.

B.4.3 Calculation of droplet size using measured noble gas concentrations in rainfall

In addition to calculating expected noble gas patterns for diffusive mass transfer of noble gases into a raindrop, the model described in section B.4.2, can also be used to provide a range of droplet sizes for corresponding rainfall event using measured noble gas concentrations in rainwater. Similar to the assumptions in section B.4.2, if it is assumed that: a) noble gas concentrations in raindrops start as ice and; b) noble gas concentrations of ice crystals within clouds are similar to the average ice concentrations in lake Vida, Antarctica [*Malone et al.*, 2010], the total amount of noble gases transferred (parameter F_i) can be calculated for each rainwater sample collected using equation (3). From the calculated F_i value for a given sample (equation 3), parameter X is then calculated from the inverse of F_i as follows:

$$F_i^{-1} = X = \frac{2}{\pi}\left(1 - \sqrt{1 - \left(\pi \times F_i \middle/ 3\right)}\right) - \frac{F_i}{3}, \qquad \text{if } (F_i < 0.9) \qquad (4)$$

or,

$$F_i^{-1} = X = \frac{-1}{\pi^2}\log\left(\frac{\pi^2\left(1-F_i\right)}{6}\right), \qquad \text{if } (F_i > 0.9) \qquad (5)$$

Because $X=Dt/a^2$, the time taken 't' by a specific noble gas in a raindrop of size 'a' to achieve the corresponding 'F_i' value can be calculated. Since the size of raindrop 'a' is unknown, the time required for equilibration F_i value to be achieved (parameter 't' in equations 1 and 2) for a specific sample is calculated for a range of droplet diameters between 0.019 and 10mm (red lines, Fig. 3.3) assuming diffusion coefficients for all noble gases at a temperature of 0˚C. This will yield the maximum possible equilibration times for each gas since diffusion is slowest at 0˚C (see below for values of diffusion coefficients at 0˚C). Because noble gas diffusion coefficients are only well known between 5 and 35˚C [*Jähne et al*., 1987], values at 0˚C were approximated by the following temperature dependency [*Eyring*, 1936]:

$$D_i = A_i \times \exp\left(E_a / RT\right) \qquad (6)$$

where D_i is the diffusion coefficient for noble gas 'i' (where i=He, Ne, Ar, Kr, Xe) at any temperature 'T' (ºK), 'R' is the universal gas constant of 8.314 J/K-mol, 'E_a' and 'A' are fit parameters given by *Jähne et al.* [1987]. Diffusion coefficients at 0˚C for noble gases calculated through equation (6) yield values of 4.74×10^{-9}, 2.34×10^{-9}, 1.44×10^{-9}, 0.88×10^{-9}, 0.66×10^{-9} m^2/s for He, Ne, Ar, Kr and Xe respectively. The range of equilibration times (parameter 't' in equations 1, 2) calculated from measured noble gas concentrations using the above procedure for each sample (red lines, Fig. 3.3) is further compared with the time 't_z' taken for a raindrop of specific size to fall to the ground from the cloud base (blue lines, Fig. 3.3). 't_z' is calculated as the ratio of cloud condensation altitude and the terminal velocity 'V_t' of a droplet, which is defined as the maximum velocity of a falling raindrop at which the

gravitational force equals the drag force acting on the drop [see e.g., *Testik and Barros*, 2007]. Cloud condensation altitudes between 0.5 and 5 kms (Fig. 3.3) were assumed based on most probable condensation altitudes from weather sounding data (Fig. B7) and terminal velocity was calculated using the formulations given by *Beard* [1976] for droplet diameters between 0.019 and 7mm (Fig. B9). Terminal velocities calculated using *Beard* [1976] formulations agree well with values obtained from empirical relations provided by *Rogers* [1989], *Atlas et al.* [1973] and *Best* [1950] for droplet sizes between 0.08 and 1.5mm, 0.6 and 5.8mm and 0.3 and 6mm respectively (Fig. B9). Comparison of the time 't' taken by a specific noble gas in a raindrop of size 'a' to achieve the corresponding 'F_i' value (red lines, Fig. 3.3) calculated earlier and the time 't_z' taken for a raindrop of specific size to reach the ground (blue lines, Fig. 3.3), will yield a solution space of droplet size and equilibration time corresponding to any specific event. From weather sounding data (e.g., Fig. B7), if a specific condensation altitude can be identified (Table B3), the range of droplet sizes can further be constrained. This model approach is described further below with a specific example.

For example, sample nr4-2 shown in Figure 3.3 yields F_i values of 0.5, 0.5, 0.7, 0.7, 0.6 for He, Ne, Ar, Kr and Xe based on equation (3) and measured concentrations in rainwater and assuming an ice origin of noble gases in rainwater as described above. Using equation (4), these F_i values yield X values of 0.038, 0.028, 0.078, 0.059 and 0.058 for He, Ne, Ar, Kr and Xe, respectively. Assuming raindrop diameters between 0.019 and 10mm, a range of time 't', taken to achieve the calculated X values is obtained and plotted in Fig 3.3 (red lines). The time 't' taken to achieve a certain value of X and consequently, F_i is faster for the lighter noble gases (He, Ne) as compared to the heavier noble gases (Ar, Kr, Xe). This can also be illustrated by the temporal evolution of noble gases in raindrops of 0.1mm and

5mm in radius at a given temperature (assumed as 0˚C here; Fig. B10). As shown in Fig. B10, the lighter noble gases He and Ne reach equilibrium faster than Ar, Kr and Xe because of their higher diffusion coefficients for a given temperature as compared to the heavier noble gases. The time 't' taken to achieve a certain value of X (red lines, Fig. 3.3) is then compared with the time 't_z' for a raindrop to reach the ground (blue lines, Fig. 3.3). Comparison of these two time values yields the area indicated as "solution space" (shaded area, Fig. 3.3) defined by equilibration times of 100, 300, 500, 1000s and droplet sizes of 0.38, 1.3 and 6.5mm diameter. However, this range of drop sizes can be further constrained using weather sounding data for this sample which indicates a likely condensation altitude of ~4.5km (15000 ft; at ~0˚C; Table B3). Assuming this condensation altitude yields corresponding range of drop sizes between ~1and ~6mm for the rainfall event during the nr4-2 sample collection (Fig. 3.3). Similarly, average raindrop sizes can thus be estimated for different samples with mass-dependent patterns. Table B3 summarizes the range of raindrop sizes estimated for all mass-dependent samples (Fig. 3.1.c) where weather-sounding data yields an approximate condensation altitude. Estimated drop sizes for mass-dependent samples are large and range between 0.45 and 10mm in diameter. These estimated droplet sizes generally fall within the maximum critical diameter of raindrops observed in nature, which, depending on the amount of airstream turbulence, is usually between 6-8mm but may reach diameters as large as 10mm [*Rogers and Yau*, 1989]. In addition, large drop sizes are generally associated with heavier rainfall (e.g., *Marshall and Palmer* [1948]). Because large drop sizes are estimated using our calculations above for samples with mass-dependent noble gas patterns, our results imply that precipitation events for these samples are associated with heavier rainfall. Indeed, heavy rainfall was observed both by direct observations and through

surface weather station records during the collection of mass-dependent samples (sec. B.2).

Another interesting observation from these calculations is that small raindrops (fog) of 0.1mm or less in diameter would only take 0.39s, 0.78s, 1.27s, 2.09s, 2.76s or less to reach ~90% equilibrium for He, Ne, Ar, Kr and Xe (cf. Fig. B10). This suggests that, if only mass-dependent diffusive processes were occurring in fogs, concentrations of noble gases would be expected to be in equilibrium with the surface conditions. However, our measurements show that this is clearly not the case suggesting that additional processes that are not presently understood are affecting noble gases dissolution in fogs. Further detailed investigation, including analysis of noble gases in fogs is critical to understanding these processes. Such information is useful in the fields of meteorology, atmospheric and climate sciences, in addition to hydrology and and environmental engineering.

B.5 Time taken for noble gas disequilibrium patterns in rainfall to re-equilibrate at the surface

B.5.1 Introduction

Measured He, Ne, Ar, Kr and Xe concentrations in all rainwater samples from southeast Michigan are not in equilibrium with surface conditions and deviate from expected ASW values. Specifically, rainwater samples display a maximum deviation of 29%, -11%, -26%, -33% and -36% with respect to ASW for He, Ne, Ar, Kr and Xe , respectively (cf. Section 3.4). Rainwater is typically assumed to re-equilibrate at surface conditions on the order of a few minutes [see e.g., *Mazor,* 1972; *Klump et al.*, 2007]. While *Mazor* [1972] did not provide any calculations for this assumption, *Klump et al.* [2007] utilize a simple calculation based on diffusive length of noble gases to show that a water film of several millimeters in thickness would be in equilibrium with the atmosphere within 10 min. However, neither study used actual rainwater measurements to calculate the time taken by noble gases in rainwater to re-equilibrate at the surface. Below, we utilize a detailed model of diffusion in a plane sheet of water to calculate the time required for our measured maximum disequilibrium patterns in rainwater to re-equilibrate at surface conditions using realistic water depth values from precipitation data in Michigan.

B.5.2 Model Description

The total amount of noble gases diffusing into or out of a plane sheet of water is given by

the infinite series solutions [*Crank*, 1975]:

$$F_i = 1 - \sum_{n=0}^{\infty} \frac{8}{(2n+1)^2 \pi^2} \exp\left\{ -(2n+1)^2 \pi^2 X \Big/ 4 \right\} \qquad (1)$$

or,

$$F_i = 2(X)^{0.5} \left\{ \pi^{-0.5} + 2\sum_{n=1}^{\infty} (-1)^n ierfc\left(\frac{n}{\sqrt{X}} \right) \right\} \qquad \text{if } X<0.6465 \quad (2)$$

$$where, \quad X = \frac{Dt}{l^2} \qquad (3)$$

F_i is the fraction of noble gas 'i' (where, 'i'=He, Ne, Ar, Kr and Xe) transferred at any given time 't', 'l' is the depth of water (or thickness of water film), D is the diffusion coefficient of noble gases and 'n' is the n^{th} term of the infinite series solution. Equations (1), (2) and (3) can be utilized to solve for parameter 'X' by setting F_i=29%, -11%, -26%, -33% and -36% for He, Ne, Ar, Kr and Xe, respectively. From calculated vales of 'X', the time 't' taken to re-equilibrate can be obtained from equation (3) given the diffusion coefficient 'D' of noble gases and water depth or thickness of water film 'l'. Diffusion coefficients at a temperature of 25˚C were used in our calculations because it is close to the mean measured surface air temperature at the time of collection of rainwater samples (Table B1). Values for noble gas diffusion coefficients at 25˚C are given by *Bourg and Sposito* [2008]. In addition, water depth or thickness of water film 'l' was chosen based on measured hourly precipitation data from the Ann Arbor weather station during the period of sample collection (May-September, 2011). During the period of sample collection, precipitation as high as 8.2cms was recorded

in one hour. While this represents an extreme value, multiple rainfall events record precipitation of 1cm or more in one hour during this time period. Consequently, we utilize a water depth of 1cm to calculate the time 't' required for noble gases in rainwater to re-equilibrate using equation (3). Results of these calculations are presented below.

B.5.3 Model Results and Discussion

Considering a water depth of 1 cm, the maximum measured He excess of 29% in rainfall would take 900.5s (or ~15 minutes) at 25˚C to reach equilibrium with surface conditions. Similarly, maximum deviations of -11%, -26%, -33% and -36% for Ne, Ar, Kr and Xe measured in rainfall would take ~3.3mins, ~34mins, ~72mins and ~108mins, respectively, to reach equilibrium with surface conditions for a water depth of 1 cm and 25˚C. Our calculations show that re-equilibration is faster for the lighter noble gases He and Ne as compared to the heavier noble gases Ar, Kr and Xe due to both their higher diffusion coefficients and lower initial disequilibrium levels with respect to surface conditions. In addition, it should be noted that a smaller water depth 'l' would also lead to shorter re-equilibration times for all noble gases, in addition to processes such as turbulent mixing, if present. Nevertheless, our calculations show that the typical assumption that re-equilibration of rainwater at the surface is completed within a few minutes [see e.g., *Mazor,* 1972; *Klump et al.*, 2007] is more applicable for lighter noble gases and smaller water depths (<1cms) while heavier noble gases and greater water depths require re-equilibration times on the order of hours.

Noble gas concentrations of rainfall and fog will thus be recorded in groundwater

systems if the time taken to re-equilibrate with surface conditions is greater than the time taken to reach the water table. This is likely the case at high altitudes of the Galapagos Islands where rapid water infiltration due to the presence of fractures or thin soil cover [*Warrier et al*., 2012] allows little time for noble gas to re-equilibrate at the surface. However, sedimentary aquifer systems typically have thicker unsaturated zones and longer infiltration times allowing sufficient time for rainwater to re-equilibrate with ground air. This, in turn, allows the use of noble gases in paleoclimate reconstructions (e.g. *Kipfer et al.*, 2002, *Castro et al.*, 2007, 2012, *Alvarado et al.*, 2009).

References

Alvarado, J. A. C., F. Barbecot, R. Purtschert, M. Gillon, W. Aeschbach-Hertig, and R. Kipfer (2009), European climate variations over the past half-millennium reconstructed from groundwater, Geophysical Research Letters, 36.

Atlas, D., R. C. Srivastava, and R. S. Sekhon (1973), Doppler radar characteristics of precipitation at vertical incidence, *Rev. Geophys.*, 11, 1–35.

Beard, K. V. (1976), Terminal velocity and shape of cloud and precipitation drops aloft, *J. Atmos. Sci.*, 33, 851–864

Best, A. C. (1950), Empirical formulae for the terminal velocity of water drops falling through the atmosphere, *Q. J. R. Meteorol. Soc.,* 76, 302–311.

Bourg, I. C., and G. Sposito (2008), Isotopic fractionation of noble gases by diffusion in liquid water: Molecular dynamics simulations and hydrologic applications, Geochimica et Cosmochimica Acta, 72(9), 2237-2247.

Castro, M. C., C. M. Hall, D. Patriarche, P. Goblet, and B. R. Ellis (2007), A new noble gas paleoclimate record in Texas—Basic assumptions revisited, Earth Planet. Sci. Lett., 257, 170–187, doi:10.1016/j.epsl.2007.02.030.

Castro, M. C., R. B. Warrier, C. M. Hall, and K. C. Lohmann (2012), A late Pleistocene-Mid-Holocene noble gas and stable isotope climate and subglacial record in southern Michigan, Geophys. Res. Lett., 39(19), L19709.

Crank, J. (1975), *The mathematics of diffusion*, viii, 414 p. pp., Clarendon Press, Oxford, [Eng].

Eyring H. (1936) Plasticity and diffusion as examples of absolute reaction rates. *J. Chem. Phys.* 4, 283–291.

Hall, C. M., M. C. Castro, K. C. Lohmann, and T. Sun (2012), Testing the noble gas paleothermometer with a yearlong study of groundwater noble gases in an instrumented monitoring well, Water Resour. Res., 48(4), W04517.

Jähne B., Heinz G., and Dietrich W. (1987) Measurement of the diffusion coeffi**ci**ents of sparingly soluble gases in water. *J. Geophys. Res.* 92, C10., 10767–10776.

Kipfer, R., W. Aeschbach-Hertig, F. Peeters, and M. Stute (2002), Noble Gases in Lakes and Ground Waters, *Reviews in Mineralogy and Geochemistry*, *47*(1), 615-700.

Klump, S., Y. Tomonaga, P. Kienzler, W. Kinzelbach, T. Baumann, D. M. Imboden, and R. Kipfer (2007), Field experiments yield new insights into gas exchange and excess air formation in natural porous media, Geochimica et Cosmochimica Acta, 71(6), 1385-1397.

Lippmann, J., M. Stute, T. Torgersen, D. P. Moser, J. A. Hall, L. Lin, M. Borcsik, R. E. S. Bellamy, and T. C. Onstott (2003), Dating ultra-deep mine waters with noble gases and 36Cl, Witwatersrand Basin, South Africa, *Geochimica et Cosmochimica Acta*, 67(23), 4597-4619.

Malone, J. L., M. C. Castro, C. M. Hall, P. T. Doran, F. Kenig, and C. P. McKay (2010), New insights into the origin and evolution of Lake Vida, McMurdo Dry Valleys, Antarctica - A noble gas study in ice and brines, *Earth and Planetary Science Letters*, *289*(1-2), 112-122.

Marshall, J. S., and W. M. Palmer (1948), The distribution of raindrops with size, J. Meteorol., 5, 165–166.

Mazor, E. (1972), Paleotemperatures and other hydrological parameters deduced from noble gases dissolved in groundwaters; Jordan Rift Valley, Israel, Geochimica et Cosmochimica Acta, 36(12), 1321-1336.

Rogers, R. R. (1989), Raindrop collision rates, *J. Atmos. Sci.*, 46, 2469–2472.

Rogers, R. R., and M. K. Yau (1989), *A short course in cloud physics*, xiv, 290 p. pp., Butterworth-Heinemann, Oxford ; Boston.

Testik, F. Y., and A. P. Barros (2007), Toward elucidating the microstructure of warm rainfall: A survey, *Rev. Geophys.*, *45*(2), RG2003.

Warrier, R. B., M. C. Castro, and C. M. Hall (2012), Recharge and source-water insights from the Galapagos Islands using noble gases and stable isotopes, Water Resour. Res., 48(3), W03508.

Table B1: Rainwater sampling location, date and time of collection, measured surface air temperature (T), noble gas concentrations and measured He isotopic ratios (R) normalized to atmospheric He ratio (R_a). Samples from Milan and Ann Arbor were collected at altitudes of 215m and 290m a.s.l respectively. Surface weather station records used to derive appropriate precipitation characteristics for corresponding rainfall event is also indicated.

Sample	Location	Date	Time (UTC[a])	T (°C)	He (x 10^{-8}) (ccSTPg^{-1})	Ne ($x10^{-7}$) (ccSTPg^{-1})	Ar (x 10^{-4}) (ccSTPg^{-1})	Kr (x 10^{-8}) (ccSTPg^{-1})	Xe (x 10^{-9}) (ccSTPg^{-1})	R/R_a[b]	+/- 1s	Surface weather station record used
nr1	Milan	15/5/11	15:40	8.2	4.67	1.78	3.66	8.70	12.43	0.95	0.02	Ann Arbor
n2a	Milan	4/7/11	0:27	25.0	5.56	1.94	3.03	6.50	8.34	0.97	0.02	-
nr2b	Milan	4/7/11	0:27	25.0	4.57	1.67	2.57	5.20	6.48	0.93	0.02	-
nr3-1	Milan	23/7/11	15:00	27.0	4.67	1.55	2.13	4.21	4.87	-	-	Custer
nr3-2	Milan	23/7/11	15:30	21.4	4.63	1.74	2.63	5.29	6.55	0.98	0.03	"
nr4-1	Ann Arbor	23/7/11	21:35	26.0	4.62	1.70	2.69	5.28	6.42	0.98	0.03	Ann Arbor
nr4-2	Ann Arbor	23/7/11	21:35	26.0	4.99	1.55	1.99	3.91	5.10	0.93	0.03	"
nr5-1	Milan	27/7/11	23:40	23.5	4.51	1.71	2.68	5.51	7.30	1.05	0.02	Ann Arbor
nr5-2	Milan	28/7/11	5:00	22.5	5.28	1.74	2.80	5.72	7.43	1.03	0.04	"
nr6	Milan	29/7/11	8:25	22.6	4.37	1.64	2.60	5.30	7.26	0.98	0.02	Ann Arbor
nr7	Milan	3/8/11	7:00	24.0	5.44	1.80	2.92	6.05	7.78	0.96	0.12	Ann Arbor
nr8	Milan	6/8/11	18:40	28.6	4.39	1.68	2.72	5.49	7.17	0.99	0.14	Custer
nr9	Milan	9/8/11	9:35	20.8	4.72	1.72	2.87	5.94	7.56	1.18	0.16	Ann Arbor
nr10-1	Milan	9/8/11	21:05	23.1	5.22	1.68	2.74	5.48	6.94	1.15	0.07	Willow Run
nr10-2	Milan	9/8/11	21:55	20.3	4.44	1.66	2.65	5.41	6.75	1.02	0.03	"
nr11	Milan	14/8/11	11:40	18.4	4.96	1.79	2.99	6.55	8.88	1.05	0.03	Ann Arbor
nr12	Milan	24/8/11	7:50	19.6	4.52	1.78	3.23	7.03	9.61	1.05	0.04	Custer
nr13	Milan	4/9/11	0:47	23.9	5.32	1.82	3.02	6.75	8.84	0.92	0.04	Ann Arbor
nr14	Milan	9/9/11	15:10	18.5	5.06	1.78	3.14	6.91	9.38	1.04	0.03	Ann Arbor

[a]UTC is Coordinated Universal Time. UTC=Eastern Standard time+4 hours during daylight savings in USA.

[b]R is the measured $^3He/^4He$ ratio and Ra is the atmospheric $^3He/^4He$ ratio of $1.384x10^{-6}$ [*Clarke et al.*, 1976]

Table B2: Compiled hourly surface weather observations from individual weather station records**.** Data description for each column in Table S2 including units, abbreviations and weather codes are provided in detail by NCDC (http://hurricane.ncdc.noaa.gov/cdo/3505doc.txt). Because of the large size of this data file, the reader is referred to (https://docs.google.com/open?id=0B3ra0NvYPTwOZWFwSFVqdlJGbEU).

Table B3: Estimated condensation altitudes and raindrop sizes for individual precipitation events corresponding to mass-dependent samples based on diffusive mass-transfer model.

Mass-depdendent sample	Likely condensation altitude (kms)	Droplet size (mm)	
		Minimum	Maximum
n2a[1]	-	-	-
nr2b[1]	-	-	-
nr3-1[1]	-	-	-
nr3-2[1]	-	-	-
nr4-1	4.5	0.45	2
nr4-2	4.5	1.2	6
nr5-1	4.5	0.7	1.8
nr5-2	4.5	0.7	10
nr6	4.5	0.7	3
nr7	4.5	0.5	10
nr9	3	0.6	3
nr10-1	4	0.7	8
nr10-2	4	0.9	3
nr11	3	0.55	3
nr13	3.5	0.5	10

[1]Weather Sounding not available

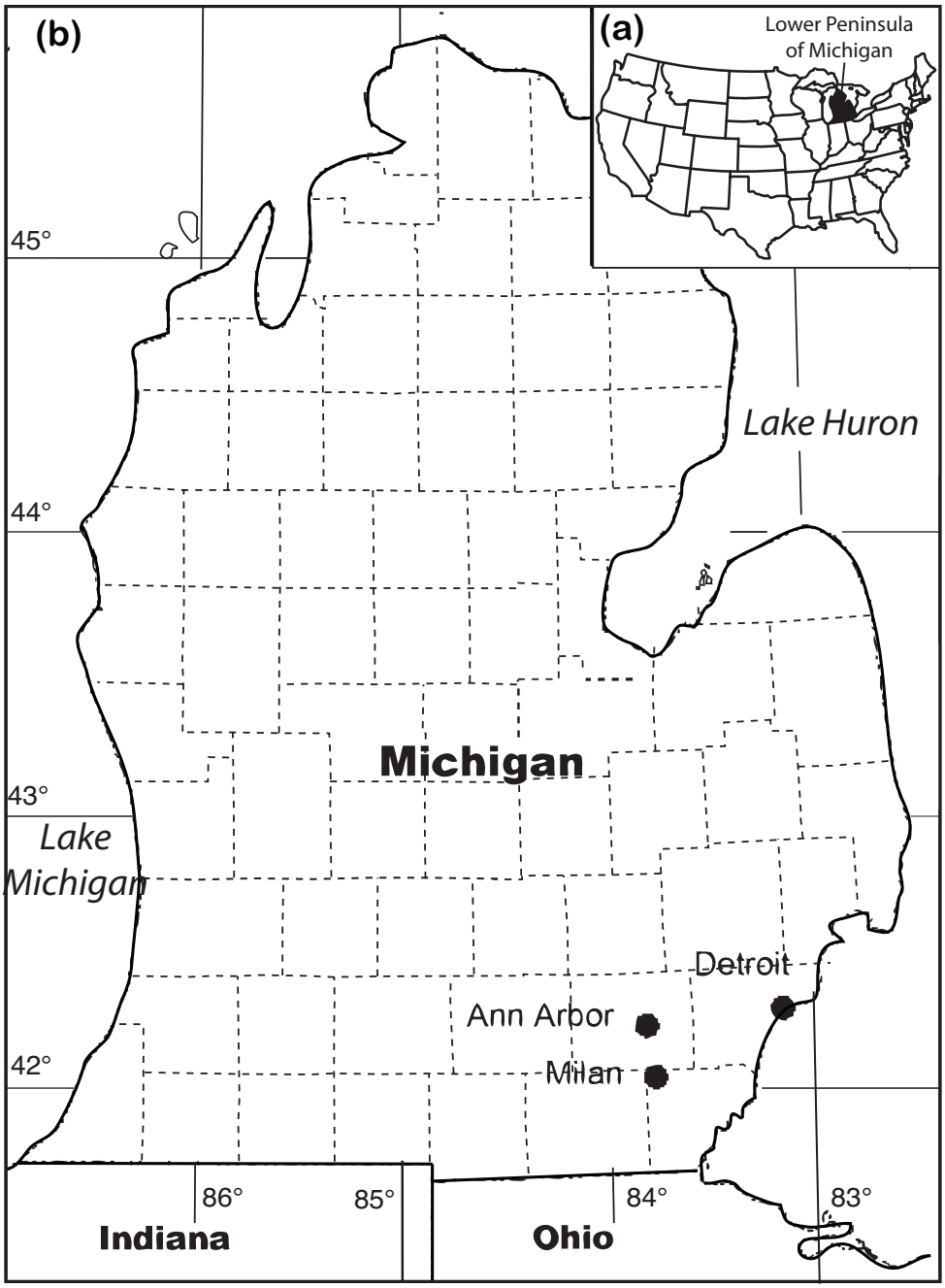

Figure B1: (a) Location of Michigan and (b) rainwater sample collection sites in Ann Arbor and Milan. Base map and locations are obtained through map services from U.S. Geological Survey, National Geospatial Program (http://nationalmap.gov/).

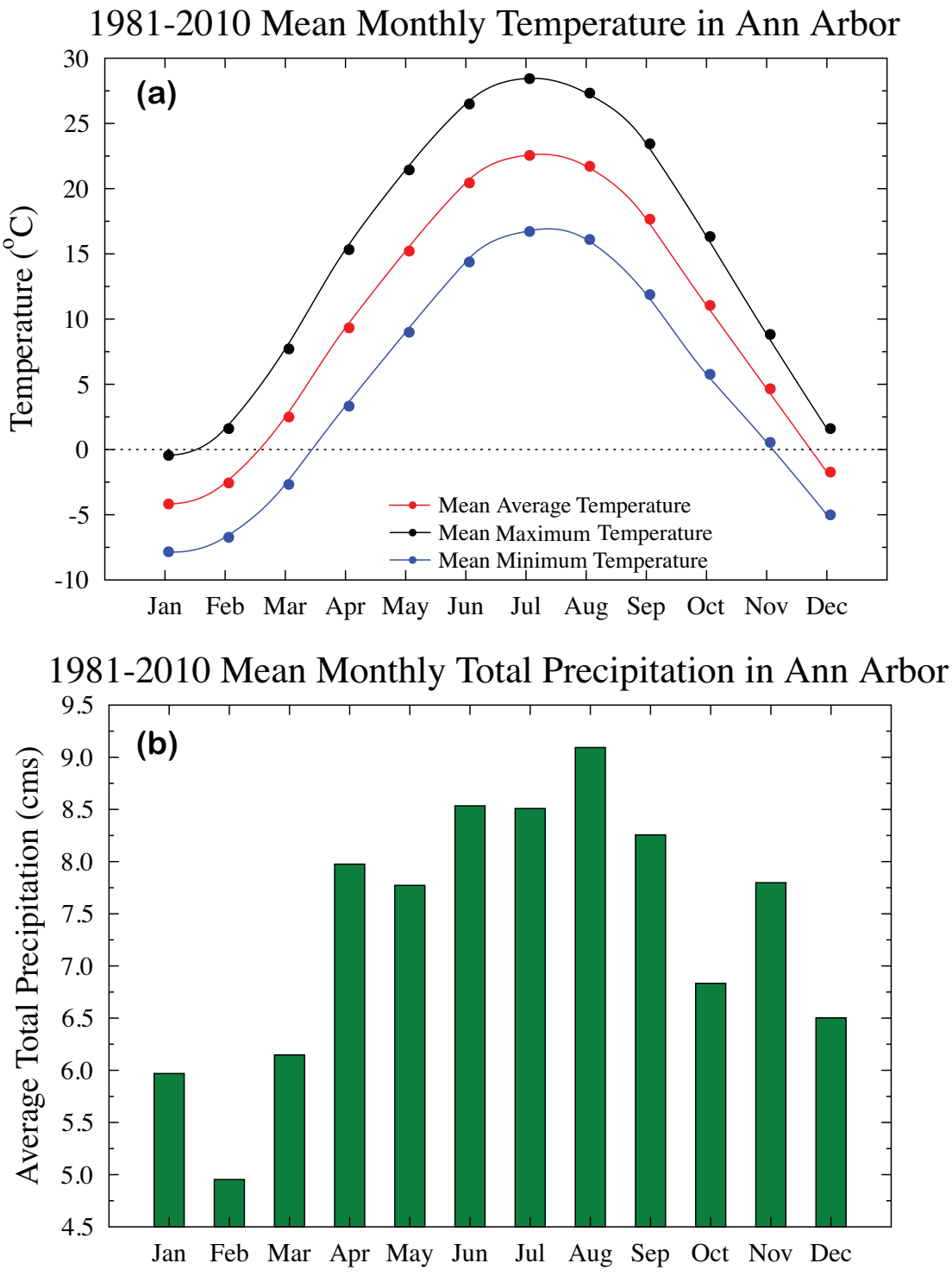

Figure B2: 1981-2010 Mean climatological summary for Ann Arbor (Station ID: USC00200230; 42.28˚N, 83.77˚W) located in southeast Michigan (a) Monthly mean total precipitation and (b) monthly mean maximum, minimum and average temperatures.

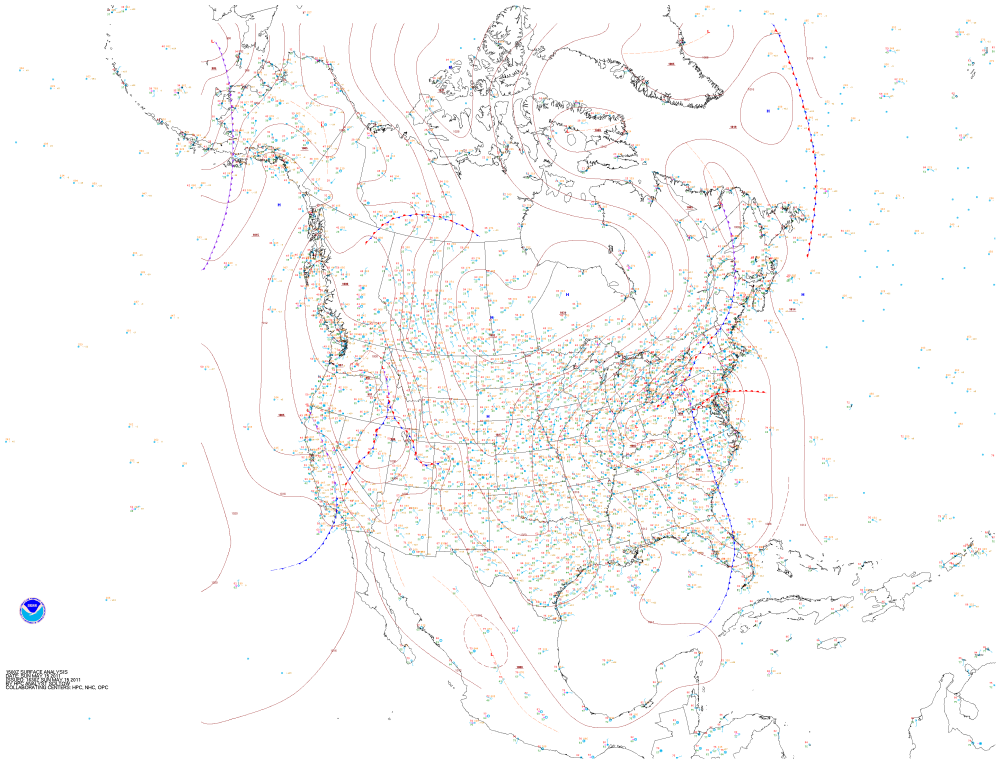

Figure B3: Surface analyses map of North America issued by the Hydrometeorological Prediction Center corresponding to nr1 precipitation event.

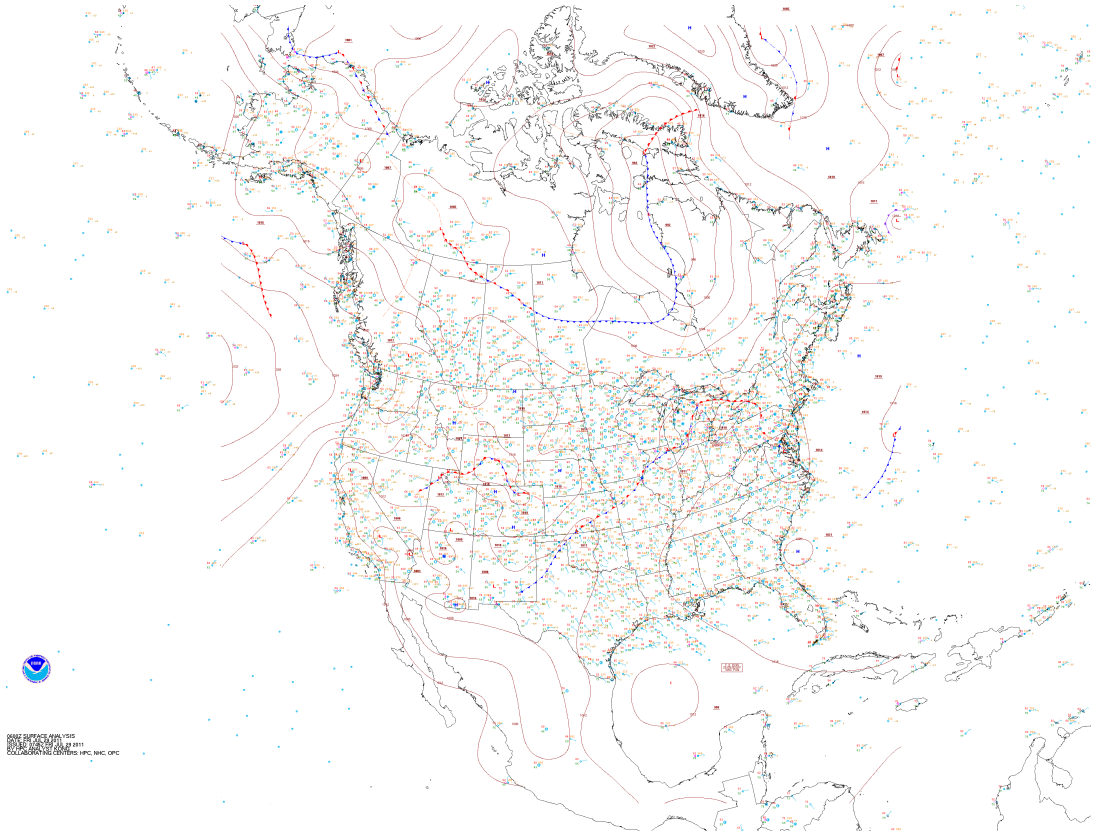

Figure B4: Surface analyses map of North America issued by the Hydrometeorological Prediction Center corresponding to nr6 precipitation events.

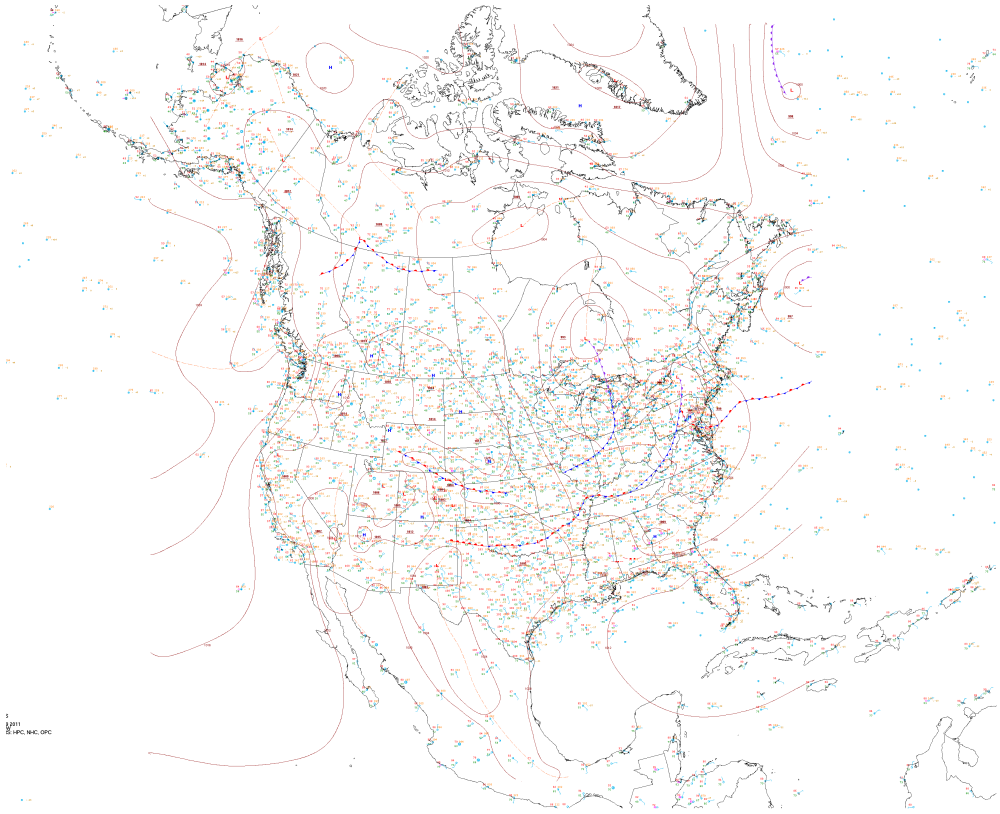

Figure B5: Surface analyses map of North America issued by the Hydrometeorological Prediction Center corresponding to nr10-1/10-2 precipitation event.

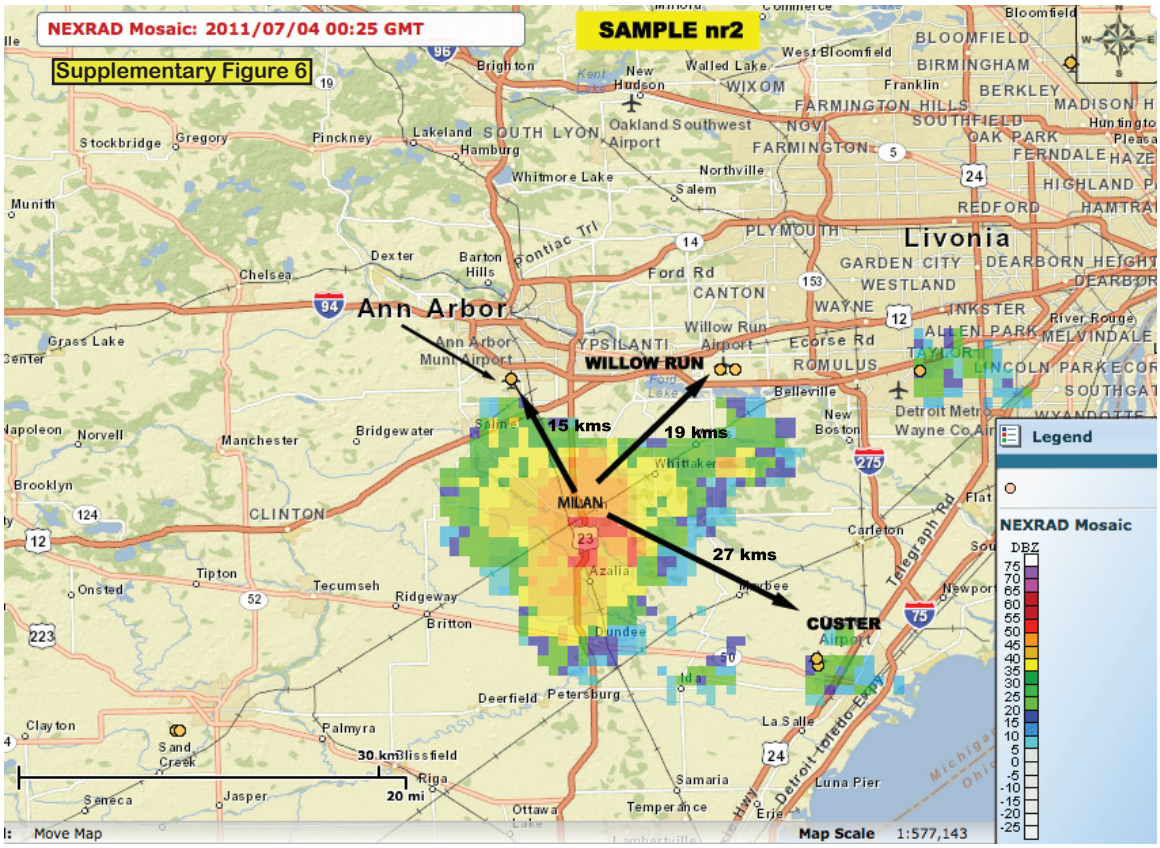

Figure B6: Doppler radar (NEXRAD) image for southeast Michigan at 00:25 UTC on July 4th, 2011. Location of hourly surface weather stations near Ann Arbor and Milan are also indicated (orange circles).

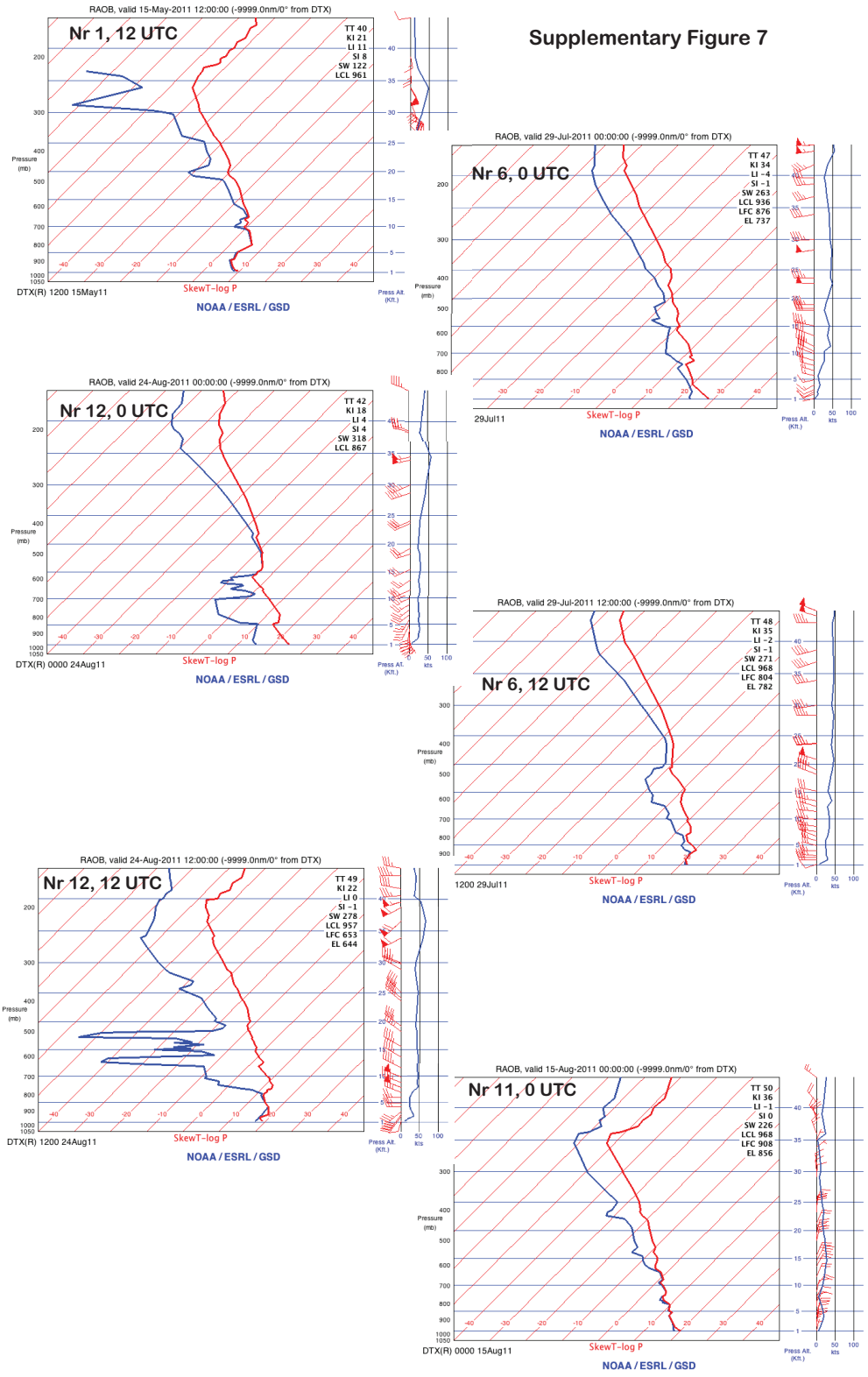

Figure B7: SkewT-log P plot of weather balloon measurements of temperature and dew point at Detroit, MI for samples nr1, 6, 11 and 12.

Supplementary Figure 8

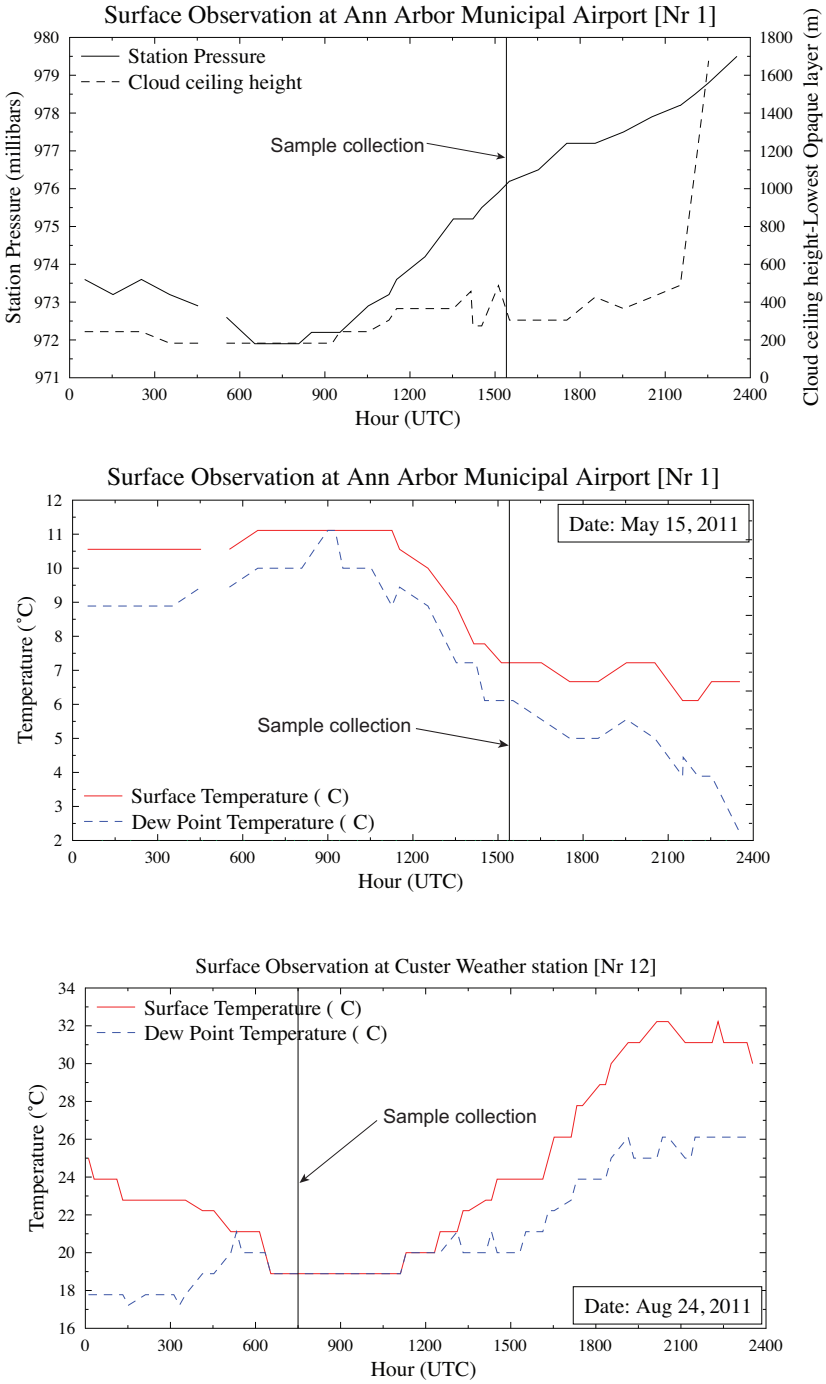

Figure B8: Plot of surface pressure, temperature, dew point and cloud ceiling height measurements for samples nr1 and nr12 measured at Ann Arbor and Custer weather stations respectively.

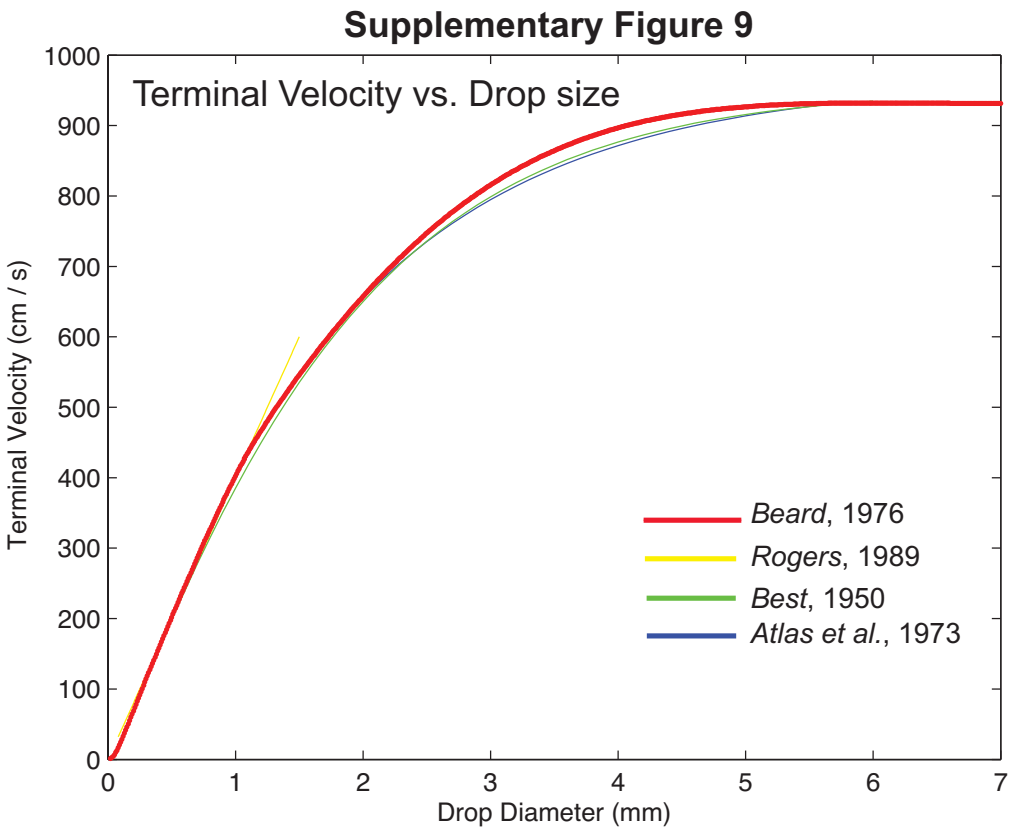

Figure B9: Terminal velocity for raindrops using multiple formulations.

Supplementary Figure 10

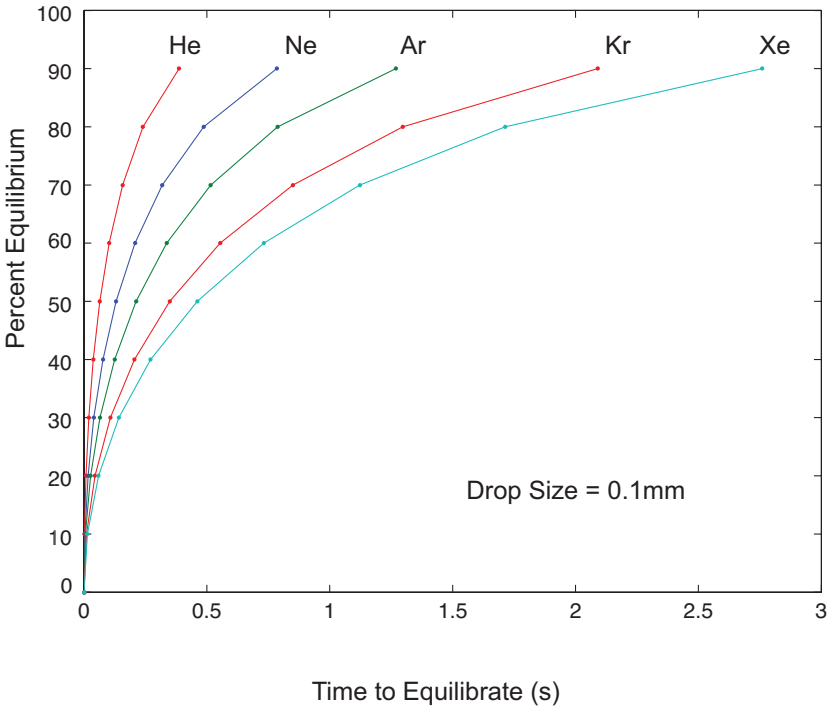

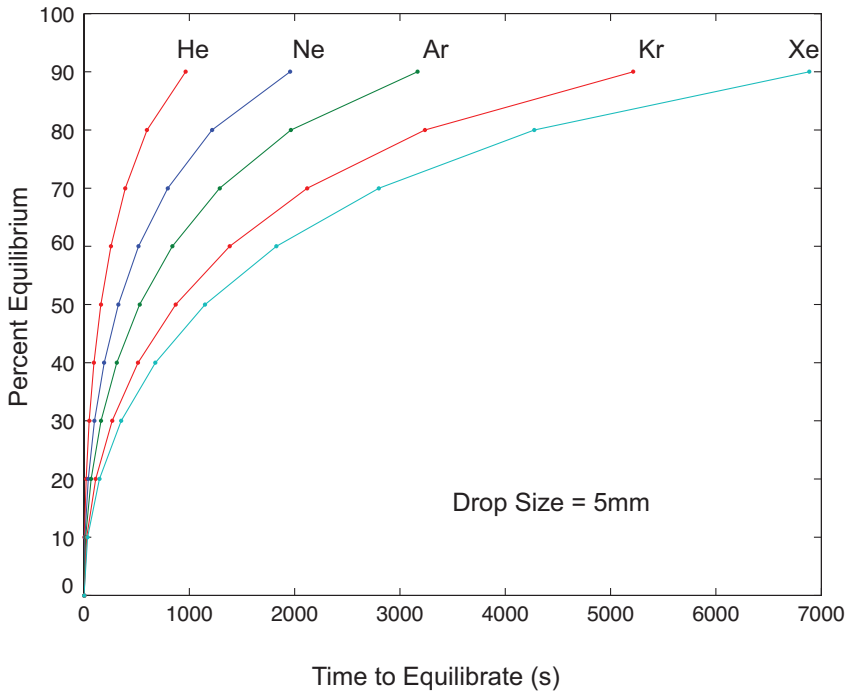

Figure B10: Time taken for noble gases to achieve diffusive equilibrium through mass transfer in/out of a raindrop of radius 0.1mm and 5mm.

APPENDIX C : SUPPLEMENTARY MATERIAL FOR CHAPTER 4

C.1 Introduction

This appendix includes supplementary material related to chapter 4. Specifically, noble gas elemental concentrations, results and discussion of inverse fitting noble gas temperatures (NGT) using various NGT models are provided in Table C1, Table C4, section C.2, Fig. C1 and Fig. C2. Results and discussion of determining calibrated calendar ages for all groundwater samples using ^{14}C correction models with major ion data are described in section C.3 and Table C2, Table C3. In addition, section C.4 includes a statistical discussion of climatic events identified in the paleoclimatic reconstruction. Results for percent snow contribution using stable isotopic data are presented in Table C5. Impact of dispersion on preservation of climatic signals from the Younger Dryas and Mid-Holocene in the Saginaw and Marshall aquifer is included in section C.5 along with plots of calendar age vs. recharge distance for Saginaw and Marshall aquifer samples in Fig. C3 and Fig. C4.

C.2 Discussion of NGT model results for all Saginaw samples and compatibility between Saginaw and Marshall NGT records

C.2.1 Introduction

Measured noble gas concentrations in groundwater are used to determine noble gas temperatures (NGTs), i.e., the water table temperature at the time recharge occurs, using inverse NGT models. Commonly used models in NGT studies include the unfractionated air (UA) model [*Stute and Schlosser*, 1993], the continuous equilibration (CE) model [*Aeschbach-Hertig et al.*, 2000, 2008] and the oxygen depletion (OD) model [*Hall et al.*, 2005]. These models largely vary in their mechanisms to deconvolve the temperature dependent ASW component from the excess air component [see, e.g., *Kipfer et al.*, 2002]. In particular, while the UA model assumes complete dissolution of the excess air component with a noble gas composition identical to that of standard air, the CE model allows for partial dissolution of noble gases from entrapped air bubbles in addition to accounting for the possibility of degassing through a fractionation parameter (F). In contrast, the OD model relaxes the assumption that soil air has standard atmospheric composition because of a net loss of O_2 in the unsaturated zone (due to consumption via biological activity) without an equivalent build up of CO_2. Such a loss of active suite of gases observed in the unsaturated zone [*Hall et al.*, 2005, *Castro et al.*, 2007, *Sun et al*., 2008; *Aeschbach-Hertig*, *W.*, personal communication] leads to an increase in partial pressures of all noble gases that is accounted for in the OD model through a pressure adjustment factor (P_{OD}) [*see e.g., Hall et al*., 2005, *Sun et al*., 2008].

The OD model first proposed by *Hall et al*. [2005] has been successfully utilized in a number of subsequent studies [*Castro et al.*, 2007; *Sun et al.*, 2008; *Sun et al.*, 2010].

An additional constraint of all NGT models is that they can only account for atmospheric noble gas compositions and this can be verified through noble gas isotopic ratios [e.g., $^{20}Ne/^{22}Ne$, $^{21}Ne/^{22}Ne$, $^{40}Ar/^{36}Ar$; see, e.g., *Ozima and Podosek*, 2002]. Unlike all other Saginaw samples that show measured noble gas isotopic ratios (not shown) within $\pm 1\sigma$ or $\pm 2\sigma$ error of the atmospheric value, sample sg3 has $^{20}Ne/^{22}Ne$ (9.91 ± 0.04) and $^{21}Ne/^{22}Ne$ (0.0299 ± 0.0002) ratios greater ($> \pm 2\sigma$ error) than corresponding atmospheric values [9.8, 0.0290; *Ozima and Podosek*, 2002]. While excess ^{21}Ne results from nucleogenic reactions between α-particles from U-Th decay and O and Mg atoms in the crust [*Wetherill*, 1954; *Hilton and Porcelli*, 2003], excess ^{20}Ne typically has a mantle origin [see e.g., *Castro et al.*, 2009, *Graham*, 2002]. Mantle signatures in stable tectonic settings have previously been documented [*Torgersen et al.*, 1995; *Castro*, 2004; *Siegel et al.*, 2004], including near the recharge area of the Marshall aquifer [*Ma et al.*, 2005], and have been attributed to the presence of a local deep permeable fault. Because NGT models do not account for the addition of crustal or mantle noble gas excesses, sg3 cannot be included in the NGT discussion below.

Measured noble gas concentrations (Ne, Ar, Kr and Xe) for all Saginaw samples except sg3 were fit to the UA, CE and OD models assuming a mean recharge altitude of 275m and 0g/l salinity. As previously noted by *Sun et al*. [2010], simultaneously fitting temperature, excess air and P_{OD} factor in the OD model is an ill-posed problem. Instead, for the OD model, we fit the entire suite of Saginaw samples for NGTs and excess air assuming a single P_{OD} factor, as previously done by *Hall et al.* [2005], *Castro et al.*

[2007], and *Sun et al.* [2008, 2010]. P_{OD} factors of 1.0, 1.05, 1.1, 1.15 and 1.2 were considered and Table C4 shows the results of inverse fitting measured noble gas concentrations for all 21 Saginaw samples to the UA and OD models for varying P_{OD} factors. CE model results are discussed in detail elsewhere [*Warrier et al.*, in review]. As shown below, both the CE and UA model provide good, comparable fits (cf., Figure C1).

C.2.2 Discussion of NGT results for all Saginaw samples – Old vs. young samples

Overall, NGT results indicate that 18 out of 21 samples (excluding sg3) converge using the UA and OD models (Table C4). Three samples (sg1a, sg1b and sg12b) that cannot be fit using the UA and OD models have depleted noble gas concentrations. We illustrate this in Table C1 by showing Ne concentrations relative to modern day recharge conditions. We denote this value ΔNe(0) where:

$$\Delta Ne(0) = Ne_{measured}/Ne_{ASW}(0)$$

and $Ne_{ASW}(0)$ is the ASW concentration expected for modern recharge conditions (9.1ºC, 275 m altitude). In the table ΔNe(0) is tabulated as percent values. This is a modification of the definition used by *Aeschbach-Hertig et al.* [2002] in that it is NGT model independent. As can be seen in Table C1, samples sg1a, sg1b and sg12b display large negative ΔNe(0) values and poor fits for these three samples using the UA and OD models reflecting the inability of these models to account for degassing. For all other samples, goodness of fit of measured noble gas concentrations to any particular NGT model is indicated by a χ^2 statistic (Table C4), which is the sum of the squared deviations between the modeled and measured concentrations, weighted with the experimental 1σ

errors. χ^2 statistics determined from the inverse fits of noble gas concentrations provide a unique tool to assess the applicability of specific NGT models used to invert the data. When analyzing an entire suite of samples, goodness-of-fit is usually tested using the mean square weighted deviate (MSWD), which is related to the χ^2 value determined in the inverse fit by MSWD=χ^2/ν, where ν, is the number of degrees of freedom for the entire suite of samples [see e.g., *Ballentine and Hall*, 1999, *Sun et al.*, 2010]. The UA and OD models with two fit parameters (NGT, excess air), four measured values (Ne, Ar, Kr, Xe), and 18 samples considered has 36 and 35 degrees of freedom (ν), respectively. This corresponds to a UA model MSWD of 25.77 and OD model MSWD between 25.54 (assuming P_{OD}=1.05) and 23.09 (assuming P_{OD}=1.20) for the entire suite of samples. Ninety-five percent of datasets with ν=36 and ν=35 will have a MSWD below 1.42. Our comparison of MSWD from UA and OD models at the 95% confidence level suggests that there is a significant misfit of these NGT models when the sampled dataset is taken in its entirety. Significant misfit between observed data and conceptual models suggest that a number of samples may not adhere to the underlying assumptions of these models.

In particular, our results indicate that all samples with groundwater ages greater than the LGM (except sg13; Table C4) indicate poor fits using both UA and OD models (cf. Table C4). Most samples older than the LGM display high χ^2 values for each sample ($\geq$100), do not converge or display non-physical values for NGTs (Table C4). In particular, as many as five samples (sg8a, sg8b, sg14, sg15, sg16) with ages greater than the LGM display UA model NGTs below the freezing point of water (0˚C; Table C4), a point at which it is physically impossible for recharge to occur and the Henry constants used for the NGT inversion are no longer applicable. Poor model fits for samples with

ages older than the LGM may partly be related to the extremely high noble gas excesses (ΔNe(0)) observed for these samples relative to mean recharge conditions (see Table C1). The origin of extremely high atmospheric noble gas excesses for these older samples are discussed in detail elsewhere [*Warrier et al.*, in review]. Distinct noble gas patterns and stable isotope signatures for older (≥LGM) samples suggest that, for statistical purposes, the group of old (≥LGM) and young samples (≤LGM) may, as a first order approximation, be assumed to represent independent subsets. Assuming each sample group (older than LGM vs. younger than LGM) as an independent subset, the goodness of fit of each model (UA and OD) can be assessed. For seven samples with ages beyond LGM (cf. Tables C2, C4), the UA model yields MSWD=55.98 at ν =14, and the OD model yields MSWD between 56.53 and 47.20 for P_{OD} of 1.05 and 1.20, respectively. Ninety-five percent of datasets with ν =14 and ν =13 should have MSWD below 1.69 and 1.72 respectively. As expected, MSWD calculated for all old samples are greater than corresponding values obtained assuming the dataset in its entirety. Our results thus suggest that NGTs derived using the UA and OD models for all older samples (>LGM), except sg13, are not reliable and may not be appropriate for a paleoclimatic reconstruction.

By contrast, all samples with groundwater ages younger than the LGM yield better fits when considered as a single dataset. In particular, the UA and OD models with 11 young samples (ν =22 and 21 respectively for UA and OD models) yield MSWD of 6.55 (UA model) and between 7.29 (P_{OD}=1.05) and 9.27 (P_{OD}=1.2), respectively. Ninety-five percent of datasets with ν =22 and ν =21 should have MSWD less than 1.54 and 1.56 respectively. Although our MSWD results for all young samples from the UA and OD

models are not significant at the 95% confidence level, NGTs calculated for young samples are far more suitable for a paleoclimatic reconstruction than those for samples older than the LGM. NGT and excess air error estimates have been adjusted upwards by a factor of $(MSWD)^{1/2}$ to account for the extra degree of misfit of the models to the data (see e.g., *Ballentine and Hall*, 1999). Hence, the goodness-of-fit for each sample (χ^2) is appropriately reflected in NGT and excess air error estimates and is subsequently included in the paleoclimatic discussion (see Section 4.5).

C.2.3 Choice of the NGT model used in the paleoclimatic reconstruction (samples younger than the LGM)

Choice of NGT model results used in the paleoclimatic reconstruction (Section 4.5) is first based on a comparison of MSWD obtained from all three tested models (UA, OD and CE), among other factors (discussed below). While MSWD for all samples younger than the LGM shows comparable (good) fits for both the UA and CE models [MSWD≈6.5; see also *Warrier et al.*, in review], the OD model displays poorer fits for P_{OD} values greater than 1 (see below). Indeed, as shown in Figure S2, overall best fit (minimum $\Sigma\chi^2$) for the suite of all 11 young (≤LGM) samples is obtained for a P_{OD} factor of 1.0. A P_{OD} factor of 1.0 indicates that soil air has an O_2 and noble gas partial pressures equivalent to that of standard air and further suggests that the UA or CE models would yield accurate NGT values [see e.g., *Hall et al.*, 2005, *Aeschbach-Hertig et al.*, 2000]. Thus the UA model is better suited to explain all young Saginaw samples compared to the OD model with P_{OD} >1. For the purposes of a paleoclimatic discussion invoking

temperature differences during different climatic events (Section 4.5), the choice of NGT model (UA vs CE model) is largely irrelevant as shown by *Sun et al.* [2010]. Indeed, despite systematic offsets in NGTs and excess air between individual NGT models, models agree remarkably well when estimating temperature differences. Comparison of UA and CE model NGT results (Figure C1) for all Saginaw and Marshall groundwater [*Ma et al.,* 2004] samples younger than the LGM yields similar results to *Sun et al.* [2010]. In particular, our comparison yields a good linear fit (r^2= 0.77) between NGTs derived using both models and lend greater confidence to the accuracy of NGT estimates for all young samples. In addition, a best-fit line to all data (Figure C1) indicates a positive offset (1.1˚C) suggesting that CE model derived NGTs are on average 1.1˚C higher than the UA model derived NGTs. Although the NGT offset between UA and CE models is low, combining NGT results from both models for a more detailed paleoclimatic reconstruction will yield apparent temperature variations that are artifacts of the choice of NGT estimation method [*Sun et al.,* 2010]. Thus, paleoclimatic reconstruction and temperature changes for all young groundwater samples (Section 4.5) with robust NGT estimates are made only using the UA NGT model in the present study. This is important because it allow us to make a direct comparison with the UA NGT results of *Ma et al.* [2004] (see chapter 4).

C.2.4. Bias to low NGTs in the recharge area of the Marshall aquifer and compatibility of the Saginaw and Marshal records

While our modern Saginaw sample displays a NGT value very close to the

MAAT of 9.1 ± 0.8˚C in southern Michigan [Figure 4.3.a], the mean of modern samples from the Marshall (m1, 6, 7, 8, 9) of 6.3 ± 0.8˚C [Figure 4.3.a, *Ma et al*., 2004] displays a strong bias to low NGTs. As pointed out by *Ma et al.* [2004], some of these "modern" samples could possibly be hundreds of years old and representative of a cooler period instead. NGTs over several degrees cooler than present were recorded elsewhere at the beginning of the last millennium [e.g., *Castro and Goblet*, 2003, *Castro et al.*, 2007]. On the other hand, other Marshall modern samples which are truly representative of present time are likely recording specific recharge conditions at the time they were sampled rather than true soil air temperature. Indeed, field observations and noble gas measurements strongly suggest that at least part of this bias is due to net depletion of O_2 in the soil air due to biological processes without corresponding build-up of CO_2, leading to higher noble gas partial pressures [*Hall et al.*, 2005, *Sun et al., 2008*]. Our modern Saginaw NGT value shows that soil air noble gas partial pressures are similar to standard air and suggest that recharge conditions for this sample are distinct from those of the Marshall modern samples. Through a year-long continuous monitoring in an instrumented well in southern Michigan, *Hall et al.* [2012] have shown that large precipitation events such as Hurricane Ike can significantly modify recharge conditions within aquifer systems and bring O_2 depleted soil air back to standard conditions, with simultaneous incorporation of high levels of EA at the water table. Saginaw sample sg2's EA value is at a level similar to that measured in the Glacial Drift aquifer following Hurricane Ike suggesting the occurrence of a major storm event prior to recharge. By contrast, modern Marshall samples are compatible with conditions prior to Hurricane Ike [*Hall et al.*, 2012]. It is thus possible that modern Marshall NGTs are reflecting mostly

recharge conditions rather than the MAAT. The study of *Hall et al.* [2012] suggests, however, that the NGT temperature proxy should be viewed as an average of recharge conditions over several years. In view of the recent results of *Hall et al.* [2012] it is possible and maybe likely that having the NGT modern record averaged over several years might lead to the entire removal of this bias. Only a continuous (over at least a 1-year period) noble gas study in the Marshal recharge area will allow us to confirm this. However, even in the event that such bias to low NGTs in the Marshall recharge area would apply to all the Marshall NGT record, it can be shown that all the main conclusions of this study would still apply (please see below).

To assess the impact of such bias over the entire Marshall NGT record and the compatibility of both the Saginaw (presenting no such bias) and the Marshall records, we estimated and compared the NGT record for the Saginaw calculated with the OD model for a P_{OD} factor of 1 (equivalent to the UA model) and that for the Marshall aquifer with a P_{OD} factor of 1.085 (cf. Table C4). Indeed, a P_{OD} of 1.085 was previously identified by *Sun et al.* [2010] as the best fit for the entire set of Marshall samples. Such a comparison reconciles the NGT differences in the recharge area. Our results show that all the main climatic events and transitions identified through the UA model for both records remain and are compatible with regional estimates from independent proxies. More specifically, the observed differences between the UA and OD models are:

C.2.4.1 Onset of the YD

Our combined NGT record from the UA model points to a cooling of ~3.3 ± 1˚C (m12b-

sg9, Figure 4.3.a) at the onset of the YD. Comparitively, OD model results indicate a cooling of 5.7 ± 3.2˚C at the onset of the YD (m12b-sg9, Table C4). Cooling estimates at the onset of the YD estimated using both UA and OD models are compatibile with regional cooling estimates between 3-5.6˚C obtained through independent proxies in the MidWest including pollen [*Viau et al*., 2006], macrofossils and fish remains [*Peteet et al.*, 1993] as well as endogenic lake calcite in northeastern USA [*Hou et al.*, 2007; *Yu*, 2007; *Zhao et al.*, 2010]. In addition, excess air results from both the UA and OD models show a distinct increase (m12b-sg9, 11; Figure 4.4. a, Table C4) at the onset of the YD indicating a transition from a warm, humid (BOA) environment to a cool, arid one (YD).

C.2.4.2 Termination of the YD

Our combined UA NGT record displays a general warming trend (sg12a, m13, sg5b, sg5a) within this time period of 4.3 ± 1.8˚C (sg9-sg5a, Figure 4.3.a). In particular, such a warming estimate was made using only Saginaw samples (sg9 and sg5a) and thus, no change in warming estimates at the termination of the YD is expected based on the choice of the NGT model (UA vs. OD models).

C.2.4.3 MH warming

Our combined UA model NGT record points to a MH warming of 2.9 ± 0.8˚C (m4b-sg6b; Figure 4.3.a) while OD model results for the same samples point to a warming of 0.6 ± 0.1˚C.. Numerous proxies in the Midwest, including fossil pollen [*Winkler et al.*,

1986; *Viau et al.*, 2006] and speleothems [*Dorale et al.*, 1992] show evidence for a temperature increase of ~0.5-4˚C between ~6kyrs and ~3kyrs BP [e.g., *Kirby et al.*, 2002]. Thus, our MH warming estimates obtained from both UA and OD models correlate well with regional proxy data. In addition, both UA and OD models show increased EA values between the onset of the MH warming at ~5.4kyrs BP (m4b, Figure 4.4.a) and its peak at ~4.1 kyrs (sg6b, Figure 4.4.a), a sign of increasing aridity within a warmer climate. This change to arid climatic regimes is also well documented through a host of regional studies including vegetation changes [*Bartlein et al.*, 2011; *Baker et al.*, 1998] and low lake levels [*Manny et al.*, 1978; *Winkler et al.*, 1986].

C.2.4.4 Similar to the YD termination event, UA NGT cooling of 1.7 ± 0.9˚C between ~4.1kyrs and ~2.9kyrs BP (Figure 4.3.a) was estimated using only Saginaw samples (sg6b, sg4a) and thus, do not change anything in the MH cooling record whether or not the bias to older Marshall samples would apply. Thus, cooling estimates at the end of the MH is ~1.7˚C irrespective of the choice of NGT model (UA vs. OD).

It can thus be seen that all the main characteristics of our paleoclimatic reconstruction based on the UA NGT model remain, irrespective of the NGT model used. Again, and based on recently published results by *Hall et al*. [2012], it is possible, however, that the bias to low NGTs in the Marshall recharge area will vanish once the recharge NGT record is averaged over a period of several years.

C.3 Determining calibrated calendar groundwater ages for all Saginaw samples

C.3.1 Methods

Groundwater samples were collected in 500-ml glass bottles from all sampling locations to determine groundwater ages following sampling procedures described in *Ma et al.* [2004]. Analysis of carbon isotopes ($^{13}C/^{12}C$, ^{14}C) were made at the NOSAMS facility at Woods Hole Oceanographic Institution using procedures outlined in *Jones et al.* [1990]. NSF support to NOSAMS (OCE-9807266) is appreciated.

C.3.2 Calculation of calibrated calendar groundwater ages

Measured carbon isotopic ratios ($\delta^{13}C$) as well as ^{14}C activity values along with measurement uncertainties are shown in Table C2. Measured ^{14}C activity values for Saginaw aquifer samples ranges from 0.2% modern C (pMC) to 86.1 pMC (Table C2). Four conventional geochemical and isotopic correction models [*Pearson and White*, 1967; *Evans et al.*, 1979; *Fontes and Garnier*, 1979 ; *Eichinger*, 1983] are applied to all samples to convert measured ^{14}C activity values into ^{14}C ages after accounting for the addition of "dead" carbon. Model corrections for the addition of "dead" carbon were done using measured major ion data (Table C3) as well as aqueous carbonate speciation calculated with the geochemical modeling program Web-phreeq [*Saini-Eidukat and Yahin*, 1999; Table C2]. Initial values used for all other model parameters are similar to those reported by *Ma et al.* [2004]. Corrected ^{14}C ages obtained from the four conventional age correction models yield consistent results for all samples and appear to

be fairly insensitive to the individual correction procedure. Samples sg1a, sg1b and sg2, which are located close to the recharge area (Figure 4.1) display negative corrected apparent ^{14}C ages using all models and are regarded as modern samples. ^{14}C ages for all remaining 19 samples reported in the Table C2 are obtained using the *Fontes and Garnier* [1979] correction model (F&G). F&G model ages are reported in this study because it utilizes both geochemical and isotopic balances to derive corrected ^{14}C ages and also facilitate paleoclimatic comparisons (Section 4.5) with previously reported F&G corrected ^{14}C ages for samples from the Marshall aquifer [*Ma et al.*, 2004]. Although the F&G model corrected ^{14}C ages are reported (Table C2), associated ^{14}C age errors for each sample are determined from the maximum range in corrected initial ^{14}C activity produced by different correction models using a standard propagation of errors technique. Because such an error estimate encompasses the entire range of corrected activity values produced by different correction techniques, reported ^{14}C age errors represent a conservative estimate.

Except for modern samples (sg1a, sg1b, sg2) and sample sg14, F&G model corrected ^{14}C ages and derived errors for all the remaining Saginaw aquifer samples along with all non-modern Marshall aquifer samples [*Ma et al.*, 2004] were subsequently converted to calibrated calendar ages (cal BP relative to AD 1950; Table C2) using the CALIB 6.1 program [*Stuiver and Reimer*, 1993] and IntCal'09 calibration dataset [*Reimer et al.*, 2009]. The low ^{14}C activity and high ^{14}C age (^{14}C age = 48060 ± 2720 yrs) displayed by sg14 fall beyond the calibration range (0 - 46400 ^{14}C yrs) for the IntCal'09 calibration dataset and indicates very old groundwater ages. Calendar age results for all other Saginaw aquifer samples (Table C2) show that as many as 15 out of 22 samples

range in age from modern to ~13.1kyrs. The remaining seven samples (sg8a, sg8b, sg10, sg13, sg14, sg15, sg16) display calibrated calendar ages beyond the Last Glacial Maximum.

C.4 Statistical Analysis of abrupt Climatic events

C.4.1 Introduction

As mentioned in Section 4.4, Saginaw and Marshall aquifer samples were combined to develop a detailed paleoclimatic record in southern Michigan since the LGM. Groundwater age distribution within this combined dataset indicates that most samples are not evenly distributed since the LGM (Figs. 4.3, 4.4). Instead, samples appear to be clustered around abrupt climatic events including the onset and termination of the Younger Dryas (YD) as well as the Mid-Holocene (MH) climatic events. In particular, the onset and termination of the YD at ~12,9kyrs BP and ~11,6kyrs BP, respectively, are each represented by five samples from the Saginaw and Marshall aquifers (Figs. 4.3, 4.4). Similarly, warming at the onset of the MH climatic event between ~5.4 kyrs BP and ~4.1 kyrs BP followed by subsequent cooling between ~4.1kyrs and 2.9kyrs BP are indicated by four samples each (Figs. 4.3, 4.4). In addition, most remaining samples used in the paleoclimatic reconstruction are modern in age with only a few samples displaying ages ≥ ~15 kyrs BP (m14a, m14b, m15) and two samples that are not representative of any particular climatic event described in this study (m2a, 2b).

Clustering of samples at these abrupt climatic shifts and, in particular, at the onset and termination of the YD can either be due to (1) a sampling bias related to the availability of wells to sample and authorization to go into the owner's properties to sample their groundwater; and/or (2) both the YD and MH climatic events were dry periods and therefore, it is expected that reduced recharge might have occurred during these periods which, in turn, drastically reduces the probability of finding groundwater with ages corresponding to the mid period of these climatic events. While hypothesis (2) seems more likely, it is not possible at present to determine why groundwater age distribution of the combined Marshall and Saginaw aquifer datasets is clustered around abrupt climatic shifts. However, such a clustered groundwater age distribution allows for a detailed reconstruction of the timing and magnitude of abrupt climatic oscillations if individual climatic events are statistically distinct. Statistical analyses of abrupt climatic events identified in this study are presented in detail below.

Abrupt climatic oscillations identified in this study (onset and termination of Younger Dryas and Mid-Holocene oscillations) are thought to have occurred on very short time scales [50-3000yrs; *Taylor et al.*, 1997, *Viau et al.*, 2006]. Because groundwater age dating through ^{14}C yields coarse age resolution (i.e., large age errors, cf. Table C2) and because NGT results from multiple samples may overlap within error for these temperature climatic perturbations, it is critical to: (1) identify whether samples within a specific time period (climatic event) represent actual variations in temperature or are simply representative of a single average temperature and; (2) whether ^{14}C age resolution is sufficient to distinguish between rapid climatic events that occur on short time scales such as the onset and termination of the Younger Dryas. Below, we test both

conditions through statistical analysis.

C.4.2 Do identified abrupt climatic events represent actual temperature (NGT) variations?

In order to test whether the abrupt cooling of the Younger Dryas (YD) identified through NGTs represents an actual climatic variation, a chi square test was performed on the samples falling within this time period (m12b, m12a, sg7, sg11, sg9, sg5a, sg5b, sg12a, m13, cf. Table C2, C4). The null hypothesis (H_0) tested is that NGTs from all samples within the YD represent one single temperature (weighted mean) while the alternate hypothesis (H_a) is that all samples do not represent one single temperature but instead, a range of temperatures representative of the climatic variations that took place during the YD. The null hypothesis is rejected if chi squared probability (p) is less than 0.05 or 5%. Chi square values were calculated as the sum of squared differences between measurements and weighted mean normalized by weighted standard deviation. A Chi square value of 18.7 is obtained for the tested group of YD samples. For eight degrees of freedom, this chi square value corresponds to a probability of less than 0.017. Because the calculated probability is less than 0.05, we can reject the null hypothesis and conclude that samples within the YD do indeed represent climatic variations 95% of the time.

A similar chi square test was performed on a group of six samples (m4a, m4b, sg6a, sg6b, sg4a, sg4b; cf. Tables C2, C4) within the Mid-Holocene assuming a similar null hypothesis (H_0) and similar rejection criterion ($p<0.05$). The sum of Chi-squares for the Mid-Holocene group of samples yields a value of 19.5 with a p value of 0.0015 for

five degrees of freedom. Because this p-value is less than the rejection criterion ($p<0.05$), we can reject the null hypothesis and conclude that all Mid-Holocene samples do not represent one single temperature but instead represent climatic variations at least 95% of the time.

This statistical analysis to both set of samples within the YD and mid-Holocene period allow us to state with confidence that NGT variations observed within these two periods are indeed representative of the climatic perturbations that took place during these two periods.

C.4.3 Is ^{14}C age resolution sufficient to distinguish between abrupt climatic events?

Because ^{14}C age resolution is relatively coarse, it is necessary to evaluate whether two groups of samples that represent closely timed climatic events have sufficient age resolution to distinguish between these events. For example, our climatic record shows a group of five samples (m12a, m12b, sg7, sg9, sg11) that likely represents the onset of the Younger Dryas (~12.9kyrs BP) while another group of four samples (sg12a, sg5a, sg5b, m13) likely represents the termination of the Younger Dryas (~11,6kyrs BP). Because these two events are closely timed (~1000yrs), it is important to distinguish whether ages within these two groups are statistically different, thus representing two individual climatic events or whether they represent climatic variations within a single climatic event. To address this issue we utilize a two-sample Z-statistical test to compare mean ages from the two groups of samples at the beginning and end of the Younger Dryas. We define the null hypothesis (H_0) as the mean ages in the two groups of samples that are not

different while the alternate hypothesis (H_a) is that mean ages in the two groups are indeed different and representative of individual climatic events. As indicated previously, we reject the null hypothesis at the 95% confidence level. Samples from the beginning of the Younger Dryas yield a mean age of 12949.8 yrs with a standard deviation of 84.55 yrs while samples at the end of the Younger Dryas yield a mean age of 11041yrs and standard deviation of 56.07 yrs. The two-sample Z-statistic yields a probability of less than 0.0001 that these two groups would have indistinguishable ages thus rejecting the null hypothesis. It is thus concluded that the two groups of samples at the beginning and end of the YD do indeed represent individual climatic events. Similarly, samples at the onset (m4a, m4b) and termination (sg4a, sg4b) of the mid-Holocene climatic event are also relatively closely timed (~2,400yrs). Similar to samples from the YD, we utilize a two-sample Z-statistical test to compare mean ages from the two groups of samples assuming a similar null hypothesis (H_0) and rejection criterion ($p<0.05$). Samples from the onset of the MH yield a mean age of 5339 yrs with a standard deviation of 844.5 yrs while samples at the end of the MH yield a mean age of 2940yrs and standard deviation of 1197 yrs. The two-sample Z-statistic yields a probability of 0.024 that these two groups would have indistinguishable ages, thus rejecting the null hypothesis. In addition, it was also concluded that samples from the beginning and end of the MH climatic event represent actual climatic variations. Combining statistical test results from NGTs and ages for MH samples, it can clearly be seen that observed rapid warming and cooling during this period are indeed representative of climatic oscillations.

C.5 Impact of dispersion on preservation of climatic signals from the Younger Dryas and Mid-Holocene in the Saginaw aquifer

To assess the impact of dispersion on the resolution of climatic records in confined aquifers, *Stute and Schlosser* [1993] simulated the smoothing of a periodic climatic signal through a one-dimensional approach. They concluded that high-frequency fluctuations occurring on a time scale ≤1kyrs have already completely disappeared at the very beginning of the record. Among their underlying assumptions was a constant pore velocity of 1 myr^{-1} throughout the aquifer. Preservation of high or low frequency climatic signals is intrinsically related to the specific hydrodynamic characteristics of each individual system. Many productive aquifers, including the Carrizo (e.g., *Castro et al*., 2007) and Saginaw (this study) aquifers have water velocities greater or far greater than the previously assumed value of 1m yr^{-1} by *Stute and Schlosser* [1993]. The critical parameters for a good preservation of the signal are the duration of the climatic perturbation and the pore velocity. Distance for which the signal will be preserved will increase with increased velocity. For a similar pore velocity, preservation of the signal will depend directly on the duration of the climatic perturbation (see, e.g., *Castro et al*., 2007).

Similarly to *Stute and Schlosser* [1993], *Castro et al.* [2007] analyzed the behavior of a periodic climate signal to describe, in their specific case, a fluctuation of noble gas concentrations in the water table translating into NGT variations. Such periodic behavior deals with a succession of peaks separated by a constant time interval T (period). As time since the initial pulse increases, partial superposition of the peaks will occur, leading to

smoothing and eventually a loss of signal. Castro et al. (2007) have shown that proper preservation of a periodic climate signal can be assessed in terms of the dimensionless number CG given by:

$$CG = \frac{VT}{\sqrt{\alpha Vt}} = \frac{VT}{\sqrt{\alpha L}} \quad (1)$$

where L is the distance covered by the signal, t is the time since the climatic event occurred, α is the longitudinal dispersivity, and V is the horizontal pore velocity. More specifically, their simulations have shown that the signal is almost entirely lost for CG=2.5, while extremely sharp for CG=5. Similar to the analysis by *Stute and Schlosser* [1993], their analysis assumed an average dispersivity value of 100 m. Below, following a similar approach to that of *Castro et al*. [2007] we determine the CG values for the Younger Dryas (YD) as well as the Mid-Holocene (MH) climatic shifts identified in the Saginaw and Marshall aquifers assuming that both are periodic rather than discrete climate events. Behavior of a discrete high frequency pulse signal (e.g., an abrupt change in climate such as the YD) is distinct and contrasts greatly with that one of a periodic signal. In particular, *Castro et al.* [2007] have shown that discrete signals are much better preserved over time than periodic climate signals. Below, we show that even in the event that the YD and MH climate events were periodic, their climate signals would have been preserved in the Saginaw and Marshall aquifers.

Average pore velocity in the study area of the Saginaw aquifer was determined by establishing the relationship between distance from the recharge area (northeast of Jackson, MI; cf. Table C1) for our samples located along the southern flow line (cf. Figure 4.1) and used in the paleoclimate reconstruction and their respective calendar ages

(Figure C3). This relationship yields a good positive linear correlation (r = 0.83) between both and indicates an average pore velocity of 5.37 m yr^{-1} in this region (cf. Figure C3). Linear correlation between age and recharge distance in the Saginaw aquifer is expected taking into account the homogenous nature of the aquifer (no change in lithology) and absence of major compaction due to its shallow nature. Similar to the analyses by *Stute and Schlosser* [1993] and *Castro et al.* [2007], an average dispersivity value of 100m is assumed in all the calculations below.

Our NGT record indicates that the YD climatic event occurred at ~13 kyrs BP and represents a perturbation that lasted ~1.3 kyrs (between 12.9 kyrs BP and 11.6 kyrs BP; T=2.6 kyrs). This yields a CG value of 5.3 for the YD and shows that the signal of this climatic event would still be extremely sharp even if such event was periodic rather than discrete. Similarly, our NGT record shows that the MH climatic event occurred at ~5.4 kyrs BP and represents a perturbation that lasted ~2.5 kyrs (between 5.4 kyrs BP and 2.9 kyrs BP; T=5 kyrs). This yields a CG=15.8 and suggests that the MH climatic signal is entirely preserved even in the event that such climate signal would have a periodic nature. Our analysis thus shows that both the YD and MH climatic events are well preserved in the noble gas record of the Saginaw aquifer system.

Groundwater flow in the Marshall aquifer is more complicated than in the Saginaw aquifer. In particular, there are two opposing flow directions from the south and the samples collected [*Ma et al.*, 2004], unlike most of the Saginaw samples do not belong to one single flow line but to parallel flow lines. Like the Saginaw, the Marshall is a homogenous aquifer composed of productive sandstone. Due to absence of both significant lithological changes and major compaction due to its shallow depth (≤~170m

in our study area), an approximate linear relationship between age and recharge distance is thus expected. Following a similar procedure to that of the Saginaw aquifer (above), calendar ages for all samples were plotted versus recharge distance. Because a lower bound for pore velocity is the critical factor for the dispersion analysis, we looked for a linear relationship providing the lowest pore velocity (cf. Figure S4). The lowest pore velocity value is 2.9 m $yr^{-1}$and this value was used in the calculations of the CG parameter. This represents the most conservative scenario. This yields a CG value of 3.9 for the YD and shows that the signal of this climatic event would still be preserved even if such an event was periodic rather than discrete (see, e.g., *Castro et al*., 2007). In addition, the MH displays a CG value of 11.7 and suggests that the MH climatic signal would be entirely preserved even in the event that such a climate signal was periodic. Our analysis thus shows that both the YD and MH climatic events are also well preserved in the noble gas record of the Marshall aquifer system.

C.6 Description of Table C1

Table C.1. Sample numbers, location, distance from recharge area and measured Ne, Ar, Kr and Xe elemental concentrations.

Column 1, 'Sample_Number', sample number.

Column 2, 'Lat.', Latitude of sample location, in degrees North.

Column 3, 'Long.', Longitude of sample location, in degrees West.

Column 4, 'Rech. Dist.', Distance from recharge area, in Kms.

Column 5, 'Ne', measured volume of Ne, in 1e-7 ccSTP/g, 1.3%, 1 sigma error.

Column 6, 'Ar', measured volume of Ar, in 1e-4 ccSTP/g, 1.3%, 1 sigma error.

Column 7, 'Kr', measured volume of Kr, in 1e-7 ccSTP/g, 1.5%, 1 sigma error.

Column 8, 'Xe', measured volume of Xe, in 1e-8 ccSTP/g, 2.2%, 1 sigma error.

Column 9, 'delta Ne (0)', Ne concentrations relative to modern day recharge conditions (275m, 9.1 degrees C), in %.

Table C1. Sample numbers, location, distance from recharge area and measured Ne, Ar, Kr and Xe elemental concentrations.

Column 1 Sample_Number	Column 2 Lat.	Column 3 Long.	Column 4 Rech. Dist.	Column 5 Ne	Column 6 Ar	Column 7 Kr	Column 8 Xe	Column 9 ΔNe(0)
Samples with groundwater ages younger than the LGM								
sg1a	42.53	-84.39	19	0.868	2.675	0.726	1.273	-56
sg1b	"	"	"	1.108	3.186	0.891	1.502	-44
sg2	42.6	-84.4	28	2.55	4.246	0.939	1.47	30
sg3	42.68	-84.41	37	2.642	4.864	1.105	1.426	34
sg4a	42.68	-84.62	39	2.666	4.786	1.079	1.643	35
sg4b	"	"	"	2.546	4.669	1.069	1.634	29
sg5a	42.85	-84.52	57	2.479	4.207	0.994	1.706	26
sg5b	"	"		2.778	4.709	1.096	1.806	41
sg6a	42.93	-84.53	65	2.753	4.796	1.079	1.532	40
sg6b	"	"	"	2.835	4.711	1.055	1.515	44
sg7	43.01	-84.54	74	2.699	4.661	1.061	1.711	37
sg9	43.24	-84.32	96	3.157	5.146	1.161	1.927	60
sg11	43.45	-84.31	112	3.168	5.332	1.157	1.727	61
sg12a	42.83	-84.43	53	2.756	4.771	1.114	1.829	40
sg12b	"	"		1.713	2.729	0.639	1.07	-13
Samples with groundwater ages beyond the LGM								
sg8a	43.21	-84.3	95	3.685	6.251	1.375	2.052	87
sg8b	"	"	"	3.683	6.311	1.392	2.108	87
sg10	43.38	-84.11	120	3.75	6.254	1.331	1.575	90
sg13	43.51	-84.06	133	3.189	5.177	1.175	1.855	62
sg14	43.65	-84.16	137	4.295	7.236	1.359	1.78	118
sg15	43.72	-83.97	155	4.418	7.198	1.482	1.673	124
sg16	43.73	-83.97	155	4.394	7.267	1.545	2.015	123
ASW 275m, 9.1°C, 0M NaCl	*	*		1.969	3.815	0.906	1.323	*

C.7 Description of Table C2

Table C2. Measured stable isotopic composition of Saginaw and Marshall [Ma et al., 2004] aquifer samples from all sampling sites along with measured carbon isotopic data. Also shown are 14C age results (+/-1 sigma) from the Fontes and Garnier correction model along with calibrated calendar ages (+/-1 sigma).

Column 1, 'Sample_number', sample number.

Column 2, 'del18O', oxygen stable isotopic composition, per mil relative to VSMOW.

Column 3, 'err_del18O', uncertainty in oxygen stable isotopic composition, per mil, 1 sigma error.

Column 4, 'del_D', hydrogen stable isotopic composition, per mil relative to VSMOW.

Column 5, 'err_del_D', uncertainty in hydrogen stable isotopic composition, per mil, 1 sigma error.

Column 6, 'd-excess', deuterium excess, in per mil.

Column 7, 'NOSAMS_references', accession number of 14C measurement at NOSAMS facility, Woods Hole Oceanographic Institution.

Column 8, 'del_13C', carbon stable isotopic composition, per mil.

Column 9, '14C', measured 14C activity, percentage modern carbon.

Column 10, 'err_14C', uncertainty in measured 14C activity, percentage modern carbon.

Column 11, 'F_G_14C_age', calculated 14C groundwater ages (Fontes and Garnier, 1979), 14C years.

Column 12, 'err_F_G_age', uncertainty in calculated 14C groundwater ages, 14C years, 1 sigma error.

Column 13, 'Calibrated_Age', Calibrated calendar ages using the IntCal'09 calibration dataset, cal BP relative to AD 1950.

Column 14, 'Lower_bound', lower bound uncertainty in calibrated calendar ages, cal. BP yrs, 1 sigma error.

Column 15, 'Upper_bound', upper bound uncertainty in calibrated calendar ages, cal. BP yrs, 1 sigma error.

Table C2. Measured stable isotopic composition of Saginaw and Marshall [*Ma et al*., 2004] aquifer samples from all sampling sites along with measured carbon isotopic data. Also shown are 14C age results (+/-1 sigma) from the Fontes and Garnier correction model along with calibrated calendar ages (+/-1 sigma).

Table C2.

Column 1	Column 2	Column 3	Column 4	Column 5	Column 6	Column 7	Column 8	Column 9
Sample_number	del18O	err_del18O	del_D	err_del_D	d-excess	NOSAMS_references	del_13C	14C
sg1a	-9.65	0.06	-64	0.26	13.2	OS- 72903	-10.1	58.50%
sg1b	"	"	"	"	"	"	"	"
sg2	-8.83	0.11	-61.01	1.09	9.63	OS- 72399	-11.75	86.10%
sg3	-9.43	0.11	-65.52	0.63	9.92	OS- 72400	-13.44	43.40%
sg4a	-8.49	0.04	-59.17	0.73	8.75	OS- 72904	-13.84	51.60%
sg4b	"	"	"	"	"	"	"	"
sg5a	-8.99	0.02	-61.93	0.39	9.99	OS- 72905	-12.62	18.80%
sg5b	"	"	"	"	"	"	"	"
sg6a	-9.07	0.07	-62.2	0.75	10.36	OS- 72906	-14.09	46.70%
sg6b	"	"	"	"	"	"	"	"
sg7	-9.47	0.09	-65.14	0.67	10.62	OS- 72401	-14.09	19.00%
sg8a	-13.74	0.1	-101.4	0.74	8.48	OS- 73092	-10.77	1.20%
sg8b	"	"	"	"	"	"	"	"
sg9	-10.52	0.06	-73.59	0.59	10.57	OS- 72402	-12.12	15.10%
sg10	-12.83	0.11	-89.86	1.31	12.74	OS- 72403	-10.93	3.40%
sg11	-10.27	0.07	-73.04	0.67	9.12	OS- 72774	-13.13	17.30%
sg12a	-9.1	0.11	-63	0.87	9.8	OS- 72907	-12.65	18.70%
sg12b	"	"	"	"	"	"	"	"
sg13	-11.04	0.11	-79.57	0.55	8.75	OS- 72404	-12.23	0.30%
sg14	-14.3	0.07	-100.89	0.46	13.51	OS- 72405	-12.74	0.20%
sg15	-17.48	0.05	-124.03	0.62	15.81	OS- 72908	-11.73	1.40%
sg16	-15.98	0.11	-118.62	0.43	9.18	OS- 72406	-11.66	0.40%
Marshall samples[a]								
m1	-9.1	0.1	-62.8	1.00	10	OS-41508	-11.9	64%
m2a	-9	0.1	-61.9	1.00	10.1	OS-41509	-13.5	31.80%
m2b	null	null	null	null	10.1	null	null	null
m3	-9.6	0.1	-63.1	1.00	13.7	OS-41510	-12.1	49.60%
m4a	-9.3	0.1	-61.6	1.00	12.8	OS-41511	-13.6	36.10%
m4b	null	null	null	null	12.8	null	null	null
m6	-9.1	0.1	-63.4	1.00	9.4	OS-41512	-10.2	61.10%
m7	-9.1	0.1	-61.8	1.00	11	OS-41513	-11.7	61.60%
m8	-9.3	0.1	-62.4	1.00	12	OS-41514	-10	56.10%
m9	-9	0.1	-62.1	1.00	9.9	OS-41515	-12.6	59.40%
m10a	-10.8	0.1	-77.3	1.00	9.1	OS-41516	-13.2	30.40%
m10b	null	null	null	null	9.1	null	null	null
m11	-9.8	0.1	-67.2	1.00	11.2	OS-41517	-11.8	52.40%
m12a	-8.8	0.1	-58	1.00	12.4	OS-41641	-13.4	17.80%
m12b	null	0.1	null	1.00	12.4	null	null	null
m13	-8.6	0.1	-56.7	1.00	12.1	OS-41642	-13.5	21.80%
m14a	-8.7	0.1	-56.3	1.00	13.3	OS-41643	-14.3	9.30%
m14b	null	0.1	null	1.00	13.3	null	null	null
m15	-8.8	0.1	-61.1	1.00	9.3	OS-41644	-12.5	12.50%

[a]Data from Ma et al., 2004

Table C2.

Column 10	Column 11	Column 12	Column 13	Column 14	Column 15
err_14C	F_G_^{14}C_age	err_F_G_age	Calibrated_Age	Lower_bound	Upper_bound
0.30%	modern	-	modern	-	-
"	"	"	"	"	"
0.30%	modern	-	modern	-	-
0.20%	3604	779	3976	2948	4886
0.20%	2726	1026	2940	1690	4084
"	"	"	"	"	"
0.20%	9645	514	11065	10256	11765
"	"	"	"	"	"
0.20%	3703	1042	4096	2844	5327
"	"	"	"	"	"
0.10%	11174	1091	13060	11308	14256
0.00%	30605	299	35092	34719	35324
"	"	"	"	"	"
0.10%	10928	227	12818	12638	13071
0.10%	22156	126	26647	26278	26802
0.10%	11085	789	12899	11802	13862
0.10%	9659	453	11076	10392	11725
"	"	"	"	"	"
0.00%	42614	1165	45937	44794	46823
0.10%	48060	2720	Outside calculation range		
0.00%	30471	374	35014	34631	35281
0.00%	41726	531	45179	44771	45571
0.30%	modern	null	modern	null	null
0.20%	6046	674	6855	6188	7583
null	null	null	null	null	null
0.30%	780	800	930	251	1341
0.10%	4726	699	5339	4524	6211
null	null	null	null	null	null
0.20%	modern	null	modern	null	null
0.30%	modern	null	modern	null	null
0.20%	modern	null	modern	null	null
0.20%	modern	null	modern	null	null
0.10%	6377	663	7194	6498	7852
null	null	null	null	null	null
0.20%	432	780	687	-4	979
0.10%	11142	658	12976	12141	13781
null	null	null	null	null	null
0.20%	9558	667	10957	10148	11982
0.10%	17384	655	20734	19908	21470
null	null	null	null	null	null
0.10%	12778	784	15265	14126	16452

C.8 Description of Table C3

Table C3. Measured major ion data along with calculated aqueous carbonate speciation.

Column 1, 'Sample_number', sample number.

Column 2, 'pH', pH measured during sampling.

Column 3, 'Sam_Temp', groundwater temperature measured during sampling, degrees C.

Column 4, 'Alk', measured carbonate alkalinity, meq/kg.

Column 5, 'Ca', calcium concentration, millimole/L.

Column 6, 'Na', sodium concentration, millimole/L.

Column 7, 'K', potassium concentration, millimole/L.

Column 8, 'Mg', magnesium concentration, millimole/L.

Column 9, 'Cl', chloride concentration, millimole/L.

Column 10, 'Fe', total Iron concentration, millimole/L.

Column 11, 'SO4', SO4 concentration, millimole/L.

Column 12, 'Si', total silica concentration, millimole/L.

Column 13, 'NO3', NO3 concentration, millimole/L.

Column 14, 'Al', total aluminium concentration, millimole/L.

Column 15, 'B', total boron concentration, millimole/L.

Column 16, 'Ba', total barium concentration, millimole/L.

Column 17, 'Br', total bromide concentration, millimole/L.

Column 18, 'F', total fluoride concentration, millimole/L.

Column 19, 'Li', total lithium concentration, millimole/L.

Column 20, 'Mn', total manganese concentration, millimole/L.

Column 21, 'Sr', total strontium concentration, millimole/L.

Column 22, 'Zn', total zinc concentration, millimole/L.

Column 23, 'TDIC', dissolved inorganic carbon calculated in Web-phreeq, mM.

Column 24, 'H2CO3', H2CO3 concentration calculated in Web-phreeq, mM.

Column 25, 'HCO3-', HCO3- concentration caculated in Web-phreeq, mM.

Column 26, 'CO3 2-', CO3 2- concentration caculated in Web-phreeq, mM.

Column 27, 'Log_PCO2', CO2 partial pressure calculated in Web-phreeq, atm.

Column 28, 'Salinity', measured salinity data in g/l.

Table C3.

Column 1	Column 2	Column 3	Column 4	Column 5	Column 6	Column 7	Column 8	Column 9	Column 10	Column 11	Column 12	Column 13
Sample Number	pH	Sam Temp	Alk	Ca	Na	K	Mg	Cl	Fe	SO4	Si	NO3
		*C	mM	mM	mM	mM	mM	mM	mM	mM	mM	mM
sg1	7.58	9.1	5.9000	2.8088	0.2262	0.0246	1.5834	0.7242	0.0199	1.1940	0.2900	0.0000
sg2	7.65	9.3	5.3411	1.6977	0.6969	0.0632	0.9835	0.3502	0.0061	0.3710	0.1403	0.0000
sg3	7.57	10.3	4.8979	1.6759	0.5120	0.1407	0.5225	0.0883	0.0036	0.1269	0.1708	0.0000
sg4	7.81	8	4.3435	0.0226	5.6769	0.0263	0.0138	0.1112	0.0087	0.4717	0.2072	0.0000
sg5	7.54	14.8	4.3589	1.3986	0.2209	0.0742	1.0148	0.0791	0.0003	0.1510	0.1321	0.0113
sg6	7.68	9.4	6.3395	1.3321	0.7086	0.0558	1.5281	0.0296	0.0089	0.1291	0.2032	0.0000
sg7	7.85	11.3	4.3417	0.7665	2.0322	0.0391	0.5929	0.0614	0.0030	0.2702	0.2283	0.0000
sg8	7.43	5.5	3.8373	3.0354	7.8265	0.0946	1.4822	5.1540	0.0082	4.4566	0.1675	0.0093
sg9	7.59	6.9	3.7988	2.8971	2.5850	0.0419	1.0440	0.4589	0.0017	3.5187	0.1996	0.0000
sg10	8.1	5.7	3.7072	0.7345	25.2004	0.2509	0.4268	20.9891	0.0015	2.6937	0.1063	0.0000
sg11	7.8	7.2	4.5000	1.3159	3.4220	0.0537	0.8798	1.6696	0.0005	0.8008	0.1722	0.0038
sg12	7.46	14	4.9750	1.4506	0.2723	0.0821	0.9648	0.0346	0.0385	0.2130	0.1501	0.0000
sg13	8.32	19.8	4.5452	0.1976	9.0993	0.0432	0.1829	2.1606	0.0009	1.4519	0.1543	0.0037
sg14	8.19	9.8	5.4787	0.4201	21.1356	0.1299	0.1312	15.5744	0.0143	1.2404	0.1014	0.0000
sg15	8	9.4	3.3837	1.2477	19.0928	0.1977	0.5752	18.2156	0.0036	1.6121	0.1051	0.0000
sg16	7.95	9.1	3.3452	2.3223	67.4188	0.3462	1.0971	63.9365	0.0137	1.8321	0.1023	0.0000

Table C3.

Column 14	Column 15	Column 16	Column 17	Column 18	Column 19	Column 20	Column 21	Column 22	Column 23	Column 24	Column 25
Al	B	Ba	Br	F	Li	Mn	Sr	Zn	TDIC	H2CO3	HCO_3^-
mM	mM	mM	mM	mM	mM	mM	mM	mM	mM	mM	mM
0.0006	0.0012	0.0009	0.0000	0.0019	0.0003	0.0004	0.0014	0.0002	6.255	0.3965	5.686
-0.0005	0.0101	0.0000	0.0000	0.0019	0.0014	0.0003	0.0019	0.0002	5.627	0.3128	5.2
0.0024	0.1373	0.0006	0.0000	0.0056	0.0052	0.0002	0.0413	0.0001	5.207	0.3404	4.777
0.0013	0.0149	0.0000	0.0000	0.0040	-0.0005	0.0000	0.0001	0.0051	4.504	0.1868	4.289
0.0004	0.0451	0.0009	0.0000	0.0047	0.0027	0.0001	0.0099	0.0027	4.635	0.2955	4.245
0.0011	0.0130	0.0015	0.0000	0.0071	0.0035	0.0004	0.0156	0.0001	6.645	0.344	6.151
0.0007	0.0277	0.0007	0.0000	0.0108	0.0009	0.0003	0.0077	0.0001	4.468	0.1561	4.244
-0.0003	0.0223	0.0001	0.0067	0.0027	0.0044	0.0005	0.0101	0.0004	4.215	0.3895	3.729
-0.0007	0.0054	0.0001	0.0000	0.0041	0.0000	0.0003	0.0088	0.0007	4.047	0.2631	3.694
-0.0005	0.1284	0.0000	0.0164	0.0045	0.0095	0.0004	0.0047	0.0049	3.749	0.07806	3.583
0.0015	0.0231	0.0004	0.0063	0.0042	0.0031	0.0003	0.0058	0.0005	4.666	0.1951	4.383
-0.0003	0.0295	0.0010	0.0000	0.0043	0.0028	0.0013	0.0104	0.0018	5.343	0.4098	4.831
-0.0006	0.0346	0.0002	0.0049	0.0118	0.0008	0.0000	0.0024	0.0003	4.517	0.0455	4.376
0.0002	0.0962	0.0002	0.0210	0.0085	0.0048	0.0002	0.0031	0.0001	5.497	0.08632	5.296
0.0009	0.1201	0.0004	0.0214	0.0031	0.0080	0.0003	0.0122	0.0001	3.43	0.08271	3.264
0.0007	0.0756	0.0005	0.0788	0.0030	0.0191	0.0005	0.0228	0.0032	3.39	0.08344	3.152

Table C3.

Column 26	Column 27	Column 28
CO_3^{2-}	Log_P_{CO2}	Salinity
10^{-6} M	atms	g/l
9.512	-2.14	0.65
9.767	-2.24	0.48
7.517	-2.19	0.40
10.73	-2.49	0.44
7.053	-2.19	0.36
12.47	-2.2	0.50
12.89	-2.52	0.38
4.293	-2.21	1.18
6.059	-2.36	0.78
20.5	-2.9	1.85
11.1	-2.48	0.56
6.576	-2.06	0.41
52.41	-2.94	0.71
40.42	-2.8	1.51
16.12	-2.82	1.51
16.89	-2.81	4.32

C.9 Description of Table C4

Results of inverse fitting measured noble gas concentrations for all Saginaw samples using the unfractionated air (UA) and oxygen depletion (OD) models assuming a recharge altitude of 275m, 0g/l salinity. Samples that do not converge using a specific model are indicated as '*' along with samples that display groundwater ages beyond the last glacial maximum (LGM). Mean squared weighted deviates for all samples as well as groups of young and old samples are also indicated. OD model results for Marshall samples at a recharge altitude of 300m and POD factor of 1.085 are also indicated.

Column 1, 'Sample_number', sample number.

Column 2, 'UA_NGT', fitted UA model noble gas temperatures (NGTs), in degrees C.

Column 3, 'UA_NGT_err', uncertainty of UA model NGTs in degrees C, 1 sigma error.

Column 4, 'UA_EA', fitted UA model excess air volume, ccSTP/g.

Column 5, 'UA_EA_err', uncertainty of UA model excess air volume, ccSTP/g, 1 sigma error.

Column 6, 'UA_Chi2', UA model chi-squared goodness of fit, no units.

Column 7, 'P_OD', assumed OD factor for inverse OD model fit, no units.

Column 8, 'OD_NGT', fitted OD NGT assuming P_OD in Column 7, in degrees C.

Column 9, 'EA', fitted OD model excess air volume assuming P_OD in Column 7, in ccSTP/g.

Column 10, 'err_NGT', uncertainty of OD model NGTs in degrees C for P_OD in Column 7, 1 sigma error.

Column 11, 'err_EA', uncertainty of OD model excess air volume for P_OD in Column 8.7, ccSTP/g, 1 sigma error.

Column 12, 'Chi square', OD model chi-squared goodness of fit for P_OD in Column 7, no units.

Column 13, 'P_OD', assumed OD factor for inverse OD model fit, no units.

Column 14, 'OD_NGT', fitted OD NGT assuming P_OD in Column 13, in degrees C.

Column 15, 'EA', fitted OD model excess air volume assuming P_OD in Column 13, in ccSTP/g.

Column 16, 'err_NGT', uncertainty of OD model NGTs in degrees C for P_OD in Column 13, 1 sigma error.

Column 17, 'err_EA', uncertainty of OD model excess air volume for P_OD in Column 13, ccSTP/g, 1 sigma error.

Column 18, 'Chi square', OD model chi-squared goodness of fit for P_OD in Column 13, no units.

Column 19, 'P_OD', assumed OD factor for inverse OD model fit, no units.

Column 20, 'OD_NGT', fitted OD NGT assuming P_OD in Column 19, in degrees C.

Column 21, 'EA', fitted OD model excess air volume assuming P_OD in Column 19, in ccSTP/g.

Column 22, 'err_NGT', uncertainty of OD model NGTs in degrees C for P_OD in Column 19, 1 sigma error.

Column 23, 'err_EA', uncertainty of OD model excess air volume for P_OD in Column 19, ccSTP/g, 1 sigma error.

Column 24, 'Chi square', OD model chi-squared goodness of fit for P_OD in Column 19, no units.

Column 25, 'P_OD', assumed OD factor for inverse OD model fit, no units.

Column 26, 'OD_NGT', fitted OD NGT assuming P_OD in Column 25, in degrees C.

Column 27, 'EA', fitted OD model excess air volume assuming P_OD in Column 25, in ccSTP/g.

Column 28, 'err_NGT', uncertainty of OD model NGTs in degrees C for P_OD in Column 25, 1 sigma error.

Column 29, 'err_EA', uncertainty of OD model excess air volume for P_OD in Column 25,

ccSTP/g, 1 sigma error.

Column 30, 'Chi square', OD model chi-squared goodness of fit for P_OD in Column 25, no units.

Column 31, 'P_OD', assumed OD factor for inverse OD model fit, no units.

Column 32, 'OD_NGT', fitted OD NGT assuming P_OD in Column 31, in degrees C.

Column 33, 'EA', fitted OD model excess air volume assuming P_OD in Column 31, in ccSTP/g.

Column 34, 'err_NGT', uncertainty of OD model NGTs in degrees C for P_OD in Column 31, 1 sigma error.

Column 35, 'err_EA', uncertainty of OD model excess air volume for P_OD in Column 31, ccSTP/g, 1 sigma error.

Column 36, 'Chi square', OD model chi-squared goodness of fit for P_OD in Column 31, no units.

Column 37, 'Sample', Marshall sample name, no units.

Column 38, 'P_OD', OD model factor, P_OD assumed, no units.

Column 39, 'OD_NGT', fitted OD NGT assuming P_OD in Column 38, in degrees C.

Column 40, 'OD_NGT_err', uncertainty of OD model NGTs in degrees C for P_OD in Column 38, 1 sigma error.

Column 41, 'OD_EA', fitted OD model excess air volume assuming P_OD in Column 38, in ccSTP/g.

Column 42, 'OD_EA_err', uncertainty of OD model excess air volume for P_OD in Column 38, ccSTP/g, 1 sigma error.

Table C4.

Column 1	Column 2	Column 3	Column 4	Column 5	Column 6	Column 7	Column 8
Sample_number	UA_NGT	UA_NGT_err	UA_EA	UA_EA_err	UA_Chi2	P_OD	OD_NGT (˚C)
Samples with groundwater ages younger than the LGM							
sg1a	*	*	*	*	*	1	*
sg1b	*	*	*	*	*	1	*
sg5a	5.9	1.5	2.31E-03	8.34E-04	38.60	1	6.03339
sg2	8.0	0.8	3.08E-03	4.28E-04	9.70	1	8.14104
sg4a	3.7	0.6	3.27E-03	3.60E-04	6.30	1	3.82095
sg4b	3.9	0.5	2.61E-03	2.72E-04	3.90	1	3.98432
sg5b	3.2	0.9	3.68E-03	5.67E-04	14.40	1	3.32835
sg6a	4.5	0.8	3.91E-03	4.94E-04	11.30	1	4.57363
sg6b	5.4	0.6	4.44E-03	3.60E-04	5.70	1	5.42279
sg7	4.1	0.8	3.41E-03	4.59E-04	10.00	1	4.18882
sg9	1.6	0.9	5.59E-03	6.58E-04	15.30	1	1.7899
sg11	2.2	1.0	5.93E-03	6.94E-04	17.00	1	2.33341
sg12a	2.7	0.8	3.50E-03	5.10E-04	11.80	1	2.77335
sg12b	*	*	*	*	*	1	*
Samples with groundwater ages beyond the LGM							
sg8a	-2.4	1.1	8.18E-03	9.38E-04	23.2	1	-2.41493
sg8b	-2.9	1.0	8.07E-03	9.08E-04	21.7	1	-2.90896
sg10	1.1	3.0	9.49E-03	2.51E-03	162.6	1	1.09426
sg13	1.7	0.5	5.82E-03	3.86E-04	5.2	1	1.7344
sg14	-0.8	3.3	1.25E-02	3.20E-03	204.2	1	-0.84329
sg15	-0.8	3.8	1.33E-02	3.67E-03	255.2	1	-0.82978
sg16	-3.9	2.3	1.23E-02	2.42E-03	111.6	1	-3.87207
Sum of Chi2 for all samples					927.70		
n					18		
MSWD_all samples					25.77		
Sum of Chi2 for old samples					783.700		
n					7		
MSWD_old samples					55.98		
Sum of Chi2 for young samples					144.00		
n					11		
MSWD_young samples					6.55		

Table C4.

Column 9 Exc. Air	Column 10 err_NGT	Column 11 err_EA	Column 12 Chi square	Column 13 P_OD	Column 14 OD_NGT (˚C)	Column 15 Exc. Air
*	*	*	*	1.05	*	*
*	*	*	*	1.05	*	*
2.29E-03	1.482	9.58E-04	39.4	1.05	7.51012	1.90E-03
3.10E-03	0.82202	5.21E-04	11.2	1.05	9.63854	2.70E-03
3.31E-03	0.59598	4.31E-04	7.0	1.05	5.22485	2.90E-03
2.64E-03	0.47122	3.28E-04	4.4	1.05	5.3945	2.23E-03
3.68E-03	0.88961	6.65E-04	15.3	1.05	4.7392	3.28E-03
3.95E-03	0.76831	5.60E-04	11.2	1.05	5.98093	3.54E-03
4.47E-03	0.56279	4.10E-04	5.7	1.05	6.84928	4.06E-03
3.43E-03	0.77086	5.55E-04	11.3	1.05	5.61108	3.03E-03
5.61E-03	0.9351	7.93E-04	17.1	1.05	3.16544	5.20E-03
6.01E-03	0.95429	8.08E-04	17.7	1.05	3.69786	5.59E-03
3.50E-03	0.79796	6.01E-04	12.7	1.05	4.17242	3.10E-03
*	*	*	*	1.05	*	*
8.18E-03	1.06334	9.38E-04	23.2	1.05	-1.14526	7.74E-03
8.07E-03	1.01878	9.08E-04	21.7	1.05	-1.64608	7.64E-03
9.49E-03	3.01891	2.51E-03	162.6	1.05	2.38432	9.05E-03
5.82E-03	0.53805	3.86E-04	5.2	1.05	3.10321	5.41E-03
1.25E-02	3.34327	3.20E-03	204.2	1.05	0.41279	1.20E-02
1.33E-02	3.754	3.67E-03	255.2	1.05	0.40888	1.28E-02
1.23E-02	2.32537	2.42E-03	111.6	1.05	-2.65974	1.18E-02
			936.66			
			18			
			26.76			
			783.659			
			7			
			60.28			
			153.00			
			11			
			7.29			

Column 16	Column 17	Column 18	Column 19	Column 20	Column 21	Column 22
err_NGT	err_EA	Chi square	P_OD	OD_NGT (˚C)	Exc. Air	err_NGT
*	*	*	1.1	*	*	*
*	*	*	1.1	*	*	*
1.60285	1.02E-03	44.17	1.1	8.94786	1.51E-03	1.72384
0.87759	5.46E-04	12.19	1.1	11.0966	2.31E-03	0.94198
0.56679	4.02E-04	6.07	1.1	6.59089	2.50E-03	0.55185
0.45345	3.10E-04	3.93	1.1	6.76675	1.83E-03	0.45532
0.98397	7.22E-04	17.98	1.1	6.1121	2.88E-03	1.08066
0.68514	4.90E-04	8.52	1.1	7.35034	3.14E-03	0.60367
0.48176	3.45E-04	3.98	1.1	8.23757	3.66E-03	0.40609
0.83558	5.91E-04	12.74	1.1	6.9952	2.63E-03	0.90726
1.00528	8.37E-04	18.97	1.1	4.50351	4.79E-03	1.08021
0.90712	7.54E-04	15.39	1.1	5.02501	5.18E-03	0.86573
0.8863	6.55E-04	15.04	1.1	5.53372	2.69E-03	0.97782
*	*	*	1.1	*	*	*
1.00013	8.67E-04	19.76	1.1	0.0888	7.32E-03	0.94
0.9598	8.41E-04	18.58	1.1	-0.41872	7.21E-03	0.90463
2.97169	2.43E-03	151.91	1.1	3.63837	8.63E-03	2.92512
0.58854	4.15E-04	5.93	1.1	4.435	5.00E-03	0.65149
3.3157	3.12E-03	193.74	1.1	1.6332	1.16E-02	3.28884
3.72089	3.58E-03	242.09	1.1	1.61221	1.24E-02	3.68828
2.27136	2.33E-03	102.82	1.1	-1.48221	1.14E-02	2.21813
		893.81				
		18				
		25.54				
		734.84				
		7				
		56.53				
		158.98				
		11				
		7.57				

Table C4.

Column 23	Column 24	Column 25	Column 26	Column 27	Column 28	Column 29	Column 30	Column 31
err_EA	Chi square	P_OD	OD_NGT (°C)	Exc. Air	err_NGT	err_EA	Chi square	P_OD
*	*	1.15	*	*	*	*	*	1.2
*	*	1.15	*	*	*	*	*	1.2
1.07E-03	48.97	1.15	10.34963	1.12E-03	1.84488	1.13E-03	53.82	1.2
5.75E-04	13.46	1.15	12.51819	1.93E-03	1.01331	6.06E-04	14.95	1.2
3.85E-04	5.53	1.15	7.92203	2.10E-03	0.55189	3.78E-04	5.32	1.2
3.06E-04	3.81	1.15	8.10404	1.44E-03	0.47609	3.14E-04	4.00	1.2
7.78E-04	20.83	1.15	7.45003	2.48E-03	1.17895	8.34E-04	23.82	1.2
4.24E-04	6.36	1.15	8.68481	2.74E-03	0.52419	3.62E-04	4.61	1.2
2.85E-04	2.72	1.15	9.59061	3.26E-03	0.35528	2.45E-04	1.82	1.2
6.29E-04	14.42	1.15	8.34414	2.23E-03	0.98416	6.71E-04	16.31	1.2
8.83E-04	21.05	1.15	5.80708	4.38E-03	1.15877	9.31E-04	23.30	1.2
7.07E-04	13.49	1.15	6.31779	4.77E-03	0.83067	6.67E-04	11.96	1.2
7.10E-04	17.58	1.15	6.86024	2.30E-03	1.0715	7.64E-04	20.30	1.2
*	*	1.15	*	*	*	*	*	1.2
8.02E-04	16.83	1.15	1.29009	6.90E-03	0.88324	7.42E-04	14.34	1.2
7.80E-04	15.92	1.15	0.77597	6.79E-03	0.85367	7.25E-04	13.69	1.2
2.35E-03	142.01	1.15	4.85928	8.21E-03	2.87912	2.28E-03	132.86	1.2
4.51E-04	6.99	1.15	5.73267	4.60E-03	0.72331	4.92E-04	8.29	1.2
3.05E-03	184.09	1.15	2.8208	1.12E-02	3.26264	2.98E-03	175.12	1.2
3.49E-03	229.92	1.15	2.78305	1.19E-02	3.65614	3.41E-03	218.57	1.2
2.24E-03	94.78	1.15	-0.33669	1.09E-02	2.1656	2.16E-03	87.39	1.2
	858.74						830.47	
	18						18	
	24.54						23.73	
	690.53						650.26	
	7						7	
	53.12						50.02	
	168.20						180.21	
	11						11	
	8.01						8.58	

Table C4.

Column 32	Column 33	Column 34	Column 35	Column 36		Column 38	Column 39	Column 40	Column 41
OD_NGT (˚C)	Exc. Air	err_NGT	err_EA	Chi square		Sample	P_OD	OD_NGT	OD_NGT_err
						Marshall samples fit to OD model assuming a recharge altitude of 300m			
*	*	*	*	*		***(Ma et al., 2004) and a P_{OD} factor of 1.085 (Sun et al., 2010)***			
*	*	*	*	*		m1	1.085	9.3	1.1
11.71803	7.39E-04	1.9659	1.18E-03	58.70		m2a	1.085	5.8	1.0
13.90592	1.55E-03	1.09007	6.40E-04	16.62		m2b	1.085	5.5	0.7
9.22086	1.71E-03	0.56656	3.81E-04	5.39		m3	1.085	8.3	1.1
9.40894	1.05E-03	0.51311	3.33E-04	4.47		m4a	1.085	5.3	0.3
8.7556	2.09E-03	1.27835	8.88E-04	26.95		m4b	1.085	4.8	0.4
9.98693	2.35E-03	0.44728	3.04E-04	3.23		m6	1.085	8.9	1.0
10.911	2.87E-03	0.36216	2.45E-04	1.24		m7	1.085	9.6	1.0
9.66051	1.84E-03	1.06501	7.13E-04	18.38		m8	1.085	7.4	0.4
7.07873	3.99E-03	1.24015	9.79E-04	25.71		m9	1.085	6.9	0.3
7.57879	4.37E-03	0.80251	6.33E-04	10.76		m11	1.085	6.4	0.3
8.15455	1.90E-03	1.16669	8.17E-04	23.16		m12a	1.085	6.3	0.8
*	*	*	*	*		m12b	1.085	7.3	0.4
						m13	1.085	5.1	0.9
2.46111	6.48E-03	0.83022	6.86E-04	12.24		m14a	1.085	3.4	1.0
1.94048	6.37E-03	0.80739	6.75E-04	11.83		m14b	1.085	3.6	0.3
6.04955	7.79E-03	2.83365	2.21E-03	124.39		m15	1.085	4.6	0.3
6.99881	4.20E-03	0.80136	5.36E-04	9.79					
3.97808	1.07E-02	3.23705	2.91E-03	166.76					
3.92387	1.15E-02	3.62443	3.33E-03	207.96					
0.77928	1.05E-02	2.11371	2.07E-03	80.60					
				808.18					
				18					
				23.09					
				613.57					
				7					
				47.20					
				194.61					
				11					
				9.27					

Table C4.

Column 42 OD_EA	Column 43 OD_EA_err
8.33E-03	7.52E-04
8.36E-03	7.09E-04
1.42E-03	4.17E-04
-7.20E-06	5.40E-04
2.22E-03	2.00E-04
1.74E-03	2.44E-04
3.14E-04	4.81E-04
5.22E-04	4.84E-04
1.15E-02	3.15E-04
1.40E-03	1.87E-04
2.35E-03	2.00E-04
2.54E-03	4.81E-04
2.78E-03	2.06E-04
1.27E-03	5.21E-04
3.57E-03	6.63E-04
4.16E-03	2.34E-04
2.88E-03	2.10E-04

C.10 Description of Table C5

Percent contribution of snow vs. precipitation for all Saginaw and Glacial Drift aquifer samples based on stable isotope data. Values for mean snow and rain end members are also indicated.

Column 1, 'Sample_number', sample number.

Column 2, 'del18O', oxygen stable isotopic composition, per mil relative to VSMOW.

Column 3, 'err_del18O', uncertainty in oxygen stable isotopic composition, per mil, 1 sigma error.

Column 4, 'del_D', hydrogen stable isotopic composition, per mil relative to VSMOW.

Column 5, 'err_del_D', uncertainty in hydrogen stable isotopic composition, per mil, 1 sigma error.

Column 6, '% Snow', Snow contribution, in %

Column 7, '% Rain', Rain contribution, in %

Table C5.

Column 1	Column 2	Column 3	Column 4	Column 5	Column 6	Column 7
Sample_number	del18O	err_del18O	del_D	err_del_D	**% Snow**	% Rain
sg1	-9.65	0.06	-64.00	0.26	29%	71%
sg2	-8.83	0.11	-61.01	1.09	26%	74%
sg3	-9.43	0.11	-65.52	0.63	30%	70%
sg4	-8.49	0.04	-59.17	0.73	25%	75%
sg5	-8.99	0.02	-61.93	0.39	27%	73%
sg6	-9.07	0.07	-62.20	0.75	27%	73%
sg7	-9.47	0.09	-65.14	0.67	29%	71%
sg8*	**-13.74**	**0.10**	**-101.40**	**0.74**	**57%**	**43%**
sg9	-10.52	0.06	-73.59	0.59	36%	64%
sg10*	**-12.83**	**0.11**	**-89.86**	**1.31**	**48%**	**52%**
sg11	-10.27	0.07	-73.04	0.67	35%	65%
sg12	-9.10	0.11	-63.00	0.87	28%	72%
sg13	-11.04	0.11	-79.57	0.55	40%	60%
sg14*	**-14.30**	**0.07**	**-100.89**	**0.46**	**57%**	**43%**
sg15*	**-17.48**	**0.05**	**-124.03**	**0.62**	**74%**	**26%**
sg16*	**-15.98**	**0.11**	**-118.62**	**0.43**	**70%**	**30%**
Mean Rain	-4.81	0.12	-26.48	1.41		
Mean Snow	-21.31	0.11	-157.62	1.16		
Hall et al., 2005						
4	-9.66	0.03	-59.93	0.14	26%	74%
5	-9.33	0.04	-58.71	0.1	25%	75%
6	-9.49	0.01	-60.77	0.11	26%	74%
7	-9.53	0.02	-59.04	0.08	25%	75%
8	-9.52	0.02	-61.24	0.02	27%	73%
9	-9.33	0.01	-61.73	0.36	27%	73%
10	-9.45	0.03	-61.61	0.36	27%	73%
11	-9.48	0.03	-60.23	0.77	26%	74%
				Mean	**26%**	**74%**

*Samples with groundwater ages beyond the LGM

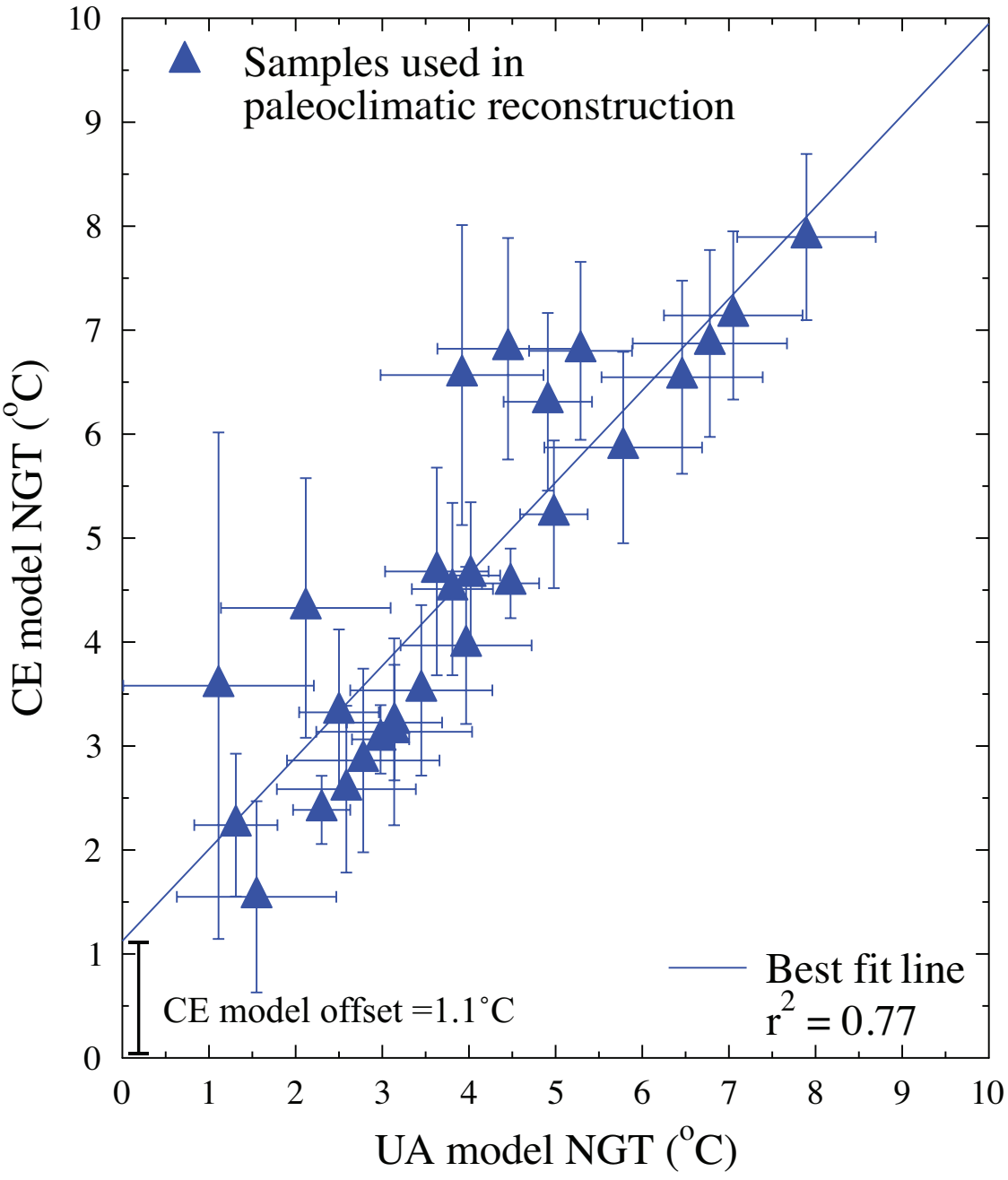

Figure C1. Comparison of CE and UA model NGTs for all Saginaw and Marshall aquifer samples younger than the LGM.

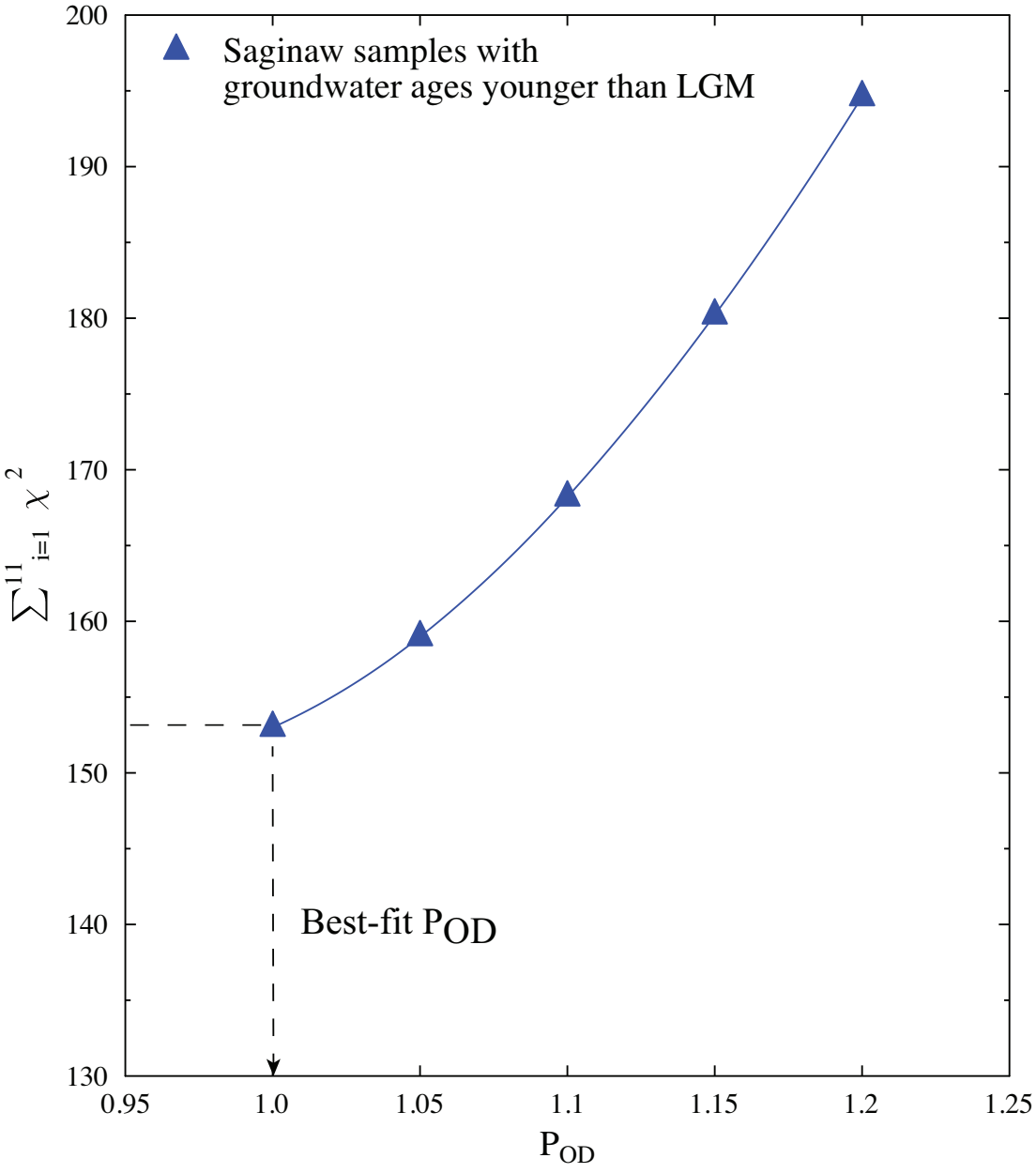

Figure C2. Chi squared fits to entire suite of groundwater samples with ages less than LGM for varying OD model factor, POD.

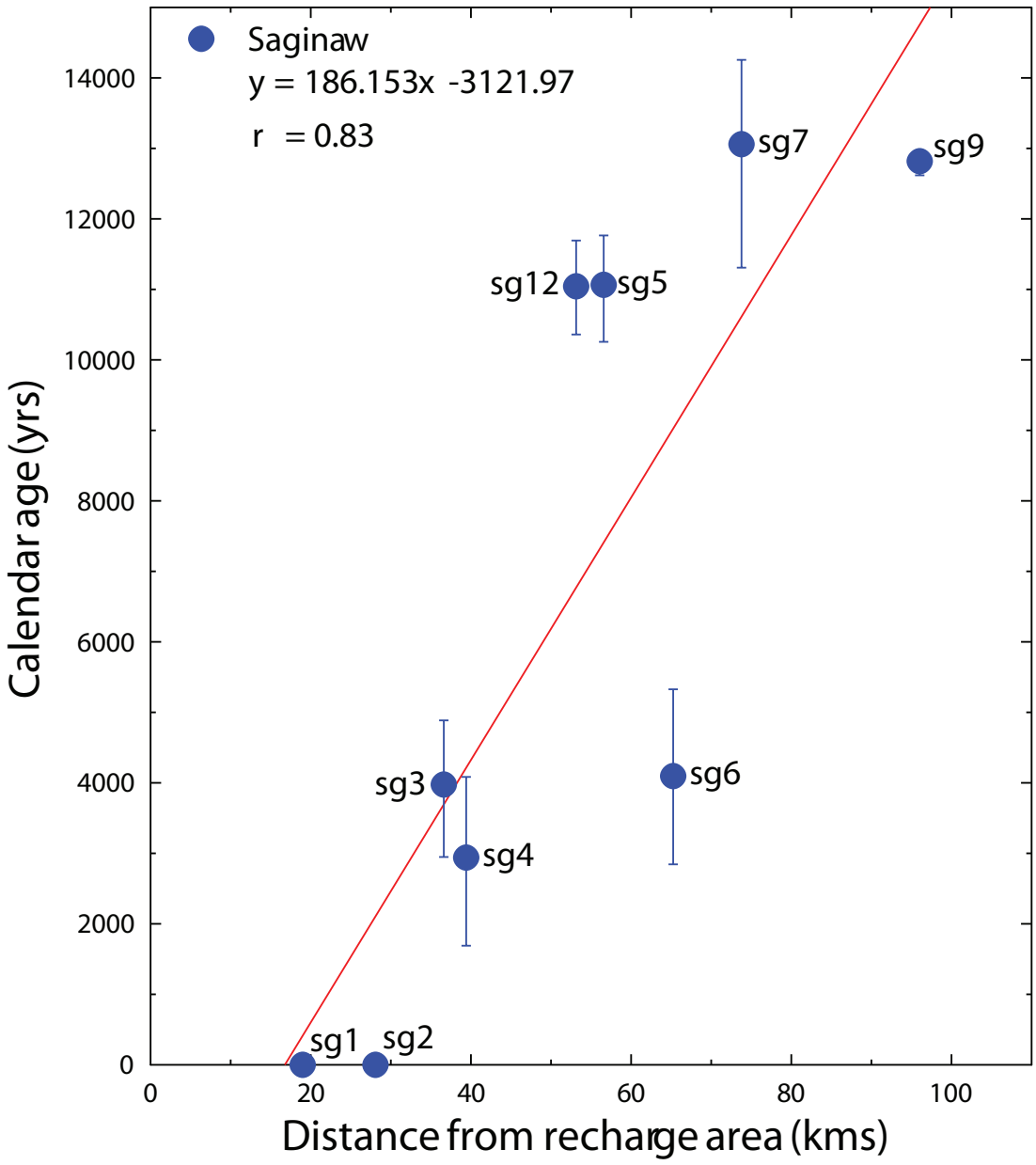

Figure C3. Calendar age as a function of distance from recharge area for all Saginaw samples used in the paleoclimatic reconstruction in this study.

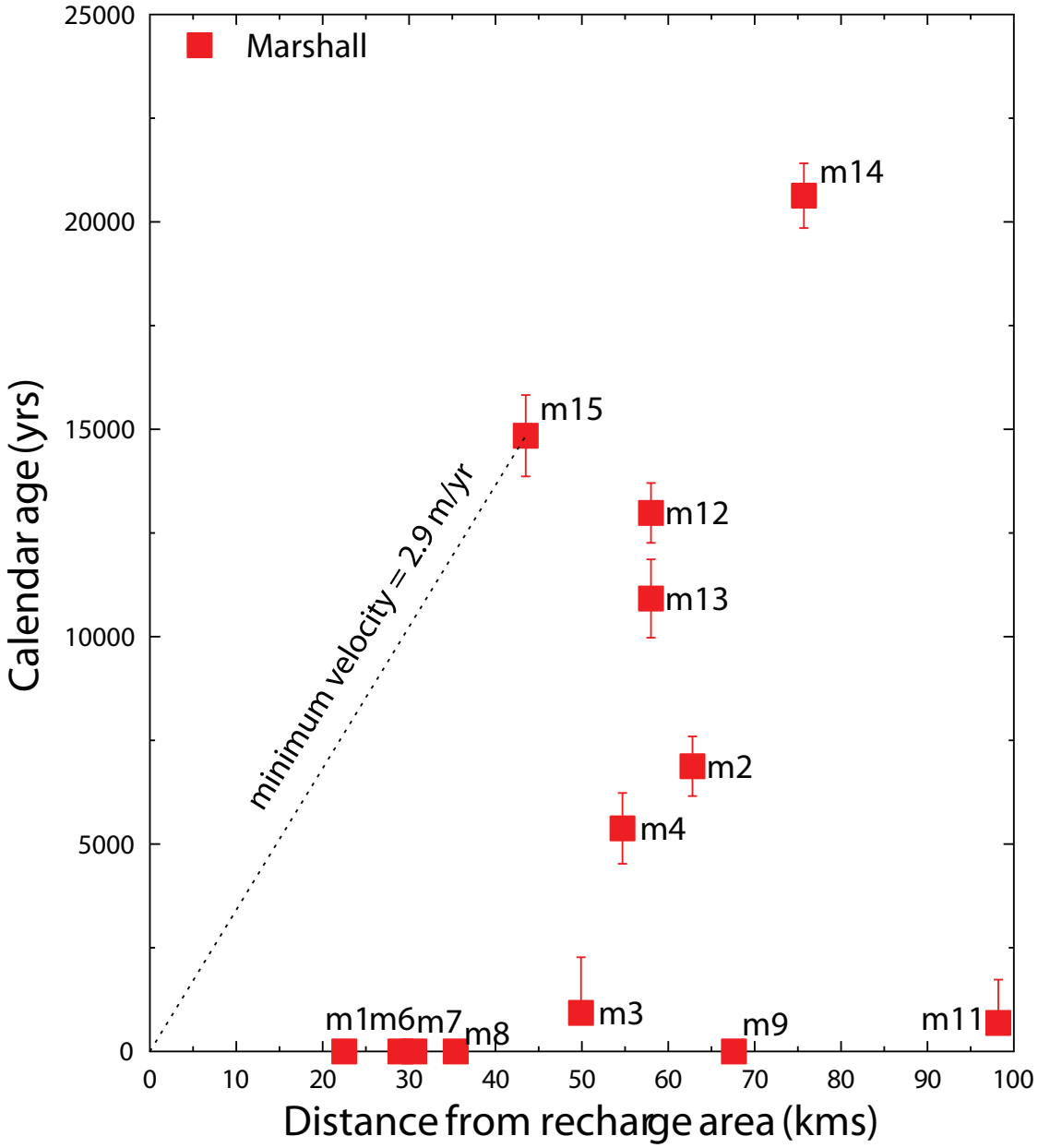

Figure C4. Calendar age as a function of distance from recharge area for all Marshall samples used in the paleoclimatic reconstruction in this study.

References

Aeschbach-Hertig, W., F. Peeters, U. Beyerle, and R. Kipfer (2000), Paleotemperature reconstruction from noble gases in ground water taking into account equilibration with entrapped air, *Nature*, *405*, 1040–1044.

Aeschbach-Hertig, W., M. Stute, J. F. Clark, R. F. Reuter, and P. Schlosser (2002), A paleotemperature record derived from dissolved noble gases in groundwater of the Aquia Aquifer (Maryland, USA), *Geochimica et Cosmochimica Acta*, *66*(5), 797-817.

Aeschbach-Hertig, W., H. El-Gamal, M. Wieser, and L. Palcsu (2008), Modeling excess air and degassing in groundwater by equilibrium partitioning with a gas phase, *Water Resour. Res.*, *44*.

Baker, R. G., L. A. Gonzalez, M. Raymo, E. A. Bettis, M. K. Reagan, and J. A. Dorale (1998), Comparison of multiple proxy records of Holocene environments in the midwestern United States, *Geology*, *26*(12), 1131-1134.

Ballentine, C. J., and C. M. Hall (1999), Determining paleotemperature and other variables using noble gas concentrations in water., *Geochim. Cosmochim. Acta.*, *63*, 2315-2336.

Bartlein, P., et al. (2011), Pollen-based continental climate reconstructions at 6 and 21 ka: a global synthesis, *Climate Dynamics*, *37*(3), 775-802.

Castro, M.C., Goblet, P. (2003), Noble gas thermometry and hydrologic ages: Evidence for late Holocene warming in Southwest Texas. Geophysical Research Letters 30.

Castro, M. C. (2004), Helium sources in passive margin aquifers, A new evidence for a significant mantle ^{3}He source in aquifers with unexpectedly low in situ 3He/4He production, *Earth and Planetary Science Letters*, *222*(3-4), 897-913.

Castro, M. C., C. M. Hall, D. Patriarche, P. Goblet, and B. R. Ellis (2007), A new noble gas paleoclimate record in Texas – basic assumptions revisited, *Earth and Planetary Science Letters*, *257*, 170-187.

Castro, M. C., L. Ma, and C. M. Hall (2009), A primordial, solar He-Ne signature in crustal fluids of a stable continental region, *Earth and Planetary Science Letters*, *279*(3-4), 174-184.

Dorale, J. A., L. A. Gonzalez, M. K. Reagan, D. A. Pickett, M. T. Murrell, and R. G. Baker (1992), A High-Resolution Record of Holocene Climate Change in Spele, *Science*, *258*(5088), 1626.

Eichinger, L. (1983), A contribution to the interpretation of 14C groundwater ages considering the example of a partially confined sandstone aquifer, *Radiocarbon*, *25*(2), 347-356.

Evans, G. V., R. L. Otlet, A. Downing, R. A. Monkhouse, and G. Rae (1979), *Some problems in the interpretation of isotope measurements in United Kingdom*

aquifers,, IAEA, Vienna.

Fontes, J. C., and J. M. Garnier (1979), Determination of the Initial 14C Activity of the Total Dissolved Carbon: A Review of the Existing Models and a New Approach *Water Resour. Res.*, *15*(2), 399-413.

Graham, D. W. (2002), Noble Gas Isotope Geochemistry of Mid-Ocean Ridge and Ocean Island Basalts: Characterization of Mantle Source Reservoirs, *Reviews in Mineralogy and Geochemistry*, *47*(1), 247-317.

Hall, C. M., M. C. Castro, K. C. Lohmann, and L. Ma (2005), Noble gases and stable isotopes in a shallow aquifer in southern Michigan: Implications for noble gas paleotemperature reconstructions for cool climates, *Geophys. Res. Lett.*, *32*(18), L18404.

Hall, C. M., M. C. Castro, K. C. Lohmann, and T. Sun (2012), Testing the noble gas paleothermometer with a yearlong study of groundwater noble gases in an instrumented monitoring well, *Water Resour. Res.*, *48*(4), W04517.

Hilton, D. R., and D. Porcelli (2003), *Noble gases as mantle tracers. In: The Mantle and Core (ed. Carlson, R.W.)*, Elsevier-Pergamon, Oxford.

Hou, J., Y. Huang, W. W. Oswald, D. R. Foster, and B. Shuman (2007), Centennial-scale compound-specific hydrogen isotope record of Pleistocene-Holocene climate transition from southern New England, *Geophys. Res. Lett.*, *34*(19), L19706.

Jones, G.A., A.P. McNichol, and K.F. VonReden (1990), The National Ocean Sciences AMS facility at Woods Hole Oceanographic Institiution. Nucl. Inst. Meth. Phys. Res., v 52, 278-284.

Kipfer, R., W. Aeschbach-Hertig, F. Peeters, and M. Stute (2002), Noble Gases in Lakes and Ground Waters, *Reviews in Mineralogy and Geochemistry*, *47*(1), 615-700.

Kirby, M. E., H. T. Mullins, W. P. Patterson, and A. W. Burnett (2002), Late glacial-Holocene atmospheric circulation and precipitation in the northeast United States inferred from modern calibrated stable oxygen and carbon isotopes, *Geological Society of America Bulletin*, *114*(10), 1326-1340.

Ma, L., M. C. Castro, and C. M. Hall (2004), A late Pleistocene-Holocene noble gas paleotemperature record in southern Michigan, *Geophys. Res. Lett.*, *31*(23), L23204.

Ma, L., M. C. Castro, C. M. Hall, and L. M. Walter (2005), Cross-formational flow and salinity sources inferred from a combined study of helium concentrations, isotopic ratios, and major elements in the Marshall aquifer, southern Michigan, *Geochem. Geophys. Geosyst.*, *6*(10), Q10004.

Manny, B. A., R. G. Wetzel, and R. E. Bailey (1978), Paleolimnological sedimentation of organic carbon, nitrogen, phosphorus, fossil pigments, pollen, and diatoms in a hypereutrophic, hardwater lake: A case study of eutrophism. , *Polskie Archiwum Hydrobiologii*, *25*, 243-267.

Ozima, M., and F. A. Podosek (2002), *Noble gas geochemistry*, xiv, 286 p. pp., Cambridge University Press, Cambridge, UK ; New York.

Pearson, F., Jr., , and D. White (1967), Carbon 14 Ages and Flow Rates of Water in Carrizo Sand, Atascosa County, Texas *Water Resour. Res.*, *3*(1), 251-261.

Peteet, D. M., R. A. Daniels, L. E. Heusser, J. S. Vogel, J. R. Southon, and D. E. Nelson (1993), Late-glacial pollen, macrofossils and fish remains in northeastern U.S.A.-The Younger Dryas oscillation: A contribution to the 'North Atlantic seaboard programme' of IGCP-253, 'Termination of the Pleistocene', Quaternary Science Reviews, 12(8), 597-612.

Reimer, P. J., et al. (2009), INTCAL09 AND MARINE09 RADIOCARBON AGE CALIBRATION CURVES, 0–50,000 YEARS CAL BP, *Radiocarbon*, *51*(4), 1111-1150.

Saini-Eidukat, B., and A. Yahin (1999), Web-phreeq: a WWW instructional tool for modeling the distribution of chemical species in water, *Computers & Geosciences*, *25*(4), 347-353.

Siegel, D. I., K. A. Lesniak, M. Stute, and S. Frape (2004), Isotopic geochemistry of the Saratoga springs: Implications for the origin of solutes and source of carbon dioxide, *Geology*, *32*(3), 257-260.

Stuiver, M., and P. J. Reimer (1993), Extended 14C database and revised CALIB radiocarbon calibration program, *Radiocarbon 35*, 215-230.

Stute, M., and P. Schlosser (Eds.) (1993), *Principles and applications of the Noble gas paleothermometer: in Climate Change in Continental Isotopic Recors*, 89– 100 pp., AGU, Washington, D. C.

Sun, T., C. M. Hall, M. C. Castro, K. C. Lohmann, and P. Goblet (2008), Excess air in the noble gas groundwater paleothermometer: A new model based on diffusion in the gas phase, *Geophysical Research Letters*, *35*(19).

Sun, T., C. M. Hall, and M. C. Castro (2010), Statistical properties of groundwater noble gas paleoclimate models: Are they robust and unbiased estimators?, *Geochem. Geophys. Geosyst.*, *11*(Q02002).

Taylor, K. C., et al. (1997), The Holocene-Younger Dryas Transition Recorded at Summit, Greenland, *Science*, *278*(5339), 825-827.

Torgersen, T., S. Drenkard, M. Stute, P. Schlosser, and A. Shapiro (1995), Mantle Helium in ground waters of eastern North-America- Time and space constraints on sources, *Geology*, *23*(8), 675-678.

Yu, Z. C. (2007), Rapid response of forested vegetation to multiple climatic oscillations during the last deglaciation in the northeastern United States, *Quaternary Research*, *67*(2), 297-303.

Viau, A. E., K. Gajewski, M. C. Sawada, and P. Fines (2006), Millennial-scale temperature variations in North America during the Holocene, *J. Geophys. Res.*, *111*(D9), D09102.

Wetherill, G. W. (1954), Variations in the Isotopic Abundances of Neon and Argon Extracted from Radioactive Minerals, *Physical Review*, *96*(3), 679-683.

Winkler, M. G., A. M. Swain, and J. E. Kutzbach (1986), Middle Holocene dry period in the northern Midwestern United States: Lake levels and pollen stratigraphy, *Quaternary Research*, *25*(2), 235-250.

Zhao, C., Z. Yu, E. Ito, and Y. Zhao (2010), Holocene climate trend, variability, and shift documented by lacustrine stable-isotope record in the northeastern United States, *Quaternary Science Reviews*, *29*(15-16), 1831-1843.

APPENDIX D : SUPPLEMENTARY MATERIAL FOR CHAPTER 5

D.1 Introduction

This auxiliary material contains supporting information for chapter 5. Description of CE model results is included in D.2. Calculation of maximum noble gas excesses that can be produced by an O_2 depletion mechanisms are described in D.3. Measured noble gas isotopic ratios for all Saginaw aquifer samples along with atmospheric and crustal end-member ratios are provided in Table D1. Measured noble gas concentrations and isotopic ratios along with sampling location, well depth and salinity for Marshall aquifer sample, M-16, is provided in Table D2. Measured ^{22}Ne, ^{36}Ar, ^{84}Kr and ^{130}Xe for all Saginaw aquifer samples and Marshall aquifer sample are provided in Table D3. Diffusion and solubility constants used for modeling Rayleigh fractionation effects on atmospheric noble gases are provided in Table D4.

D.2 Description of CE model results for all Saginaw aquifer samples

Description of CE model results

Measured noble gas concentrations (Ne, Ar, Kr and Xe) for all Saginaw samples were fit to the CE model assuming a mean recharge altitude of 275m and 0g/l salinity. Table 5.2 summarizes the results of inverse fitting measured noble gas concentrations for all 22 Saginaw samples.

Model results indicate that 17 out of 22 samples converge using the CE model. In particular, four out of five samples that do not converge (sg3, 5a, 10 and 15) indicate excessively high excess air values. This tendency of the CE model to sometimes overestimate the amount of excess air was previously discussed by *Sun et al.* [2010]. In addition, sample sg12b, which indicated depleted noble gas patterns (Figure 5.2) could not be fitted using the CE model. However, other Saginaw samples with depleted noble gas concentrations (sg1a, 1b) could be adequately fit using the CE model with F>1 (cf. Table 5.2). Although the CE model is generally capable of adequately describing degassed samples [*Aeschbach-Hertig et al.*, 2008], we ignore at present the reason underlying the inability of the CE model to adequately fit sg12b. For all other samples, goodness of fit of measured noble gas concentrations to any particular NGT model is given by χ^2 (Table 5.2), which is the sum of the squared deviations between modeled and measured concentrations, weighted with the experimental 1σ errors. χ^2 statistics determined from the inverse fits of noble gas concentrations provide a unique tool to assess the applicability of specific NGT models used to invert the data. When analyzing an entire suite of samples, goodness-of-fit is usually tested using the mean square

weighted deviate (MSWD), which is related to the χ^2 value determined in the inverse fit by MSWD=χ^2/N, where N, is the number of degrees of freedom for the entire suite of samples (see e.g., *Aeschbach-Hertig et al*., 1999, *Ballentine and Hall*, 1999, *Sun et al*., 2010). The CE model with three fit parameters (F, ν and q), four measured values (Ne, Ar, Kr, Xe), and 17 samples considered has 17 degrees of freedom (N). The sum of χ^2 values for these 17 samples (cf. Table 5.2) corresponds to a MSWD of 10.89. Ninety-nine percent of datasets (p=0.01) should have a MSWD below 6.63 with 17 degrees of freedom. Our comparison of MSWD at the 99% confidence level suggests that there is a misfit between measured and model concentrations when the dataset with 17 samples is taken in its entirety. Closer inspection of model results suggests that significant misfit arises due to poor fits for samples sg14 and sg8b. In particular, sg8b indicates NGTs below the freezing point of water (0˚C), a temperature at which it is physically impossible for recharge to occur and the Henry constants used for the NGT inversion are no longer applicable. Indeed, if one excludes these samples, the overall goodness of fit is improved to yield a MSWD of 5.67, which is acceptable at the 99% confidence level. Thus, analyses of CE model parameters presented in this study include only 13 samples with adequate fits (p>0.01) and exclude degassed samples (sg1a, 1b, 12b), samples that do not converge (sg3, 5a, 10, 15) as well as samples sg14 and sg8b.

D.3 Calculation of maximum noble gas excesses that can be produced by an O_2 depletion mechanism

One of the core assumptions of the noble gas thermometer is that the composition of soil air in the unsaturated zone is identical to air with 100% relative humidity. However, *Hall et al.* [2005] and *Castro et al.* [2007] questioned this core assumption in order to account for the systematic bias of NGTs to values below average ground temperature. In particular, they argued that if a significant amount of O_2 is consumed by biological activity without an equivalent build up of gaseous CO_2, partial pressures of all other gases should be elevated so as to conserve total atmospheric pressure. *Sun et al*. [2008] subsequently measured dissolved oxygen (DO) at the water table as well as CO_2 in the unsaturated zone just above the water table in the Glacial Drift aquifer in southern Michigan. They found only ~45% of the DO saturation values without being compensated by increased CO_2. This suggests that the unsaturated zone was missing about 10-11% of its original suite of active gases. Below, we calculate the maximum excess of noble gases that can be produced by such an oxygen depletion mechanism. Maximum excess of noble gases by oxygen depletion will be produced if all the soil O_2 was consumed by biological activity and was subsequently not replaced by any gaseous CO_2 or other gases. If the composition of soil air is assumed to originally be identical to the atmosphere, ~21% of dry soil air would be made up of O_2 [*Ozima and Podosek*, 2002]. If all of this O_2 is consumed by biological activity without being replaced by any gases, soil air would contain solely 79% of its original suite of active gases. In order to maintain total atmospheric pressure, a loss of all O_2 in the soil air would thus lead to an increase in excess of all other gases by:

((100/79)-1)*100=26.6%

Thus, maximum excesses of noble gases that can by produced by an oxygen depletion mechanism is only ~26.6%. By contrast, large observed noble gas excesses (Figure 5.2) in Saginaw samples from the SL region are between ~80-124% $C_{Ne}/C_{ASW,Ne}$ suggesting that the oxygen depletion mechanism, if present, is likely to only be a minor contribution to the observed excesses.

D.4 Description of Table D1: Measured noble gas isotopic ratios and end-member ratios for atmosphere, crust and mantle reservoirs.

1. Column 1: "Sample No.", Sample number
2. Column 2: "$^{20}Ne/^{22}Ne$", measured $^{20}Ne/^{22}Ne$, no units.
3. Column 3: "$\pm 1\sigma$", 1 sigma error in $^{20}Ne/^{22}Ne$, no units.
4. Column 4: "$^{21}Ne/^{22}Ne$", measured $^{21}Ne/^{22}Ne$, no units.
5. Column 5: "$\pm 1\ \sigma$", 1 sigma error in 21Ne/22Ne, no units.
6. Column 6: "$^{38}Ar/^{36}Ar$", measured $^{38}Ar/^{36}Ar$, no units.
7. Column 7: "$\pm 1\sigma$", 1 sigma error in $^{38}Ar/^{36}Ar$, no units.
8. Column 8: "$^{40}Ar/^{36}Ar$", measured $^{40}Ar/^{36}Ar$, no units.
9. Column 9: "$\pm 1\sigma$", 1 sigma error in $^{40}Ar/^{36}Ar$, no units.
10. Column 10: "$^{86}Kr/^{84}Kr$", measured $^{86}Kr/^{84}Kr$, no units.
11. Column 11: "$\pm 1\sigma$", 1 sigma error in $^{86}Kr/^{84}Kr$, no units.
12. Column 12: "$^{129}Xe/^{130}Xe$", measured $^{129}Xe/^{130}Xe$, no units.
13. Column 13: "$\pm 1\sigma$", 1 sigma error in $^{129}Xe/^{130}Xe$, no units.
14. Column 14: "$^{132}Xe/^{130}Xe$", measured $^{132}Xe/^{130}Xe$, no units.
15. Column 15: "$\pm 1\sigma$", 1 sigma error in $^{132}Xe/^{130}Xe$, no units.
16. Column 16: "$^{134}Xe/^{130}Xe$", measured $^{134}Xe/^{130}Xe$, no units.
17. Column 17: "$\pm 1\sigma$", 1 sigma error in $^{134}Xe/^{130}Xe$, no units.
18. Column 18: "$^{136}Xe/^{130}Xe$", measured $^{136}Xe/^{130}Xe$, no units.
19. Column 19: "$\pm 1\sigma$", 1 sigma error in $^{136}Xe/^{130}Xe$, no units.

Table D1

Sample No.	$^{20}Ne/^{22}Ne$	± 1s	$^{21}Ne/^{22}Ne$	± 1s	$^{38}Ar/^{36}Ar$	± 1s	$^{40}Ar/^{36}Ar$	± 1s	$^{86}Kr/^{84}Kr$	± 1s	$^{129}Xe/^{130}Xe$	± 1s	$^{132}Xe/^{130}Xe$	± 1s	$^{134}Xe/^{130}Xe$	± 1s	$^{136}Xe/^{130}Xe$	± 1s
sg1a	9.87	0.16	0.0285	0.0003	0.1894	0.0014	295.1	0.7	0.3065	0.0011	6.517	0.065	6.637	0.064	2.566	0.024	2.194	0.021
sg1b	9.82	0.04	0.0293	0.0002	0.1892	0.0009	295.6	0.8	0.3025	0.0018	6.492	0.036	6.623	0.038	2.556	0.014	2.165	0.011
sg2	9.84	0.03	0.0294	0.0002	0.1871	0.0021	295	0.6	0.306	0.0008	6.479	0.035	6.573	0.032	2.555	0.013	2.165	0.011
sg3	9.91	0.04	0.0299	0.0002	0.1881	0.0018	295.3	0.5	0.3068	0.0011	6.524	0.046	6.671	0.053	2.586	0.02	2.2	0.016
sg4a	9.82	0.05	0.0293	0.0003	0.1867	0.002	294.5	1	0.3071	0.001	6.473	0.085	6.625	0.066	2.569	0.027	2.207	0.024
sg4b	9.74	0.03	0.0287	0.0001	0.1872	0.0006	296.3	0.9	0.3057	0.0023	6.45	0.03	6.567	0.029	2.553	0.009	2.169	0.009
sg5a	9.85	0.04	0.0283	0.0004	0.1878	0.0018	296.7	0.7	0.3063	0.001	6.439	0.085	6.611	0.093	2.548	0.037	2.156	0.033
sg5b	9.8	0.03	0.0291	0.0002	0.1873	0.0004	295.7	0.9	0.3049	0.0019	6.549	0.027	6.658	0.025	2.578	0.008	2.193	0.008
sg6a	9.88	0.06	0.0294	0.0003	0.1875	0.0026	295.3	0.7	0.3045	0.0009	6.472	0.088	6.581	0.083	2.571	0.034	2.165	0.03
sg6b	9.8	0.03	0.029	0.0002	0.1877	0.0009	295	0.7	0.3045	0.002	6.505	0.027	6.626	0.026	2.568	0.01	2.184	0.008
sg7	9.82	0.03	0.0292	0.0003	0.188	0.0006	295.6	0.8	0.3046	0.0022	6.475	0.028	6.566	0.033	2.556	0.012	2.17	0.01
sg9	9.84	0.04	0.0293	0.0002	0.1875	0.0024	295.9	0.7	0.3048	0.0008	6.391	0.113	6.503	0.127	2.562	0.048	2.153	0.042
sg11	9.79	0.04	0.0289	0.0002	0.1877	0.0005	295.1	0.8	0.3046	0.0021	6.523	0.031	6.609	0.033	2.559	0.011	2.189	0.009
sg12a	9.83	0.02	0.0292	0.0002	0.1882	0.0007	295	0.9	0.3059	0.002	6.502	0.026	6.618	0.03	2.563	0.011	2.176	0.009
sg12b	9.83	0.04	0.0294	0.0002	0.1877	0.0018	295.8	0.5	0.3048	0.0008	6.542	0.058	6.622	0.057	2.575	0.023	2.176	0.019
Samples in Saginaw Lowlands area																		
sg8a	9.75	0.03	0.0289	0.0002	0.1881	0.0006	295.7	0.9	0.3044	0.002	6.52	0.032	6.638	0.033	2.576	0.011	2.204	0.011
sg8b	9.83	0.06	0.0295	0.0003	0.1877	0.0017	295.5	0.9	0.3055	0.0011	6.47	0.064	6.615	0.066	2.565	0.028	2.179	0.024
sg10	9.8	0.03	0.029	0.0001	0.1884	0.0008	296	1.1	0.3057	0.0024	6.493	0.026	6.607	0.027	2.572	0.011	2.179	0.009
sg13	9.79	0.03	0.0293	0.0001	0.1887	0.0007	295.7	0.8	0.3075	0.0024	6.53	0.039	6.658	0.036	2.568	0.014	2.175	0.012
sg14	9.78	0.05	0.029	0.0002	0.1857	0.0021	296.6	1.3	0.3053	0.001	6.416	0.067	6.565	0.069	2.53	0.029	2.164	0.026
sg15	9.82	0.03	0.0293	0.0002	0.1871	0.0005	295.1	1	0.3068	0.0024	6.479	0.028	6.604	0.029	2.569	0.011	2.186	0.009
sg16	9.79	0.02	0.0289	0.0001	0.1869	0.0006	296.2	0.9	0.3052	0.002	6.512	0.039	6.612	0.039	2.555	0.014	2.178	0.013
Air[a]	9.8		0.029		0.188		295.5		0.3052		6.496		6.607		2.563		2.176	

[a]Ozima and Podosek (2002)

D5. Description of Table D2: Measured noble gas concentrations and isotopic ratios along with sampling location, well depth and salinity for Marshall aquifer sample, M-16

1. Column 1: "Sample No.", Sample number, no units.
2. Column 2: "Lat.", Latitude, degrees.
3. Column 3: "Long.", Longitude, degrees.
4. Column 4: "Well depth", sampling well depth, meters.
5. Column 5: "Salinity", salinity, g/l.
6. Column 6: "Ne", measured Ne concentration, ccSTP/g.
7. Column 7: "Ar", measured Ar concentration, ccSTP/g.
8. Column 8: "Kr", measured Kr concentration, ccSTP/g.
9. Column 9: "Xe", measured Xe concentration, ccSTP/g.
10. Column 2: "$^{20}Ne/^{22}Ne$", measured $^{20}Ne/^{22}Ne$, no units.
11. Column 3: "$\pm 1\sigma$", 1 sigma error in $^{20}Ne/^{22}Ne$, no units.
12. Column 4: "$^{21}Ne/^{22}Ne$", measured $^{21}Ne/^{22}Ne$, no units.
13. Column 5: "$\pm 1\ \sigma$", 1 sigma error in 21Ne/22Ne, no units.
14. Column 6: "$^{38}Ar/^{36}Ar$", measured $^{38}Ar/^{36}Ar$, no units.
15. Column 7: "$\pm 1\sigma$", 1 sigma error in $^{38}Ar/^{36}Ar$, no units.
16. Column 8: "$^{40}Ar/^{36}Ar$", measured $^{40}Ar/^{36}Ar$, no units.
17. Column 9: "$\pm 1\sigma$", 1 sigma error in $^{40}Ar/^{36}Ar$, no units.
18. Column 10: "$^{86}Kr/^{84}Kr$", measured $^{86}Kr/^{84}Kr$, no units.
19. Column 11: "$\pm 1\sigma$", 1 sigma error in $^{86}Kr/^{84}Kr$, no units.
20. Column 12: "$^{129}Xe/^{130}Xe$", measured $^{129}Xe/^{130}Xe$, no units.
21. Column 13: "$\pm 1\sigma$", 1 sigma error in $^{129}Xe/^{130}Xe$, no units.

22. Column 14: "$^{132}Xe/^{130}Xe$", measured $^{132}Xe/^{130}Xe$, no units.

23. Column 15: "$\pm 1\sigma$", 1 sigma error in $^{132}Xe/^{130}Xe$, no units.

24. Column 16: "$^{134}Xe/^{130}Xe$", measured $^{134}Xe/^{130}Xe$, no units.

25. Column 17: "$\pm 1\sigma$", 1 sigma error in $^{134}Xe/^{130}Xe$, no units.

26. Column 18: "$^{136}Xe/^{130}Xe$", measured $^{136}Xe/^{130}Xe$, no units.

27. Column 19: "$\pm 1\sigma$", 1 sigma error in $^{136}Xe/^{130}Xe$, no units.

Table D2. Sample number, location, well depth, salinity, noble gas concentrations and isotopic ratios for a Marshall brine sample located in the Saginaw lowlands (SL) area.

Sample No.	Lat. (deg)	Long. (deg)	Well depth (m)	Salinity (g/l)	Ne (ccSTP/g)	Ar (ccSTP/g)	Kr (ccSTP/g)	Xe (ccSTP/g)	$^{20}Ne/^{22}Ne$	± 1σ	$^{21}Ne/^{22}Ne$	± 1σ
M-16	43.63	-84.13	313	217	2.420E-7	1.47E-4	1.71E-8	1.73E-9	9.71	0.04	0.0336	0.0047

$^{38}Ar/^{36}Ar$	± 1σ	$^{40}Ar/^{36}Ar$	± 1σ	$^{86}Kr/^{84}Kr$	± 1σ	$^{129}Xe/^{130}Xe$	± 1σ	$^{132}Xe/^{130}Xe$	± 1σ	$^{134}Xe/^{130}Xe$	± 1σ	$^{136}Xe/^{130}Xe$	± 1σ
0.1912	0.0152	309.7	5.6	0.3044	0.0013	6.534	0.105	6.650	0.086	2.572	0.045	2.177	0.034

D.6 Description of Table D3: Measured ^{22}Ne, ^{36}Ar, ^{84}Kr and ^{130}Xe for all Saginaw aquifer samples and Marshall aquifer sample.

1. Column 1: "^{22}Ne", Measured ^{22}Ne concentration, ccSTP/g.
2. Column 2: "^{36}Ar", Measured ^{36}Ar concentration, ccSTP/g.
3. Column 3: "^{84}Kr", Measured ^{84}Kr concentration, ccSTP/g.
4. Column 4: "^{130}Xe", Measured ^{130}Xe concentration, ccSTP/g.

Table D3. Measured ^{22}Ne, ^{36}Ar, ^{84}Kr and ^{130}Xe for all Saginaw aquifer samples as well as a Marshall brine sample (cf. Table D2)[a].

Sample No.	^{22}Ne (ccSTP/g)	^{36}Ar (ccSTP/g)	^{84}Kr (ccSTP/g)	^{130}Xe (ccSTP/g)
sg1a	7.96E-09	9.00E-07	4.14E-08	5.16E-10
sg1b	1.02E-08	1.07E-06	5.08E-08	6.10E-10
sg2	2.35E-08	1.43E-06	5.35E-08	6.01E-10
sg3	2.41E-08	1.64E-06	6.30E-08	5.75E-10
sg4a	2.46E-08	1.61E-06	6.15E-08	6.67E-10
sg4b	2.37E-08	1.57E-06	6.10E-08	6.69E-10
sg5a	2.28E-08	1.42E-06	5.66E-08	6.94E-10
sg5b	2.56E-08	1.58E-06	6.25E-08	7.29E-10
sg6a	2.52E-08	1.61E-06	6.15E-08	6.26E-10
sg6b	2.62E-08	1.58E-06	6.01E-08	6.15E-10
sg7	2.49E-08	1.57E-06	6.05E-08	7.01E-10
sg9	2.90E-08	1.73E-06	6.62E-08	7.97E-10
sg11	2.93E-08	1.79E-06	6.59E-08	7.03E-10
sg12a	2.54E-08	1.60E-06	6.35E-08	7.43E-10
sg12b	1.58E-08	9.18E-07	3.64E-08	4.35E-10
Samples in Saginaw Lowlands area				
sg8a	3.42E-08	2.10E-06	7.84E-08	8.31E-10
sg8b	3.39E-08	2.12E-06	7.93E-08	8.57E-10
sg10	3.46E-08	2.10E-06	7.59E-08	6.41E-10
sg13	2.95E-08	1.74E-06	6.70E-08	7.49E-10
sg14	3.97E-08	2.43E-06	7.75E-08	7.29E-10
sg15	4.07E-08	2.42E-06	8.45E-08	6.81E-10
sg16	4.06E-08	2.44E-06	8.81E-08	8.20E-10
Marshall aquifer				
M-16	2.23E-08	4.95E-07	9.74E-09	7.03E-11

[a]Errors of ^{22}Ne, ^{36}Ar, ^{84}Kr and ^{130}Xe are ±1.3%, ±1.3%, ±1.5% and ±2.2% respectively. All uncertainties are at ±1σ level of confidence.

D.7 Description of Table D4: Diffusion and solubility constants used for modeling Rayleigh fractionation effects on atmospheric noble gases.

1. Column 1: Atmospheric noble gas.
2. Column 2: “D at 40˚C”, Diffusion coefficient at 40˚C, cm^2/s.
3. Column 3: “D at 100˚C”, Diffusion coefficient at 100˚C, cm^2/s.
4. Column 4: “H at 40˚C”, Henry’s law constant at 40˚C, atms kg mol-1.
5. Column 5: “H at 120˚C”, Diffusion coefficient at 40˚C, atms kg mol-1.

Table D4. Diffusion and solubility constants used for modeling Rayleigh fractionation effects on atmospheric noble gases.

	D at 40°C[a] (x 10^{-5} cm^2s^{-1})	D at 100°C[a] (x 10^{-5} cm^2s^{-1})	H at 40°C[b] (atm kg mol^{-1})	H at 120°C[b] (atm kg mol^{-1})
^{22}Ne	5.31 ± 0.16	13.27 ± 0.04	7.20E+03	1.88E+03
^{36}Ar	3.83 ± 0.12	10.51 ± 0.32	3.51E+03	1.10E+03
^{84}Kr	2.73 ± 0.08	9.51 ± 0.29	2.20E+03	7.82E+02
^{130}Xe	2.24 ± 0.07	8.5 ± 0.26	1.54E+03	5.69E+02
α ($^{22}Ne/^{36}Ar$)	1.38 ± 0.06	1.26 ± 0.05	2.05	1.71
α ($^{84}Kr/^{36}Ar$)	0.71 ± 0.03	0.9 ± 0.04	0.63	0.71
α ($^{130}Xe/^{36}Ar$)	0.58 ± 0.02	0.81 ± 0.03	0.44	0.52

[a] Calculated after Jähne et al., 1987 and Bourg and Sposito, 2008. ±3% error assumed for diffusion coefficients on account of high temperatures (see e.g., Lipmann et al., 2003)

[b] Henry's law constants for 4.4M NaCl brine solution calculated after Crovetto et al., 1982, Smith, 1985 and Smith and Kennedy, 1983. Because of a lack of solubility data for high temperatures and salinities, Henry's law constants at 120°C are calculated for a freshwater value.

References

Aeschbach-Hertig, W., F. Peeters, U. Beyerle, Kipfer, R., 1999. Interpretation of dissolved atmospheric noble gases in natural waters. Water Resources Research 35, 2779-2792.

Aeschbach-Hertig, W., El-Gamal, H., Wieser, M., Palcsu, L., 2008. Modeling excess air and degassing in groundwater by equilibrium partitioning with a gas phase. Water Resour. Res. 44.

Ballentine, C.J., Hall, C.M., 1999. Determining paleotemperature and other variables using noble gas concentrations in water. Geochim. Cosmochim. Acta. 63, 2315-2336.

Castro, M.C., Hall, C.M., Patriarche, D., Goblet, P., Ellis, B.R., 2007. A new noble gas paleoclimate record in Texas – basic assumptions revisited. Earth and Planetary Science Letters 257, 170-187.

Hall, C.M., Castro, M.C., Lohmann, K.C., Ma, L., 2005. Noble gases and stable isotopes in a shallow aquifer in southern Michigan: Implications for noble gas paleotemperature reconstructions for cool climates. Geophys. Res. Lett. 32, L18404.

Ozima, M., Podosek, F.A., 2002. Noble gas geochemistry. Cambridge University Press, Cambridge, UK ; New York.

Sun, T., Hall, C.M., Castro, M.C., Lohmann, K.C., Goblet, P., 2008. Excess air in the noble gas groundwater paleothermometer: A new model based on diffusion in the gas phase. Geophys. Res. Lett. 35, L19401.

Sun, T., Hall, C.M., Castro, M.C., 2010. Statistical properties of groundwater noble gas paleoclimate models: Are they robust and unbiased estimators? Geochem. Geophys. Geosyst. 11.